Multiphoton Excited Spectroscopy with Plasmonic and Composite Nanostructures

D i s s e r t a t i o n

zur Erlangung des akademischen Grades

d o c t o r r e r u m n a t u r a l i u m

(Dr. rer. nat.)

im Fach Chemie

Spezialisierung Physikalische und Theoretische Chemie

eingereicht an der

Mathematisch-Naturwissenschaftlichen Fakultät der

Humboldt-Universität zu Berlin

von

M. Sc. Fani Madzharova

Präsidentin der Humboldt-Universität zu Berlin

Prof. Dr.-Ing. Dr. Sabine Kunst

Dekan der Mathematisch-Naturwissenschaftlichen Fakultät

Prof. Dr. Elmar Kulke

Gutachter/in: 1. Prof. Dr. Janina Kneipp
2. Prof. Dr. Peter Hildebrandt
3. Prof. Dr. Wolfgang Schuhmann

Tag der mündlichen Prüfung: 22. Oktober 2019

Abstract

Multiphoton excited spectroscopy and microscopy are of great importance for the optical characterization of materials and molecules. The underlying non-linear effects can be greatly enhanced when they take place in the local fields of plasmonic nanostructures. Surface enhanced hyper Raman scattering (SEHRS) spectroscopy is a two-photon excited approach particularly useful for the vibrational characterization of organic samples due to its high sensitivity with respect to molecular environment and orientation. Applications of SEHRS strongly rely on the plasmonic enhancement by which the low cross sections of the spontaneous hyper Raman scattering (HRS) can be overcome. The aim of this work was to extend the understanding of the enhancement in SEHRS generated by plasmonic and composite nanomaterials, and to apply these nanostructures in SEHRS experiments complemented by the non-linear parametric process of second harmonic generation (SHG) and by surface enhanced Raman scattering (SERS), for the comprehensive probing of organic molecules and materials.

The enhancement from gold nanoparticles with different sizes and shapes as well as from metal films comprised of periodically arranged voids was investigated in SEHRS experiments at 1064 nm excitation using the crystal violet dye and by numerical simulations. The results indicate that aggregates of large spherical gold nanoparticles and nanorods in solution provide very strong electromagnetic enhancement of HRS, suggesting gold nanostructures as very promising SEHRS substrates with several advantages over silver nanoparticles that have mainly been discussed in previous SEHRS studies. Moreover, the homogeneity of the signal, reproducibility in terms of fabrication, and substrate stability can be significantly improved compared to previous approaches by using nanovoid arrays. Further developments of enhancing nanostructures towards multimodal multiphoton spectroscopic applications are demonstrated here by the synthesis and optical characterization of plasmonic-barium titanate nanocomposites. Experiments and numerical simulations with these composite nanoparticles show the possibility of a combined SHG, SEHRS and SERS probing with potential use in bioanalysis. A systematic study on the interaction of amino acids and aromatic thiols with gold and silver nanoparticles was conducted with 1064 nm-excited SEHRS and SERS excited in the visible spectral range. The non-resonant SEHRS spectra of the molecules demonstrate

the complementarity of vibrational spectroscopic information that can be obtained using multiphoton excited approaches together with one-photon excited SERS. In conclusion, this work underlines that a better understanding and a rational design of improved plasmonic nanostructures allow to combine SEHRS and other multiphoton excited effects, and to use them in analytical chemistry and biophysics.

Zusammenfassung

Mehrphotonen-angeregte Spektroskopie und Mikroskopie sind von großer Bedeutung für die optische Charakterisierung von Materialien und Molekülen. Die zugrunde liegenden nichtlinearen Effekte können erheblich verstärkt werden, wenn sie in den lokalen Feldern plasmonischer Nanostrukturen stattfinden. Die oberflächenverstärkte Hyper-Raman-Streuung (SEHRS) beruht auf Zweiphotonen-Anregung und ist aufgrund ihrer hohen Empfindlichkeit in Bezug auf die molekulare Umgebung und Orientierung für die schwingungsspektroskopische Strukturaufklärung organischer Proben besonders gut geeignet. Anwendungen von SEHRS beruhen stark auf der plasmonischen Verstärkung, mit der die geringen Querschnitte der spontanen Hyper-Raman-Streuung (HRS) um mehrere Größenordnungen erhöht werden können. Ziel dieser Arbeit war es, das Verständnis der durch plasmonische und Komposit-Nanomaterialien verursachten SEHRS-Verstärkung zu vertiefen und diese Nanostrukturen in SEHRS-Experimenten, die durch den nichtlinearen parametrischen Prozess der Frequenzverdopplung (SHG) und der oberflächenverstärkten Raman-Streuung (SERS) ergänzt werden, zur umfassenden Untersuchung organischer Moleküle und Materialien anzuwenden.

Die SEHRS-Verstärkung von Goldnanopartikeln unterschiedlicher Form und Größe sowie von Metallfilmen bestehend aus periodisch angeordneten Hohlräumen (Nanovoids) wurde in Experimenten mit dem Farbstoff Kristallviolett bei einer Anregungswellenlänge von 1064 nm und durch numerische Simulationen untersucht. Die Ergebnisse zeigen, dass Aggregate von großen kugelförmigen Goldnanopartikeln und Nanostäbchen in Lösung eine sehr hohe elektromagnetische SEHRS-Verstärkung bewirken. Demnach sind Goldnanostrukturen vielversprechende SEHRS-Substrate, die mehrere Vorteile gegenüber den in früheren SEHRS-Studien hauptsächlich benutzten Silbernanopartikeln aufweisen. Darüber hinaus können die Homogenität des Signals, die Reproduzierbarkeit in Bezug auf die Herstellung und die Substratstabilität im Vergleich zu früheren Ansätzen durch Verwendung von Nanovoids signifikant verbessert werden. Die Weiterentwicklung von Nanostrukturen für die multimodale Mehrphotonen-Spektroskopie ist hier anhand der Synthese und der optischen Charakterisierung von plasmonischen Bariumtitanat-Nanokompositen demonstriert. Experimente und numerische Simulationen mit diesen Kompositnanopartikeln zeigen die Möglichkeit

einer kombinierten SHG-, SEHRS- und SERS-Untersuchung mit potenziellem Einsatz in der Bioanalyse. Eine systematische Studie der Wechselwirkung von Aminosäuren und aromatischen Thiolen mit Gold- und Silbernanopartikeln wurde mit SEHRS bei einer Anregungswellenlänge von 1064 nm und mit SERS bei Anregungswellenlängen im sichtbaren Spektralbereich durchgeführt. Die nichtresonanten SEHRS-Spektren der Moleküle belegen die Komplementarität der schwingungsspektroskopischen Informationen, die mithilfe von Mehrphotonen-angeregten Prozessen zusammen mit Einphotonen-angeregtem SERS erhalten werden können. Zusammenfassend wurde in dieser Arbeit gezeigt, dass ein tieferes Verständnis und ein rationales Design verbesserter plasmonischer Nanostrukturen ermöglichen, SEHRS mit anderen Mehrphotonen-angeregten Effekten zu kombinieren und diese in der analytischen Chemie und Biophysik einzusetzen.

Contents

Chapter 1

Introduction

The discovery of surface enhanced Raman scattering (SERS)[1–3] has sparked a growing interest in the examination of the optical properties of nanostructured metal surfaces, which can increase weak Raman scattering (RS) signals by many orders of magnitude even at the single molecule level.[4,5] Apart from a so-called chemical contribution, the enormous enhancements were attributed mostly to the highly confined local optical fields of the nanostructures, arising from resonances of their localized surface plasmons with both the incident and the Raman scattered light.[6–9]

In general, all optical effects can benefit from enhanced local optical fields, among them several other vibrational spectroscopies, such as IR absorption,[10] hyper Raman scattering (HRS),[11,12] coherent anti-Stokes Raman scattering (CARS),[13,14] femtosecond stimulated Raman scattering (SRS),[15] and second hyper Raman scattering.[16] This led to the development of several related surface enhanced spectroscopic methods suitable to address numerous analytical and bioanalytical problems.[17–19] The main focus of this thesis is the enhancement of the incoherent, spontaneous two-photon excited Raman process of hyper Raman scattering (HRS). In HRS, the scattered photons are shifted relative to the second harmonic of the excitation wavelength. HRS is a rather weak process, resulting in intensities that are many orders of magnitude lower than those in normal Raman scattering.[20]

Surface enhanced hyper Raman scattering (SEHRS) can be regarded as the two-photon excited analogue of SERS and has been proposed very early after the discovery of SERS.[11,12] In SEHRS, the non-linear HRS is enhanced to a greater extent than linear RS is enhanced in SERS, reaching effective SEHRS cross sections similar or higher than those of two-photon excited fluorescence.[21] Due to its intrinsic characteristics, SEHRS is capable of addressing the need of spectroscopic applications regarding molecular structural sensitivity, detection sensitivity, and spectroscopic imaging. While coherent Raman processes such as (SE-)CARS

or (SE-)SRS are restricted to selected Raman lines that match the frequency difference of two excitation lasers, SEHRS is excited by two photons from the same laser and gives information about the entire vibrational spectrum. SEHRS presents several advantages, mostly relying on the multiphoton excitation, which other vibrational spectroscopies do not have. Specifically, HRS is governed by different selection rules than RS, and therefore offers complementary vibrational information.[22] Depending on the molecular symmetry, HRS may probe IR active modes or in addition so-called silent modes, which are seen neither in Raman nor in IR spectra. In a SEHRS experiment, the excitation with light in the near-infrared region, typically convenient for biological samples, is combined with the desirable detection in the visible spectral range. Besides, the two-photon excitation is favorable for microscopic applications due to the increased penetration depth and limited probed volume,[23] resulting in an improved resolution for imaging. Last but not least, SEHRS has the potential to provide new insights into the structure and interaction of molecules on surfaces, as it is much more sensitive than SERS with respect to orientation and surface environmental changes.[24–27]

This thesis also discusses the coherent non-linear optical process of second harmonic generation (SHG), where a non-centrosymmetric macromolecule or nanostructure yields an effective combination of two photons into a single photon of twice the frequency of the incident beam.[28–30] Here, SHG and SEHRS are both observed using the same optical setup and excited by the same laser illuminating molecules on nanostructured metal surfaces. SHG from centrosymmetric materials such as gold and silver originates from the symmetry breaking at the interface, and can be used to probe local field enhancements.[29,31] In non-centrosymmetric nanocrystals, SHG arises due to bulk contributions, and such harmonic probes have found wide application in multiphoton biomicroscopy.[32,33]

The aim of this work is to gain a better understanding of the factors influencing the enhancement in SEHRS experiments so that the advantages of SEHRS as a multiphoton microspectroscopic method combined with SHG and SERS can be truly exploited for comprehensive vibrational probing of molecular structures. This thesis is organized as follows. Chapter 2 provides information on the physical aspects of SEHRS, and state-of-the-art of its applications. Chapter 3 contains details on the methods used to obtain the experimental results, which are presented in Chapters 4-7. In Chapter 4, the plasmonic enhancement of HRS by different gold nanoparticles and its dependence on their size, shape, and arrangement in nanoaggregate structures is discussed based on experimental data and numerical simulations. Chapter 5 is concerned with the investigation of gold and silver nanovoid arrays

that yield high reproducibility and homogeneity of SEHRS signals, which is required for real analytical applications. In particular, the relation of SEHRS and SHG is discussed to provide important advantages for SEHRS sensing and spectroscopy. The experiments presented in Chapter 6 are devoted to the design and characterization of novel materials composed of non-linear nanocrystal core and plasmonic shell that enable imaging of complex biological materials based on SHG and on vibrational information from SEHRS and SERS spectra. An attempt to explain the experimental observations by numerical simulations will be provided. The potential of SEHRS as vibrational spectroscopy is revealed by the results discussed in Chapter 7, where HRS spectra of important organic and bioorganic molecules in the local fields of gold and silver nanostructures are reported. The selection rules in SEHRS are discussed by comparing the spectra with one-photon excited SERS data. Experiments where local environmental conditions are varied highlight the sensitivity of SEHRS compared to SERS with respect to small changes in orientation and interaction of the molecules with the metal surface. Finally, the main conclusions from the results obtained in this work are summarized in Chapter 8 along with an outlook on potential directions for SEHRS spectroscopy and its future applications.

Chapter 2

Research background

This chapter is partially based on the publication *Chem. Soc. Rev.* 2017, 46, 13, 3980-3999.

In this chapter, fundamental aspects of the physical processes related to this work will be provided. First, the most important properties of nanostructures that are responsible for their substantial application in surface enhanced spectroscopies will be briefly reviewed, together with common strategies for nanoparticle preparation, which were employed in this work. Subsequently, the basic principles of hyper Raman scattering (HRS) and its enhancement in surface enhanced hyper Raman scattering (SEHRS) will be introduced, followed by an overview of substrates used in SEHRS experiments as well as several examples highlighting the potential of SEHRS for providing comprehensive vibrational information and studying molecules on metal surfaces. Finally, some aspects of second harmonic generation (SHG) from nanoscale structures will be introduced.

2.1 Nanostructures in spectroscopy

2.1.1 Optical properties

The properties of nanoscopic objects (10-100 nm) depend on their shape and size in addition to their chemical composition, and can differ significantly from the properties of the bulk materials. For metallic nanoparticles, the optical response is governed by the excitation of localized surface plasmons-polaritons (LSPs). LSPs are electromagnetic surface modes associated with resonant stationary oscillations of the surface charge density along the physical boundaries of the metal particle (schematically depicted in Figure 2.1A).[8,34] The excitation of LSPs results in absorption and scattering of the incident light by the particle, and a strong amplification of the electric field in close proximity of the metal

nanostructure. These phenomena can be described by solving Maxwell's equations for propagation of electromagnetic fields in dielectric media.[35]

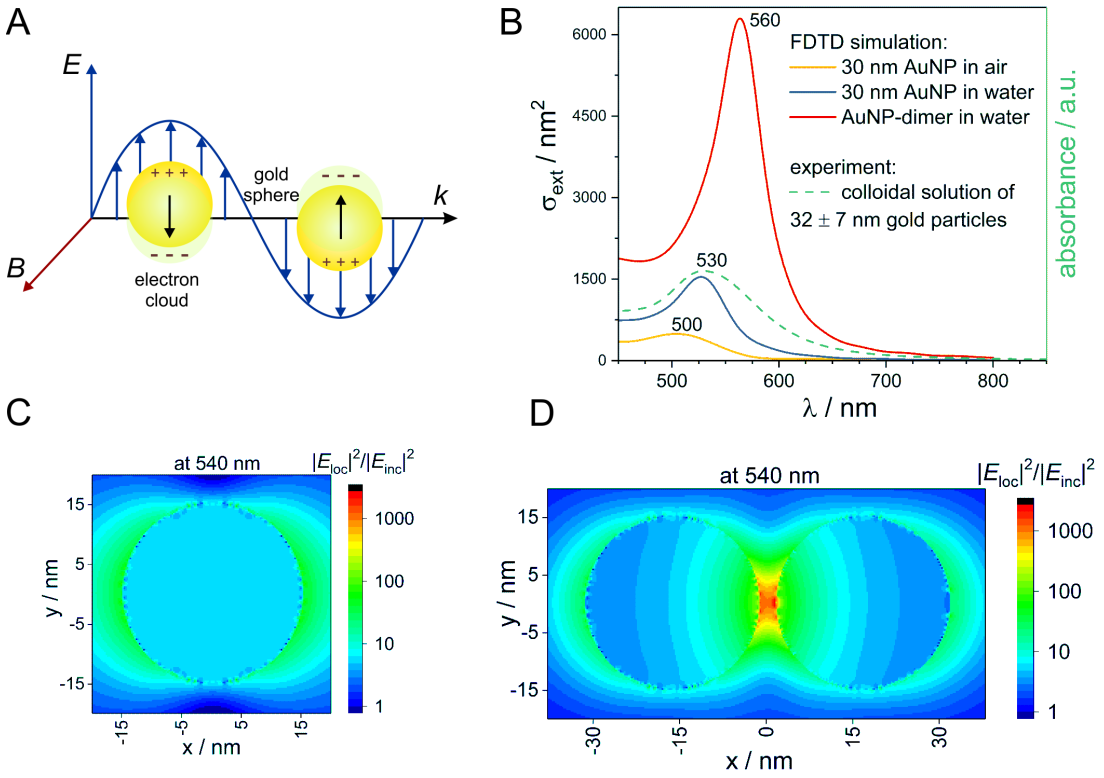

Figure 2.1: A) Schematic illustration of the collective oscillation of conducting electrons in a gold nanoparticle in resonance with the frequency of incident light. Redrawn from ref 7. B) Extinction cross section of 30 nm gold nanosphere in air (yellow line) and water (blue line), and dimer consisting of two 30 nm gold nanospheres separated by 3 nm (red line) calculated with the finite-difference time-domain (FDTD) method, and experimental UV-vis absorbance (extinction) spectrum of 32 ± 7 nm gold nanoparticle colloidal solution (dashed green line). Spatial distribution of the local electric field intensity at 540 nm for C) 30 nm gold nanosphere and D) the gold nanoparticle dimer from B calculated with FDTD using a plane wave polarized in x and propagating in z direction.

The absorption and scattering are given by their cross sections, σ_{abs} and σ_{scatt}, respectively, defined as the ratio of the power P absorbed or scattered by the particle with respect to the incident power density S_{inc} (Equation (2.1) and (2.2)). The sum of σ_{abs} and σ_{scatt} gives the extinction cross section σ_{ext} (Equation (2.3)), which is related to the total power extinguished from the incident beam by the particle that can be measured by means

of UV-vis spectroscopy (see Figure 2.1B, dashed green line). For the simplest case of a nanosphere, σ_{abs} and σ_{scatt} can be approximated as:

$$\frac{P_{\text{abs}}}{S_{\text{inc}}} = \sigma_{\text{abs}} \propto \frac{r^3}{\lambda} \cdot \text{Im}\left\{\frac{\varepsilon - \varepsilon_m}{\varepsilon + 2\varepsilon_m}\right\} \tag{2.1}$$

$$\frac{P_{\text{scatt}}}{S_{\text{inc}}} = \sigma_{\text{scatt}} \propto \frac{r^6}{\lambda^4} \cdot \left|\frac{\varepsilon - \varepsilon_m}{\varepsilon + 2\varepsilon_m}\right|^2 \tag{2.2}$$

$$\sigma_{\text{abs}} + \sigma_{\text{scatt}} = \sigma_{\text{ext}} \tag{2.3}$$

where r is the radius of the sphere, $\varepsilon = \varepsilon' + i \cdot \varepsilon''$ is the frequency-dependent complex dielectric function of the sphere, ε_m the dielectric function of the surrounding medium, and λ the wavelength of the incident radiation. The extinction cross section has a maximum at the localized surface plasmon resonance (LSPR) frequency for which $\varepsilon = -2\varepsilon_m$ applies. This condition is fulfilled for gold and silver in the visible spectral range. Furthermore, the wavelength of the LSPR depends not only on the particle permittivity but also on its size and on the surrounding medium. This is illustrated in Figure 2.1B, where the extinction cross sections of a gold nanosphere in air and water are compared (see yellow and blue lines). Nanostructures with more complex symmetry can exhibit several LSPRs, e.g. nanorods show two plasmon bands corresponding to the longitudinal and transversal plasmon modes.

One of the main consequences of the existence of LSPRs in gold and silver nanoparticles is the fact that the interaction of such nanostructures with light of frequency close to their LSPR results in strong amplification of the electric near-field. As an example, Figure 2.1C shows the local field intensity enhancement around a gold nanosphere. The electric field is highly confined within few nanometers around the particle and drops rapidly with increasing distance from its surface. For a single nanosphere, the electric near-field within the quasistatic approximation is proportional to $1/d^3$, where d is the distance from the particle surface. This extreme local field confinement is responsible for the observation of enhanced optical processes, such as hyper Raman scattering, and is therefore essential for SEHRS to take place.

Up to several orders of magnitude higher near-field enhancements can be achieved in gaps between closely arranged nanostructures, as indicated in Figure 2.1D. The hot spots are experimentally obtained e.g. by changing the ionic strength which induces particle aggregation. In the strong local fields of such nanoaggregates even single molecules can be detected.[4,5,36] Within this work, the enhancement generated by aggregegates of nanoparticles is used to observe the weak hyper Raman scattering of small organic and bioorganic molecules. The strong near-fields in hot spots result from the coupling between LSPs of

individual nanostructures, giving rise to new hybridized plasmon modes.[34,37,38] The bonding modes are red-shifted with respect to the LSPR of the single particles (compare red and blue lines in Figure 2.1B). The anti-bonding modes, also called dark-modes, usually cannot be observed in the far-field UV-vis spectrum of coupled particles but may play an important role for the enhancement of optical processes.

Nanostructured gold and silver surfaces such as periodic arrays of nanovoids, which are investigated in this thesis, also display very interesting optical properties.[39,40] In a metal film comprised of spherical cavities, surface plasmon-polaritons are localized inside the voids, while delocalized propagating surface plasmon-polaritons exist on the top surface. These resonances appear in the visible and near-infrared, and similar to the LSPs in metallic particles, depend strongly on the void diameter and depth. The LSPs as well as their coupling to the delocalized plasmon modes give rise to near-field confinement suitable for enhancement of Raman scattering.[41–43]

Dielectric nanoparticles with high values for the real part of the permittivity ε' and almost zero for the imaginary part ε'', e.g. silicon, titanium dioxide or barium titanate particles, show scattering resonances in the visible and near-IR spectral ranges.[44–47] In contrast to metallic structures, where the extinction is dominated by contributions from the electric dipole mode (Equation (2.1) and (2.2) refer to the dipole approximation), in dielectric particles higher-order multipole electric and magnetic terms have notable impact on the total extinction cross section. The cross sections and electromagnetic fields of nanospheres or core-shell spherical particles can be analytically expressed as infinite sums of multipolar contributions according to the Mie solutions of Maxwell's equations.[48] In this work, results obtained from Mie theory are used to gain a better understanding of the optical response of barium titanate nanoparticles, which is discussed in Chapter 6.

Analytical solutions of the electromagnetic problem exist only for a few limited cases, and thus simulations of the far- and near-field properties of nanoparticles with more complex geometry rely on numerical methods. The most common approaches are the discrete dipole approximation (DDA), the finite element method (FEM), the boundary element method (BEM), and the finite-difference time-domain (FDTD) method.[48] In the FDTD method, the simulation region is divided into discrete segments (Yee cells), where the electric fields are located on the edges and the magnetic fields on the faces of the cell.[49] Then, the differential Maxwell's equations in the time domain are solved on a discrete temporal grid for each

point in space. The results are then transformed into the frequency domain with Fast Fourier Transform (FFT). The FDTD method is used in Chapter 4 and 6 to calculate local field enhancements and extinction cross sections of various nanostructures to compare with the experimental results. One of the main advantages of FDTD exploited in this work is that when a broadband pulse is used as an excitation source, the response of the system can be obtained for a wide range of frequencies in a single simulation. However, FDTD becomes computationally expensive for large systems as the grid spatial discretization must be sufficiently fine to resolve the smallest objects in the model, and thus a compromise between accuracy and computation time must be made.

2.1.2 Preparation and characterization methods

The preparation and characterization of nanoparticles and nanostructured materials is an important topic in chemistry due to their widespread application in different research areas, amongst others in the field of surface enhanced spectroscopy. Noble metal nanoparticles can be obtained by bottom-up wet chemical methods.[50,51] Typically, the process involves one-step synthesis utilizing a soluble metal precursor, a reducing agent, and a stabilizing agent, which prevents the particles from aggregating. The most common approach for the preparation of gold and silver sols, also used in this work, is the reduction with sodium citrate.[52,53] The colloid formation starts by a nucleation process, which involves the reduction of the metal ions to metal atoms. Once nucleation has occurred, small metal clusters undergo a growth step to form larger particles. For colloidal gold, the particle diameter can be adjusted by varying the stoichiometric ratio between gold(III) chloride and sodium citrate.[54] The higher the amount of sodium citrate with respect to a fixed amount of gold, the more gold nuclei are formed, resulting in higher nanoparticle concentration but with smaller sizes.[54] Typically, when used for the preparation of 15-50 nm sized gold colloids, this method yields stable, monodisperse spherical particles. Colloids with larger particle sizes are less monodisperse, and the particle shape deviates from the spherical one. Gold and silver sols can be produced also with other reducing agents, for example hydroxylamine that was employed in this work to synthetize spherical silver particles.

The fabrication of anisotropic metal nanostructures is more complex and requires different synthetic conditions. For the preparation of gold nanorods, which show two plasmon resonance peaks thus being interesting potential substrates for SEHRS, a seed-mediated

growth approach is usually applied.[55,56] This is a two-step method, where nucleation and growth are performed separately. First, small gold seeds (below 5 nm) are produced using a strong reducing agent such as sodium borohydride. Then, the seeds are injected into a growth solution containing gold(I), where they act as catalysts for the final reduction of gold(I) to gold(0) on their surface.[56] The presence of an appropriate surfactant is required in order to induce the anisotropic growth in the rod shape.

Nanoparticles consisting of a dielectric core and metal shell, exhibit interesting optical properties with high degree of tunability, which cannot be achieved by pure metal particles.[57–59] Such core-shell nanostructures can also be prepared by the seed-mediated growth approach. Typically, in the first step the surface of the dielectric core is functionalized with an appropriate ligand to link small metal seeds. Then, gold or silver precursor is reduced to form a shell that may turn out as a continuous layer or not. Simpler seedless approaches can be used as well, although surface functionalization of the cores is often required. Within this work, similar strategies were employed to prepare novel nanostructures with barium titanate core and plasmonic shell.

Nanostructured metal surfaces, another important class of substrates for surface enhanced spectroscopies, can be fabricated by various approaches, including lithography and electrochemistry. An example of such structures are nanovoids, which are usually prepared by electrochemical deposition.[41,60] In this method, first a metal electrode is covered with a monolayer of polystyrene nanospheres, followed by electrodeposition of gold or silver, filling the gaps between the polystyrene templates. Finally, the nanospheres are dissolved with an organic solvent, resulting in a metal film comprised of periodically arranged voids. The geometrical and thus plasmonic properties of the nanovoid arrays can be easily controlled by the size of polystyrene templates and electrodeposition time, which defines the height of the film. Nanovoids prepared by this method are investigated in this work for their enhancement in SEHRS and SHG.

The characterization of nanostructures is essential for their application in surface enhanced spectroscopies. One of the most powerful tools for the visualization of nanoobjects is electron microscopy, owing to the fact that the extremely short wavelengths of focused electron beams allow high spatial resolution of up to 0.1 nm.[61] In scanning electron microscopy (SEM), the electron beam is focused onto a small spot of the specimen, and usually the secondary electrons are collected. The image is constructed by raster scanning of rectangular areas and

matching the brightness of each spot (pixel) to the amount of secondary electrons. SEM is suitable for investigation of thick samples, such as the nanovoid substrates employed in this work. The spatial resolution in SEM is ~10 nm, while in transmission electron microscopy (TEM) higher resolution can be achieved. In TEM, the electrons penetrate a thin specimen, and are then imaged by appropriate lenses. Thick parts of the sample, such as metal structures, scatter or absorb higher fraction of the incident electrons, and in the resulting 2D image these parts appear dark. To image metal nanoparticles with TEM, small amounts of the colloidal solution are drop-casted on carbon coated copper grids and dried, so that the requirement for a thin sample is fulfilled. One disadvantage of electron microscopy is that the metal nanoparticles are measured in vacuum, and, in addition to possible drying artifacts, no accurate information about the structure and geometry of aggregates formed by the nanoparticles in solution, responsible for the high enhancement in SEHRS and SERS, can be acquired.

UV-vis spectroscopy provides direct information about the plasmonic far-field properties of nanoparticles. The absorbance A, typically calculated from the measured transmittance T, is defined according to the Lambert-Beer law as:[50]

$$A = -\lg(T) = -\lg\left(\frac{I_{\text{trans}}}{I_{\text{inc}}}\right) = \bar{\varepsilon} \cdot c \cdot L = \frac{\sigma_{\text{ext}} \cdot c \cdot N_A \cdot L}{\ln(10)} \tag{2.4}$$

where I_{trans} and I_{inc} are the intensities of the transmitted and incident light, respectively, c is the nanoparticle concentration, L is the path length, N_A is the Avogadro constant, $\bar{\varepsilon}$ is the decadic molar extinction coefficient, and σ_{ext} is the extinction cross section. As discussed in more detail in the previous section, σ_{ext} depends on the shape and size of the nanostructures. UV-vis spectroscopy can therefore be used to measure the far-field optical properties of novel nanostructures, or simply to estimate nanoparticle size, polydispersity (from the width of the plasmon band), and to monitor particle aggregation, which usually results in red-shifting of the plasmon band.

Another method for characterization of nanoparticles in solution is dynamic light scattering (DLS), where temporal fluctuations of Rayleigh scattering intensity are measured.[62] These fluctuations can be related to the diffusion coefficient of the particles, and their hydrodynamic diameter can be determined. DLS is mainly suitable for highly monodisperse almost ideally spherical particles, and the data becomes less reliable for other particle shapes and higher polydispersity. Within this work, DLS is used as a supporting method to UV-vis spectroscopy to prove qualitatively structural differences between different types of nanoaggregates in solution.

2.2 Surface enhanced hyper Raman scattering (SEHRS)

2.2.1 Hyper Raman scattering

The interaction of molecules with incident light can result in absorption, emission or scattering, involving transitions between the molecular (electronic, vibrational, rotational) states of the system. The vibrational Raman effect refers to light scattering phenomena associated with vibrational transitions within the electronic (ground) state of the molecule. While in normal Raman scattering (RS) the scattered photons are Stokes or anti-Stokes shifted by the energy difference between the initial and final vibrational states (Figure 2.2A), in the two-photon excited process of hyper Raman scattering (HRS), the scattered radiation occurs near the second harmonic of the excitation wavelength (Figure 2.2B and C).

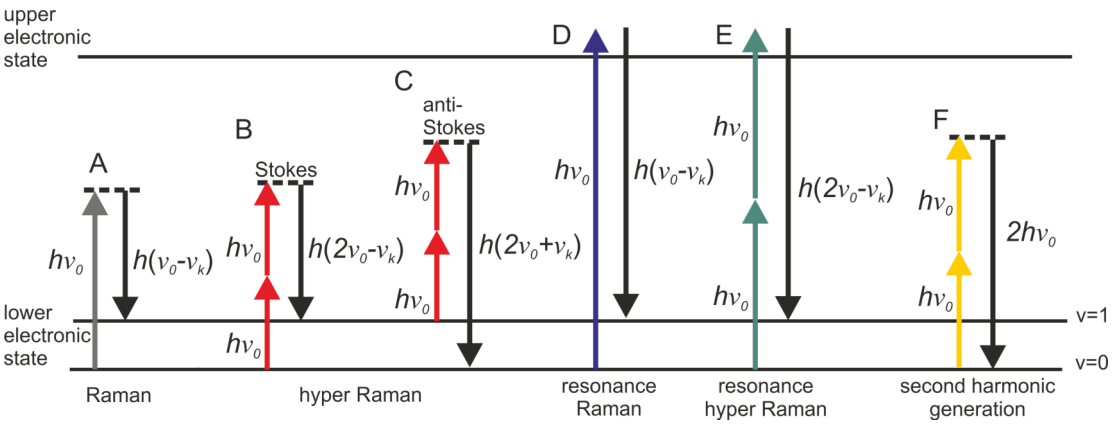

Figure 2.2: Schematic representation of vibrational: A) linear Stokes Raman scattering, B) Stokes hyper Raman scattering, C) anti-Stokes hyper Raman scattering, D) Stokes resonant Raman scattering, and E) Stokes resonant hyper-Raman scattering. In each of the cases the molecular system undergoes a vibrational transition from the initial state (v = 0 for Stokes and v = 1 for anti-Stokes) to the final state (v = 1 for Stokes and v = 0 for anti-Stokes), associated with the normal mode k with corresponding frequency ν_k. Both vibrational states belong to the electronic ground state. The diagram in E depicts one possible resonance condition.[63,64] F) The parametric process of second harmonic generation (macroscopic) or hyper Rayleigh scattering (from point emitters). Adapted from *Chem. Soc. Rev.* 2017, 46, 3980-3999 with permission from the Royal Society of Chemistry.

The number of hyper Raman Stokes photons per second n^{HRS} resulting from the annihilation of two photons at frequency ν_0 and the creation of a photon at frequency $2\nu_0 - \nu_k$ (Figure 2.2B) can be expressed as:

$$n^{\mathrm{HRS}} = N\sigma^{\mathrm{HRS}} n_0^2 \tag{2.5}$$

$$\sigma^{\mathrm{HRS}} \propto \langle |\beta_{fi}|^2 \rangle \tag{2.6}$$

where N is the total number of scattering molecules, n_0 is the excitation intensity (in photons per cm^2 per second), σ^{HRS} is the HRS cross section, and β_{fi} is the transition hyperpolarizability associated with the molecular transition between the initial and the final state.[20,63,65] The brackets denote orientation averaging. HRS as a non-linear process is relatively weak with σ^{HRS} being on the order of $10^{-65}\,\mathrm{cm}^4\mathrm{s}$, and becomes significant when a sufficiently intense electric field is applied.[66] For comparison, cross sections of normal RS σ^{RS} are on the order of 10^{-30}-$10^{-25}\,\mathrm{cm}^2$.[66]

The transition hyperpolarizability β_{fi} arises from the quadratic term in the expansion of the induced transition dipole moment p_{fi} in terms of the perturbing electromagnetic field ($p_{fi} = \alpha_{fi} \cdot E_0 + \frac{1}{2}\beta_{fi} : E_0 E_0 + \cdots$) that is considered to be the main origin of the scattered radiation.[67] Equation (2.6) shows that the selection rules for HRS are governed by the hyperpolarizability, and therefore differ from those of normal RS, which depend on the transition polarizability α_{fi}.[67] For example, modes, which are inactive in both IR and RS, can be hyper Raman allowed, and all IR active modes are also hyper Raman allowed.[22] To that end, IR absorption, RS, and HRS are complementary vibrational spectroscopic methods.

The frequency-dependent transition polarizability and hyperpolarizability can be described within the framework of time-dependent perturbation theory.[63,67] The tensor elements of α_{fi} and β_{fi} increase under resonance conditions when the frequency ν_0 for Raman (Figure 2.2D) and the frequencies ν_0 or $2\nu_0$ for hyper Raman (Figure 2.2E) approach that of an electronic transition.[20,64] This gives rise to increased Raman and hyper Raman cross sections, and consequently increased signal intensities at visible or near-IR (for HRS) excitation wavelengths in experiments with dye molecules such as crystal violet or rhodamine 6G, which are frequently used throughout this thesis. The resonance enhancement in HRS can reach values up to $10^4 - 10^6$ for selected modes.[68,69]

A result of the quantum mechanical treatment of α_{fi} and β_{fi} is that the transition (hyper)polarizability can be expressed as partial derivative of the molecular (hyper)polarizability

with respect to the normal coordinates of the molecule.[67] Therefore, the simulation of Raman and hyper Raman spectra involves determination of the vibrational frequencies and normal modes with an appropriate electronic structure method, calculation of the polarizability and hyperpolarizability, their derivatives (e.g. by finite differentiation), and appropriate orientation averaging according to the illumination-observation geometry.

While the calculation of hyper Raman intensities,[70–72] especially in resonance with electronic transitions,[73,74] is still a topic of ongoing research and technical implementation (but not focus of this thesis), normal modes, and IR and Raman intensities can be evaluated using commercially available quantum chemistry software. In Chapter 7 of this work, density functional theory (DFT) was employed to determine the energy and consequently the vibrational frequencies of small organic molecules in order to assign the bands observed in SERS and SEHRS spectra. DFT uses ground state electron density instead of many electron wavefunction to determine the energy of the system according to the Hohenberg–Kohn theorem.[75–77] Within the Kohn-Sham approximation[78] the total energy can be expressed as a functional of the electron density:

$$E[\rho] = T[\rho] + V_{\text{ext}}[\rho] + E_{\text{XC}}[\rho] \tag{2.7}$$

where $T[\rho]$, $V_{\text{ext}}[\rho]$ and $E_{\text{XC}}[\rho]$ are the kinetic energy, external potential and exchange-correlation functionals, respectively. $T[\rho]$ and $V_{\text{ext}}[\rho]$ are known exactly, but the exchange-correlation term is not and must be approximated. Here, the B3LYP (Becke, three-parameter, Lee-Yang-Parr)[79] exchange-correlation functional is employed, which was found to be accurate for small organic molecules.[75] After optimization of the molecular structure and calculation of the total energy, the harmonic vibrational frequencies can be obtained by diagonalization of the mass weighted Hessian matrix (second derivatives of the energy with respect to atomic coordinates).

2.2.2 Enhancement in SEHRS

Surface enhanced hyper Raman scattering spectroscopy is concerned with the observation of very strong hyper Raman signals, when the scattering molecule is in close proximity to rough metal surfaces or plasmonic nanoparticles. This surface enhancement includes contributions from both metal-light and metal-molecule interactions, giving rise to the so-called electromagnetic (EM) and chemical enhancement mechanisms, respectively.

The strong amplification of electromagnetic fields near plasmonic nanostructures when localized surface plasmons are excited, as described in Section 2.1, is considered to be responsible for the EM enhancement mechanism. In a scattering process, as is the case in SEHRS and surface enhanced Raman scattering (SERS),[1–3,9] plasmonic enhancement is operative in both the incident and the scattered field.

In contrast to the electromagnetic field enhancement that is determined by the plasmonic properties of the metal nanostructure, the chemical enhancement is highly molecule specific. The SEHRS spectrum is governed by the hyperpolarizability of the metal-molecule complex. The chemical mechanism can be further divided into contributions arising from 1) metal-molecule ground state interactions and from 2) resonances of the excitation wavelength with metal-molecule charge-transfer transitions or simply with electronic transitions of the adsorbed molecule,[80–82] where the electronic states can be altered by the presence of the metal. Theoretical studies show that the chemical contribution to the overall enhancement in SEHRS can be larger than the corresponding chemical enhancement for SERS.[25,70,83,84] Nevertheless, numerous studies show that the main contributions to the very high SEHRS enhancement is related to confined local fields of plasmonic structures.

Considering electromagnetic and chemical enhancement mechanisms and including them into Equation (2.5), the number of SEHRS photons n^{SEHRS} can be written as:

$$n^{\mathrm{SEHRS}} = N' \sigma^{\mathrm{SEHRS}} n_0^2 \tag{2.8}$$

with a SEHRS cross section:

$$\sigma^{\mathrm{SEHRS}} = \sigma_{\mathrm{ads}}^{\mathrm{HRS}} \left| M_{\mathrm{ex}}(\nu_0) \right|^4 \left| M_{\mathrm{rad}}(\nu_{\mathrm{HRS}}) \right|^2 \tag{2.9}$$

$\sigma_{\mathrm{ads}}^{\mathrm{HRS}}$ represents the chemical enhancement effect and is related to the transition hyperpolarizability of the adsorbed molecule on the metal surface $\beta_{fi}^{\mathrm{ads}}$:

$$\sigma_{\mathrm{ads}}^{\mathrm{HRS}} \propto \langle |\beta_{fi}^{\mathrm{ads}}|^2 \rangle \tag{2.10}$$

$M(\nu)$ describe the excitation (at ν_0) and radiation (at ν_{HRS}) field enhancement factors:

$$|M(\nu)|^2 = \frac{|E_{\mathrm{loc}}(\nu)|^2}{|E_{\mathrm{inc}}(\nu)|^2} \tag{2.11}$$

where E_{loc} is the enhanced local electric field and E_{inc} is the field in the absence of the metal structure at the excitation (ν_0) or scattering ($\nu_{\mathrm{HRS}} = 2\nu_0 - \nu_k$) frequencies. Due to the strong distance-dependence of the EM field enhancement (see Section

2.1.1), the number of scatters contributing to the SEHRS signal N' is restricted only to molecules in close proximity of the nanoparticle.

Since HRS depends on the square of the incident radiation intensity (Equation (2.5)), the enhancement factor for the incident light in SEHRS scales with E_{loc}^4, while for the excitation in SERS only with E_{loc}^2. This shows that HRS can benefit even more than RS from electromagnetic enhancement, if the incident and scattered frequencies are both in resonance with the localized surface plasmons. Despite the very different Raman and hyper Raman cross sections, SERS and SEHRS spectra can appear at comparable signal levels and, for example, can be measured in the same spectrum using the first and second diffraction order of a double grating spectrometer, respectively.[85] The high signal intensities in SEHRS enable measuring two-photon excited vibrational spectra down to the limit of single-molecules[36,86,87] and to collect hyper Raman spectra also at the anti-Stokes side.[21,88]

In an experiment overall SEHRS enhancement factors can be evaluated by comparing signal intensities from HRS and SEHRS spectra (see Equation (3.8), Chapter 3) as it is hard to distinguish between the chemical and electromagnetic contributions because both are always included.[89] However, the electromagnetic enhancement can be estimated empirically for a given absorbance spectrum of the plasmonic sample (see Equation (3.2), Chapter 3).[90,91] In electrodynamic simulations of plasmonic nanostructures, theoretical SEHRS EM enhancement factors may be approximated, in analogy to SERS,[89] by multiplying the electric field enhancements obtained after solving the excitation problem for both incident and scattering frequencies, that is $|M_{\mathrm{ex}}(\nu_0)|^4 \, |M_{\mathrm{ex}}(\nu_{\mathrm{HRS}})|^2$.

2.2.3 Plasmonic nanostructures for SEHRS

SEHRS experiments require nanostructures providing high enhancement factors, so that the low cross sections of HRS on the order of $10^{-65}\,\mathrm{cm^4 s}$ can be overcome. In general, SEHRS experiments have typically been carried out with nanostructures similar or the same as those used in SERS. While the first observation of SEHRS was made on silver micro powder,[12] subsequent investigations employed roughened electrodes[70,83,92] and colloidal solutions of metal nanoparticles,[11,93,94] which have remained the main two types of enhancing nanostructures for SEHRS.

It is well known from SERS theory and experiments that hot spots with extremely high field enhancement occur in the spaces between particles in fractal structures such as nanoaggregates.[8,95–97] In SEHRS, the effect of aggregation is even more important because aggregated nanoparticles can support plasmon resonances in a wide spectral range from 400 nm to 1200 nm, although they are not always visible in the far field scattering spectrum.[8,37,38,98] According to the electromagnetic theory for SEHRS (Equation (2.9)), this allows to enhance both the incident and scattered fields, whose frequencies are widely separated, and thus to optimize the total enhancement.

As mentioned above, typical plasmonic nanostructures for SERS have been directly transferred to SEHRS experiments. More recent results indicate that it is not necessarily an optimum strategy to directly draw conclusions about the enhancement in SEHRS from the enhancement yielded with a particular type of nanostructure in SERS. On the one hand, this is due to different requirements regarding the plasmonic properties. In particular, the design of nanostructures with multiple plasmon resonances to match the incident and scattering frequencies in HRS, active in the same physical region of space has been proposed.[99–101] On the other hand, the surface chemistry of the nanoparticles, which both determines the formation of nanoaggregates (i.e., the plasmonic properties) and at the same time influences the interaction of the molecules with the metal surface plays an important role for the enhancement. For example, nanoaggregates formed by citrate reduced silver nanoparticles yield higher overall SEHRS intensities than nanoaggregates from hydroxylamine reduced silver nanoparticles, although exactly the opposite is found for SERS.[26] In silver nanoaggregates, enhancement was discussed for individual nanostructures, assessing the plasmonic properties as a function of polarization.[102,103] Such experiments provide evidence that it is important to design suitable plasmonic materials for SEHRS, and to further understand the factors that influence SEHRS enhancement in the experiments. First theoretical discussions aiming for an optimization of plasmonic nanostructures for SEHRS, e.g. by considering different geometries including double resonant antennas in the visible and UV, and silver heptamers supporting Fano resonances, were reported.[99,104] Further research focusing on the development of SEHRS active nanostructures providing uniform and high enhancement should be the key for obtaining comprehensive vibrational information by means of SEHRS.

A very important feature of both aggregated nanoparticles and electrochemically roughened electrodes is that their structure is neither well defined, nor that it is clear if similar hot spots are equally distributed throughout the sample. There have been several attempts

to improve the homogeneity of SEHRS enhancement in nanostructured materials. For example, silver nanocrystal-modified silicon nanowires were found to provide a more spatially uniform response than silver nanoparticles deposited as a film on glass.[105] In particular, chemically immobilized silver nanoparticles on glass slides, well known for their homogeneous SERS enhancement,[106] have proven to be well-suited for SEHRS hyperspectral mapping experiments.[107] In addition, fabrication of well-defined structures with nanoscale gaps, commonly used in SERS,[108–110] has been implemented also in SEHRS.[111] Anisotropic silver dimer arrays were the first artificially designed nanostructures employed in SEHRS measurements.[111] However, relatively little work has been done in this direction for SEHRS and further optimization of the electromagnetic enhancement should be possible.

SEHRS with nanoparticles and nanoaggregates

In recent work, the majority of SEHRS experiments are carried out using aggregates of metal nanoparticles as enhancing structures. Such nanoparticles can be easily prepared by standardized wet chemical methods, although their reproducibility is often not optimum. As an example, silver nanoparticles with diameters in the range of 50-100 nm obtained by reduction of silver nitrate with sodium citrate[53] have been most frequently used.[85,93,112–116] Fewer reports employ other preparation techniques for silver nanoparticle solutions resulting in nanostructures with diameters below 50 nm and different surface chemistry, specifically the reduction with hydroxylamine,[26] borohydride,[116] tannic acid,[86] hydrazine[117] or hydrogen gas.[94] Also, silver nanoparticles prepared by green synthesis in situ in intact onion epidermal cells were shown to have sufficient SEHRS activity,[118] highlighting the potential of such an approach for exploiting SEHRS in bioanalysis. For the latter purpose, gold nanoparticles would be ideally suited. However, so far there have been extremely few reports on the observation of SEHRS on gold nanostructures,[21,119] and the potential of gold SEHRS substrates has not been systematically investigated yet.

The aggregation of nanoparticles is often induced by addition of sodium chloride,,[103,114,120–122] sodium bromide,[36,123] potassium chloride[93,117,124] or other electrolytes in the nanoparticle solutions. Each type of electrolyte at a given concentration can produce a unique aggregate morphology and surface coverage with ions, which can result in differences between the SEHRS spectra of the same compound.[123,125] Nevertheless, it is very difficult to distinguish between chemical effects induced by co-adsorbed ions and effects due to different fields and field gradients that can arise from different gap sizes or aggregate

geometry as a reason for the observed spectral changes, since both can vary simultaneously during the aggregation process. SEHRS is extremely sensitive with respect to changes in surface potential and small changes in the interaction of the molecules with the metal surfaces,[24] and depending on the molecule, the chemical contribution to the enhancement can be quite strong as well. Furthermore, the interaction of the molecule with the nanostructure – which is the main prerequisite for the molecule taking part in SEHRS (and also SERS) – depends critically on the surface charge and charge of the molecule.[26,116,126]

SEHRS with electrodes

Electrochemical SEHRS measurements on silver electrodes were found to be convenient for the investigation of small organic molecules such as pyridine, pyrazine, phenazine and related derivatives under non-resonant excitation conditions[24,72,83,92,127–129] and also to study the dependence of the SEHRS signals on surface potential.[24,72,83,92,128] To provide high local field enhancement, the electrodes are usually roughened in oxidation reduction cycles (ORC), which results in modification of the surface morphology at the nanometer scale.[83,92,127,128] To improve homogeneity and reproducibility of the surface roughness, modification of the electrode surface by dispersing chemically synthesized metal nanoparticles onto it was proposed, which allowed to reversibly obtain reproducible SEHRS spectra in a wider potential range than with an electrochemically roughened electrode.[72] The concept of silver film over nanosphere electrodes, which have more homogeneous and reproducible nanostructure morphology, has also been introduced to SEHRS.[24,129] In this type of electrode the surface roughness is produced by vapor deposition of silver on top of a nanosphere monolayer. An important advantage of this system over ORC roughened electrodes is that the concentration and chemical nature of the supporting electrolyte in an electrochemical SEHRS experiment can be varied without altering the surface morphology and thus the enhancement associated with it. In particular, this allows to investigate the effect of co-adsorbed ions on SEHRS spectra,[24] which is still not possible for measurements in nanoparticle solutions.

2.2.4 Two-photon vibrational probing using non-resonant SEHRS

The selection rules for non-resonantly excited SEHRS have been discussed by comparing SERS and SEHRS spectra from small organic molecules, including pyridine,[72,92] pyrazine,[72] trans-1,2-bis(4-pyridyl)ethylene (BPE),[24,129] benzene,[72]

para-mercaptobenzoic acid,[116,130] as well as data from nucleobases,[26,120] and recently also the dye crystal violet excited at 1570 nm.[74]

In the case of centrosymmetric molecules such as pyrazine, benzene and BPE, the Raman and hyper Raman active modes are expected to be complementary. For benzene, indeed the SERS and SEHRS spectra do not show any common bands, and the SEHRS spectra are very similar to the IR absorption data.[72] Also for pyrazine and BPE "new" Raman-inactive modes appear in the SEHRS data that are not observed in SERS, in addition to some SERS-active bands.[24,92] Although the adsorption of molecules can reduce their symmetry, so that Raman-active modes become visible in the hyper Raman spectrum as well, the detailed examination of the SERS and SEHRS spectra for these two molecules showed that little or no symmetry reduction occurs upon adsorption.[24,92]

The SEHRS and SERS spectra from non-centrosymmetric molecules such as pyridine and nucleobases display bands mostly at the same positions, although with quite different relative intensities.[26,83,120] For example, in the SEHRS and IR spectra of pyridine, Golab et al. reported less pronounced signals of the ring breathing modes.[83] Also the signal of the symmetric ring breathing mode of all five nucleobases differs between SERS and SEHRS spectra. While in SERS it is often used to estimate the adsorbate orientation with respect to the surface, this signal is weak or medium compared to other bands in SEHRS.[26,120] This mode is also very strong in the Raman but medium in the IR absorption spectra of the solid compounds. Independent of a varied surface composition (stabilization) of the silver nanoparticles,[21,26,120] the differences between the SEHRS and the SERS spectrum of adenine are consistent and obvious in all reports.

To understand the influence of the interaction of the molecule and the metal surface on the qualitative features in a SEHRS spectrum, many theoretical studies, mainly considering the model of pyridine on a silver surface, were performed.[25,70,72,83,84] Assuming perpendicular orientation of the pyridine molecule on the surface, SERS and SEHRS spectra were modeled at various levels of theory. Valley et al.[25] and Mullin et al.,[84] who also compared their calculated spectra with the experimental work by Golab et al.[83] and Li et al.,[72] respectively, showed that the normal HRS spectrum of pyridine is dramatically different from its SEHRS spectrum, while the differences between the calculated RS and SERS spectra were much smaller.[25,83,84] Other simulations have shown that slight tilting of the molecule with respect to the surface normal results in more pronounced changes in the SEHRS spectrum than in

SERS, suggesting that SEHRS is more sensitive to adsorbate orientation.[27,83] Experimentally, the higher sensitivity of SEHRS over SERS with respect to adsorbate geometry and small surface environmental changes has been reported for several species.[24,26,116] For example, the SEHRS spectra from BPE on silver electrodes displayed significant variations when the concentration and type of co-adsorbed counterions were changed,[24] and changes in the SEHRS spectra of the nucleobases thymine and uracil at different pH were much more pronounced than in the corresponding SERS data.[26]

2.3 Second harmonic generation (SHG)

Apart from the inelastic Raman scattering, the interaction of a molecule with light can result in elastic Rayleigh scattering, where the frequencies of the incident and scattered radiation are the same. The non-linear counterpart of Rayleigh scattering is hyper Rayleigh scattering, where two photons are converted in one photon of twice the frequency (Figure 1F). This process refers to the incoherent scattering from electric dipoles with size much smaller than the wavelength of the incident radiation, and its intensity depends linearly on the number of molecules. When the scattering source becomes larger than ~10nm, coherent effects begin to emerge, and the corresponding process is referred to as second harmonic generation (SHG).[29,30,131]

For a macroscopic material exposed to electromagnetic radiation, the induced polarization within the electric dipole approximation is given as a power series of the perturbing electric field E_0 according to:

$$P = \underbrace{\chi^{(1)} \cdot E_0}_{P^{(1)}} + \underbrace{\chi^{(2)} : E_0 E_0}_{P^{(2)}} + \cdots \tag{2.12}$$

where $P^{(1)}$ is the linear polarization, $P^{(2)}$ the first non-linear polarization, $\chi^{(1)}$ and $\chi^{(2)}$ are the linear and non-linear susceptibility tensors, respectively, which include bulk and surface contributions from the atoms or molecules in the material. $P^{(2)}$ oscillating at the second harmonic frequency is the source of the SHG light, and $\chi^{(2)}$ describes the electronic and symmetry properties of the non-linear material. In media possessing a center of inversion, the centrosymmetry leads to vanishing of all the tensor elements of $\chi^{(2)}$, and thus SHG is forbidden in the bulk of such materials.

The crystalline lattice structure of gold and silver is cubic face-centered that is centrosymmetric. Therefore, SHG from the bulk of plasmonic nanoparticles is symmetry forbidden within the electric dipole approximation. At the surface of the nanoparticles the centrosymmetry breaks and SHG can emerge due to surface contributions. Although the tensor elements of the surface $\chi^{(2)}$ from metals are small, the second harmonic emission can be strongly enhanced by plasmon resonances.[132–135] Rough[31,136,137] or structured[138,139] metal surfaces supporting plasmon resonances can also give rise to strong SHG signals, particularly in localized hot spots. This in principle allows probing local field enhancements of nanostructured plasmonic surfaces by SHG.

For nanoscale structures made from noncentrosymmetrical materials, such as barium titanate that is employed in this work, the whole volume of the particle participates in the frequency doubling process. For smaller particles surface contributions become more significant than in larger particles as the ratio of surface atoms to bulk atoms increases. In principle, the bulk SHG contributions should be coherent but polycrystallinity may deter correlated emission from a single particle. Apart from this, the SHG signal from randomly oriented coherent emitters in solution is rather incoherent.[29,30] Similar to plasmonic particles, SHG from high refractive index dielectric nanostructures is enhanced if the incident or the second harmonic wavelength is in resonance with intrinsic electromagnetic modes of the particle.[47,140,141] In general, nanocrystals from non-linear materials are suitable for SHG imaging of biological samples.[32,33]

Chapter 3

Materials and methods

3.1 Chemicals

Gold(III) chloride trihydrate ($HAuCl_4 \cdot 3\,H_2O$, trace metals basis), silver nitrate ($AgNO_3$, trace metals basis), hexadecyltrimethylammonium bromide (CTAB), polyvinylpyrrolidone (PVP, average mol wt 40,000), tetrakis(hydroxymethyl)phosphonium chloride solution (THPC, 80 % in water), octylamine, L-ascorbic acid, hydroxylamine hydrochloride ($NH_2OH \cdot HCl$), (3-aminopropyl)triethoxysilane (APTES), (3-mercaptopropyl)trimethoxysilane (MPTS), ethylene glycol (EG), borax / sodium hydroxide buffer solution pH 10, tryptophan, histidine, phenylalanine, tyrosine, 2-aminothiophenol (2-ATP), 3-aminothiophenol (3-ATP), 4-aminothiophenol (4-ATP), 4-mercaptobenzoic acid (*p*MBA), thiophenol, benzyl mercaptan, 2-phenylethanethiol, and L-α-phosphatidylcholine (99 %) were purchased from Sigma-Aldrich. Ammonium hydroxide solution (25 %) and sodium hydroxide (NaOH, 97 %) were purchased from Fluka. Trisodium citrate dihydrate was obtained from Th. Geyer, and hydrogen peroxide (H_2O_2, 30 %) from Carl Roth. Sodium chloride (NaCl), sodium borohydride ($NaBH_4$), hydrochloric acid (HCl, 37 %), nitric acid (HNO_3, 70 %) and crystal violet (CV) were purchased from J. T. Baker. Magnesium sulfate hydrate ($MgSO_4$) was obtained from Riedel-de Haën, and rhodamine 6G (R6G) from Lambda Physik. Barium titanate nanoparticles ($BaTiO_3$, tetragonal) were purchased from US Research Nanomaterials, Inc. Phosphate buffered saline (PBS) was purchased from Sigma-Aldrich, Dulbecco's modified Eagle's medium (DMEM), fetal calf serum (FCS), and ZellShield™ were obtained from Biochrom AG, Berlin, Germany. All solutions were prepared using Milli-Q water (USF Elga Purelab Plus purification system).

3.2 Preparation of nanostructures

Gold and silver nanoparticle synthesis

Spherical gold nanoparticles were prepared by the citrate reduction method.[53,54,142] For the synthesis of 30 nm gold nanoparticles, gold chloride solution (200 mL, 0.375 mM) was heated to 90 °C. Subsequently, sodium citrate solution (1 % by weight, 4 mL) was added under vigorous stirring, and the reaction mixture was kept boiling for 1 h. Gold nanoparticles with an average size of 14 nm were prepared by adding sodium citrate solution (96.9 mg dissolved in 8.5 mL water) in 1 mL steps to 243 mL boiling water containing $HAuCl_4$ (292 µL, 0.25 M). For the preparation of gold nanoparticles with diameters ranging from 43 to 72 nm, $HAuCl_4$ solution (50 mL, 0.3 mM) was heated to boiling. Then, different aliquots (from 350 to 500 µL) of trisodium citrate solution (1 % by weight) were added, and the reaction mixture was kept boiling for 30 min. The color of the gold colloids ranged from red to purple with increasing size of the nanoparticles.

Gold nanorods were prepared as reported previously.[56] CTAB solution (5 mL, 0.2 M) was mixed with $HAuCl_4$ (5 mL, 0.5 mM) and vigorously stirred. Next, $NaBH_4$ (0.6 mL, 0.01 M) was added, the mixture was stirred for 2 min, then left undisturbed for 2 h and used as the seed solution. The growth solution was prepared by mixing CTAB (5 mL, 0.2 M) with HCl (190 µL, 1 M) and $HAuCl_4$ (5 mL, 1 mM) under vigorous stirring. Subsequently, $AgNO_3$ (120 µL, 0.01 M), ascorbic acid (100 µL, 0.1 M), and 24 µL of the seed solution were added. The reaction mixture was shaken gently and left undisturbed overnight. All steps took place in water bath at 30 °C. Next, the solution was centrifuged for 30 min at 7800 rpm, and the precipitate was redispersed in 3 mL water. The centrifugation-redispersion cycle was performed three times. In Raman experiments 10-fold diluted solution of the nanorods was used.

Gold seeds with size of 2-3 nm, **THPC-gold**, were prepared as reported previously.[143] Aqueous solutions of sodium hydroxide (0.2 M, 1.5 mL), THPC (1 mL of a solution of 60 µL of 80 % aqueous solution diluted to 5 mL with water), and $HAuCl_4$ (2 mL, 25 mM) were subsequently added to 45.5 mL water. The resulting dark brown colloid was stirred for 30 min at room temperature and aged at 4 °C for at least one week before use in further synthesis steps.

For the preparation of **hydroxylamine reduced silver nanoparticles**,[144] $AgNO_3$ solution (10 mL, 0.01 M) was added rapidly to 90 mL water, containing hydroxylamine hydrochloride

(11 mg) and sodium hydroxide (12 mg). The reaction mixture was stirred for 30 min at room temperature, resulting in a yellowish-brown colloid.

Citrate reduced silver nanoparticles were produced by the Lee and Meisel protocol.[53] $AgNO_3$ (46 mg) was dissolved in 245 mL water and heated to boiling with extensive stirring. Next, sodium citrate solution (5 mL, 0.04 M) was added dropwise and the reaction mixture was kept boiling for 1 h, resulting in a yellowish-grey colloidal solution.

Gold and silver coated barium titanate composite nanoparticle synthesis and surface modification

For the preparation of **gold coated barium titanate nanocomposites, Au@$BaTiO_3$**, protocols for surface functionalization of barium titanate[145–149] and a seed-mediated growth approach[56] for the gold shell formation were adapted. Barium titanate particles (180 mg) were dissolved in hydrogen peroxide (30 %, 30 mL) and sonicated for 30 min at room temperature. Then, the particles in hydrogen peroxide were heated in oil bath under reflux at 110 °C for 4 h. The heating step was omitted when preparing Au@$BaTiO_3$ with smaller gold particles as shell. The particles were centrifuged at 7500 rpm for 30 min and washed with water several times, and then redispersed in 300 mL ethanol. Ammonium hydroxide (25 %, 480 µL) and APTES (2.5 mL) were added subsequently to the hydroxylated $BaTiO_3$ particles in ethanol and the mixture was stirred for 6 h at 75 °C under reflux. The particles were centrifuged for 20 min at 7500 rpm and washed with ethanol at least three times to remove excess reagents, then redispersed and stored in 60 mL ethanol at 4 °C. APTES-functionalized barium titanate nanoparticles in ethanol (5 mL) were mixed with THPC-gold (5 mL), shaken with vortex mixer for 2-3 min and left still over night. The THPC-gold functionalized $BaTiO_3$ particles were centrifuged for 10 min at 6500 rpm and washed with water three times, then redispersed in 5 mL water, and used as the seeds in the next step. CTAB solution (2 mL, 0.2 M) was mixed with HCl (100 µL, 1 M) and $HAuCl_4$ (1 mL, 0.75 mM) in a 15 mL centrifuge tube under vortex shaking. Then, ascorbic acid (150 µL, 0.01 M) was added and the solution was shaken until it turned transparent. Finally, 2 mL of the seeds were injected in the reaction mixture; the tube was shaken for 10 s and left still in water bath at 30 °C for 30 min. The particles were centrifuged for 10 min at 2000 rpm and washed with water several times until no unbound gold nanoparticles were present in the supernatant, and finally redispersed in 2 mL water. This procedure yields ca. 9 nm gold nanoparticles distributed on the surface of the barium

titanate cores. In order to increase the size of the gold nanoparticles to ca. 17 nm, one more growing cycle was performed by using the product as seeds. CTAB solution (1.5 mL, 0.2 M) was mixed with HCl (75 µL, 1 M), $HAuCl_4$ (0.75 mL, 0.67 mM), ascorbic acid (100 µL, 0.01 M), and 1.5 mL of the product from the previous step in the same conditions as described above. After several centrifugation and washing cycles, the particles were redispersed in 1.5 mL water, containing CTAB (2 µL, 0.2 M) to increase stability, and stored at room temperature. For further experiments the particles were first centrifuged and redispersed in milli-Q water.

Silver barium titanate composite nanoparticles, Ag@$BaTiO_3$, were prepared by surface functionalization of barium titanate with hydroxyl groups[145,146] and growing a silver shell in a seedless one-step synthetic route previously reported for silica-silver core-shell structures.[150] Barium titanate nanoparticles (30 mg) were dissolved in hydrogen peroxide (30 %, 10 mL) and sonicated for 1 h at room temperature. The particles were centrifuged at 7500 rpm for 15 min and washed with water several times, and then redispersed in 50 mL ethanol. Ammonium hydroxide (25 %, 80 µL) and MPTS (200 µL) were added subsequently to the $BaTiO_3$ particles and the mixture was stirred over night at room temperature. The particles were centrifuged for 15 min at 7500 rpm and washed with ethanol several times to remove excess reagents, then redispersed and stored in 10 mL ethanol at 4 °C. MPTS-functionalized $BaTiO_3$ particles (2 mL) were centrifuged, redispersed in 2 mL ethylene glycol, placed in a round bottom flask and stirred at room temperature. Silver nitrate solution in ethylene glycol (3 mL, 1 g L^{-1}), PVP solution in ethylene glycol (2 mL, 0.2 mM), and n-octylamine (5 µL) were added subsequently and the reaction mixture was stirred for 2 h. The particle solution turns from white to yellow, pink, and finally dark brown. To remove unbound silver nanoparticles, the Ag@$BaTiO_3$ particles were centrifuged for 5 min at 2000-4500 rpm and washed with ethanol many times until the supernatant was transparent. Finally, the particles were dispersed in 2 mL ethanol and stored at room temperature. For further experiments the particles were first centrifuged and redispersed in milli-Q water.

Au@$BaTiO_3$ and Ag@$BaTiO_3$ nanocomposites were **coated with lipids** according to previously reported protocol for displacement of CTAB from the surface of gold nanoparticles.[151] Liposomes were prepared by dissolving phosphatidylcholine in chloroform/methanol (1:1) mixture (10 g L^{-1}). Then, the solvent was removed under the stream of argon, and the dried lipids were rehydrated with PBS buffer. The mixture was freeze-thawed at least six times at the temperature of in liquid nitrogen and at 37 °C. After freeze-thaw cycles, the lipids were sonicated and extruded through polycarbonate membrane (pore size 0.2 µm). The

liposomes were prepared by Vesna Živanović. Next, the core-shell nanoparticles (50 µL) were mixed with the liposomes (100 µL), and sonicated for 20 min. After centrifugation and discarding the supernatant, the particles were redispersed in liposomes (200 µL) and sonicated for 20 min. This cycle was repeated three times. The particles were left over night in the lipid mixture at 4 °C, and finally centrifuged and redispersed in 50 µL water.

For **coating with *p*MBA**, the composite nanoparticles (50 µL) were incubated with aqueous *p*MBA solution (950 µL, 5×10^{-5} M) over night. The excess *p*MBA was removed by centrifugation cycles and the particles were redispersed in 50 µL water.

Cell growth and incubation with $Au@BaTiO_3$ and $Ag@BaTiO_3$ composite nanoprobes was done by Vesna Živanović. Swiss albino mouse macrophages of cell line J774 (from DSMZ, Braunschweig, Germany) were cultured in DMEM supplemented with 10 % FCS and 1 % ZellShield™ in a humidified environment at 37 °C and 5 % CO_2. For SHG and Raman experiments, J774 cells were grown as a monolayer on sterile cover-slips (Thermo Fisher Scientific, Schwerte, Germany) in a six-well plate and incubated with 120 µL of 20-fold diluted solution of the lipid or *p*MBA coated composite nanoprobes and 880 µL of standard cell culture medium for 3 h.

Preparation of nanovoid structures

Gold and silver nanovoid structures were fabricated by Denis Öhl, Ugur Kayran and João Junqueira (Ruhr-Universität Bochum, AG Elektroanalytik und Sensorik).

Gradient silver and gold nanovoid samples were prepared by bipolar electrodeposition according to a previously reported protocol.[60,152] First, Au/Ag-coated Si wafers (200 nm thickness) were decorated with 200 nm, 300 nm and 600 nm polystyrene nanospheres (Thermo Fisher Scientific, USA) utilizing a Langmuir-Blodgett trough (KSV Instruments, FIN). Briefly, 150 µL nanospheres were mixed with 300 µL EtOH and evenly distributed on the water surface. The film was compressed until a surface pressure of 50 mN m^{-1} was reached (using a $2 \times 1\,cm^2$ Pt Wilhelmy plate). During vertical retraction (2 mm min^{-1}) the surface pressure was kept constant. Only samples offering a homogeneously covered surface, as indicated by scanning electron microscopy (SEM) were used for further experiments. For bipolar electrodeposition an in-house built cell was used with a feeder electrode distance

of $d = 16$ cm (carbon rods, ⌀= 6 mm and 9 cm length, SGL Carbon GER). Bipolar electrodepositions were carried out while keeping the potential drop across the bipolar electrode ΔBE constant at 3 V for 60 s. For this purpose, the potential difference between the feeder electrodes V_{feeder} was varied between 6 and 10 V depending on the length of the bipolar electrode (BE). The depositions were done with commercial plating solutions (Ag: MetSil 500 CNF, 31 g L^{-1}, Au: ECF 60 gold plating solution 15 g L^{-1} mixed with E3 brightener EC4073 (v/v 200:1), Metalor Technologies, CH). Prior to the electrodeposition, the electrodes were incubated in the plating solution for 10 min to ensure a complete wetting of the surface. After electrodeposition, the BEs were cleaned with EtOH and H_2O followed by incubation (60 min) in dichloromethane in order to dissolve the nanospheres.

Gold and silver nanovoids with 200 nm and 300 nm nanosphere templates and uniform metal thickness were reproduced using an in-house built scanning droplet cell (SDC).[153,154] Briefly, a measuring cell consisting of polytetrafluoroethylene (⌀= 6 mm) with an integrated counter (CE, Pt wire) and reference electrode (RE, Ag/AgCl/3 M KCl) is fixed to XYZ step motors (OWIS, GER). The cell is connected to a PGU-100 bipotentiostat (IPS Jaissle, GER) whilst the signal is read out utilizing an AD/DA converter. The electrodepositions were carried out for a fixed time of 240 s for all substrates, and the applied potential used for each sample is listed in Table 3.1.

Table 3.1: Electrodeposition parameters for the fabrication of gold and silver nanovoid substrates with uniform thickness.

substrate	applied potential vs. Ag/AgCl/3 M KCl
Ag(200)	-725 mV
Ag(300)	-695 mV
Au(200)	-540 mV
Au(300)	-545 mV

3.3 Characterization methods

UV-vis spectroscopy

UV-vis spectra of liquid samples were recorded in transmission mode on a UV-vis-NIR double-beam spectrophotometer (V-670, Jasco) in the wavelength range between 300 nm and 1200 nm. For measurements of nanoparticles in solution, quartz cuvettes (Hellma,104.002-QS) of 10 mm path length were used and the samples were typically diluted 10-20 times.

In Chapter 4 the UV-vis data was used to estimate electromagnetic SERS[90] and SEHRS[91] enhancement factors G_{SERS} and G_{SEHRS}, respectively, generated by the different gold nanostructures using the following empirical relations:

$$G_{\mathrm{SERS}} = \frac{|\varepsilon(\nu_0)|^2 \, |\varepsilon(\nu_{\mathrm{RS}})|^2}{\varepsilon''(\nu_0)\varepsilon''(\nu_{\mathrm{RS}})\bar{\nu}_0\bar{\nu}_{\mathrm{RS}}} \cdot A(\nu_0)A(\nu_{\mathrm{RS}}) \tag{3.1}$$

$$G_{\mathrm{SEHRS}} = \frac{|\varepsilon(\nu_0)|^4 \, |\varepsilon(\nu_{\mathrm{HRS}})|^2}{\varepsilon''^2(\nu 0)\varepsilon''(\nu_{\mathrm{HRS}})\bar{\nu}_0^2\bar{\nu}_{\mathrm{HRS}}} \cdot A^2(\nu_0)A(\nu_{\mathrm{HRS}}) \tag{3.2}$$

where $A(\nu)$ is the measured absorbance of the sample, $\varepsilon(\nu) = \varepsilon'(\nu) + i \cdot \varepsilon''(\nu)$ is the complex dielectric function of gold at the incident laser (ν_0) and Raman or hyper Raman (ν_{RS} and ν_{HRS}) frequencies, respectively; $\bar{\nu}_0$, $\bar{\nu}_{\mathrm{RS}}$ and $\bar{\nu}_{\mathrm{HRS}}$ are the corresponding wavenumbers.

Transmission electron microscopy (TEM)

Transmission electron micrographs were taken using a Tecnai G2 20 TWIN instrument operating at 200 kV. The liquid samples were drop-casted on carbon coated copper grids. The measurements were performed by Sören Selve and Jan Simke at Zentraleinrichtung Elektronenmikroskopie (ZELMI), Technische Universität Berlin.

The average nanoparticle sizes and size distributions were determined by analysing TEM images of ∼500 particles from each particle type using the software ImageJ.[155]

The concentrations of gold and silver nanoparticle solutions were estimated according to equation (3.3), assuming complete reduction:

$$c = \frac{n \cdot M_{\mathrm{metal}}}{\bar{V}_{\mathrm{particle}} \cdot \rho_{\mathrm{metal}} \cdot V_{\mathrm{solution}} \cdot N_A} \tag{3.3}$$

where c - nanoparticle concentration, n - amount of metal, M_{metal} - molar mass of gold/silver, $\bar{V}_{\text{particle}}$ - average volume of the nanoparticle calculated from the average sizes determined by TEM (assuming spherical or cylindrical geometry for the nanorods), ρ_{metal} - density of gold/silver, V_{solution} - final volume of the colloidal solution, and N_A - Avogadro constant.

From the TEM data, the maximum possible surface coverage of nanoparticles with crystal violet and rhodemine 6G (Chapter 4) was estimated by assuming a perpendicular orientation of the dye molecules corresponding to an occupied area of $\sim$0.4 nm^2.[156] This assumption results in surface coverages of 70-110 %, depending on the respective nanoparticle solution.

Scanning electron microscopy (SEM)

Scanning electron micrographs of nanovoid structures were taken with a Quanta 3D ESEM (FEI, USA) operating at 30 kV acceleration voltage. The measurements were performed by collaborators from the group of Prof. Wolfgang Schuhmann at Ruhr-Universität Bochum, Elektroanalytik und Sensorik department. The internal function of the instrument for measuring distances was used to image the gradient nanovoid substrates at desired positions. The void diameters were determined by analyzing the SEM images with ImageJ.[155]

Dynamic light scattering (DLS)

Dynamic light scattering (DLS) measurements were performed with a Zetasizer® Nano ZS (Malvern Instruments) at BAM Federal Institute for Materials Research and Testing. The samples were diluted 1000 times, placed in polymethyl methacrylate (PMMA) cuvettes, and after 2 min of equilibration at 25 °C the samples were measured 30 times with an integration time of 20 s.

3.4 Raman experiments

All Raman and hyper Raman spectra were measured with an imaging spectrometer. Hyper Raman spectra at 1064 nm were excited with a mode-locked Nd:YVO_4 laser producing 7 ps pulses at 76 MHz repetition rate (picoTrain, HighQ GmbH) and at 830 nm with a tunable Ti:Sapphire laser (Tsunami) producing 35 ps pulses at 80 MHz repetition rate. Raman spectra

were excited at 532 nm (using the second harmonic of the 1064 nm laser or with a diode laser BWI-532-100E, B&W Tek), 633 nm (HeNe laser, Thorlabs, HRP 17), and 785 nm (diode laser DL-100, Toptica Photonics AG). The excitation light was focused onto the samples through a microscope objective (10× with NA 0.3 or 60× water immersion objective with NA 1.2), the Raman light was collected in backscattering geometry by the same objective, and detected by a liquid nitrogen cooled CCD detector. The spectral resolution was 5-8 cm^{-1}, considering the full spectral range. For all Raman experiments, the exact integration times and excitation intensities are stated in the figure captions of the presented data in the discussion chapters.

For laser intensity calculations, the radius of the focal spot of the excitation beam, r_{xy}, was determined from the Rayleigh criterion according to:

$$r_{xy} = \frac{0.61\lambda}{\mathrm{NA}} \tag{3.4}$$

The two-photon interaction volume V in a SEHRS (and SHG) experiment was approximated as a three-dimensional Gaussian volume:[23]

$$V = \pi^{\frac{2}{3}} r_{xy}^2 r_z \tag{3.5}$$

where the lateral and axial radii, r_{xy} and r_z, are defined as:

$$r_{xy} = \frac{0.320\lambda}{\mathrm{NA}\sqrt{2}} \quad \text{for} \quad \mathrm{NA} < 0.7 \qquad \text{and} \qquad r_{xy} = \frac{0.325\lambda}{\mathrm{NA}^{0.91}\sqrt{2}} \quad \text{for} \quad \mathrm{NA} > 0.7 \tag{3.6}$$

$$r_z = \frac{0.532\lambda}{\sqrt{2}} \frac{1}{n - \sqrt{n^2 - \mathrm{NA}^2}} \tag{3.7}$$

λ is the laser wavelength, NA is the numerical aperture of the objective lens, and n is the refractive index of the medium.

Sample preparation

In the SEHRS and SERS experiments with **gold nanoparticles** presented in Chapter 4, gold colloids (120 µL) were mixed with water (15 µL) or sodium hydroxide (15 µL, 1 M), and finally crystal violet or rhodamine 6G solution (15 µL) was added to obtain the desired concentration. The gold nanorods were diluted 10 times to achieve similar concentration as in the solutions of spherical nanoparticles.

The SEHRS spectra obtained with solid **nanovoid substrates** presented in Chapter 5 were measured by placing a droplet of crystal violet with the desired concentration (typically 10^{-5} M) and focusing the laser light with a 60× water immersion objective.

In Chapter 6, SERS and SEHRS spectra of crystal violet were measured by diluting the composite **$BaTiO_3$-gold or silver nanoparticles** (60 µL) with water (60 µL), followed by addition of crystal violet solution (20 µL, 10^{-5} M). The spectra of *p*MBA and lipid coated nanocomposites were measured directly by focusing the laser light through a 60× water immersion objective on a droplet of the respective nanoparticle suspension, which was placed on top of a calcium fluoride plate.

The SEHRS and SERS spectra of **amino acids** from Chapter 7.1 were measured by mixing hydroxylamine reduced silver nanoparticles (115 µL) with sodium hydroxide / borax buffer with pH 10 (15 µL), the amino acid solution with the desired concentration (15 µL), and magnesium sulfate (5 µL, 1 M).

In the experiments with **thiophenols** shown in Chapter 7.2, gold and silver colloids (120 µL) were aggregated with sodium chloride (15 µL, 1 M), and thiophenol solution (15 µL) was added to obtain the desired concentration. For SEHRS and SERS measurements of **aminothiophenols**, gold colloid (100 µL) was mixed with sodium chloride / sodium hydroxide / hydrochloric acid (10 µL, 1 M), and the aminothiophenol solution (10 µL).

In the above cases, the liquid samples were placed in microcontainers, and the excitation light was focused onto the mixtures through a 10× microscope objective (NA 0.3), unless stated otherwise.

SERS spectra of **living cells with plasmonic-$BaTiO_3$ nanocomposites** were excited at 785 nm. Before the measurements, cells were thoroughly washed with PBS buffer, in which they were also kept during the measurements. The Raman maps were obtained by focusing the laser light with a 60× water immersion objective (NA 1.2) and raster scanning areas with a step size of 1 µm.

Spectra analysis

All Raman and hyper Raman spectra were frequency calibrated using a Raman spectrum of toluene or toluene/acetonitrile (1:1) mixture. Cosmic rays were removed from the spectra using a home-build algorithm implemented in MATLAB (The Mathworks, Inc.). SEHRS spectra presented in Chapters 6 and 7 were background corrected using an automatic background correction algorithm implemented in R.[157,158]

SEHRS enhancement factors, EF, were estimated using the equation:

$$\mathrm{EF} = \frac{I_{\mathrm{SEHRS}} N_{\mathrm{HRS}}}{I_{\mathrm{HRS}} N_{\mathrm{SEHRS}}} \tag{3.8}$$

where I_{HRS} and I_{SEHRS} are the intensities of the crystal violet band at 1586 cm^{-1} in the normal HRS and SEHRS spectrum, respectively, and N_{HRS} and N_{SEHRS} are the number of crystal violet molecules in the two-photon interaction volume (Equation (3.5)) from the HRS and SEHRS experiment, respectively. It should be mentioned that Equation (3.8) gives conservative values of the EF, because it assumes that all crystal violet molecules are bound to the nanostructure and take part in the SEHRS process.

3.5 Second harmonic generation (SHG) measurements

SHG experiments were performed using an imaging spectrometer in backscattering geometry. To generate SHG, a laser operating at 850 nm with 150 fs pulses at 73 MHz repetition rate and a laser operating at 1064 nm with 6 ps pulses at 75 MHz repetition rate were used. The excitation light was focused onto the samples through a microscope objective (10× with NA 0.3 or 60× water immersion objective with NA 1.2), the backscattered SHG light was collected by the same objective, and detected by a liquid nitrogen cooled CCD detector. The signals were filtered with polarization-insensitive dichroic and bandpass filters with 20 nm full width. The exact signal acquisition times and excitation intensities are given in the figure captions of the presented data in the following chapters.

In Chapter 5, SHG signals excited at 850 nm from **gold and silver nanovoids** were collected by focusing the light directly onto the solid samples with a 10× microscope objective (NA 0.3). SHG excited at 1064 nm was measured by placing a droplet of water or crystal violet solution (10^{-5} M) on the samples and focusing the light through a 60× water immersion objective (NA 1.2).

SHG at 850 and 1064 nm in Chapter 6 was measured from 20-fold diluted solution of the **plasmonic-barium titanate composite particles** in water. The nanoparticle suspensions were placed in microcontainers, and the excitation light was focused onto the samples through a 10× microscope objective (NA 0.3).

In Chapter 7.1, for measuring SHG from **aggregates of silver nanoparticles** with tryptophan, identical samples were used as in the SEHRS experiments (see Section 3.4).

3.6 Electrodynamic simulations

Finite-difference time-domain (FDTD) simulations were done with Lumerical FDTD Solutions 8.18. In all cases, a plane wave polarized in x and propagating in negative z direction was used for excitation. The output images were normalized to the intensity of the excitation source. The refractive index of the surrounding water was set to 1.33. The frequency-dependent dielectric functions of barium titanate (for simplicity, only the ordinary axis was considered) and gold were taken from the literature.[159,160] Size correction for the gold permittivity was not considered.[161]

For simulations with **gold nanoparticle dimers and gold nanoaggregates** shown in Chapter 4 the mesh size was set to 0.5 nm and 1 nm, respectively. To calculate the SEHRS enhancement, the electric field intensity enhancements at the laser (1064 nm) and Stokes HRS (580 nm) wavelengths were multiplied, that is, $\left|\frac{E_{\mathrm{loc}}(\nu_0)}{E_{\mathrm{inc}}(\nu_0)}\right|^4 \left|\frac{E_{\mathrm{loc}}(\nu_{\mathrm{HRS}})}{E_{\mathrm{inc}}(\nu_{\mathrm{HRS}})}\right|^2$. In Chapter 4 the shorter notation $|E_{\mathrm{ex}}|^4|E_{\mathrm{HRS}}|^2$ is used instead.

In Chapter 6, for the FDTD simulations of **bare $BaTiO_3$ particles and Au@$BaTiO_3$ composite particles** a mesh size of 5 nm and 0.5 nm was used, respectively. $BaTiO_3$ sphere with a diameter of 300 nm was surrounded by 600 uniformly distributed gold nanospheres with a diameter of 17 nm, corresponding to a gold volume filling fraction of 0.287. For simulations of Au@$BaTiO_3$ composites with different core sizes (200 nm sphere, 255 nm sphere, and 250 nm rounded cuboid) the number of surrounding 17 nm gold nanospheres was chosen in such a way that the gold volume fraction is 0.287 in all cases. For simulations of **gold coated $BaTiO_3$** model systems the mesh size was set to 2 nm. The $BaTiO_3$ spheres had a homogeneous shell with defined thickness and permittivity $\varepsilon_{\mathrm{eff}}$ according to the Maxwell-Garnett effective medium formula:[162,163]

$$\varepsilon_{\mathrm{eff}}(\omega) = \varepsilon_{\mathrm{H_2O}} \frac{\varepsilon_{\mathrm{Au}}(\omega)[1+2f] - \varepsilon_{\mathrm{H_2O}}[2f-2]}{\varepsilon_{\mathrm{H_2O}}[2+f] + \varepsilon_{\mathrm{Au}}(\omega)[1-f]} \tag{3.9}$$

where $\varepsilon_{\mathrm{H_2O}}$ is 1.7689, $\varepsilon_{\mathrm{Au}}$ is the frequency-dependent complex permittivity of gold, and f the volume filling fraction of gold. The fields in the integrals for $BaTiO_3$ particles and gold-coated $BaTiO_3$ spheres (e.g. Figure 6.23, black and blue lines) correspond to the values from individual mesh cells, but for composite Au@$BaTiO_3$ structures the fields in the integrals represent the averages over 5 grid points in the x, y and z direction (e.g. regions of 2.5 nm in Figure 6.23, red lines). This average can lead to an underestimation of the contribution of the

plasmonic hot-spots to the SHG, but at the same time it helps to minimize the known problem with FDTD of obtaining artificially strong fields at regions very close to the interfaces.

Analytical extinction cross sections of $BaTiO_3$ sphere (300 nm) and gold coated $BaTiO_3$ sphere (300 nm core size, 17 nm shell thickness, 0.287 gold filling fraction) were calculated according to Mie theory[35,164] by Alvaro Nodal (Centro de Física de Materiales, San Sebastian, Spain).

3.7 Density functional theory (DFT) calculations

DFT calculations were performed with Gaussian 09[165] using the B3LYP functional[79] and 6-311G** basis set.[166] The structures of **thiophenol, benzyl mercaptan, phenylethyl mercaptan, 2-aminothiophenol, 3-aminothiophenol, and 4-aminothiophenol** were optimized, and the vibrational frequencies were calculated. Raman intensities were calculated for an excitation wavelength of 785 nm for thiophenol, benzyl mercaptan, and phenylethyl mercaptan, and 633 nm for 2-aminothiophenol, 3-aminothiophenol, and 4-aminothiophenol. The calculated vibrational frequencies were used to improve the assignment of bands observed in SEHRS and SERS spectra of the respective molecules discussed in Chapter 7.

Chapter 4

Gold nanoparticles and nanorods for plasmonic enhancement of hyper Raman scattering

This chapter is based on the publication *J. Phys. Chem. C* 2018, 122, 5, 2931-2940.

Surface enhanced hyper Raman scattering (SEHRS) as an approach for sensitive vibrational probing strongly relies on plasmonic nanostructured materials providing high enhancement factors because the hyper Raman scattering (HRS) cross sections are extremely low.[85] In surface enhanced Raman scattering (SERS) the enhancement from numerous types of gold, silver, copper, aluminum and hybrid nanostructures with different morphologies in the liquid phase and on solid supports has been explored in great detail.[108,167,168] In contrast, SEHRS experiments have been carried out mainly using traditional silver nanomaterials such as nanoparticles, nanoaggregates, and roughened electrodes.[83,113,114] Gold nanoparticles have been far less frequently used,[21,119] even though vibrational imaging and mapping of live cells with plasmonic nanoprobes and labels[169] including SEHRS[170,171] would benefit very much from the use of gold nanostructures due to their higher biocompatibility and chemical stability compared to other plasmonic substrates.

In this chapter, the SEHRS enhancement from different gold nanostructures will be discussed. SEHRS spectra of crystal violet and rhodamine 6G in the local fields of spherical gold nanoparticles of different sizes and nanorods are presented and the resulting enhancement factors are compared. The experimentally observed dependence of the overall SEHRS signal on the particle size and shape will be discussed along with finite-difference time-domain (FDTD) simulations of the electromagnetic field enhancement. In particular, the interaction

of the nanostructures with analyte molecules and with each other, leading to the formation of aggregates, will be considered, as it strongly influences the enhancement in SEHRS, and therefore is crucial for exploiting gold SEHRS nanosensors in future applications.

4.1 SEHRS in the local fields of different gold nanostructures

First, gold nanoparticles were prepared by the citrate reduction method following the Frens,[54] and Lee and Meisel[53] protocols, resulting in mostly spherical nanostructures with diameters ranging from 30 nm to 70 nm. The nanoparticle size distributions were determined from transmission electron microscopy (TEM), and TEM images of all gold particles are presented in Figure 4.1A-J. CTAB-stabilized gold nanorods with average dimensions of 80 nm $\times$ 17 nm (Figure 4.1K-L) were obtained according to the seed-mediated growth method.[56] From the TEM data, the purity of the nanorods was estimated to be 91 %. The side products included spherical and cuboid particles.

Figure 4.2A shows the UV-vis absorbance spectra of the colloidal gold nanoparticle solutions of the citrate stabilized, mostly spherical nanoparticles, displaying an increase of the absorbance maximum λ_{max} with increased nanoparticle size (Figure 4.2B). This is in accord with previous findings.[54,172,173] In the spectra from colloidal solutions containing bigger nanoparticles, e.g. with diameter above 65 nm (green lines in Figure 4.2A), the plasmon bands exhibit an extended shoulder, indicating the formation of aggregates. The chemical surface properties for all spherical nanostructures of different size are very similar, as in all syntheses citrate serves as both the reducing and capping agent. Figure 4.2C shows the UV-vis spectrum of the CTAB-stabilized gold nanorods that display strong absorbance in both the visible and near-infrared regions due the transversal and the longitudinal plasmon modes at 515 and 860 nm, respectively. The shoulder of the band at 515 nm results from contributions from the side products.[56]

SEHRS spectra of the two dyes crystal violet (CV) and rhodamine 6G (R6G) on all gold nanostructures were obtained by adding an aqueous solution of the respective molecule to the gold nanoparticle suspension. As SEHRS is a non-linear process, the signal intensity depends quadratically on the excitation intensity, which is demonstrated in Figure 4.3. Figure 4.4A shows typical SEHRS spectra yielded with spherical gold nanoparticles, and Figure 4.5 contains several spectra obtained with the gold nanorods for different concentrations of

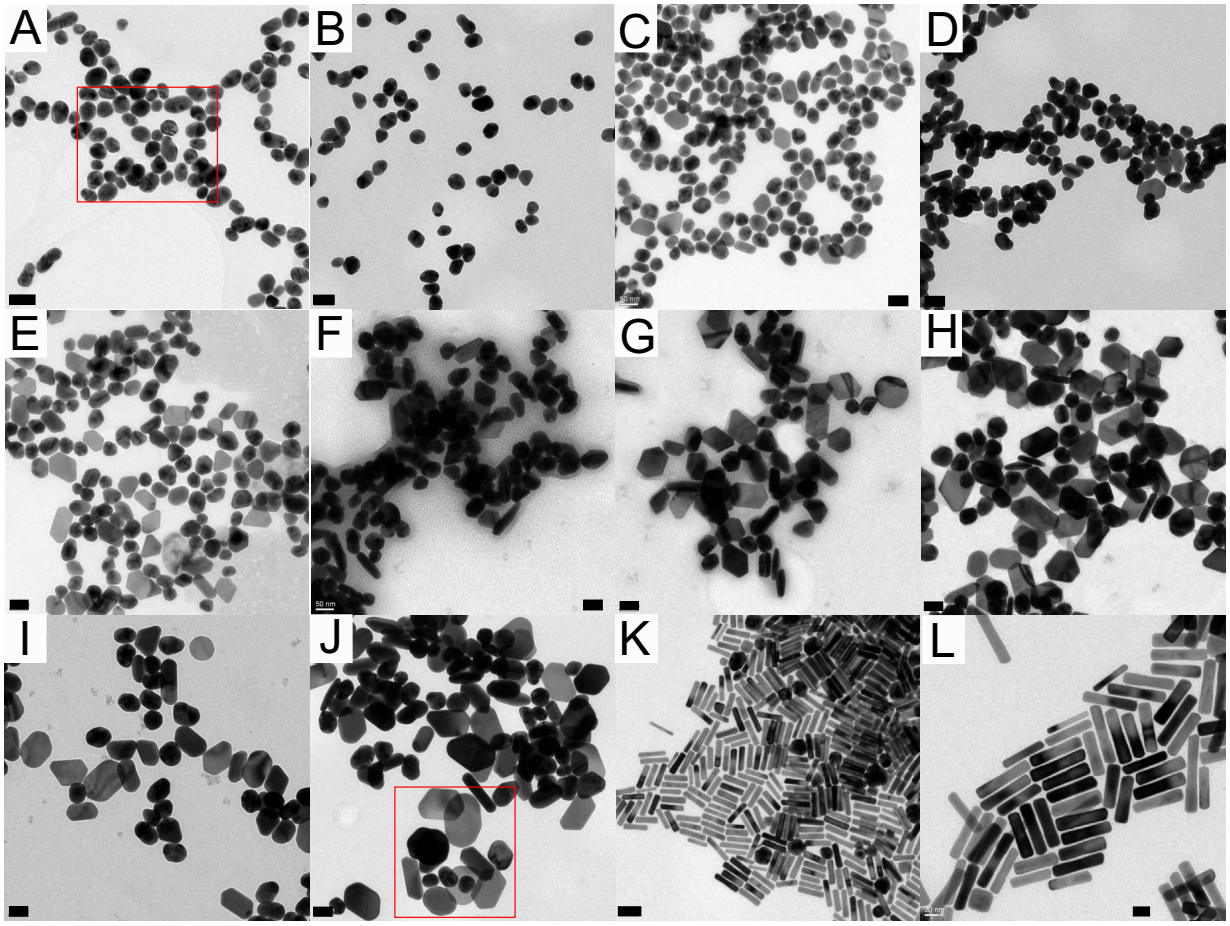

Figure 4.1: Representative transmission electron micrographs of (A-J) the spherical gold nanoparticles, and (K-L) the gold nanorods used in SEHRS experiments. Mean particle diameters: (A) 32 nm, (B) 43 nm, (C) 44 nm, (D) 47 nm, (E) 52 nm, (F) 57 nm, (G) 64 nm, (H) 68 nm, (I) 71 nm, and (J) 72 nm. The average dimensions of the gold nanorods are (80 ± 9) nm $\times$ (17 ± 3) nm. Scale bars: (A-K) 50 nm, and (L) 20 nm. Parts of TEM images in (A) and (J) marked with red squares correspond to areas, which were used in the FDTD simulations presented Section 4.2, Figure 4.15. Adapted with permission from *J. Phys. Chem. C* 2018, 122, 5, 2931-2940. Copyright 2018 American Chemical Society.

the two dyes. The SEHRS spectra of each of the molecules are qualitatively very similar, independent of the particle shape, size, and surface functionalization. Corresponding one-photon excited SERS spectra from identical samples with spherical nanoparticles are shown in Figure 4.4B. The spectra resemble those previously reported in work using gold[119] and silver nanostructures,[11,85,107,113,114] and also the qualitative differences in relative band intensities between the one- and two-photon excited spectra (compare Figure 4.4A and B), determined by the different Raman and hyper Raman selection rules, are in good agreement with previous reports.[11,119] The second harmonic of the 1064 nm wavelength, which was

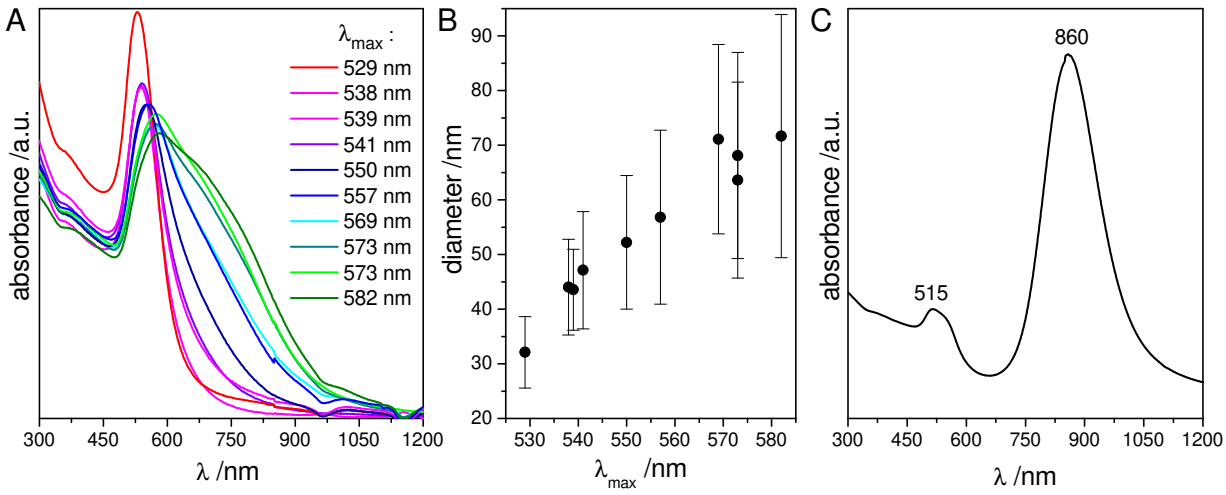

Figure 4.2: A) UV-vis spectra of the colloidal gold nanoparticle solutions used in the SEHRS experiments. B) Corresponding mean particle diameters as determined from TEM, the error bars represent the standard deviation. To determine the size, ~700 particles from each type were analyzed. C) UV-vis absorbance spectrum of the gold nanorods. Adapted with permission from *J. Phys. Chem. C* 2018, 122, 5, 2931-2940. Copyright 2018 American Chemical Society.

used to excite the SEHRS spectra shown in Figure 4.4 and Figure 4.5, is at 532 nm, which is close to the electronic transition of CV, as illustrated by the absorption spectra presented in Figure 4.6A. Therefore, there is a strong contribution of resonance enhancement[68,174,175] of the SEHRS as well as of the 532 nm excited SERS. The relatively high similarity of the SEHRS and the SERS spectrum (compare top traces in Figure 4.4A and B) indicates that the same electronic transition in CV is responsible in both one-photon and two-photon excitation.[176]

The excitation at 1064 nm allows to measure also a normal HRS spectrum of crystal violet (see Figure 4.6B), and thus to estimate an enhancement factor by comparing the intensity of the same bands in the HRS and SEHRS spectrum according to Equation(3.8). It was not possible to use rhodamine 6G for enhancement factor estimations due to very high two-photon excited fluorescence background in its HRS spectrum.

By using the crystal violet band at 1586 cm^{-1}, the enhancement factor for the gold nanoparticles was determined to range from 10^6 to 10^7 for the different spherical particles, and it is 10^7 for the nanorods. The higher enhancement generated by the gold nanorods allowed to acquire SEHRS spectra of the dyes at concentrations as low as 10^{-8} M (Figure 4.5, bottommost traces), while with spherical particles the minimum detectable concentration using the same excitation conditions was 10^{-7} M. For comparison, the enhancement factor for aggregates

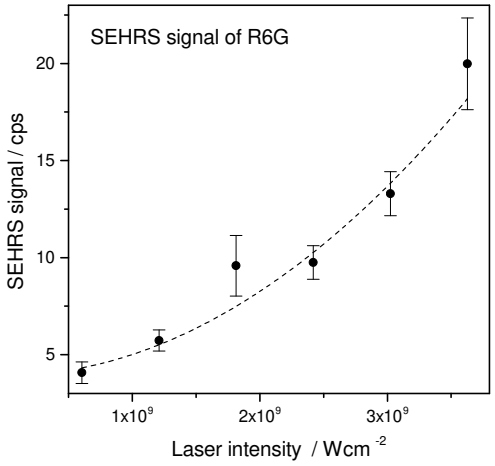

Figure 4.3: SEHRS signal (in counts per second, cps) of the rhodamine 6G band at 1530 cm^{-1} as a function of the applied laser intensity. Each value is the mean from 30 spectra that were obtained with 44 nm gold nanoparticles and 5×10^{-7} M rhodamine 6G. The dashed line is the fitted quadratic curve ($ax^2 + b$) to the data points.

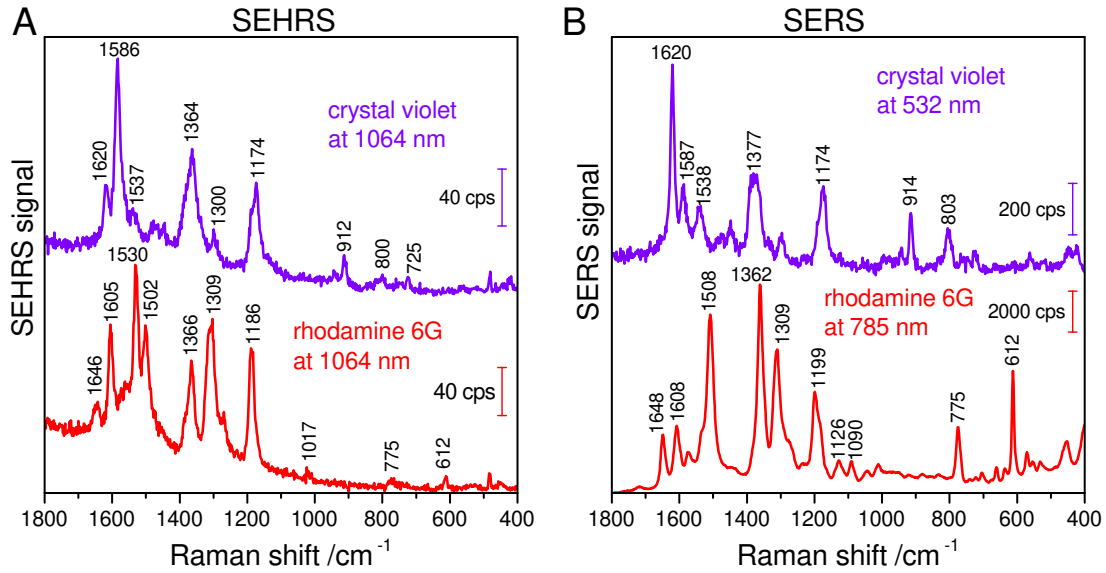

Figure 4.4: A) SEHRS and B) SERS spectra of the dye molecules crystal violet (top trace) and rhodamine 6G (bottom trace) obtained with gold nanoparticles. Excitation: 1064 nm (A), and 532 nm for CV and 785 nm for R6G (B); acquisition time: 5 s (A) and 1 s (B); laser intensity: 5×10^9 W cm^{-2} (A) and 5×10^8 W cm^{-2} for CV and 5×10^5 W cm^{-2} for R6G (B); dye concentration: 10^{-6} M. Adapted with permission from *J. Phys. Chem. C* 2018, 122, 5, 2931-2940. Copyright 2018 American Chemical Society.

of citrate reduced silver nanoparticles is on the order of 10^7 using the same experimental conditions regarding excitation and similar surface coverage of the silver nanoparticles with CV molecules as of the gold nanostructures (spectra not shown). Differing from this, Leng et

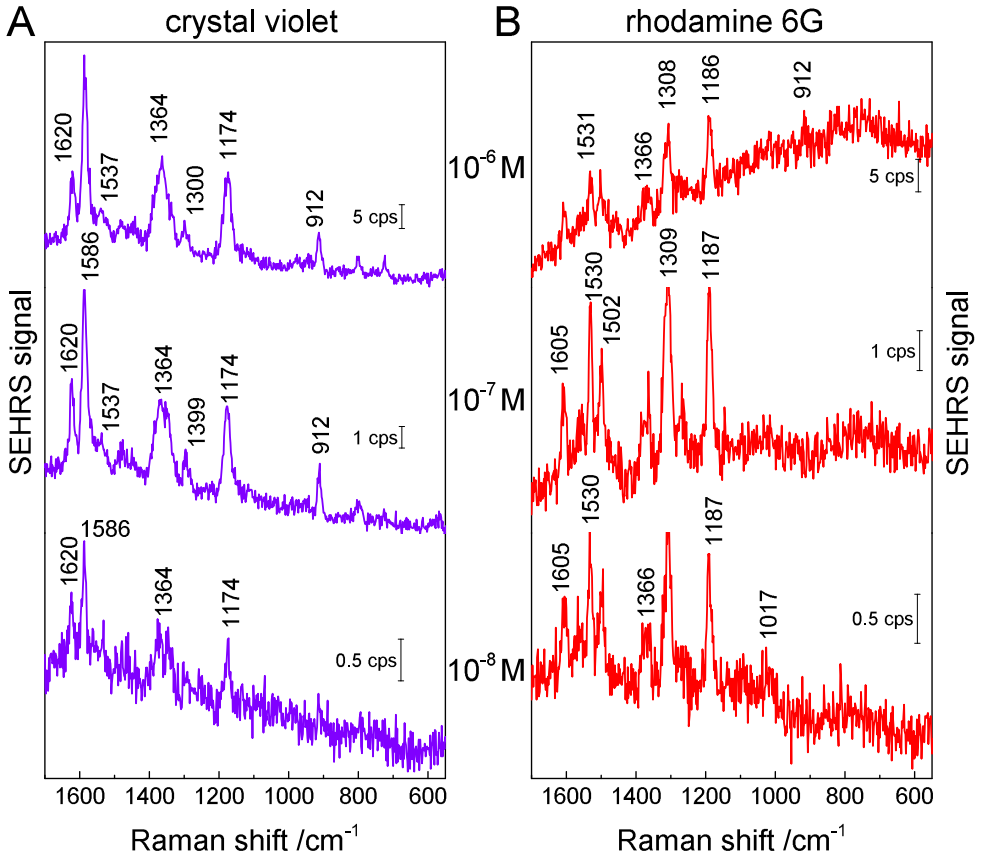

Figure 4.5: SEHRS spectra of A) crystal violet and B) rhodamine 6G in the local fields of gold nanorods at different concentrations. Excitation: 1064 nm; laser intensity: 5×10^9 W cm^{-2}; acquisition time: 5 s (uppermost rrace, 10^{-6} M), 30 s (middle trace, 10^{-7} M), and 60 s (bottommost trace, 10^{-8} M). Adapted with permission from *J. Phys. Chem. C* 2018, 122, 5, 2931-2940. Copyright 2018 American Chemical Society.

al.[114] reported an enhancement factor obtained for silver nanoaggregates with CV on the order of 10^4 at 927 nm excitation, significantly lower than the enhancement observed for the gold nanostructures in this work. Lipscomb et al.[119] discussed that the SEHRS enhancement factor for gold should be 1-2 orders of magnitude lower than for silver nanoparticles, without reporting absolute values. The experimental results here show that the plasmon enhancement on gold nanostructures acting for a SEHRS process at 1064 nm can be on the same order of magnitude as on silver nanoparticles. Similar to the observations made for an equally strong enhancement of one-photon excited SERS when gold and silver nanoparticles form nanoaggregates[177,178] - in spite of different enhancement found for isolated nanoparticles - the similar enhancement in SEHRS for gold and silver nanostructures found here also strongly suggests the important role of nanoaggregate formation.

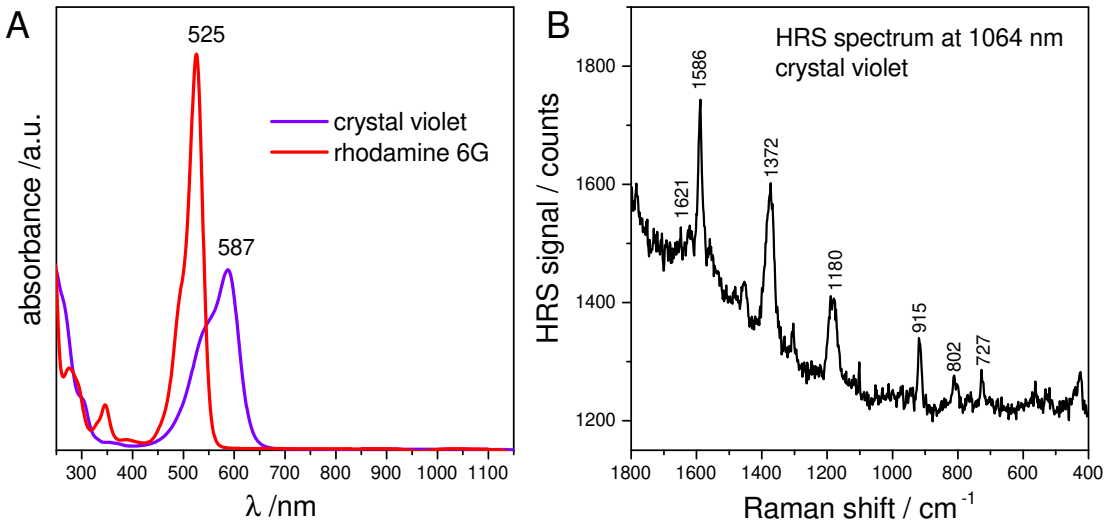

Figure 4.6: UV-vis absorption spectra of crystal violet and rhodamine 6G aqueous solutions at a concentration of 10^{-5} M. Adapted with permission from *J. Phys. Chem. C* 2018, 122, 5, 2931-2940. Copyright 2018 American Chemical Society. B) HRS spectrum of 10^{-3} M crystal violet (average of 3 spectra). Excitation: 1064 nm; laser intensity: 2×10^9 W cm^{-2}; acquisition time: 8 min. Reproduced from *Chem. Soc. Rev.* 2017, 46, 3980-3999 with permission from the Royal Society of Chemistry.

In order to analyze the plasmonic properties of the nanostructures in the different SEHRS experiments, UV-vis absorbance spectra of all samples were obtained (see Figure 4.8). The addition of dye molecules at 10^{-6} M concentration to the colloidal nanoparticle solutions results in the formation of gold nanoaggregates, which is evidenced by the broadened plasmon band in the UV-vis spectra of the mixtures compared to the spectra of the nanoparticles in the absence of the dye molecules (Figure 4.8), as well as from dynamic light scattering (DLS) data (Figure 4.9). Therefore, the observed increase in SEHRS enhancement with increasing particle size cannot be discussed in terms of electromagnetic enhancement from individual gold nanoparticles, as it has been done for SERS.[179] The differences in the absorbance spectra of the different samples clearly show that the aggregates from nanoparticles of different size have very different plasmonic properties. For example, the broadening of the plasmon band for 70 nm gold nanoparticles is greater than that for the 30 nm particles (compare Figure 4.8A and J), explaining that the associated SEHRS enhancement at one particular excitation wavelength can vary for both types of nanoaggregates. Furthermore, dynamic light scattering experiments (Figure 4.9) indicate that not only the plasmonic properties but also the size of the aggregates formed by the different gold nanoparticles differs.

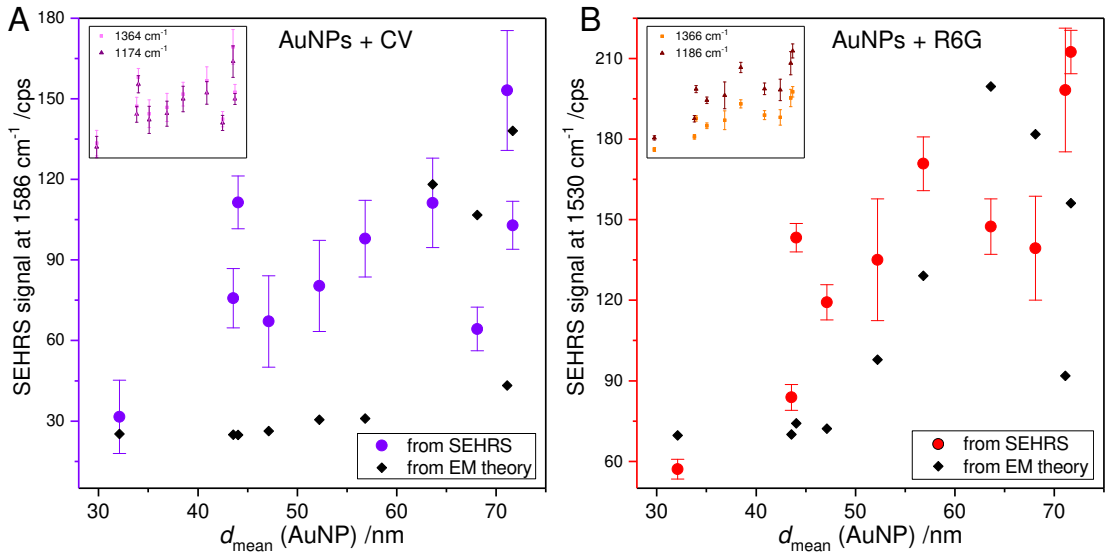

Figure 4.7: SEHRS signal (in counts per second, cps) of A) the crystal violet band at 1586 cm^{-1} (purple dots) and B) the rhodamine 6G band at 1530 cm^{-1} (red dots) as a function of the gold nanoparticle size. Each value is the mean obtained from 30 spectra. The insets show the similar SEHRS signal size dependence of the CV bands at 1364 and 1174 cm^{-1}, and R6G bands at 1366 and 1186 cm^{-1}. The black squares in A and B represent the scaled estimated electromagnetic enhancement factors determined from UV-vis absorbance spectra of the SEHRS samples (see Figure 4.8 for the original UV-vis data) based on Equation (3.2). Adapted with permission from *J. Phys. Chem. C* 2018, 122, 5, 2931-2940. Copyright 2018 American Chemical Society.

The electromagnetic SEHRS enhancement can be estimated empirically from the UV-vis absorbance spectra of the nanoparticle-dye mixtures (Figure 4.8), which contain information about the electromagnetic properties of the nanoaggregates.[90,91] Figure 4.7 compares such empirical enhancement factors (black squares, scaled for clarity) calculated according to Equation (3.2) with the actually measured SEHRS signal (colored dots). As can be seen from the data from crystal violet (Figure 4.7A), the estimated SEHRS enhancement for nanoaggregates, formed by particles with sizes from 30 nm to 60 nm, is very similar, although the measured SEHRS signal rises significantly. In the case of rhodamine 6G (Figure 4.7B) this is valid for gold aggregates from particles with sizes below 50 nm. These discrepancies support the assumption that most of the SEHRS signal originates from the "hottest" hot spots, i.e., from very few nanoaggregates, that are not observed in the far field UV-vis spectra, and whose contribution to the absorbance is "averaged out" in the absorbance of

the whole sample. Thus, SEHRS can serve as much more sensitive indicator of the presence of a few SEHRS active aggregates than UV-vis absorbance.

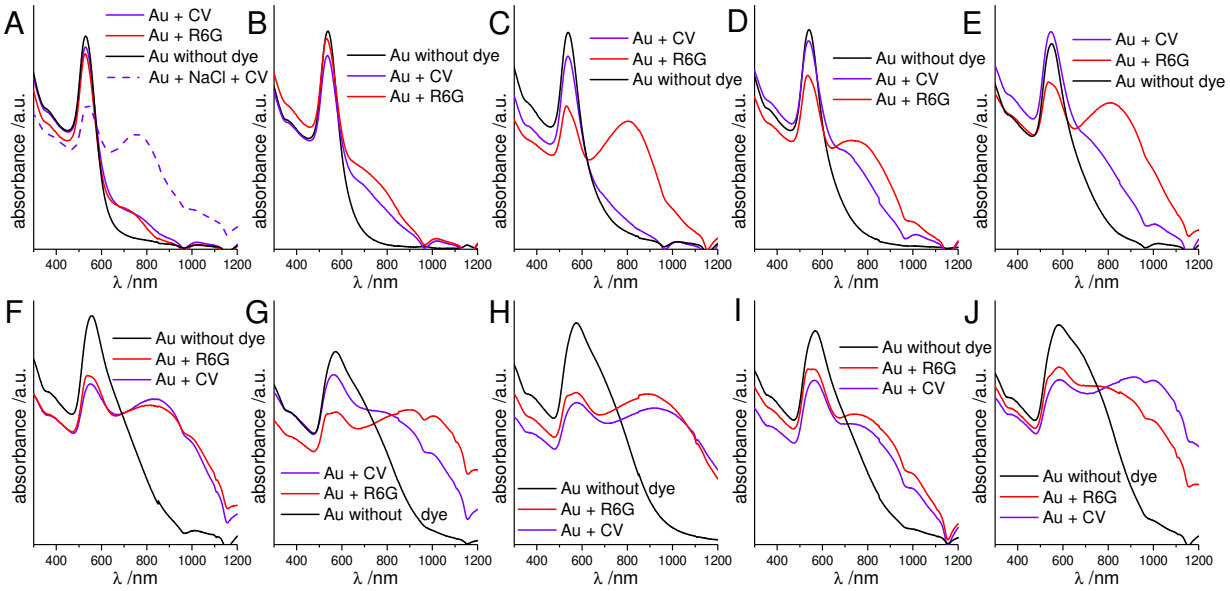

Figure 4.8: UV-vis absorbance spectra of gold nanoparticles (black lines, same data as in Figure 4.2A), gold nanoparticles with 10^{-6} M crystal violet (violet lines), and gold nanoparticles with 10^{-6} M rhodamine 6G (red lines). Mean particle diameters: (A) 32 nm, (B) 43 nm, (C) 44 nm, (D) 47 nm, (E) 52 nm, (F) 57 nm, (G) 64 nm, (H) 68 nm, (I) 71 nm, and (J) 72 nm. Adapted with permission from *J. Phys. Chem. C* 2018, 122, 5, 2931-2940. Copyright 2018 American Chemical Society.

Together with the absorbance spectra, the SEHRS signals obtained here illustrate the importance of the nanoaggregates' properties, such as arrangement of the nanoparticles in aggregates and interparticle distance that have been discussed to exert an important influence on the enhancement in SEHRS.[8,37,102,178,180,181] As mentioned above, if the dye molecules are directly added to the nanoparticles, the SEHRS signal increases with increasing size of the particles (Figure 4.7). In experiments, where first the formation of nanoaggregates was induced by addition of sodium chloride, and then the dyes were introduced into the system, the SEHRS signals from all nanoparticles are very similar. As shown in Figure 4.10, no dependence of signal on particle size can be found. The signals obtained with these pre-aggregated nanostructures are similar to those of the nanoparticles without the addition of NaCl in the medium size range, and the high intensities found especially in the larger nanoparticles are

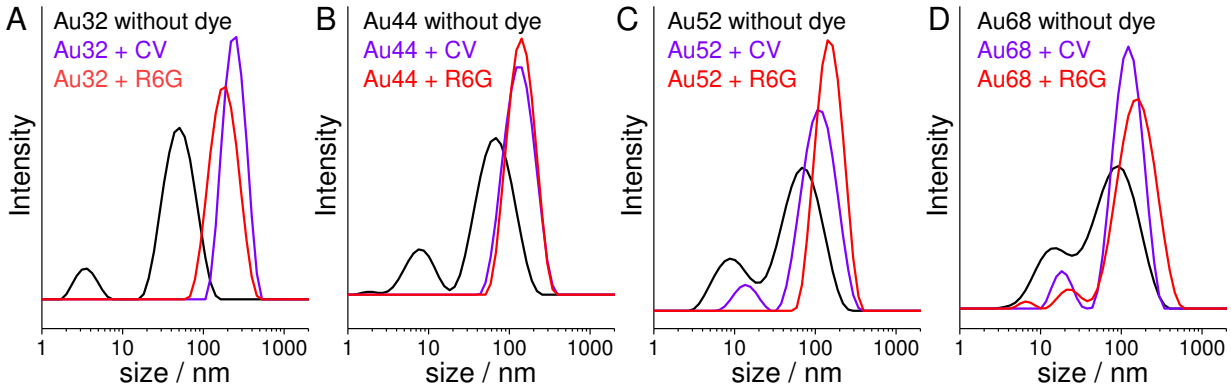

Figure 4.9: Intensity distribution of gold nanoaggregate sizes as determined by dynamic light scattering. Gold nanoparticles with mean size of (A) 32 nm, (B) 44 nm, (C) 52 nm, and (D) 68 nm. Only gold nanoparticles - black lines, gold nanoparticles with 10^{-6} M crystal violet - violet lines, and with 10^{-6} M rhodamine 6G - red lines. Adapted with permission from *J. Phys. Chem. C* 2018, 122, 5, 2931-2940. Copyright 2018 American Chemical Society.

not reached, if pre-aggregation by NaCl takes place (compare Figure 4.7 with Figure 4.10). The observed different SEHRS intensities from aggregates of the same nanoparticle solution, produced with and without pre-aggregation with NaCl, e.g., the signals generated by the 70 nm nanoparticles in Figure 4.7 and Figure 4.10, suggest that the arrangement of the nanoparticles in the aggregates plays a more significant role in determining the SEHRS enhancement than the particle size itself. The addition of sodium chloride forms gold nanoaggregates that differ regarding the nanoparticle arrangement, resulting in different plasmonic properties, compared to aggregates formed by the dyes. As an example, the UV-vis spectrum of 32 nm gold particles with NaCl and CV (dashed violet line in Figure 4.8A), and only with CV (solid violet line in Figure 4.8A) differ significantly. It is possible that the nanoaggregates with different nanoparticle arrangement and/or interparticle distances are the result of the much larger sizes of the dye molecules compared to that of the sodium and chloride ions.[182]

Figure 4.11 shows the relation between the nanoparticle size and the intensity of the CV SERS signal, obtained from identical samples as in the SEHRS experiments displayed in Figure 4.7A. In contrast to SEHRS, in SERS a decrease in the signal intensity with increasing size of the gold nanoparticles in the aggregates is observed. The experiment was performed only with CV due to the very high fluorescence background in the 532 nm excited spectra of R6G. The data shows that the gold aggregates' properties required for obtaining an optimal enhancement of CV in SERS and SEHRS are not the same. Similar observations were reported also for different types of silver nanoparticles previously.[26]

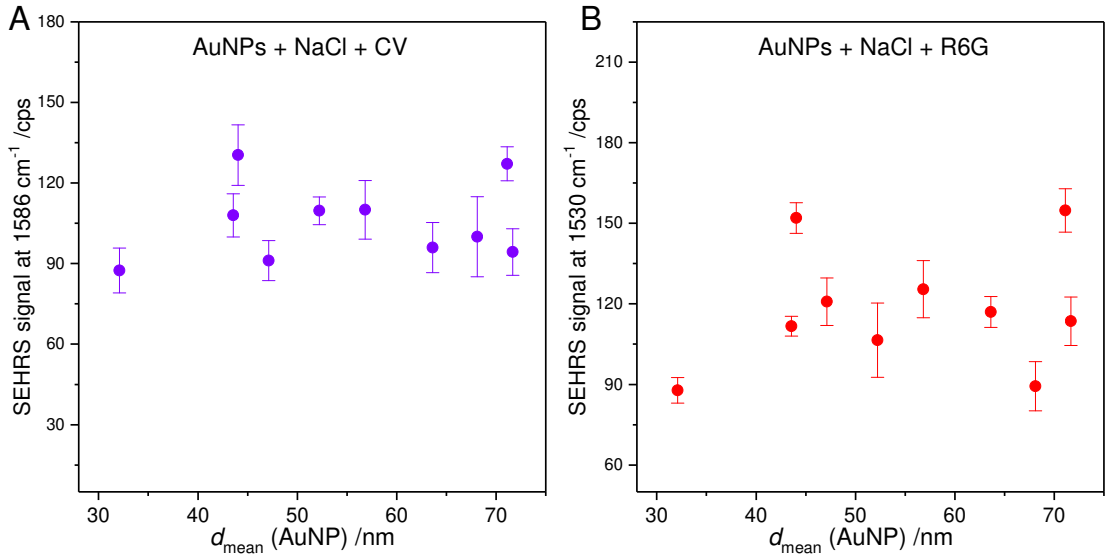

Figure 4.10: Intensity of the SEHRS signal from A) crystal violet and B) rhodamine 6G bands at 1586 cm^{-1} and 1530 cm^{-1}, respectively, as a function of the gold nanoparticle size. In contrast to Figure 4.7, the gold nanoparticles were first aggregated with sodium chloride before crystal violet or rhodamine 6G solutions were added. Each value is the mean obtained from 30 spectra. Adapted with permission from *J. Phys. Chem. C* 2018, 122, 5, 2931-2940. Copyright 2018 American Chemical Society.

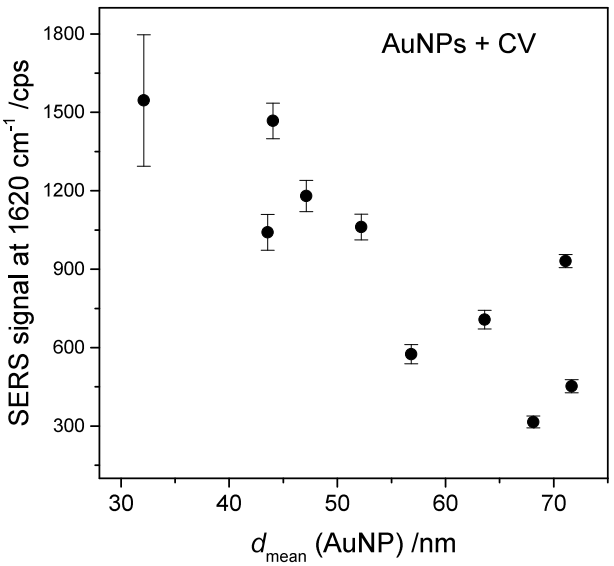

Figure 4.11: SERS signal excited at 532 nm of the crystal violet band at 1620 cm^{-1} as a function of the gold nanoparticle size. The measured samples are identical with those used in the SEHRS experiments shown in Figure 4.7A.

4.2 Electromagnetic enhancement of SEHRS from FDTD

To understand the impact of the gold nanoparticle size and shape on the electromagnetic enhancement in SEHRS observed experimentally and described in Section 4.1, 3D finite-difference time-domain (3D-FDTD) simulations were performed on simplified model systems. The electric near-field intensity enhancement at the hyper Raman excitation wavelength of 1064 nm, and at the Stokes HRS wavelength of 580 nm, corresponding to the crystal violet band at 1586 cm^{-1}, was calculated for an arrangement of two gold nanospheres with sizes of 32 nm, 44 nm and 60 nm. Figure 4.12A and B show the field intensity distributions for an interparticle distance of 2 nm at 1064 nm and 580 nm, respectively. The maximum field intensity enhancement is found in the junction between the two particles, and at 1064 nm it is ~230, ~400, and ~860 for nanoparticles in the size of 32 nm, 44 nm, and 60 nm, respectively (Figure 4.12A), showing an increase with nanoparticle size. In contrast, at the HRS wavelength of 580 nm, higher field intensities are found, however, the enhancement at the visible wavelength is almost the same for the particles of varying size, especially for the case of the gold particles of 44 nm and 60 nm in diameter, ~13200 and ~13100, respectively (Figure 4.12B).

Figure 4.13A presents the SEHRS enhancement for the three dimers, calculated from the data in Figure 4.12 according to $|E_{ex}|^4|E_{HRS}|^2$, where E_{ex} is short notation for the local field enhancement at the excitation wavelength $E_{loc}(\nu_0)/E_{inc}(\nu_0)$ and E_{HRS} for the field enhancement at the HRS wavelength $E_{loc}(\nu_{HRS})/E_{inc}(\nu_{HRS})$. The total SEHRS enhancement rises with increasing size of the particles, being one order of magnitude higher for the dimer consisting of 60 nm particles compared to 32 nm particles. The small variations of the field intensity at 1064 nm cause these significant differences in the total SEHRS enhancement because the latter depends quadratically on the excitation field intensity. Furthermore, the SEHRS enhancement also strongly depends on the distance between the particles, as shown in Figure 4.13B. Thus, the results from the dimer simulations with nanospheres are qualitatively in agreement with the experimental data from the aggregates that were formed by the addition of dye molecules shown in Figure 4.7, as well as with previous reports that have discussed the distribution of enhanced local fields in the case of SERS.[183]

The distributions of the electric near-field intensity for a dimer of gold nanorods at 1064 nm and 580 nm, and the SEHRS enhancement are presented in Figure 4.14. In the case of nanorods, the local fields at the excitation wavelength in the near-IR present the main contribution to the total SEHRS enhancement, around 4 to 5 orders of magnitude, in contrast

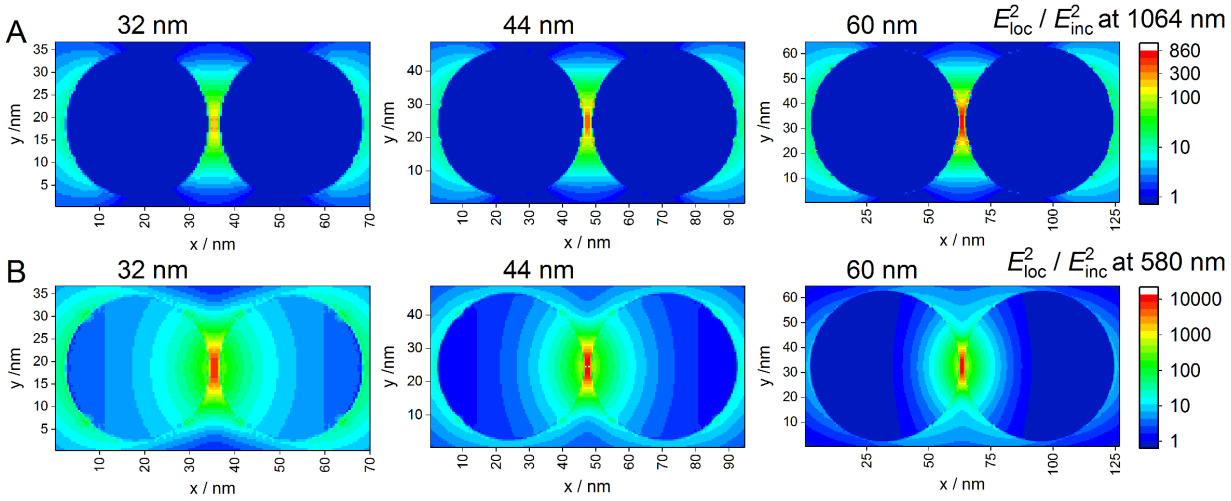

Figure 4.12: Simulated 3D finite-difference time-domain (FDTD) electric near-field intensity normalized to the incident field (E^2_{loc}/E^2_{inc}) at A) the excitation wavelength of 1064 nm and B) the Stokes HRS wavelength of 580 nm in the *xy* equatorial plane for two gold nanoparticles in aqueous environment with sizes of 32 nm (left panels), 44 nm (middle panels), and 60 nm (right panels). The interparticle distance in all cases is 2 nm. The incident wave is polarized along the *x* axis, and is propagating in *z* direction. The maximum value for the field enhancement in the junction between the two particles for (A) at 1064 nm is ~230 (for 32 nm particles), ~400 (for 44 nm particles), and ~860 (for 60 nm particles), and for (B) at 580 nm: ~8200 (for 32 nm particles), ~13200 (for 44 nm particles), and ~13100 (for 60 nm particles). Adapted with permission from *J. Phys. Chem. C* 2018, 122, 5, 2931-2940. Copyright 2018 American Chemical Society.

to the spherical nanostructures, where the fields are significantly enhanced at both, the excitation and scattering frequency (compare Figure 4.14 with Figure 4.12). The high field enhancements at the IR excitation wavelength can be attributed to plasmon resonances, yet they can also be the result of enhancement by the lightning rod effect.[184,185] The maximum SEHRS enhancement in the junction between two nanorods, as shown in Figure 4.14C, is around one order of magnitude higher than for the spherical nanoparticles. This is in accord with the experimental data, where a slightly higher enhancement factor for the gold nanorods compared to all spherical nanoparticles is found.

Results from FDTD simulations using example nanostructures that were observed in the TEM micrographs (see Figure 4.11A and J), which include particles of varying sizes and particles that are not ideally spherical or not spherical at all, are displayed in Figure 4.15. In contrast to the dimer simulations, the fields at the visible wavelength are two orders

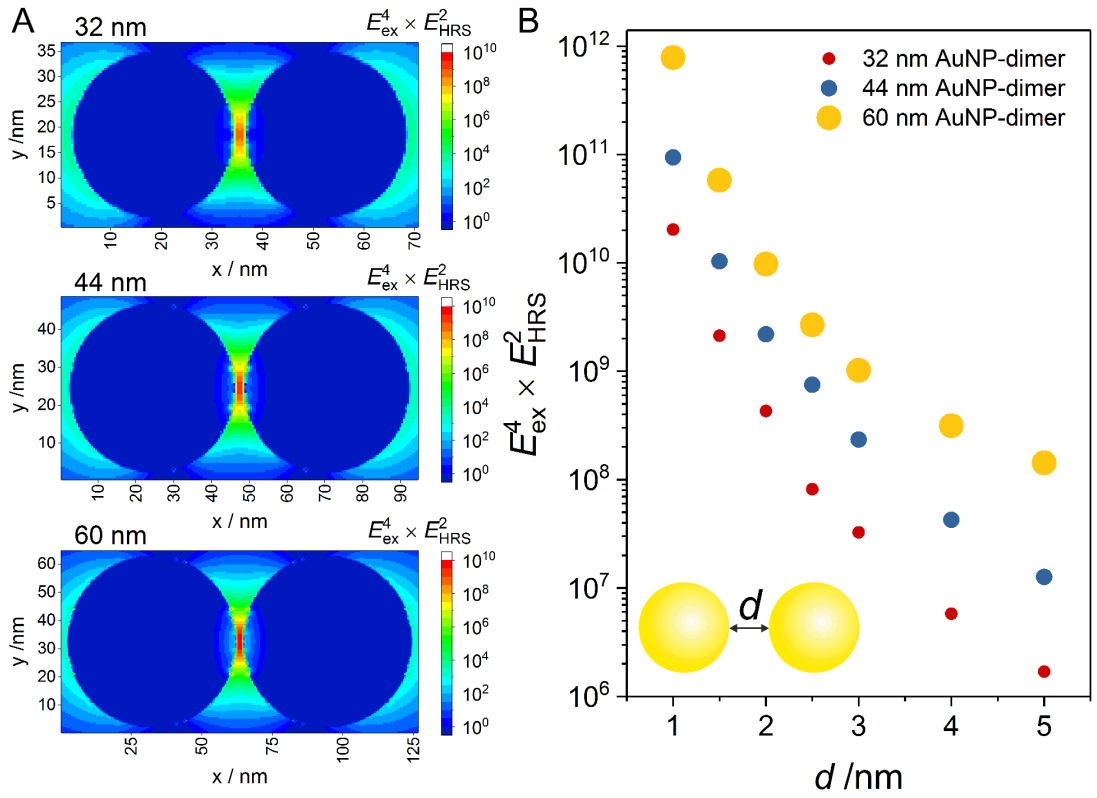

Figure 4.13: A) Spatial distribution of the SEHRS enhancement ($|E_{ex}|^4|E_{HRS}|^2$) as a result from the 3D-FDTD simulations of gold nanoparticle dimers shown in Figure 4.12. The maximum values of the SEHRS enhancement in the junction between the two nanostructures are: $10^{8.6}$ for the 32 nm particles (uppermost), $10^{9.3}$ for the 44 nm particles (middle), and 10^{10} for the 60 nm particles (bottommost). Adapted with permission from *J. Phys. Chem. C* 2018, 122, 5, 2931-2940. Copyright 2018 American Chemical Society. B) Interparticle distance dependence of the SEHRS enhancement in the junction between two gold nanoparticles calculated from 3D-FDTD simulations.

of magnitude less enhanced (compare Figure 4.12B with Figure 4.15B). Meanwhile, the field at the IR excitation wavelength shows stronger enhancement for the aggregates with many nanoparticles (compare Figure 4.12A with Figure 4.15A), which could result from plasmon resonances but also from an enhancement due to the lightning rod effect. However, at 1064 nm the maximum value of the field enhancement for the arrangement of 72 nm particles is higher than for the 32 nm particles, and at 580 nm the fields in the 72 nm particle arrangement are slightly less enhanced than the ones for the 32 nm particle arrangement, which was found also in the simulations with two gold nanoparticles. It should be noted here that the spatial coordinates with maximum field enhancement at 1064 nm are

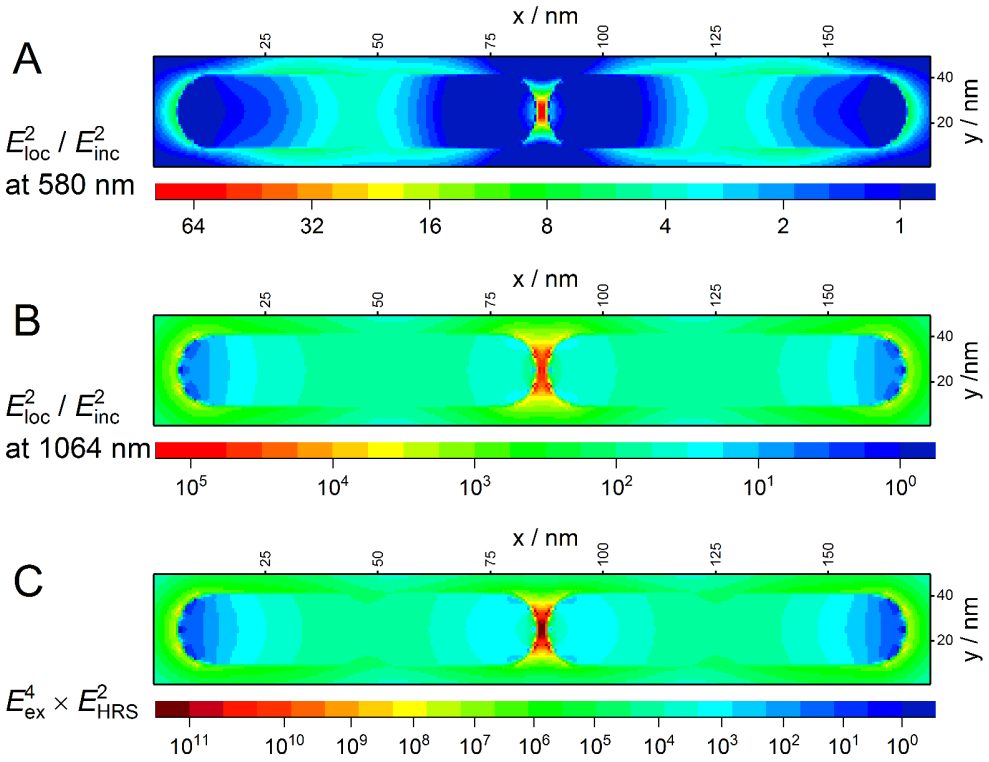

Figure 4.14: Simulated 3D-FDTD electric near-field intensity normalized to the incident field (E^2_{loc}/E^2_{inc}) at A) the excitation wavelength of 1064 nm, and B) the Stokes HRS wavelength of 580 nm in the xy equatorial plane for two gold nanorods with sizes of 80×17 nm. The two rods are separated by 2 nm. The incident wave is polarized along the x axis, and is propagating in z direction. The maximum value for the field enhancement in the junction between the two rods for (A) at 1064 nm is 10^5, and for (B) at 580 nm is 77. C) Spatial distribution of the SEHRS enhancement ($|E_{ex}|^4|E_{HRS}|^2$) as a result from the FDTD simulations in A and B. The maximum value is $10^{11.4}$. Adapted with permission from *J. Phys. Chem. C* 2018, 122, 5, 2931-2940. Copyright 2018 American Chemical Society.

not the same as for 580 nm. In agreement with the dimer simulations (Figure 4.13) and with the experiments, the arrangement of larger nanoparticles displays higher value for the maximum obtained SEHRS enhancement ($10^{9.5}$) than the arrangement of the smaller particles (10^9), as indicated in Figure 4.1C, though this difference is smaller than the one calculated for the homogeneous dimers of spherical particles.

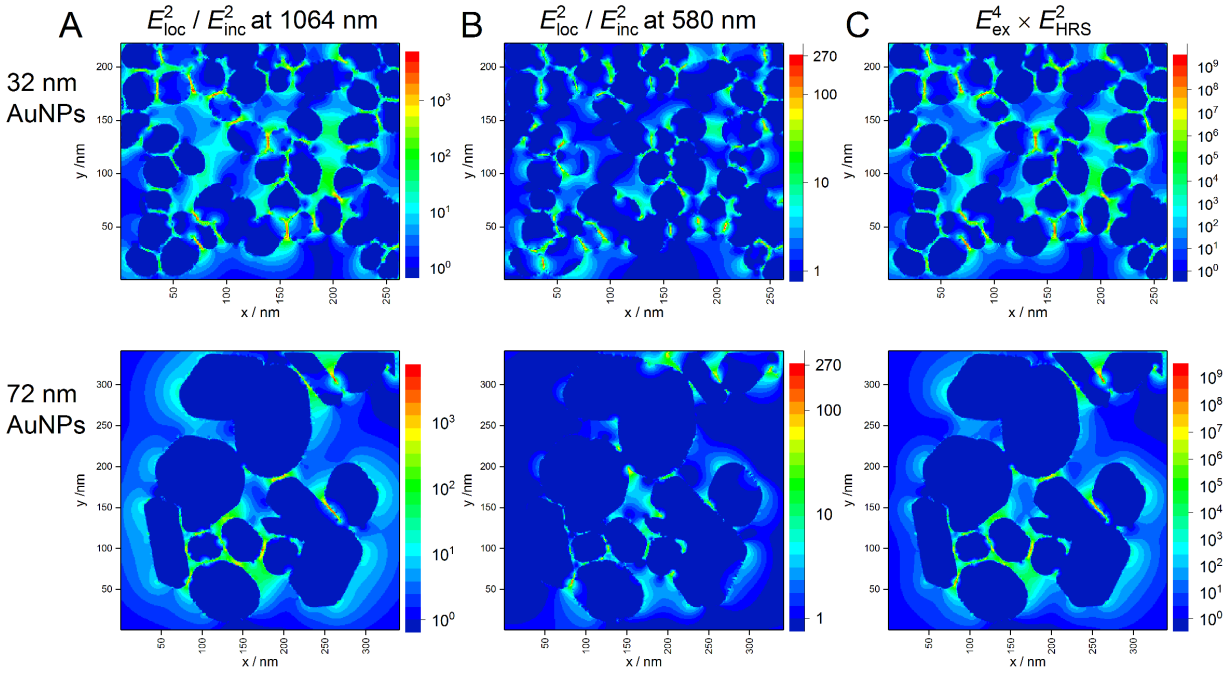

Figure 4.15: Simulated 3D-FDTD electric near-field intensity normalized to the incident field (E^2_{loc}/E^2_{inc}) at A) the excitation wavelength of 1064 nm, and B) the Stokes HRS wavelength of 580 nm for experimentally observed arrangements of gold nanoparticles in TEM. The uppermost arrangements of nanoparticles in panels A and B correspond to part of the TEM image shown in Figure 4.1A (marked with red square), and the bottommost arrangements correspond to part of the TEM image shown in Figure 4.1J (marked with red square). The incident wave is polarized along the x axis, and is propagating in z direction. The maximum value for the field enhancement for (A) at 1064 nm is $\sim$ 4700 and $\sim$ 7340, and for (B) at 580 nm is $\sim$ 280 and $\sim$ 150, for the 32 nm and 72 nm nanoparticles, respectively. C) Spatial distribution of the SEHRS enhancement ($|E_{ex}|^4|E_{HRS}|^2$) as a result from the FDTD simulations in A and B. The maximum value is 10^9 for the 32 nm particles and $10^{9.5}$ for the 72 nm particles. Adapted with permission from *J. Phys. Chem. C* 2018, 122, 5, 2931-2940. Copyright 2018 American Chemical Society.

4.3 Influence of the interaction with analyte molecules on the SEHRS enhancement

As indicated by the results shown in Section 4.1, the availability of nanoaggregates must play a key role for the observation of the strong enhancement of the HRS signals. At low crystal violet and rhodamine 6G concentration (10^{-7} M), no SEHRS spectra were obtained with spherical gold nanoparticles, even though spectra down to concentrations of 10^{-8} M were

measured when gold nanorods were used as plasmonic structures (Figure 4.5). Also, as discussed above, when aggregation of the spherical gold nanoparticles was induced by addition of sodium chloride, it was possible to collect SEHRS spectra at these concentrations (see Figure 4.16). The possibility to obtain SEHRS spectra with aggregates of the spherical nanoparticles (Figure 4.16) suggests that a R6G or CV concentration of 10^{-7} M is not sufficient for the formation of aggregates with properties that result in high enough SEHRS enhancement with these nanoparticles. The SEHRS signal from crystal violet is lower than from rhodamine 6G, indicating that crystal violet and rhodamine 6G probably interact in a different way with the gold particles. This is also supported by the different absorbance of the aggregates in the presence of crystal violet and rhodamine 6G (Figure 4.8, compare the red and purple spectra in each panel), providing evidence that nanoaggregates with different properties must form.

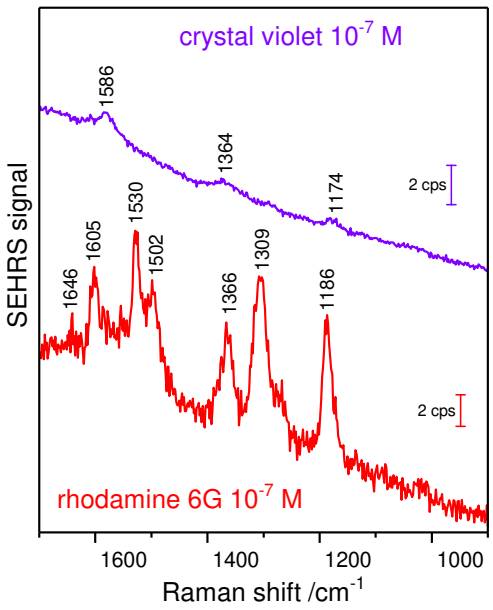

Figure 4.16: SEHRS spectra of the dye molecules crystal violet (top trace) and rhodamine 6G (bottom trace) obtained with gold nanoaggregates that were produced by pre-aggregation of gold nanoparticles with sodium chloride. Excitation: 1064 nm, acquisition time: 30 s, laser intensity: 5×10^9 W cm^{-2}, dye concentration: 10^{-7} M. The crystal violet spectrum is the mean of 30 spectra. Adapted with permission from *J. Phys. Chem. C* 2018, 122, 5, 2931-2940. Copyright 2018 American Chemical Society.

Figure 4.17A shows SEHRS signals at different dye concentrations for one of the solutions of spherical gold nanoparticles (71 nm). The SEHRS signal from both molecules depends on

their concentration (Figure 4.17A, purple points for CV and red points for R6G). There exists a narrow concentration range, for which the SEHRS signal rises rapidly, and which differs in CV and R6G. For rhodamine 6G it is possible to acquire SEHRS spectra at lower concentrations, and the saturation of the signal is reached at 5×10^{-7} M, while the crystal violet signal does not rise further only at a concentration of 1.5×10^{-6} M. The saturation of the signals can be interpreted by a maximum possible surface coverage, or a maximum coverage of hot spots, being reached at this particular concentration. Excess molecules cannot participate in the SEHRS process, nevertheless, they can lead to further aggregation of the nanoparticles and to a decrease of the signal due to the diminished surface area when aggregates form. A similar dependence is observed also for the one-photon excited SERS signal, as plotted for crystal violet in Figure 4.17B, or discussed in previous work.[179] The absorbance spectra shown in Figure 4.17C indicate that the concentration range, in which the SEHRS signal rapidly increases, is associated with significant changes in the optical properties of the gold nanoaggregates. The nanoaggregates, formed by different crystal violet concentrations, provide different enhancement. For analytical applications of SEHRS, this may present a limitation that can be addressed. As indicated by the high standard deviation of the SEHRS signal of crystal violet (Figure 4.17A) in the concentration range where SEHRS signals rise, some of the nanoaggregates at this concentration provide sufficient enhancement, and some do not.

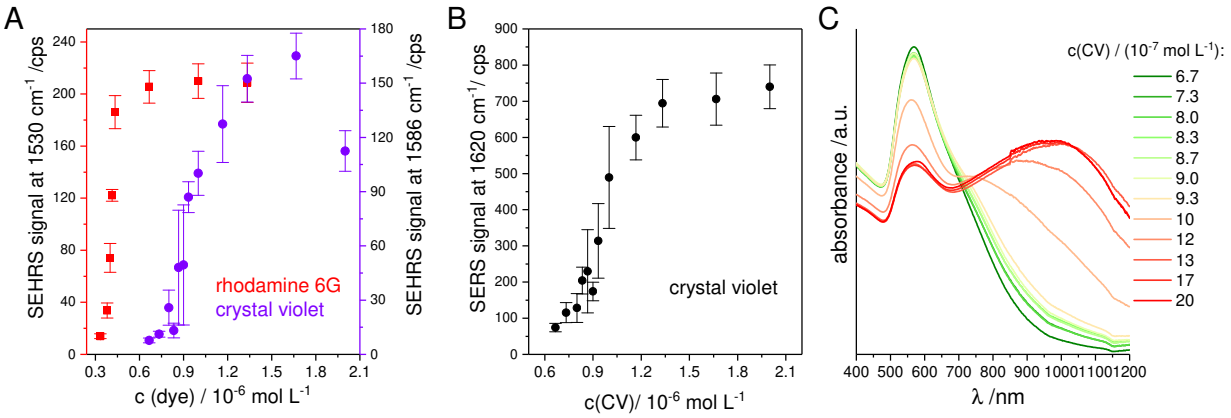

Figure 4.17: A) SEHRS and B) SERS signal from crystal violet and rhodamine 6G obtained with spherical gold nanoparticles (71 nm) as a function of the dye concentration. Excitation: 1064 nm (A) and 532 nm (B); acquisition time: 5 s (A) and 1 s (B); laser intensity: 5×10^9 W cm^{-2} (A) and 5×10^8 W cm^{-2} (B). C) UV-vis spectra from the identical samples with crystal violet used in (A) and (B). Adapted with permission from *J. Phys. Chem. C* 2018, 122, 5, 2931-2940. Copyright 2018 American Chemical Society.

Similarly to the spherical nanoparticles, the nanorods form aggregates in the presence of crystal violet and rhodamine 6G. The UV-vis spectra of gold nanorod solutions with crystal violet at different concentrations are displayed in Figure 4.18A, and indicate the presence of different types of aggregates when different amounts of the dye are added to the nanorod colloid. The fact that spectra with the nanorods can be obtained easily at a relatively low dye concentration of 10^{-8} M (Figure 4.5), indicates that already small amounts of CV and R6G can induce the formation of nanorod aggregates. This suggests a stronger interaction between the gold nanorods and the dye molecules than between the spherical nanoparticles, which could result also from the different surface chemistry of the nanostructures. Rapid changes in the optical properties of nanorod aggregates are observed for the concentration range between 1×10^{-7} and 1×10^{-6} M crystal violet, and are also associated with a strong increase of the CV SEHRS signals (see Figure 4.18B). In contrast to the spherical nanoparticles, the SEHRS signal from the nanorods rises less rapidly and in a more linear manner, and also the standard deviation is significantly lower. Thus, the higher stability of the signal could present an advantage of the nanorods over the spherical particles for future analytical applications of SEHRS, in addition to their higher enhancement. The formation of this type of nanorod aggregates has been discussed to be very beneficial for SERS as well.[186,187]

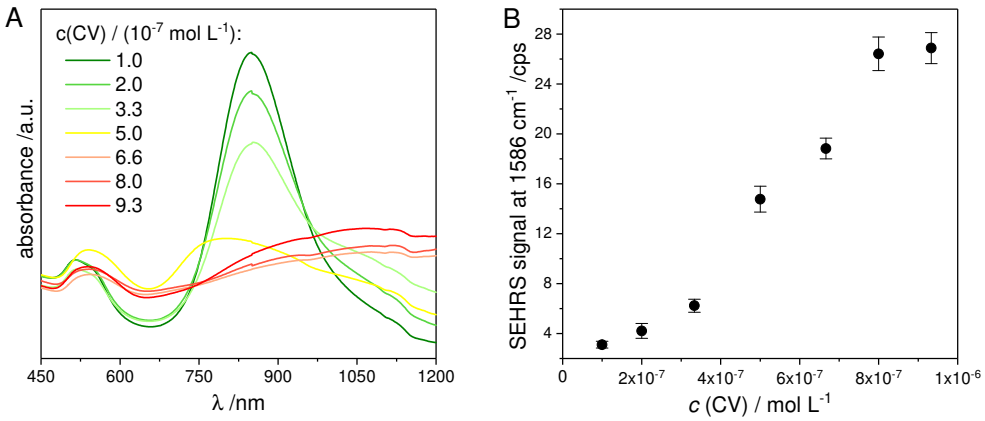

Figure 4.18: A) UV-vis absorbance spectra of gold nanorods in the presence of crystal violet at different concentrations. B) SEHRS signal of the crystal violet band at 1586 cm^{-1} as a function of the CV concentration. Excitation wavelength: 1064 nm, acquisition time: 5 s, laser intensity: 4×10^9 W cm^{-2}. The samples used in (A) are identical to the samples in (B). Adapted with permission from *J. Phys. Chem. C* 2018, 122, 5, 2931-2940. Copyright 2018 American Chemical Society.

The data presented here indicate that observing SEHRS at different concentrations of potential analyte molecules can reveal information about the interaction and adsorption of the molecule on the metal surface. The results from the comparison of crystal violet and rhodamine 6G illustrate that the affinity of the rhodamine dye to the gold surface is higher than of crystal violet, and that this affects the sensitivity of the experiment. This is of great importance if SEHRS approaches are developed in order to address real analytical applications, such as studies on the interaction of biomolecules. Similar aspects have been discussed for SERS experiments, and their discussions led to very practical developments, e.g., the arrangement of silver substrates for the detection of proteins,[188] or the immobilization of nanostructures in order to maintain defined enhancement for quantitative experiments.[189–191] The observation that rhodamine 6G has a different affinity to the gold surface than crystal violet, reflected by changes in SEHRS enhancement, suggests the possibility to use SEHRS as a tool for investigating adsorption and interaction processes.

4.4 Conclusions

The data presented in this chapter demonstrate that gold nanostructures of different size, shape and also surface functionalization provide efficient plasmonic enhancement of hyper Raman scattering. By using HRS signals of the dye crystal violet, enhancement factors for aggregates of spherical gold nanoparticles and gold nanorods were estimated to be in the same order of magnitude as enhancement factors of silver nanostructures ($10^6 - 10^7$), which have been the most frequently used SEHRS substrates so far. This strongly suggests the important role of nanoaggregate formation, independent of the nanoparticle material. The high enhancement obtained with the gold nanostructures opens new possibilities for exploiting such particles as SEHRS nanosensors, e.g., in future analytical applications involving biological samples.

As the experiments and numerical simulations of the electromagnetic enhancements show, the SEHRS signals depend on the particle size and shape. SEHRS spectra of crystal violet and rhodamine 6G, obtained with spherical citrate reduced gold nanoparticles with sizes ranging from 30 nm to 70 nm, indicate that nanoaggregates, formed in the presence of these dye molecules, yield higher SEHRS intensities with increasing size of the particles in the aggregates. This is supported by FDTD simulations of the SEHRS enhancement in junctions

between two gold nanoparticles of varying size and also by simulations of more realistic nanoparticle arrangements found in TEM, which revealed that the field enhancement at the near-IR excitation frequency was slightly more sensitive to variations of the particle size than the field enhancement of the hyper Raman scattered light in the visible. The quadratic dependence of the SEHRS signal on the intensity of the excitation light leads to a strong influence of these small changes in nanoparticle size. Furthermore, aggregates of gold nanorods showed higher SEHRS enhancement factors than aggregates of spherical gold nanostructures. Plasmon resonances at the excitation wavelength in the IR spectral range, as well as enhancement due to the lightning rod effect may contribute significantly to the total SEHRS enhancement in the local environment of aggregates and rod-like nanostructures. In particular, comparison between SEHRS and SERS experimental data showed that nanostructures with different properties are required for an optimal enhancement of the one- and two-photon Raman process.

Experiments at low dye molecule concentrations where no enhancement occurs, as well as SEHRS spectra obtained after pre-aggregation of the nanoparticles using sodium chloride indicated that the interaction of the gold particles with one another is required for the formation of nanoaggregate structures. Strong plasmonic enhancement of the HRS signals is provided when the analyte molecules induce the formation of nanoaggregates. As shown by the UV-vis and SEHRS data, the same nanoparticle solution can form aggregates with different optical properties and SEHRS enhancement, depending on the analyte molecule, its concentration, and the pre-aggregation conditions. The geometrical properties of these aggregates, specifically the arrangement of the particles in the aggregates and the interparticle distances, might be the main factor that determines the total SEHRS enhancement, in addition to the size and shape of individual particles. As demonstrated by using the examples of crystal violet and rhodamine 6G, the spherical and particularly the rod-like gold nanoparticles can be used for experiments with SEHRS that investigate interactions between different molecules and nanostructures. The experiments showed that the enhancement is influenced by the analyte molecules, and understanding this will help to control and to optimize it for potential applications of SEHRS in analytical chemistry and biophysics.

Chapter 5

Plasmon enhanced two-photon probing with gold and silver nanovoid structures

This chapter is based on the publication *Adv. Optical Mater.* 2019, 7, 1900650.

The majority of enhancing nanostructures for surface enhanced hyper Raman scattering (SEHRS) are nanoparticles, nanoaggregates, or roughened electrodes that were used in early SEHRS experiments. The morphology of these substrates is controllable only to a limited extent, and the enhancement by nanoparticles is strongly influenced by the presence and interaction of analyte molecules, as it was discussed in Chapter 4. Well-defined, top-down fabricated plasmonic structures with nanoscale gaps, often used in SERS,[108–110] could also be beneficial for SEHRS experiments.[111] Apart from the requirements of fabrication by lithography, recent theoretical and experimental works[26,99,104] indicate that an independent design and optimization of SEHRS substrates would be useful, due to the non-linear dependence of the SEHRS effect on the excitation field $|E_{\mathrm{loc}}(\nu_0)|^4|E_{\mathrm{loc}}(2\nu_0-\nu_k)|^2$ and the wide spectral separation of excitation and scattered light.

In this chapter, experiments probing the enhancement of hyper Raman scattering (HRS) and second harmonic generation (SHG) by nanostructured gold and silver films comprised of periodically arranged spherical voids will be presented. Nanovoid arrays were shown to support a variety of plasmon modes in the visible and near-IR range, depending on their structural parameters,[39,40,192] and are suitable for enhancement in SERS.[41,193–196] Reproducible void films with various geometries can be obtained by different fabrication methods, including electrochemical deposition,[41] which is relatively inexpensive and rapid

compared to nanolithographic approaches.[195,197] The nanovoid samples employed in the optical experiments here were fabricated by facile electrochemistry, and were provided by the group of Prof. Wolfgang Schuhmann at Ruhr-Universität Bochum. The SEHRS enhancement and SHG from gold and silver nanovoid arrays with different nanosphere templates and metal thickness will be compared, related phenomena will be discussed, and their potential use as SEHRS substrates will be evaluated.

5.1 Nanovoid arrays with gradually changing thickness

Nanovoid array samples with gradually changing metal layer thickness were fabricated by electrochemical deposition employing nanosphere templates with diameters of 200 nm, 300 nm, and 600 nm. In the first step, evaporated gold and silver thin films on a silicon wafer substrate were patterned with a monolayer of polystyrene nanospheres using the Langmuir-Blodgett technique. Then, a metal layer with a thickness gradient along the longitudinal direction of the substrate was generated by means of bipolar electrochemistry.[60,152] After subsequent dissolution of the polymer beads, the resulting substrates consist of a metal film comprised with periodically arranged voids that gradually change their opening sizes and inter-void distances according to the metal film thickness.

As an example of how the void structure changes along the length of the substrate (the bipolar electrode itself), Figure 5.1 presents scanning electron micrographs of gold voids templated with 600 nm nanospheres. At the edge of the wafer that was closer to the cathodic pole (referred to further as cathodic edge), the gold deposition rate is the highest, and thus the gold layer is so thick that the template polystyrene beads are covered by an amorphous metal structure (Figure 5.1A). With increasing distance from the cathodic edge, voids start appearing and their opening size increases until the point where the metal film reaches the equator of the nanospheres (Figure 5.1B-D). From this point on, the void diameter decreases and a gold film with shallow pores and larger distances between them is formed (Figure 5.1E-G). Figure 5.1H shows a schematic of the decrement of the metal film thickness from the cathodic to the anodic edge of the bipolar electrode. The distance from the cathodic edge as a measure for the metal film thickness is arbitrary for each sample due to variations in the substrate lengths, hence the potential gradients during deposition.

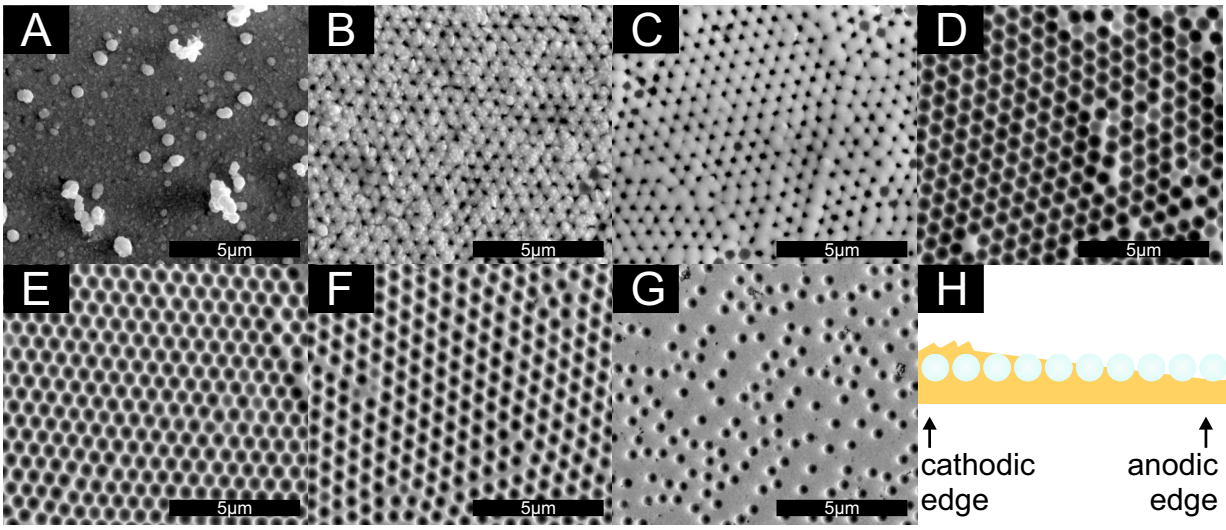

Figure 5.1: A-G) Scanning electron micrographs of an Au(600) gradient sample starting from the cathodic edge (A) moving towards the anodic edge (B-G). The sample was fabricated by Denis Öhl, João Junqueira and Ugur Kayran. H) Schematic representation of the metal thickness gradient along the bipolar electrode. Adapted from *Adv. Optical Mater.* 2019, 7, 1900650.

The non-linear response of the gradient void substrates was investigated using femtosecond excitation at 850 nm and the backscattered second harmonic generation (SHG) was recorded. Figure 5.2 shows the intensity of the SHG signal from a gold nanovoid gradient sample with 200 nm polymer nanosphere template, termed Au(200) gradient here, at different positions along the substrate. SHG signals are observed at the cathodic edge (Figure 5.2, from 1 mm to 5 mm), where the spheres are overgrown with a rough gold layer. In agreement with previous reports, the overgrowing metal film provides a nanoscopic roughness that can lead to strong enhancement of second harmonic signals in localized hot spots.[31,136,137] The SHG signals become weaker with increasing distance, when the gold deposition rate is diminished and the surface roughness slightly decreases (Figure 5.2, from 6 mm to 15 mm). In the sample shown in Figure 5.2, open nanovoids with metal layer above the equatorial plane start appearing at a distance of 16 mm, void opening sizes are indicated on the right axis. From there, with further increasing distance, the SHG intensity increases until it reaches a maximum corresponding to nanovoid structures with an opening size of 150 nm and height above the equatorial plane (Figure 5.2, from 18 mm to 20.6 mm). Further decrement of the gold layer thickness results in very rapid decrease of the SHG intensity (Figure 5.2, from 21 mm to 22 mm). According to previous discussions, electromagnetic fields in nanovoid arrays can be significantly enhanced[193,196,198] because of resonances with different, coexisting plasmon

modes in the visible and/or near-infrared, which can be tuned by altering the void diameter and height.[39,40,42] From the change in signal one can infer that the observed SHG in the void structures must be plasmon enhanced as the result of resonances of the array modes with the excitation and/or second harmonic radiation wavelengths. The increasing and decreasing SHG intensity along the thickness gradient implies that the enhancement of SHG at the given excitation wavelength of 850 nm is different for the different void heights that are present across the sample. This is in accord with previous findings for the variation of electromagnetic enhancement in SERS excitation profiles.[43,194]

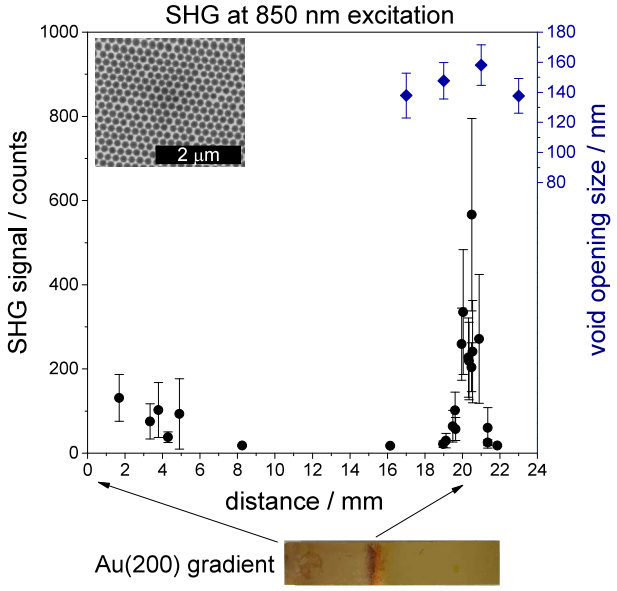

Figure 5.2: SHG signal at 425 nm from an Au(200) nanovoid gradient sample as a function of the distance from the cathodic edge of the substrate. The data points represent the average of ~100 SHG signal values obtained by raster scanning ~100 × 100 µm areas with a step size of 10 µm. Excitation: 850 nm; acquisition time: 1 s; laser peak intensity: 7×10^9 W cm^{-2}. The blue squares show the void opening sizes at the respective distances as determined from SEM. Photograph of the sample is shown below the *x*-axis, and the arrows indicate the approximate positions relative to the cathodic edge. The inset shows a SEM image at 20.6 mm from the cathodic edge where the highest SHG signal was observed. Adapted from *Adv. Optical Mater.* 2019, 7, 1900650.

The gold and silver samples obtained with 300 nm and 600 nm nanosphere templates display a similar variation of the SHG signals along their respective substrates as indicated in Figure 5.3. However, due to the different length of each silicon wafer substrate, the sub-

optimal behavior of the potential drop across the bipolar electrode, and the electrochemical dissolution of silver at the anodic edge,[152] the positions at which void structures appear are different for each sample (see dashed lines in each panel in Figure 5.3). For example, in the Au(300) gradient sample (Figure 5.3D) nanovoids appear at 13 mm, while in the Ag(300) gradient (Figure 5.3B) at 4 mm. Nevertheless, the SHG from the nanovoids first increases and then decreases in both samples (Figure 5.3D and B) like in the case of the Au(200) gradient (Figure 5.2). Typically, the length of the bipolar electrodes covered with nanovoids is short compared to the whole surface of the substrate, except for the Au(600) gradient sample where void structures yielding SHG are present from 5 to 18 mm. In all cases, the SHG from the rough gold and silver layers with overgrown polymer beads (see SHG signals from the left side of the dashed lines in Figure 5.3) is lower than the maximum values reached with actual void structures.

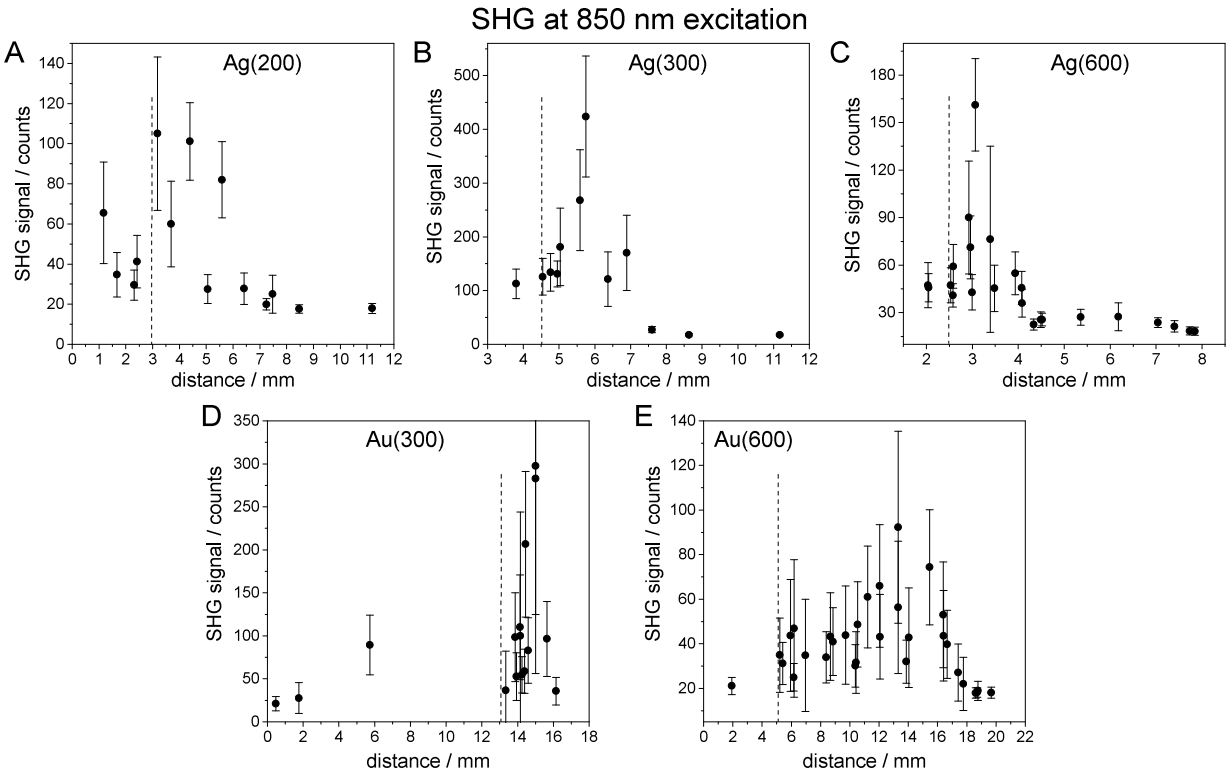

Figure 5.3: SHG signal at 425 nm from A) Ag(200), B) Ag(300), C) Ag(600), D) Au(300), and E) Au(600) gradient nanovoid samples as a function of the distance from the cathodic edge of the substrate. The data points are averages of ~100 values. The dashed lines indicate the positions from which nanovoid structures appear. Excitation: 850 nm; acquisition time: 1 s; laser peak intensity: 3×10^9 W cm^{-2} (A-C) and 7×10^9 W cm^{-2} (D-E).

The polarization dependence of the SHG from nanovoid arrays was studied by varying the incident light polarization and recording separately the x and y components of the second harmonic (SH) emission. Figure 5.4 shows SHG signals from gold nanovoid structures with 200 nm, 300 nm, and 600 nm nanosphere templates averaged over different neighbouring microscopic positions. In all cases, two perpendicular ellipsoidal emission patterns are observed, which could be summed into a circular, polarization independent total signal. This indicates that the observed signal is incoherent, which results from the contributions of randomly oriented emitters, similarly to the SH scattering of metal films.[31,138]

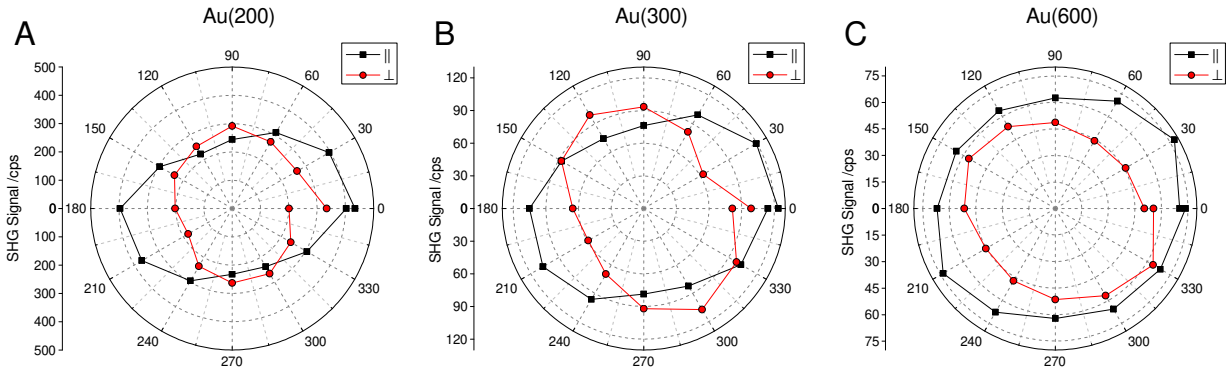

Figure 5.4: Polar plots of the SHG signal at 425 nm as a function of incident light polarization from gradient gold nanovoid samples with A) 200 nm, B) 300 nm, and C) 600 nm nanosphere templates. The polarization of the detected light was parallel (black squares) or perpendicular (red circles) to the detector slit. Each point is an average value of ~50 measurements at different neighbouring positions on the substrate. Excitation: 850 nm; integration time: 1 s; laser peak intensity: 7×10^9 W cm^{-2}.

Figure 5.5 shows examples of the SH emission pattern from single point measurements, from which the average values in Figure 5.4 were calculated. The experiments were performed using a 10× objective (NA 0.3), and the estimated two-photon focal spot diameter according to Equation (3.6) is 1300 nm, meaning that the detected signal originates from an area containing few nanovoids. While at the two positions shown in Figure 5.5A, dipolar emission patterns were observed, the probed areas within the focal spots in Figure 5.5B and C display more complex polarization dependencies that could result from dipolar and higher multipolar contributions. Yet, due to the many differently oriented emitters, the individual signals are averaged out over many different spots and the total signal from a larger area is polarization independent (Figure 5.4).

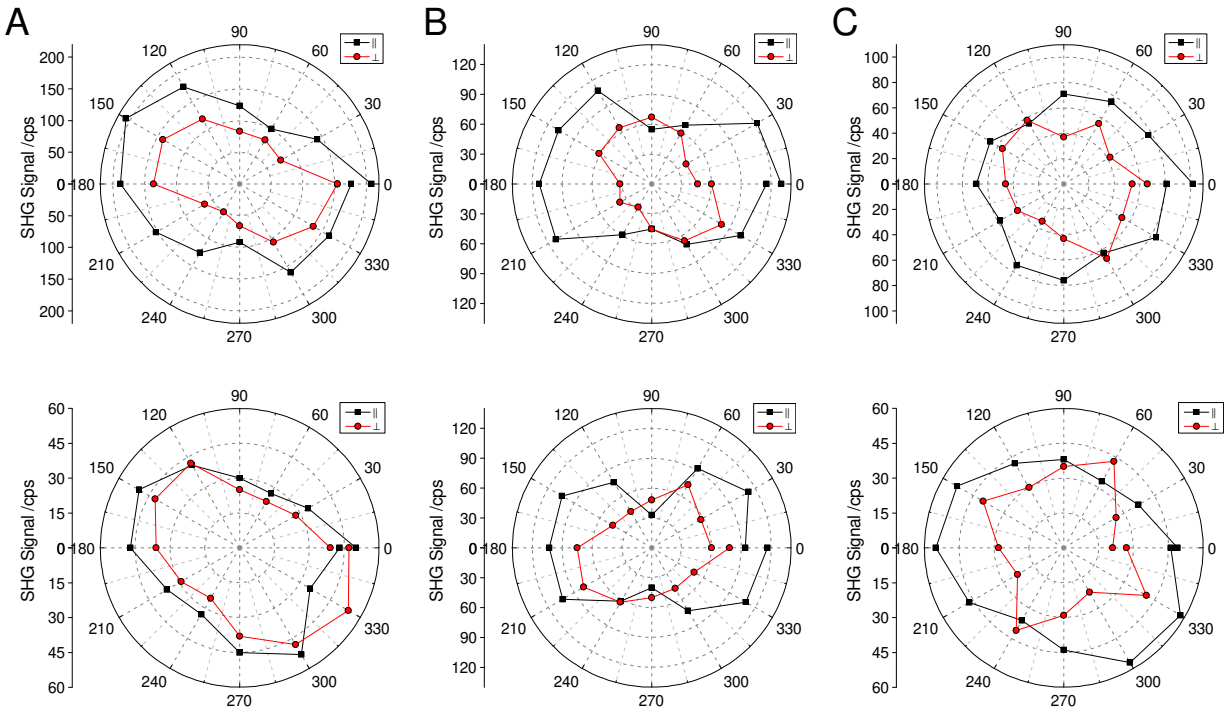

Figure 5.5: Polar plots of the SHG signal at 425 nm as a function of incident light polarization from gold nanovoids. The polarization of the detected light was parallel (black squares) or perpendicular (red circles) to the detector slit. Each panel represents single measurement at a particular microscopic position. Excitation: 850 nm; integration time: 1 s; laser peak intensity: 7×10^9 W cm^{-2}.

Next, the HRS enhancement of the gradient nanovoids was evaluated by using crystal violet (CV) as test molecule. The CV solution (10^{-5} M) was placed on top of the nanovoid substrates, and SEHRS spectra were collected using picosecond laser excitation at 1064 nm. Similar to the SHG signal, the SEHRS enhancement also varies along the length of the substrates with the gradual change in the height of the voids. Figure 5.6 shows the SEHRS signal of the CV vibration at 1585 cm^{-1} for a silver void gradient sample made with 200 nm sphere template, here referred to as Ag(200) gradient. The SEHRS intensity increases with increasing size of the void opening from 80 nm to 140 nm (Figure 5.6, from 6.5 mm to 8.5 mm). The SEHRS signal reaches a maximum for voids with 147 nm diameter and height above the equatorial plane of the spheres. Proceeding further along the longitudinal direction of the substrate, the SEHRS intensity decreases with decreasing void opening size. The last spectra with detectable enhancement were obtained with the Ag(200) gradient at voids with a diameter of 130 nm and a silver thickness below the equator of the templating spheres, corresponding to a distance of 11.5 mm from the cathodic edge (Figure 5.6).

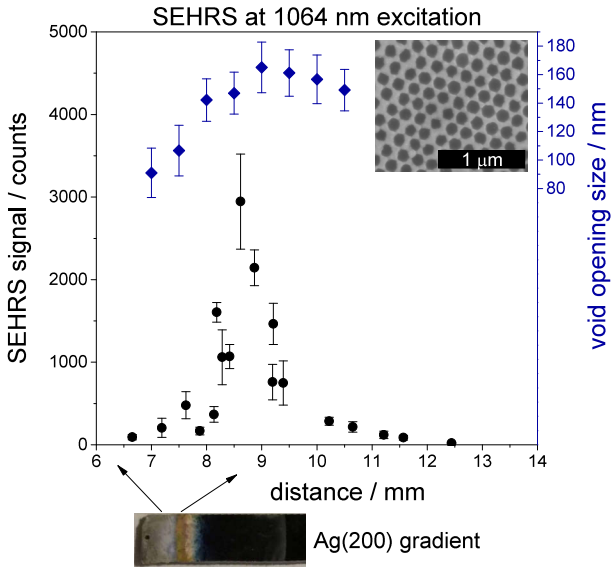

Figure 5.6: SEHRS signal of the crystal violet band at 1585 cm^{-1} obtained with an Ag(200) nanovoid gradient as a function of the distance from the cathodic edge of the substrate. The data points represent the average of ~10 values SEHRS signals obtained by raster scanning ~100 × 100 µm areas with a step size of 30 µm. Excitation: 1064 nm; acquisition time: 60 s; laser peak intensity: 1×10^{10} W cm^{-2}. The blue squares show the void opening sizes at the respective distances as determined from SEM. Photograph of the sample is shown below the *x*-axis, and the arrows indicate the approximate positions relative to the cathodic edge. The inset shows a SEM image at a distance of 8.6 mm where the highest SEHRS signal was observed. Adapted from *Adv. Optical Mater.* 2019, 7, 1900650.

Figure 5.7 shows the results from the SEHRS scanning of gold and silver gradient nanovoid substrates with 200 nm, 300 nm, and 600 nm polymer sphere templates. Unlike the Ag(200) gradient (Figure 5.6), the rest of the samples do not display clear linear increment and decrement in the SEHRS signal with changing metal film thickness. For example, Au(200) and Ag(300) gradients provide similar SEHRS enhancement over a long distance of 2 mm during which the void sizes change significantly (from 9 mm to 11 mm in Figure 5.7A and from 12 mm to 14 mm in Figure 5.7C). In general, the silver gradient void samples yield higher SEHRS intensities than the gold voids, and nanovoids with 200 nm and 300 nm nanosphere templates show stronger SEHRS enhancement than the voids with 600 nm templates. The SEHRS signals observed at positions on the left side of the dashed lines in each panel in Figure 5.7 originate from areas where the polymer spheres are fully or partially overgrown with a rough gold or silver layer. The SEHRS enhancement of sample areas with both voids and rough metal film, e.g. at 2 mm in Ag(600) and at 9 mm

in Au(200) gradients (Figure 5.7B and C), respectively, can be relatively similar to the enhancement of areas homogeneously covered with voids.

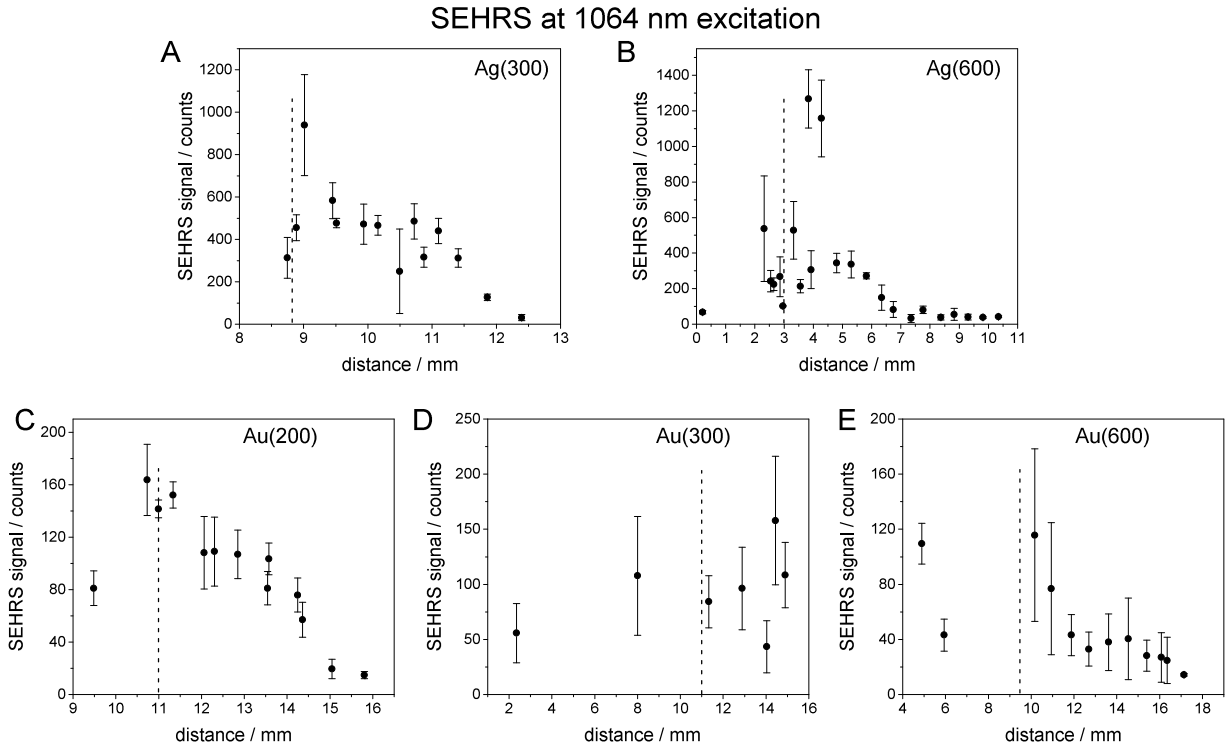

Figure 5.7: SEHRS intensity of the CV band at 1585 cm^{-1} obtained with A) Ag(300), B) Ag(600), C) Au(200), D) Au(300), and E) Au(600) gradient nanovoid samples as a function of the distance from the cathodic edge of the substrate. The data points are averages of ~10 values. The dashed lines indicate the positions from which nanovoid structures appear. Excitation: 1064 nm; acquisition time: 60 s; laser peak intensity: 1×10^{10} W cm^{-2}.

The void diameters from all gradient substrates that yielded the strongest SHG and SEHRS signals were determined from SEM images taken at the respective positions of the samples, and are summarized in Table 5.1. The normalized thickness of the respective structures is given in Table 5.1 as calculated from the geometrical relations depicted in Figure 5.8. The data in Table 5.1 show that most nanovoid sizes, which yielded strongest 1064 nm-excited SEHRS, agree (within the precision of the diameter measurements) with the sizes that result in maximum SHG signals at 850 nm excitation (compare second and fourth row in Table 5.1). Comparing the sizes of silver nanovoids that give the highest enhancement in SEHRS with those that have been reported to result in the highest one-photon SERS signals employing the same 200 nm and 300 nm template spheres in previous work, it was

found that optimum void structures for 1064 nm excited SEHRS and 532 nm excited SERS are very different. This provides further evidence that the plasmonic enhancement of the near-IR excitation field plays a more important role in electromagnetic enhancement of SEHRS than the visible hyper Raman field, in agreement with the discussion in Chapter 4 on the enhancement of SEHRS with plasmonic nanoparticles in solution and on surfaces. For void arrays obtained with 200 nm and 300 nm sphere templates, respectively, the void opening sizes yielding the highest signals both in SEHRS and SHG are almost the same for gold and silver (Table 5.1). Interestingly, the calculated normalized thickness (Figure 5.8) from the determined void diameters (Table 5.1), assuming ideal geometries, is ~0.8 for all structures, independent of the material and nanosphere template size. This indicates that plasmon modes existing in the voids in such thick layers must contribute to the high enhancement of the two-photon processes excited in the near-IR region. Furthermore, an increased roughness of the void rims, especially when void heights are above the template sphere equator (for example compare Figure 5.1C with E) could add to the electromagnetic field enhancement and higher signals in SEHRS and SHG, in line with enhanced SHG from nanocavities with rough rims that has been reported previously.[138]

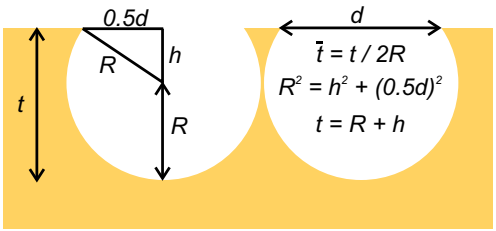

Figure 5.8: Schematic of a spherical cavity with void diameter d, radius R, metal film thickness t, and normalized thickness $\bar{t}$. Adapted from *Adv. Optical Mater.* 2019, 7, 1900650.

Table 5.1: Void opening sizes that yielded the highest SHG (at 850 nm) and SEHRS (at 1064 nm) signals along the gold and silver gradient samples with 200 nm, 300 nm, and 600 nm nanosphere templates as determined from SEM, and respective calculated normalized thickness $\bar{t}$ values. Adapted from *Adv. Optical Mater.* 2019, 7, 1900650.

void gradient	Ag(200)	Au(200)	Ag(300)	Au(300)	Ag(600)	Au(600)
SHG max	141±6 nm	150±7 nm	238±6 nm	248±13 nm	356±13 nm	479±20 nm
$\bar{t}$	0.85	0.83	0.80	0.78	0.90	0.81
SEHRS max	147±10 nm	156±16 nm	222±16 nm	231±11 nm	401±19 nm	447±45 nm
$\bar{t}$	0.84	0.81	0.84	0.82	0.87	0.83

5.2 Gold and silver voids as nanostructured solid phase SEHRS substrates

The SEHRS experiments with gradient nanovoids discussed in Section 5.1 demonstrated that nanovoid arrays can provide sufficient enhancement of HRS. Thus, gold and silver nanovoids with uniform thickness, similar to the voids in the gradient samples that yielded high signals in the two-photon experiments, were fabricated in a conventional three-electrode electrochemical setup. The reproduction of distinct void sizes, i.e. void heights that were observed in the gradient samples is not straightforward, since it is not known which exact potential is applied at each position on the bipolar electrode. In order to tune the void diameter and height according to the desired sizes in Table 5.1, a thorough optimization procedure using a high-throughput scanning droplet cell (SDC)[153,154] was carried out at Ruhr-Universität Bochum by Denis Öhl and Joao Junqueira to determine the optimal electrodeposition parameters. Multiple spots (1 mm in diameter) with gold and silver nanovoid structures of uniform sizes utilizing 200 nm and 300 nm nanosphere templates were fabricated. To help illustrate the design of the substrates, Figure 5.9 shows a photograph of gold nanovoid sample with 300 nm template, where the red circles represent areas with nanovoids. The deposited void spots appear similar regarding their color, which indicates that the height and size of the nanovoids is the same in different spots, since nanovoids with different normalized thickness exhibit different optical properties.[39] In some of the spots, voids were not deposited at all (see Figure 5.9), which could occur due to bubble formation in the SDC setup. Figure 5.10 shows representative scanning electron micrographs of the samples produced with different templates, termed Ag(200), Ag(300), Au(200), and Au(300),

together with the void opening sizes determined by SEM to verify the matching with the sizes that gave the most intense two-photon signals in the gradient substrates (Table 5.1).

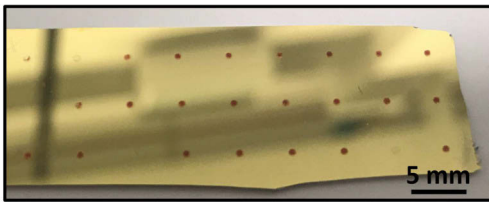

Figure 5.9: Photograph of Au(300) nanovoid substrate (taken by Denis Öhl). The red circles are the void spots deposited by SDC. Adapted from *Adv. Optical Mater.* 2019, 7, 1900650.

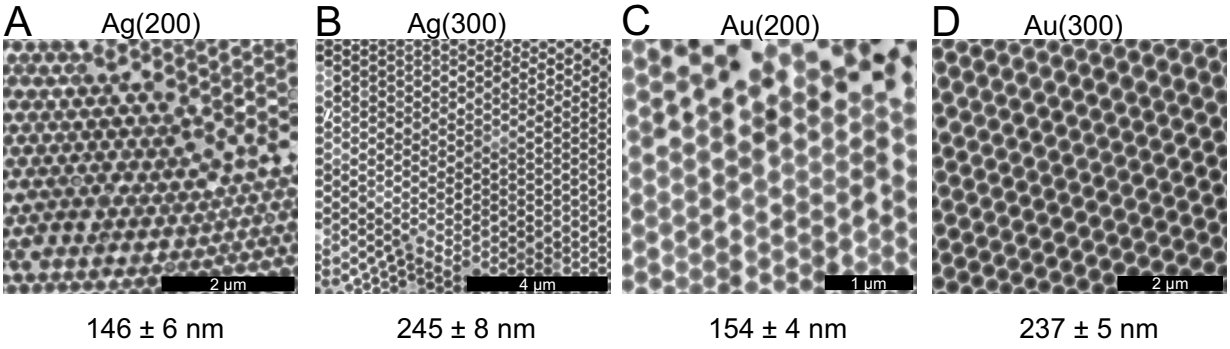

Figure 5.10: Scanning electron micrographs of the A, B) silver and C, D) gold nanovoids with A, C) 200 nm and B, D) 300 nm polymer nanosphere templates obtained after optimization using SDC electrodeposition. The average sizes of the void openings are listed below the SEM images; in all cases, the metal film is above the equator of the spheres. Adapted from *Adv. Optical Mater.* 2019, 7, 1900650.

The optimized nanovoid samples were characterized in SEHRS and SHG experiments, both excited at 1064 nm with picosecond laser pulses. Figure 5.11A shows the quadratic dependence of the SHG signal on excitation intensity for Ag(200) and Au(200) nanovoids. This confirms the two-photon parametric process of SHG. Likewise, the square dependence of the SEHRS signal on laser excitation intensity is displayed in Figure 5.11B. The SHG and SEHRS signal generated by the silver nanovoids is stronger than that generated by the gold voids. While silver nanovoids exhibited SHG and SEHRS already at an excitation intensity of ~10^8 W cm^{-2}, with gold voids, a peak laser intensity above ~10^9 W cm^{-2} is

required. The quadratic dependence of the two-photon signals indicates the high stability of the plasmonic structures over the applied intensity range. However, the gold voids are more stable than the silver voids at higher laser intensities. For the gold voids, the square dependence of both SHG and SEHRS is maintained for peak laser intensities of up to 2×10^{10} W cm^{-2} (Figure 5.11A, B), while for silver voids the signal dependence on excitation intensity after 2×10^{9} W cm^{-2} shows more of a linear character rather than quadratic (data not shown here). The observation of a strong and stable SEHRS signal generated by the gold nanovoids is very promising for bioanalytical applications and supports the so far very few reports of SEHRS with gold nanostructures.[21,119,199,200]

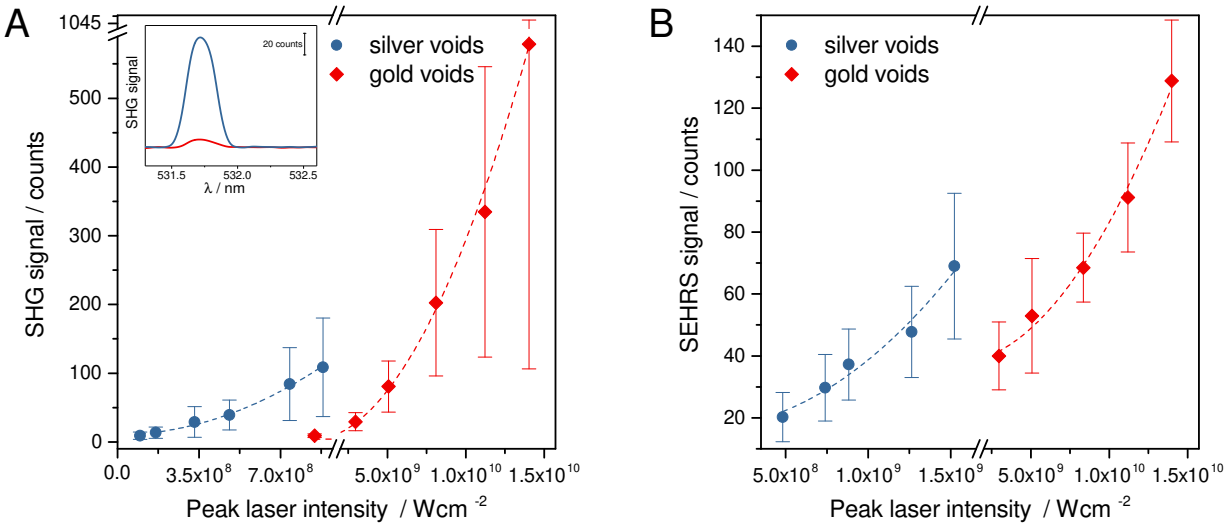

Figure 5.11: A) SHG signal, and B) SEHRS intensity of the crystal violet band at 1585 cm^{-1} from Au(200) and Ag(200) nanovoids as a function of the applied peak laser intensity. The dashed lines are the fitted quadratic curves ($ax^2 + b$) to the data points. The inset in (A) shows the SHG signal from gold and silver voids at ~9×10^{8} W cm^{-2}. Excitation: 1064 nm; acquisition time: 2 s (A) and 60 s (B). Adapted from *Adv. Optical Mater.* 2019, 7, 1900650.

SHG of the four types of optimized nanovoid structures was investigated using pulsed laser excitation at 850 nm and 1064 nm by raster scanning areas of different spots on the substrates. Representative SHG maps of each nanovoid sample at 850 nm and at 1064 nm are shown in Figure 5.12 and Figure 5.13, respectively. As can be inferred from the SHG imaging data, the SHG signal variation within larger microscopic areas of one substrate and for the same metal voids with different diameters is quite similar (compare e.g. Figure 5.12A with B and Figure 5.12C with D). This variation is even more pronounced in the data set

with 1064 nm excitation (Figure 5.13). For the measurements at 850 nm, a 10× objective (NA 0.3) was employed, and a 60× objective (NA 1.2) at 1064 nm, which corresponds to a two-photon focal spot diameter of ~1300 and ~415 nm, respectively (Equation (3.6)). According to the two-photon focal spot diameter, the SHG signal at 1064 nm excitation originates from (the surroundings of) less than two nanovoids at each pixel of an SHG image. Therefore, the signal can vary, depending on which part of the nanostructure is responsible for the observed SHG, in addition to small inhomogeneities due to the metal film growth. Despite the small variation between the different positions in one respective substrate, the Ag(200) voids display the strongest SHG signal at both excitation wavelengths, followed by the Ag(300) and Au(200) voids (compare the different panels in Figure 5.12 and Figure 5.13). The weakest overall SHG was observed with the Au(300) samples.

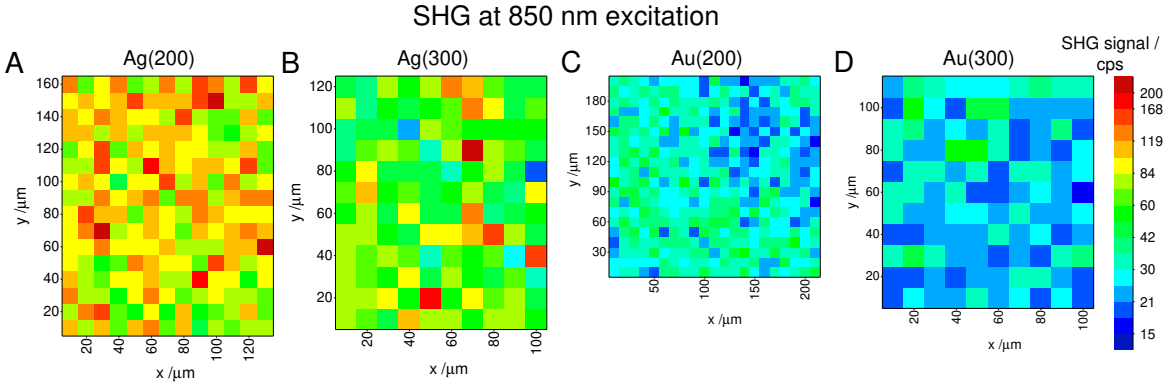

Figure 5.12: Images based on the SHG signal at 425 nm from A, B) gold and C, D) silver nanovoids produced with A, C) 200 nm and B, D) 300 nm nanosphere templates corresponding to void opening sizes of A) ~146 nm, B) ~245 nm, C) ~154 nm, and D) ~237 nm. Excitation: 850 nm; acquisition time: 1 s; peak laser intensity: 7×10^9 W cm^{-2} (5 mW average power); step size: 10 µm.

SEHRS spectra of crystal violet were obtained using gold and silver nanovoids with 200 nm and 300 nm nanosphere templates by raster scanning areas of the nanovoid substrates. Representative spectra with the four different nanovoid structures are presented in Figure 5.14, and SEHRS maps of scanned areas based on the CV ring stretching vibration at 1585 cm^{-1} are shown in Figure 5.15. The spectra resemble those reported in previous work using gold (compare with Figure 4.4A or Figure 4.5A in Chapter 4) and silver nanoparticles.[113,114] Ag(200) voids show the highest and Au(300) the lowest SEHRS enhancement (Figure 5.15).

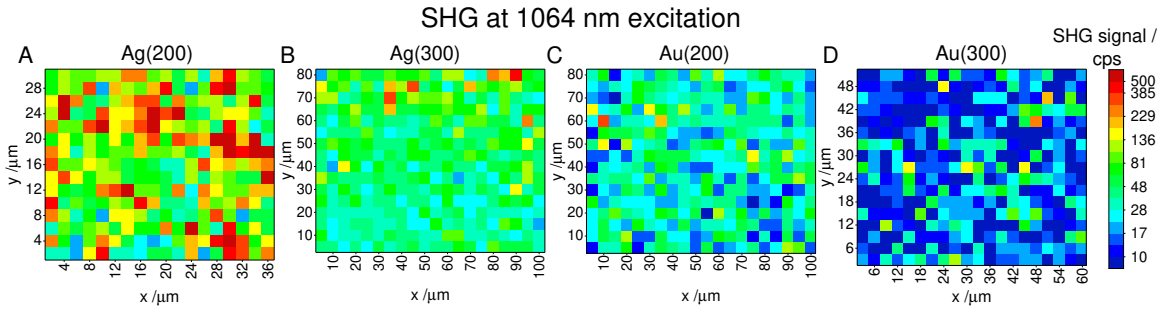

Figure 5.13: Images based on the SHG signal at 532 nm from A, B) gold and C, D) silver nanovoids produced with A, C) 200 nm and B, D) 300 nm nanosphere templates corresponding to void opening sizes of A) ~146 nm, B) ~245 nm, C) ~154 nm, and D) ~237 nm. Excitation: 1064 nm; acquisition time: 1 s; peak laser intensity: 7×10^8 W cm^{-2} (5 mW average power); step size: 2 µm (A), 5 µm (B and C), and 3 µm (D). Adapted from *Adv. Optical Mater.* 2019, 7, 1900650.

However, different from the comparison of SHG signals, Au(200) voids give higher signals than Ag(300) nanovoids in SEHRS (compare Figure 5.15B with C). As evidenced by the signal being on the same order of magnitude for SEHRS spectra obtained from different macroscopic nanovoid spots, the enhancement provided by Ag(300), Au(200), and Au(300) nanostructures, respectively, is very homogeneous (compare different maps within Figure 5.15B, C and D). Since SEHRS is an extremely sensitive probe of both plasmonic properties[199] and surface potential,[24] the homogeneous enhancement supports the SEM data regarding the reproducible fabrication of the different macroscopic nanovoid spots on one silicon wafer by means of SDC. Although the Ag(200) voids showed more variation in the SEHRS intensities between different spots with nanovoid structures (compare different maps in Figure 5.15A), the homogeneous SEHRS signals within each respective spot indicates a high homogeneity at the microscopic level.

To estimate the enhancement factors (EF) of the different nanovoid arrays, the absolute SEHRS signal intensities, on which the maps in Figure 5.15 are based, were compared with the signal from a normal HRS spectrum of crystal violet. The enhancement factors are ranging between 10^3 and 10^4 for Ag(200) and Au(200), while for Ag(300) and Au(300), the lower value of 10^3 was assigned. These values are very conservative because it is assumed that all CV molecules in the two-photon focal volume (Equation (3.5)) take part in the SEHRS process. The maximum possible coverage assuming planar surface of the nanovoids and perpendicular orientation of the CV molecules is less than 1 %, which implies that proba-

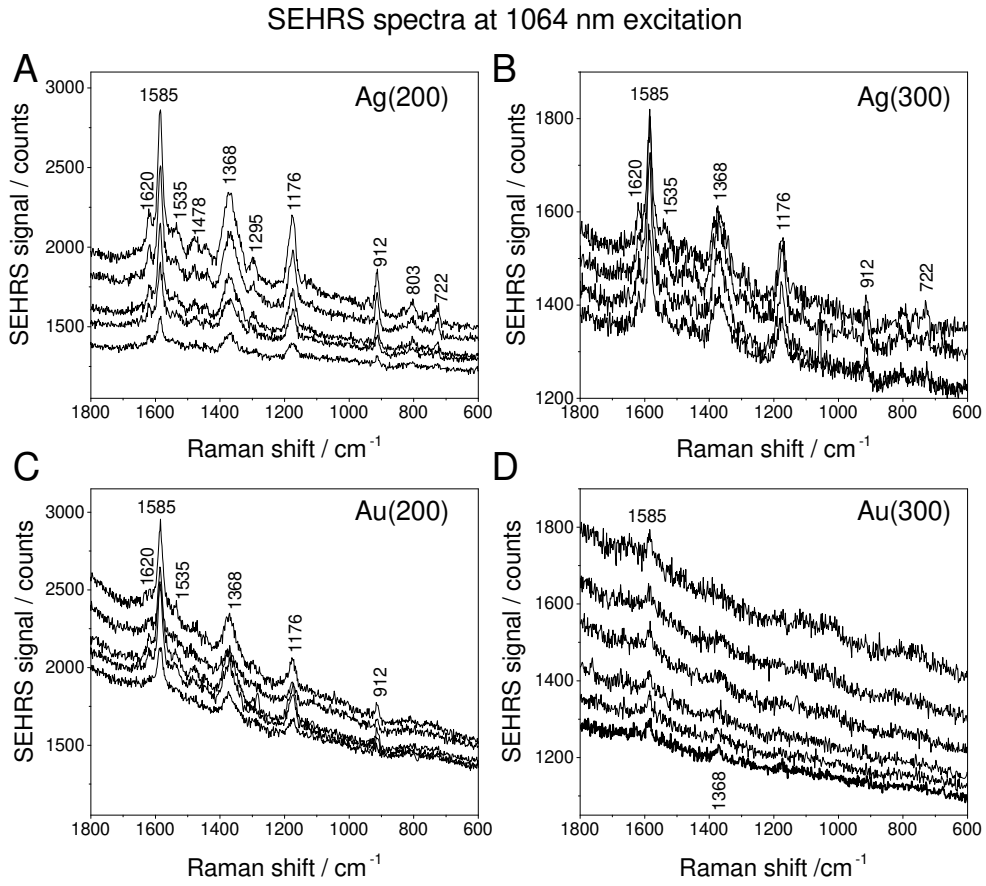

Figure 5.14: Representative SEHRS spectra of CV obtained from a solution placed as a droplet onto the nanovoid substrate, extracted from the SEHRS maps shown in Figure 5.15 obtained with A, B) silver and C, D) gold nanovoids produced with A, C) 200 nm and B, D) 300 nm nanosphere templates corresponding to void opening sizes of A) ~146 nm, B) ~245 nm, C) ~154 nm, and D) ~237 nm. Excitation: 1064 nm; acquisition time: 60 s; laser peak intensity: 1×10^{10} W cm^{-2} (50 mW average power); CV concentration: 10^{-5} M. Adapted from *Adv. Optical Mater.* 2019, 7, 1900650.

bly not all molecules interact with the surface. The estimated EFs are therefore two-three orders of magnitude lower than from gold nanoaggregates, as discussed in Chapter 4. In spite of the lower SEHRS signals obtained with the nanovoid arrays, they still present numerous advantages as SEHRS substrates over nanoparticles in solution due to the more homogeneous and reproducible enhancement, as well as stability of the substrate structure, which cannot be modified by chemical or electrostatic interactions with the analyte molecules as it is in the case of nanoaggregates in solution.

It must be mentioned here that for the EF estimations, a direct comparison of SEHRS and HRS spectra was not possible because a normal HRS spectrum of CV could not be acquired

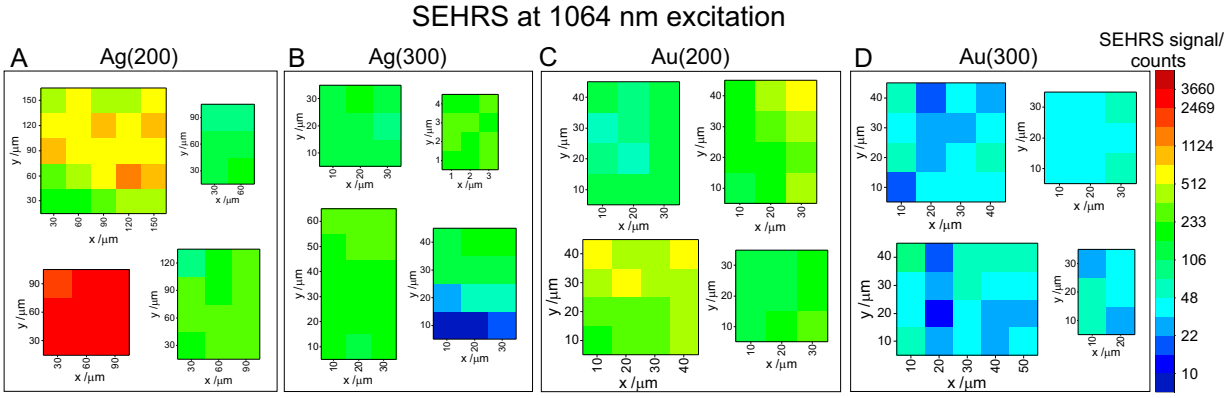

Figure 5.15: SEHRS maps of A, B) silver and C, D) gold nanovoids produced with A, C) 200 nm and B, D) 300 nm nanosphere templates, corresponding to void opening sizes of A) ~146 nm, B) ~245 nm, C) ~154 nm, and D) ~237 nm, based on the intensity of the crystal violet band at 1585 cm^{-1}. Each map was obtained from a different macroscopic spot. Excitation: 1064 nm; acquisition time: 60 s; laser peak intensity: 1×10^{10} W cm^{-2}; concentration of crystal violet in a droplet placed on the surface of the nanovoid arrays: 10^{-5} M; step size: 30 µm (A), 10 µm (B, C, D), and 1 µm for the right uppermost map in (B). Adapted from *Adv. Optical Mater.* 2019, 7, 1900650.

using the same laser excitation intensity as in the experiments with nanovoids. A normal HRS spectrum of crystal violet was obtained only from very concentrated solutions (10^{-3} M) and moderate peak laser intensities as in Figure 4.6 from Chapter 4. Increasing the laser power during HRS measurements of crystal violet led to lower signal or even no signal at all in the recorded spectra compared to measurements at lower excitation intensity using the same CV concentration and integration time. To obtain microspectroscopic data of the nanovoid array substrates, a 60× water immersion objective (NA 1.2) was employed, and the corresponding laser peak intensity was not in the range in which normal HRS spectra could be acquired. Therefore, in the EF estimations, the signal intensity was corrected for the different excitation intensities. However, it is not clear whether the square dependence of the normal HRS signal of crystal violet would be maintained at higher intensities, which possibly further lowered the values of the estimated enhancement factors. One possible reason for the signal diminishment at high laser power could be the photoionization and subsequent photochemical decomposition of crystal violet into compounds with lower Raman cross sections.[201,202] Interestingly, this did not appear during SEHRS measurements with 10^{-5} M CV, implying that the metal could provide additional relaxation channels that compete with the photoionization process.

SEHRS spectra of crystal violet with silver nanovoids were obtained also at different dye concentrations. Figure 5.16A shows SEHRS spectra with 10^{-6} M CV drop-casted on the nanovoid substrate, where the signal intensity in photon counts is about one order of magnitude lower than in spectra with 10^{-5} M CV (Figure 5.16B). The signal in SEHRS spectra with more concentrated CV solution (10^{-4} M, Figure 5.16C) is significantly lower than in the spectra with 10^{-5} M dye solution. This could be possibly caused by re-absorption of the Raman scattered light from other molecules in the concentrated solution, as CV has an absorption peak at ~590 nm (see Figure 4.6A in Chapter 4 for UV-vis absorbance spectrum of CV).

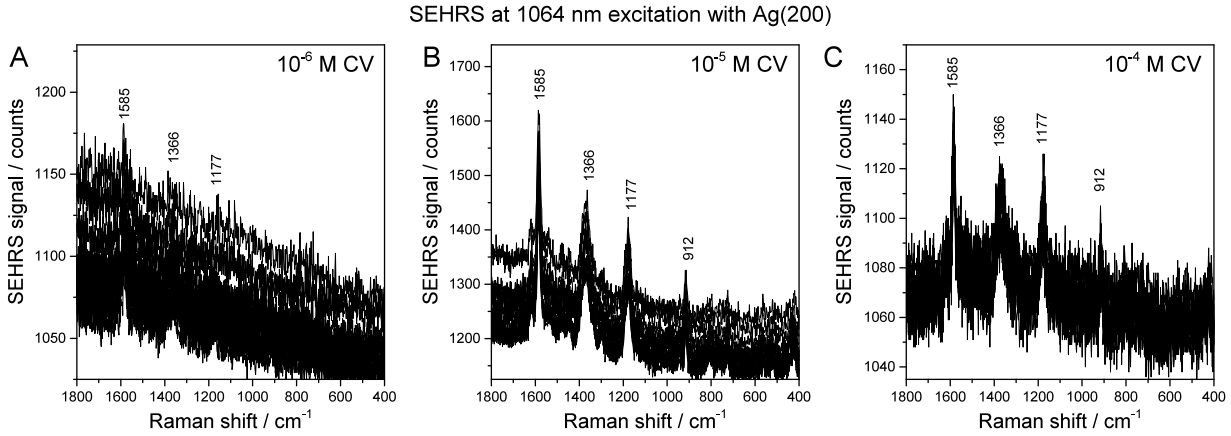

Figure 5.16: SEHRS spectra of crystal violet obtained with Ag(200) nanovoids at a concentration of A) 10^{-6} M, B) 10^{-5} M, and C) 10^{-4} M. Excitation: 1064 nm; acquisition time: 30 s; laser peak intensity: 1×10^{10} W cm^{-2}.

5.3 SHG and SEHRS from nanovoids with analyte molecules

In the following, a series of experiments will be discussed, in which SHG from optimized nanovoid arrays with crystal violet solution on their surface and SEHRS spectra from the same position in the sample were measured subsequently. Figure 5.17 shows the SHG signal, SEHRS intensity, and background in the respective SEHRS spectra that were obtained with Ag(200) nanovoids. The intensity of the crystal violet bands clearly correlates with the observed background in the spectra – the higher the SEHRS signal, the more pronounced are the background contributions (compare Figure 5.17B and C). Possible origins of the

SEHRS background were discussed in terms of the nanostructure properties for experiments with nanoaggregates previously.[103,117] Moreover, at the sample positions where the SEHRS intensity was high, strong SHG was observed (compare Figure 5.17A with B). Together with the observation that the highest SHG and SEHRS data were obtained with nanovoids of the same sizes (Table 5.1), this indicates that those nanostructures supporting high SEHRS enhancement also provide high SHG signals. Based on this observation, SHG can be employed for fast screening of suitable SEHRS substrates, instead of using nanomaterials optimized for strong SERS enhancement in SEHRS experiments, which has often been the strategy for designing SEHRS substrates so far.

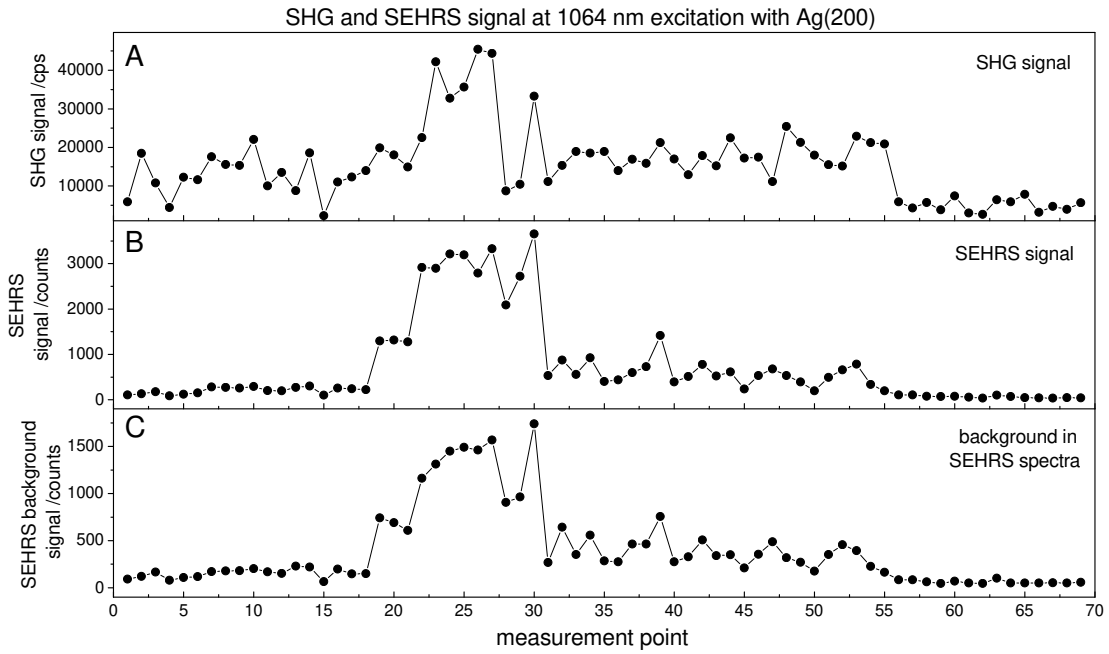

Figure 5.17: A) SHG signal, B) SEHRS signal of the CV band at 1585 cm^{-1}, and C) background in the respective SEHRS spectra in (B) obtained from Ag(200) substrate with 10^{-5} M CV solution. The data were obtained from 4 different macroscopic spots – measurement number 1-21 from spot 1, 22-30 from spot 2, 31-55 from spot 3, and 56-69 from spot 4. Excitation: 1064 nm; acquisition time: 1 s for SHG and 60 s for SEHRS; peak laser intensity: 1×10^{10} W cm^{-2} (50 mW average power). Adapted from *Adv. Optical Mater.* 2019, 7, 1900650.

On the other hand, the correlation between SHG and SEHRS was observed with Ag(200) nanovoids but not with the rest of the nanovoid substrates. This is indicated in Figure 5.18 where the SHG signal, the intensity of SEHRS and background in SEHRS for Ag(300),

Au(200), and Au(300) nanovoid arrays are shown. While at some of the measurement points in Ag(300) voids, higher SHG signals correspond to higher SEHRS intensity (e.g. positions 1-3 and 16-18 in Figure 5.18A), no such correlation was found for the gold nanovoid arrays (Figure 5.18B and C). In order to investigate what is the origin of this difference, SHG from the four types of nanovoid arrays in the presence and in the absence of CV was measured, and the data are presented in Figure 5.19. As can be seen from the SHG maps in Figure 5.19A and B, the SHG signal from gold nanovoids did not change upon addition of CV. In the case of Ag(200) and Ag(300), the average SHG signal from the mapped area increases by a factor of ~2 in the presence of CV. Figure 5.20A shows the dependence of the SHG signal on the crystal violet concentration for gold and silver nanovoid arrays. While in the experiment with gold nanovoids the signal did not change (red squares in Figure 5.20A), it rose linearly for silver nanovoids starting from a CV concentration of 10^{-6} M (blue circles in Figure 5.20A). The SHG measurements in the above described experiments were done immediately after drop-casting the CV solution. Figure 5.20B shows the time dependence of the average SHG signal from silver nanovoids with 10^{-5} M CV solution. The latter slightly increased over time, indicating that an equilibrium between adsorbed CV molecules and free molecules in the solution is still establishing.

Despite the fact that the observed increase in SHG intensity from silver nanovoids with CV versus without CV is only about a factor of 2 and the standard deviations of the averaged values over the whole mapped areas are large, the increase is yet systematic and reproducible. Therefore, it could be attributed to contributions from the dye molecules. Furthermore, this SHG from CV must be surface enhanced, since no SHG could be obtained from CV solutions using various concentrations and excitation intensities without the nanovoid substrates, thus making it impossible to estimate an enhancement factor. Enhanced SHG from CV was not observed with gold nanovoids. The reason for this could be a different chemical or electrostatic interaction between the dye molecules with gold and silver. Since silver is more reactive than gold, possibly the interaction with silver is stronger, or the excitation or scattered radiation could be in resonance with a transition in the silver-CV adsorbate, inducing a chemical enhancement contribution.

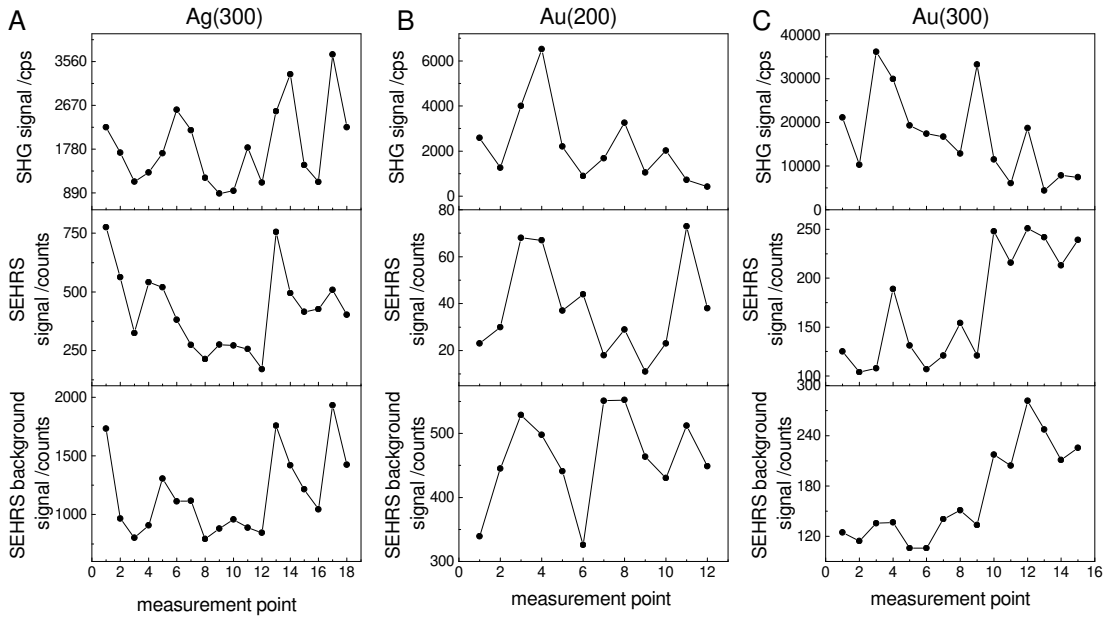

Figure 5.18: SHG signal (uppermost panels), SEHRS signal of the CV band at 1585 cm^{-1} (middle panels), and background in the respective SEHRS spectra (lowermost panels) from A) Ag(300), B) Au(200), and C) Au(300) substrates with 10^{-5} M crystal violet solution. The data was obtained from different macroscopic spots: measurement number 1-9 from spot 1 and 10-18 from spot 2 (A); measurement number 1-12 from spot 1 and 13-18 from spot 2 (B); and 1-15 from only one spot (C). Excitation: 1064 nm; acquisition time: 1 s for SHG and 60 s for SEHRS; peak laser intensity: 1×10^{10} W cm^{-2} (50 mW average power).

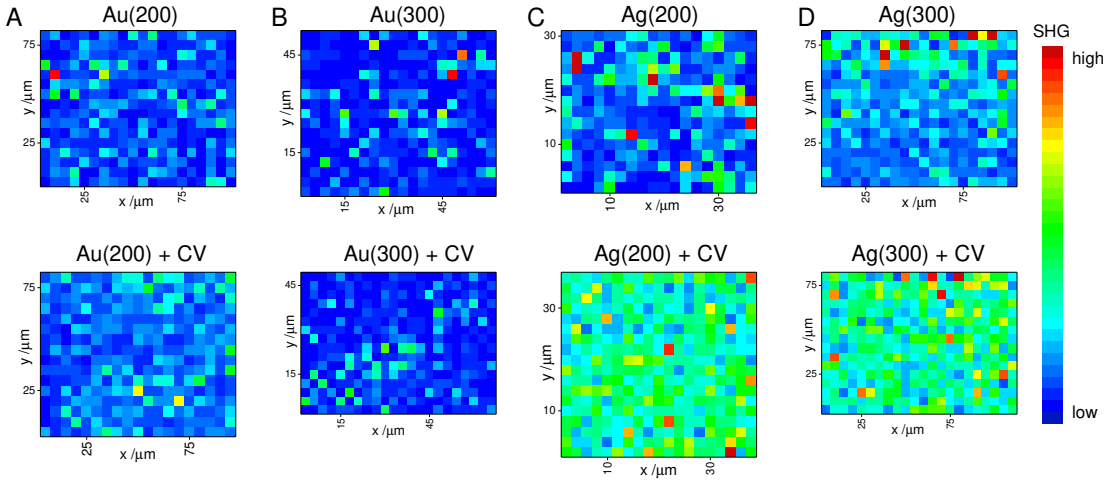

Figure 5.19: SHG maps of A) Au(200), B) Au(300), C) Ag(200), and D) Ag(300) nanovoids with water (upper panels) and with 10^{-5} M CV solution (lower panels) drop-casted directly before the measurement. The SHG signal is normalized within each of the panels A-D. Excitation: 1064 nm; acquisition time: 1 s; peak laser intensity: 7×10^{8} W cm^{-2}.

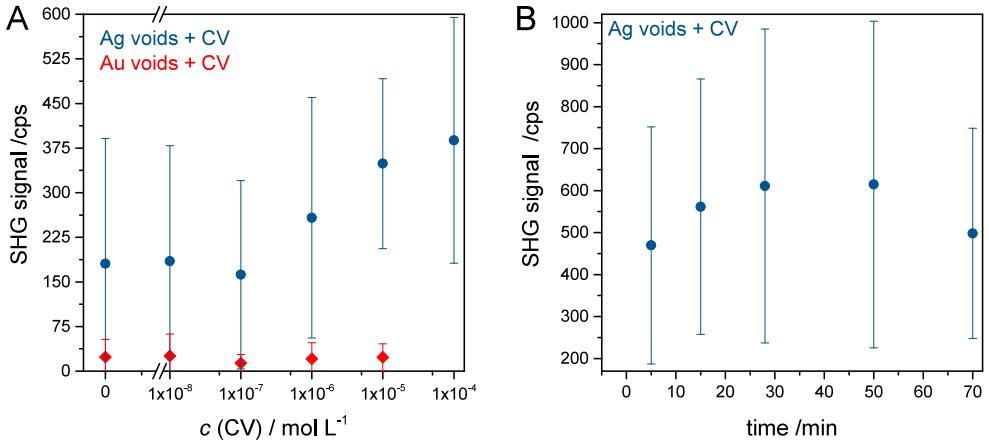

Figure 5.20: A) SHG signal from Ag(200) nanovoids (blue circles) and Au(300) nanovoids (red squares) with different CV concentrations. B) SHG signal from Ag(200) nanovoids with 10^{-5} M CV as a function of time. The data points in A and B are averages over ~500 values obtained after raster scanning areas of ~50 × 50 µm. Excitation: 1064 nm; acquisition time: 1 s; peak laser intensity: 7×10^8 W cm^{-2} (3 mW average power).

5.4 Conclusions

In this chapter, the non-linear optical properties of gold and silver nanovoid arrays were investigated by means of SEHRS and SHG. A multitude of different gold and silver nanovoid structures were fabricated by bipolar electrodeposition using nanosphere templates of three different sizes, and the void structural parameters that provide high enhancement in SEHRS and SHG were identified. SEHRS and SHG screening experiments along gradient nanovoid samples revealed that nanovoids with different heights show significantly different enhancement in both two-photon processes. In addition, nanovoids yielding the strongest SEHRS at 1064 nm and SHG at 850 nm excitation have nearly the same structural parameters. This suggests that utilizing SHG as a fast screening tool for identifying nanostructures supporting high SEHRS enhancement could provide more advantages than adapting substrates optimized for one-photon SERS in SEHRS experiments. Pre-screening of a microscopic surface, e.g. of a sensor probed by SEHRS, by fast acquisition of the monochromatic SHG signal, could ensure selection of sample positions that provide optimum enhancement for the collection of two-photon vibrational spectra.

The optimum void sizes giving the highest enhancement of the two-photon process of SEHRS at 1064 nm excitation differ from nanovoid sizes that provide the highest enhancement at 532 nm in one-photon excited SERS found in previous work,[152] pointing towards the

importance of plasmon modes with resonances at the near-IR frequencies used to excite SEHRS. The highest SEHRS and SHG intensities from gradient nanovoid samples with 200 nm, 300 nm, and 600 nm nanosphere templates were found for voids with a normalized thickness of ~0.8, independent of the material or template size. Resonances of the excitation and/or scattered light with plasmon modes existing only in such thick nanovoids could be responsible for the observed high enhancement of two-photon processes at near-IR excitation wavelengths. Additionally, an enhancement of electromagnetic fields could arise due to increased roughness of the nanovoid rims and metal film around them, when the metal film is growing above the equator of the densely packed nanosphere templates.

Quadratic dependence of the SEHRS and the SHG signal from gold and silver nanovoids was observed, which proves the two-photon nature of both processes. Polarization resolved SHG measurements indicate that the macroscopic SHG from nanovoid arrays is incoherent.

Comparing the potential of different nanovoid structures for use as substrates in SEHRS, it was found that both the gold and the silver voids with 200 nm and 300 nm nanosphere templates and void opening sizes of ~150 nm and ~240 nm, respectively, provide sufficient enhancement of this process. Silver nanovoids yield stronger SEHRS enhancement than gold voids, but gold nanovoid arrays show improved stability at high laser excitation intensities. The estimated enhancement factors for gold and silver nanovoids range between $10^3 - 10^4$, thus being lower than the values of nanoaggregates in solution discussed in Chapter 4. Nevertheless, nanovoid substrates reveal many advantages for SEHRS spectroscopy and imaging applications with respect to homogeneity, reproducible fabrication, and stability that remained unaddressed so far in SEHRS experiments with other plasmonic substrates.

Chapter 6

Plasmonic - barium titanate composite nanoparticles as multifunctional optical nanoprobes

This chapter is based on the publication *Adv. Funct. Mater.* 2019, 29, 1904289.

Multiphoton excited imaging and microspectroscopy require nanoprobes that can give different non-linear optical signals in order to develop multimodal detection and sensitive chemical characterization of biological samples. Several generations of optical nanoprobes and labels, strongly varying in chemical composition and size range, have been developed in the past two decades to match the specific requirements of different multiphoton excited spectroscopic methods regarding functionality. Among others, they include customized organic dyes[203,204] and quantum dots[205] for one- and two-photon excited fluorescence, perovskite-type nanocrystals as harmonic probes,[32,33] and gold and silver nanoparticles that can be used as plasmonic probes for surface enhanced hyper Raman scattering (SEHRS) imaging of cells and tissues.[169,170] Extending the capabilities of nanoprobes that deliver chemical information through a vibrational signature with the requirements of fast non-linear imaging would allow truly multimodal optical imaging based on both chemical structural information with morphology at the microscopic level, and thus could be very beneficial for microspectroscopic studies of biological objects.

In this chapter, the synthesis and characterization of novel optical nanoprobes, that are gold and silver coated barium titanate composite nanoparticles, is presented. Barium ti-

tanate is chosen as the core material because of its non-linear optical properties and well established use as harmonic probe in SHG biomicroscopy.[32,146,206–208] Surrounding the non-linear nanocrystals with a shell of gold and silver nanoparticles allows to take advantage of the strongly enhanced Raman and hyper Raman process in the near fields of these plasmonic structures. First, synthetic aspects of the composite nanostructure preparation will be discussed, followed by their optical characterization using UV-vis spectroscopy and second harmonic generation (SHG). To understand how the optical properties of barium titanate particles are altered by the presence of the plasmonic moieties, numerical simulations of related model systems will be presented. Finally, the multifunctionality of the plasmonic-barium titanate nanocomposites will be demonstrated by using them as nanoprobes for SERS, SEHRS, and SHG.

6.1 Synthesis of plasmonic - barium titanate nanocomposites

Commercially available polycrystalline barium titanate ($BaTiO_3$) nanoparticles in the tetragonal crystal structure, which is associated with high second order susceptibility, were used as starting material for the preparation of all nanocomposites discussed below. Transmission electron micrographs of the particles are shown in Figure 6.1A and B. The $BaTiO_3$ particles are non-spherical, and have a very broad size distribution with an average size of 256 ± 84 nm as indicated in Figure 6.1C.

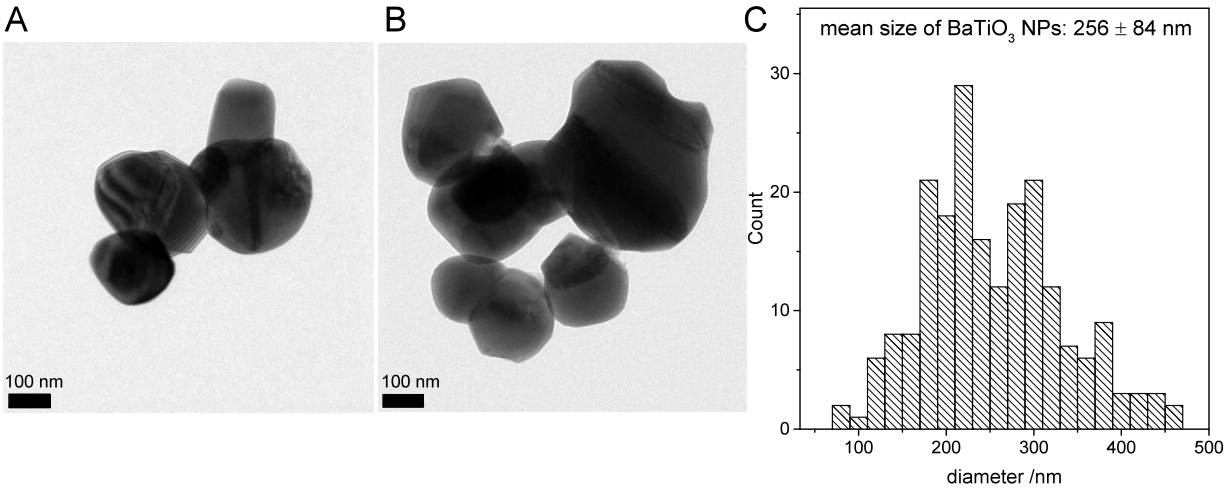

Figure 6.1: A, B) Transmission electron micrographs, and C) size distribution of the barium titanate nanoparticles. Adapted from *Adv. Funct. Mater.* 2019, 29, 1904289.

To create plasmonic moieties on the surface of $BaTiO_3$ nanocrystals several synthesis steps including surface functionalization and metal reduction are required. In principle, the reactions involved are adapted from approaches for synthesis of the better understood silica-core metal-shell nanosystems[149,150,209] because similar chemical reactivity of the particle surface may be expected. Figure 6.2 shows a simplified schematic of the synthetic route for obtaining gold coated barium titanate composites, termed Au@$BaTiO_3$ here, and silver coated barium titanate composites, termed Ag@$BaTiO_3$.

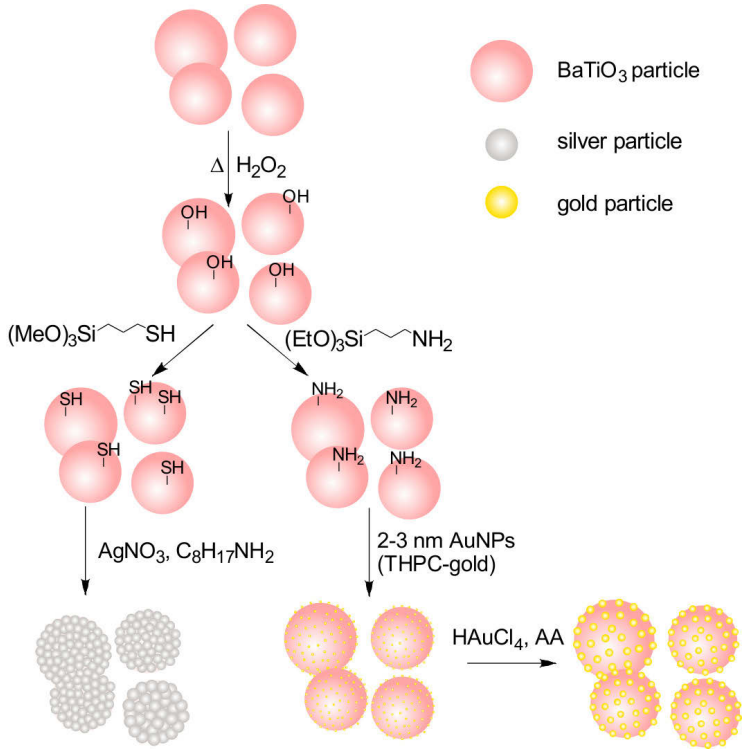

Figure 6.2: Schematic representation of Au@$BaTiO_3$ and Ag@$BaTiO_3$ preparation. Adapted from *Adv. Funct. Mater.* 2019, 29, 1904289.

In the first step, common for the preparation of both Au@$BaTiO_3$ and Ag@$BaTiO_3$ composites, barium titanate particles were pre-treated with hydrogen peroxide (H_2O_2) to increase the amount of surface hydroxyl groups[145,146] so that the subsequent silanization reaction with (3-aminopropyl)triethoxysilane (APTES) or (3-mercaptopropyl)trimethoxysilane (MPTS) would be promoted. To optimize this step, the $BaTiO_3$ particles were exposed to H_2O_2 at room temperature or at 110 °C for 2-4 hours in ambient conditions. TEM images of the products reveal that if the reaction is carried out at room temperature the particles remain the same (data not shown). However, the reaction with H_2O_2 at high temperature visibly modifies the surface layer of the particles. This was observed also in previous work, and the

treatment with H_2O_2 was discussed to cause an excessive loss of barium ions leading to the degradation of the particle surface and its structure.[148,210] Although the degradation of the $BaTiO_3$ particle surface seems to be unfavorable at first sight, it proved to be beneficial for growing a gold shell. Therefore, barium titanate particles treated with hydrogen peroxide both at room temperature and at 110 °C were used in the next steps.

6.1.1 Seed-mediated growth approach for preparation of Au@$BaTiO_3$

For the synthesis of Au@$BaTiO_3$, a seed-mediated growth approach was applied. Briefly, small gold seeds were attached to the surface of $BaTiO_3$ nanoparticles following previously published work,[147,148] and then for the subsequent growth step another protocol typically used for gold nanorods preparation was adapted.[56] First, hydroxylated $BaTiO_3$ particles were boiled with APTES in ethanol to functionalize the surface with amine groups. This reaction does not visibly change the particles. Next, small gold seeds (2-3 nm, THPC-gold) dispersed in water were attached to the surface of APTES-functionalized barium titanate by mixing both solutions overnight. After this step, precipitation of the particles by centrifugation is required in order to separate the $BaTiO_3$ nanocrystals from unbound gold nanoparticles. This is important to ensure that the gold growth in the next steps occurs only on the barium titanate surface. Figure 6.3A-D shows transmission electron micrographs of barium titanate nanoparticles with modified surface layer (treated with H_2O_2 at 110 °C for 2 hours) after attachment of THPC-gold, abbreviated here as THPC-gold@$BaTiO_3$. The core particles are covered homogeneously with THPC-gold. In Figure 6.3B and D one can clearly see the modified surface layer of $BaTiO_3$, which appears lighter in contrast compared to the inner parts of the $BaTiO_3$ particles. The THPC-gold particles are residing on top and probably inside the partially degraded surface layer as indicated in Figure 6.3D.

The gold particles from the THPC-gold@$BaTiO_3$ structures act as seeds for the growth in the next synthesis step where gold chloride is reduced with ascorbic acid in the presence of hexadecyltrimethylammonium bromide (CTAB). During this reaction, the size of the gold particles on the $BaTiO_3$ surface increases. Figure 6.4 shows TEM images of $BaTiO_3$ particles with 9 ± 2 nm gold nanoparticles on their surface, termed 9 nm Au@$BaTiO_3$ here. These composite particles were obtained after one gold deposition cycle using barium titanate without modified surface layer (treated with H_2O_2 at room temperature).

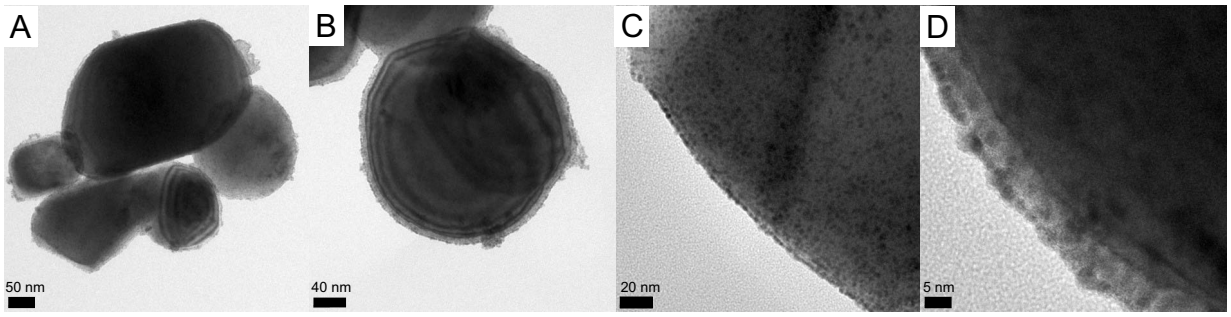

Figure 6.3: Examples of transmission electron micrographs of THPC-gold@$BaTiO_3$. Adapted from *Adv. Funct. Mater.* 2019, 29, 1904289.

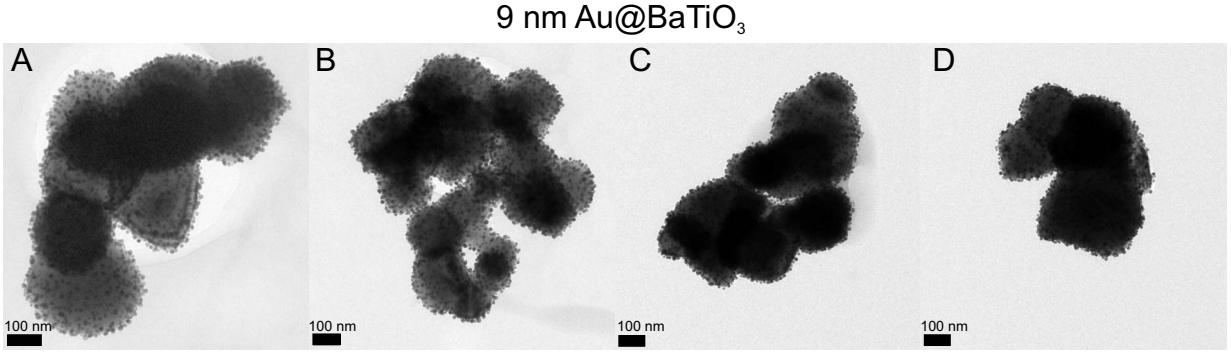

Figure 6.4: Examples of transmission electron micrographs of 9 nm Au@$BaTiO_3$. The $BaTiO_3$ nanoparticles were pre-treated with H_2O_2 at room temperature. Adapted from *Adv. Funct. Mater.* 2019, 29, 1904289.

The gold deposition cycle resulted not only in increasing the size of the gold nanoparticles but also their detachment from the barium titanate surface. This is indicated by the UV-vis spectrum of the supernatant obtained after precipitating 9 nm Au@$BaTiO_3$ nanocomposites by centrifugation (Figure 6.5). While the peak at 380 nm corresponds to excess $[AuBr_4^-]$,[211] the band at 530 nm can be attributed to gold nanoparticles (see Figure 4.2A). The electrostatic interaction between the ATPES-functionalized $BaTiO_3$ nanoparticles and the THPC gold seeds[212] may not be strong enough to prevent detachment of the gold particle when it becomes heavier during the growth reaction.

If $BaTiO_3$ particles with modified surface layer are used in the growth step, detachment of gold nanoparticles is also observed, as indicated by the UV-vis spectrum of the supernatant after precipitation of the composite particles (similar as in Figure 6.5). However, it was possible to perform a second gold deposition cycle, after which the size of the gold particles on the $BaTiO_3$ surface was increased to 17 ± 6 nm. Transmission electron micrographs of such 17 nm Au@$BaTiO_3$ nanocomposites are presented in Figure 6.6A-D. The TEM images

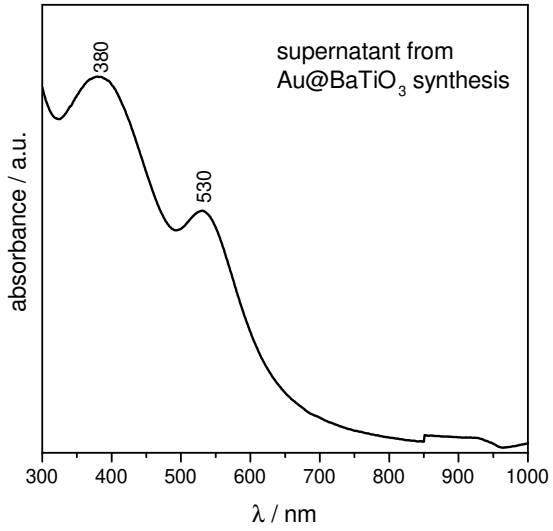

Figure 6.5: UV-vis spectrum of the supernatant obtained after precipitating $Au@BaTiO_3$ from the gold shell growth step. Adapted from *Adv. Funct. Mater.* 2019, 29, 1904289.

in Figure 6.6C and D indicate that the bigger gold nanoparticles reside partially inside the modified barium titanate surface layer, which probably hinders their detachment.

The separation of $Au@BaTiO_3$ nanocomposites from reaction mixtures containing also unbound gold nanoparticles is crucial for obtaining the final products. Here, the nanocomposites were centrifuged several times at low speed until the supernatant was transparent, and until the UV-vis spectra of the supernatant did not exhibit a band at 530 nm corresponding to the free gold nanoparticles. The UV-vis spectra of the nanocomposites will be discussed in Section 6.2.1. No free gold nanoparticles were found in TEM experiments with 9 nm $Au@BaTiO_3$ and 17 nm $Au@BaTiO_3$ samples.

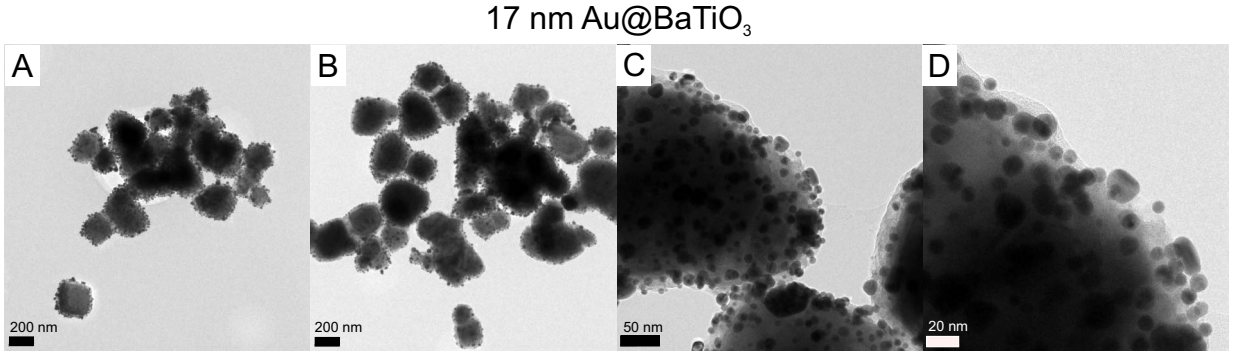

Figure 6.6: Transmission electron micrographs of 17 nm $Au@BaTiO_3$. The $BaTiO_3$ nanoparticles were pre-treated with H_2O_2 at 110 °C for 4 hours. Adapted from *Adv. Funct. Mater.* 2019, 29, 1904289.

To summarize, Au@$BaTiO_3$ composite nanostructures, in which mainly single ~9 nm or ~17 nm gold nanoparticles are densely distributed on the surface of $BaTiO_3$ nanocrystals, were obtained using a modified seed-mediated growth approach. Previous works[147,148] considering $BaTiO_3$-core gold-shell nanoparticle preparation suggest using aged gold(I) hydroxide (AuOH) solution for reduction with formaldehyde or sodium borohydride ($NaBH_4$) in the growth step. Here, this strategy failed because the obtained $BaTiO_3$ particles were not homogeneously covered with gold. TEM images of products from reduction of AuOH with $NaBH_4$, ascorbic acid, and formaldehyde in the presence of THPC-gold@$BaTiO_3$ are presented in Figure 6.7A, B and C, respectively. While some $BaTiO_3$ particles are densely covered with gold nanoparticles even larger than 17 nm in size, others remain almost without any gold on their surface. Therefore, the reduction of gold(III) chloride in the presence of CTAB and the THPC-gold@$BaTiO_3$ particles was chosen as the main synthetic route for the preparation of Au@$BaTiO_3$ nanocomposites, and the optical experiments presented in the following sections consider only the 9 nm Au@$BaTiO_3$ and 17 nm Au@$BaTiO_3$ composite nanoparticles.

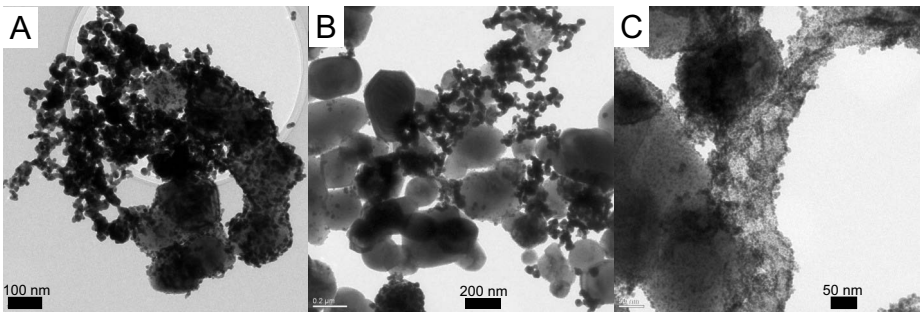

Figure 6.7: Examples of transmission electron micrographs of the products obtained by reducing AuOH solution in the presence of THPC-gold@$BaTiO_3$ nanoparticles with A) sodium borohydride, B) ascorbic acid, and C) formaldehyde. Side products (unbound gold nanoparticles) of different size are also present in the samples.

6.1.2 Seedless synthesis of Ag@$BaTiO_3$

$BaTiO_3$-silver core-shell nanocomposites were prepared using a seedless synthetic route originally proposed for silica-silver core-shell structures.[150] For this purpose, hydroxylated $BaTiO_3$ nanoparticles were functionalized with thiol groups in a silanization reaction with MPTS. MPTS was chosen instead of APTES due to the high affinity of silver to sulfur which

could promote nucleation of silver on the $BaTiO_3$ surface. In the next step, silver nitrate was reduced with octylamine in the presence of MPTS-functionalized barium titanate particles and polyvinylpyrrolidone (PVP) in ethylene glycol (Figure 6.2). This approach yielded $BaTiO_3$ particles with almost continuous silver shells, which consist of aggregated silver nanoparticles with an average diameter of 40 ± 9 nm. Figure 6.8A-D shows transmission electron micrographs of the Ag@$BaTiO_3$ nanocomposites.

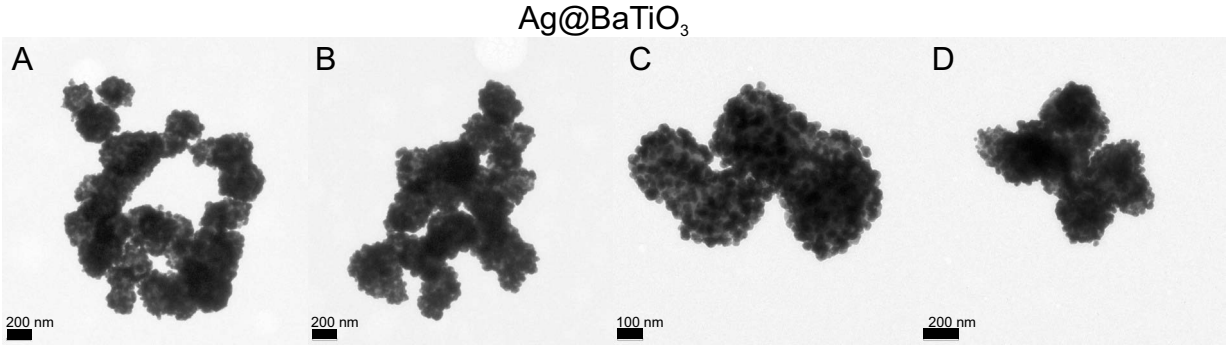

Figure 6.8: Examples of transmission electron micrographs of Ag@$BaTiO_3$. Adapted from *Adv. Funct. Mater.* 2019, 29, 1904289.

During the silver reduction step free silver nanoparticles unbound to the $BaTiO_3$ surface are also formed in the solution. This is indicated by the band at 435 nm in the UV-vis spectrum (Figure 6.9) of Ag@$BaTiO_3$ obtained directly from the reaction mixture without purification of the products by centrifugation. Thus, also the preparation of Ag@$BaTiO_3$ requires several purifications steps. In the UV-vis spectrum of the final product the band at 435 nm is not present (discussed in Section 6.2.1), and during TEM investigation of the samples no free silver nanoparticles were found.

Two additional strategies were tested for the synthesis of Ag@$BaTiO_3$ nanoparticles. The first one involved reduction of silver nitrate with hydroxylamine hydrochloride in the presence of MPTS-treated $BaTiO_3$ nanoparticles in water. This approach resulted mostly in the formation of free silver nanoparticles as indicated by the TEM image shown in Figure 6.10A. The second strategy also involved reduction of silver nitrate by hydroxylamine hydrochloride in water, but in the presence of THPC-gold@$BaTiO_3$ particles, so that the gold seeds could act as nucleation sites for silver growth. However, TEM images of the products (Figure 6.10B) show that only some of the $BaTiO_3$ particles are covered with small silver clusters in an

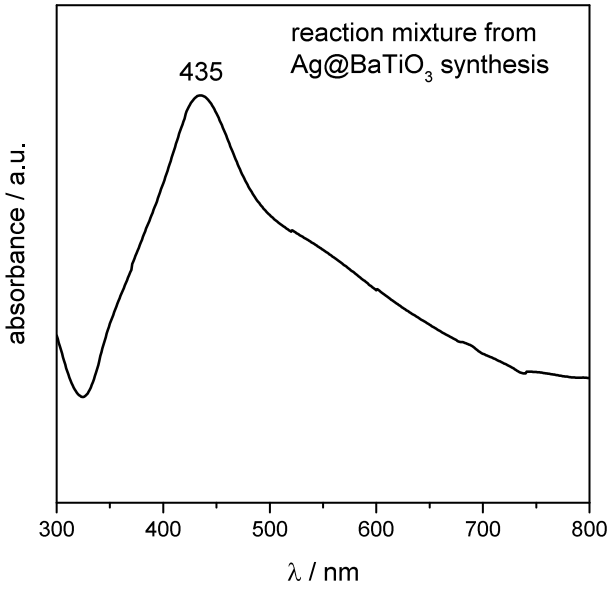

Figure 6.9: UV-vis spectrum of the reaction mixture from $Ag@BaTiO_3$ synthesis.

inhomogeneous manner, while others remain covered only with very small particles that must be the THPC-gold. Since none of these approaches yielded $BaTiO_3$ particles either homogeneously covered with silver nanoparticles or with a continuous shell, only the 40 nm $Ag@BaTiO_3$ nanocomposites (Figure 6.8) produced by silver reduction in ethylene glycol in the presence of PVP are considered for further experiments.

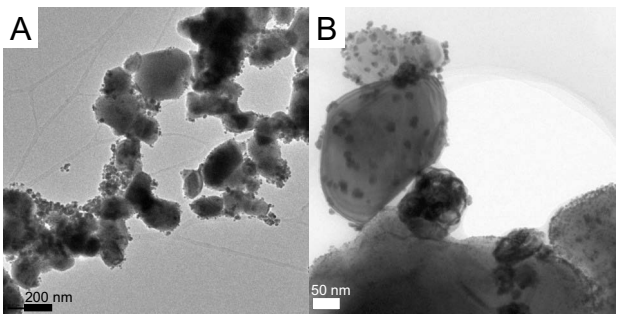

Figure 6.10: Examples of transmission electron micrographs of the products obtained by reduction of silver nitrate by hydroxylamine hydrochloride in the presence of A) MPTS-functionalized $BaTiO_3$, and B) THPC-gold@$BaTiO_3$.

6.2 Influence of the plasmonic moiety on the optical properties

6.2.1 UV-vis absorbance and SHG experiments

The optical properties of the $BaTiO_3$ nanoparticles, and how they are altered by the presence of gold and silver shell in the Au@$BaTiO_3$ and Ag@$BaTiO_3$ nanocomposites were investigated by means of UV-vis spectroscopy and second harmonic generation (SHG). Figure 6.11A shows UV-vis spectra of $BaTiO_3$ nanoparticles treated with H_2O_2 at room temperature and at 110 °C.

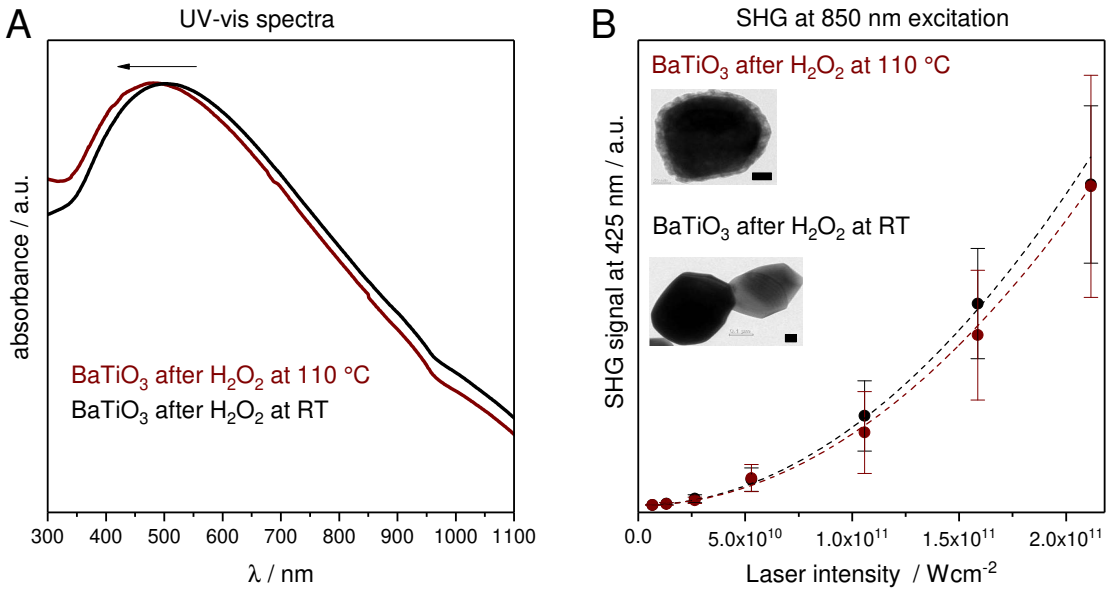

Figure 6.11: A) UV-vis spectra and B) SHG signal from $BaTiO_3$ nanoparticles treated with hydrogen peroxide at room temperature (black) and at 110 °C (brown) as a function of the peak laser intensity. Excitation: 850 nm; acquisition time: 1 s. The values represent the mean of 15 measurements and the error bars illustrate the standard deviation; the dashed lines are the fitted quadratic curves ($ax^2 + b$) to the data points. The insets show TEM images of the two kinds of $BaTiO_3$ particles; scale bars: 50 nm. Adapted from *Adv. Funct. Mater.* 2019, 29, 1904289.

The spectra exhibit broad bands at 480 nm for the heated particles with modified surface layer, and at 500 nm for the particles without modified surface. Since barium titanate is a dielectric material with high values for the real part and almost zero for the imaginary

part of the complex permittivity in the visible spectral range,[160] the band in the spectrum should be dominated by scattering. Interestingly, the peak maximum of $BaTiO_3$ nanoparticles with partially degraded surface layer is blue-shifted compared to one of the original particles. As will be discussed in the next section, this might be due to an effective decrease of their volume. Despite this, the modified surface layer is almost not affecting the SHG intensity of the particles, which is very important for their application as SHG nanoprobes. This is demonstrated in Figure 6.11B where the SHG signals from $BaTiO_3$ particles with and without modified surface layer are compared.

The UV-vis absorbance spectra of the gold coated nanoparticles, 9 nm Au@$BaTiO_3$ and 17 nm Au@$BaTiO_3$ (Figure 6.12), show bands at 550 nm and 578 nm, respectively, in addition to the bands at ~480-500 nm that are present also in the spectra of the bare $BaTiO_3$ particles (Figure 6.11A). The emergence of such new resonant peaks in other related systems has been explained by the excitation of the plasmonic modes of the metallic particles[149,213,214] shifted by the dielectric environment and due to an interaction and/or aggregate formation of neighboring gold nanoparticles on the barium titanate surface. As will be discussed in more details in Section 6.2.2, an alternative picture, treating the gold nanoparticles as a homogeneous layer characterized by effective optical properties which modify the resonances of the bare barium titanate particles, may also be considered.[162,215,216]

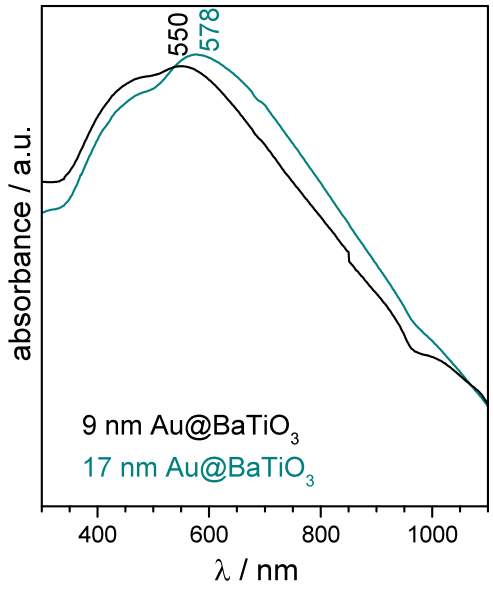

Figure 6.12: UV-vis spectra of 9 nm Au@$BaTiO_3$ (black) and 17 nm Au@$BaTiO_3$ (green). Adapted from *Adv. Funct. Mater.* 2019, 29, 1904289.

In a control experiment, APTES-functionalized $BaTiO_3$ particles were mixed with separately prepared 14 nm sized gold nanoparticles. The UV-vis spectra of the pure $BaTiO_3$ particles, 14 nm gold particles, and the mixture of both are presented in Figure 6.13. The plasmon band of the gold nanoparticles is at 518 nm (see red line in Figure 6.13) and it does not shift upon addition of the $BaTiO_3$ particles (see blue line in Figure 6.13). The plasmon resonances of single 9 nm or 17 nm gold nanoparticles are expected to be at ~520-530 nm and below.[173,179] Thus, the control experiment supports that the peaks at 550 nm and 578 nm in the UV-vis spectrum of the 9 nm and 17 nm Au@$BaTiO_3$ composites (Figure 6.12) result from the interaction of the $BaTiO_3$ cores with the small gold nanoparticles attached to their surface.

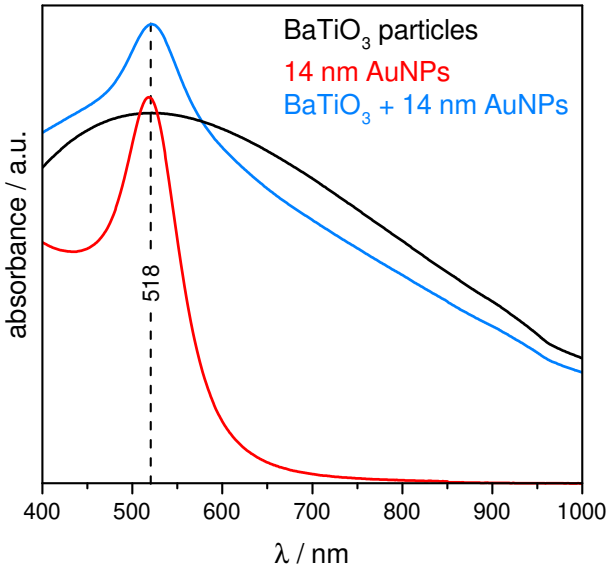

Figure 6.13: UV-vis spectra of APTES-functionalized $BaTiO_3$ particles (black), citrate-stabilized gold nanoparticles with an average size of 14 nm as determined from TEM (red), and a mixture of both (blue).

Figure 6.14 shows the UV-vis absorbance spectrum of the Ag@$BaTiO_3$ nanocomposites. The spectrum exhibits only one very broad band from the visible to the near IR with a maximum at 530 nm, which could be attributed to the formation of silver nanoparticle aggregates[217] on the barium titanate surface (for TEM images see Figure 6.8).

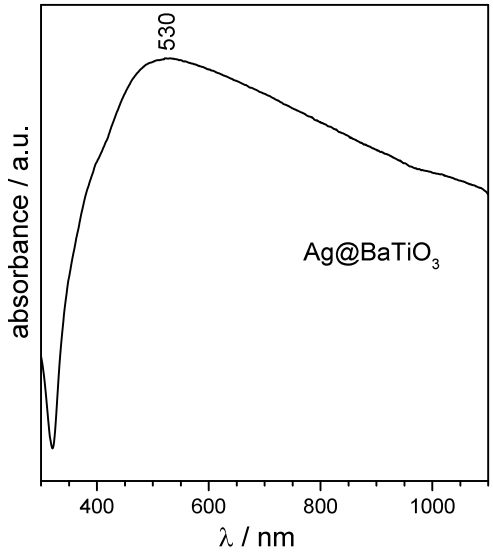

Figure 6.14: UV-vis spectrum of Ag@$BaTiO_3$ nanocomposites. Adapted from *Adv. Funct. Mater.* 2019, 29, 1904289.

The SHG of the plasmonic-$BaTiO_3$ nanocomposite systems was investigated using pulsed laser excitation at 850 nm and 1064 nm. Strong SHG signals from aqueous solutions of all composite nanoparticles in backscattering collection geometry were obtained at both wavelengths. Figure 6.15 shows the quadratic dependence of the SHG signal on the excitation intensity of Au@$BaTiO_3$ nanostructures excited at 850 nm. This confirms the two-photon parametric process of SHG. In addition, one can see from Figure 6.15 that the SHG intensity from 9 nm Au@$BaTiO_3$ and 17 nm Au@$BaTiO_3$ is nearly the same.

The SHG intensity from pristine $BaTiO_3$ nanoparticles and Au@$BaTiO_3$ nanocomposites are compared in Figure 6.16. While for excitation at 1064 nm the SHG signal from Au@$BaTiO_3$ composites is ~4 times lower (in the whole intensity range) relative to the signal from pristine $BaTiO_3$ particles (Figure 6.16A, compare red and black symbols), at 850 nm the SHG intensity of the composites is only ~2 times lower than that from the bare $BaTiO_3$ particles (Figure 6.16B, compare red and black symbols). Similar results were obtained for Ag@$BaTiO_3$ composites (Figure 6.17). For excitation at 1064 nm the SHG intensity from Ag@$BaTiO_3$ is ~4 times lower relative to the pristine $BaTiO_3$ particles (Figure 6.17A), and at 850 nm the SHG intensity of the composites is reduced by a factor of ~10 (Figure 6.17B). Comparing the effect of different excitation wavelengths on the signals from Au@$BaTiO_3$ and Ag@$BaTiO_3$, the composites with gold yielded higher SHG signals at 850 nm than at 1064 nm, and with silver higher SHG signals at 1064 nm than at 850 nm. Due to the fact that the two lasers operate in different power ranges, one should refrain from a comparison of absolute intensities at both

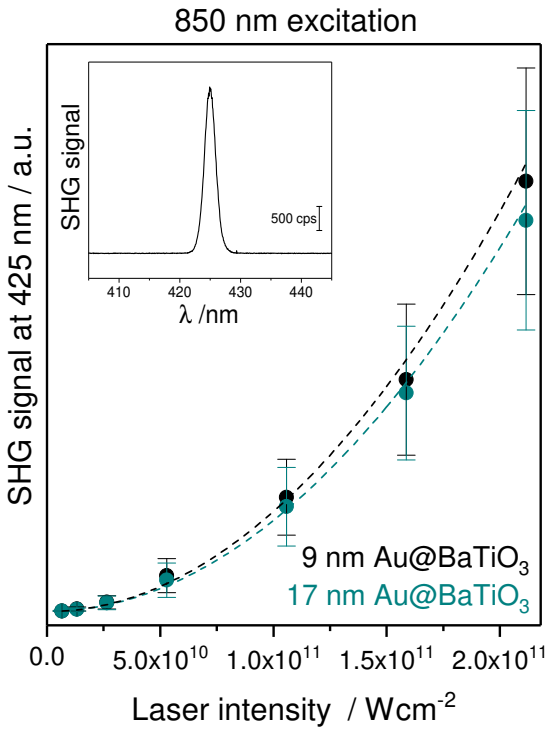

Figure 6.15: SHG signal from 9 nm Au@$BaTiO_3$ (black) and 17 nm Au@$BaTiO_3$ (green) excited at 850 nm as a function of the peak laser intensity. The values represent the mean of 30 measurements with 1 s acquisition time; the dashed lines display the fitted quadratic curves ($ax^2 + b$) to the data points. The insight shows a SHG spectrum of 17 nm Au@$BaTiO_3$ at 5×10^{10} W cm^{-2}. Adapted from *Adv. Funct. Mater.* 2019, 29, 1904289.

excitation wavelengths. Nevertheless, the different ratios for SHG intensity from pristine and metal coated $BaTiO_3$ particles at the two different excitation wavelengths clearly indicate a frequency dependence of the SHG signals. This is in accord with previous experimental work discussing the frequency dependence of SHG from $BaTiO_3$ nanocrystals, with the latter being enhanced at the intrinsic optical resonances of the particle.[32,47]

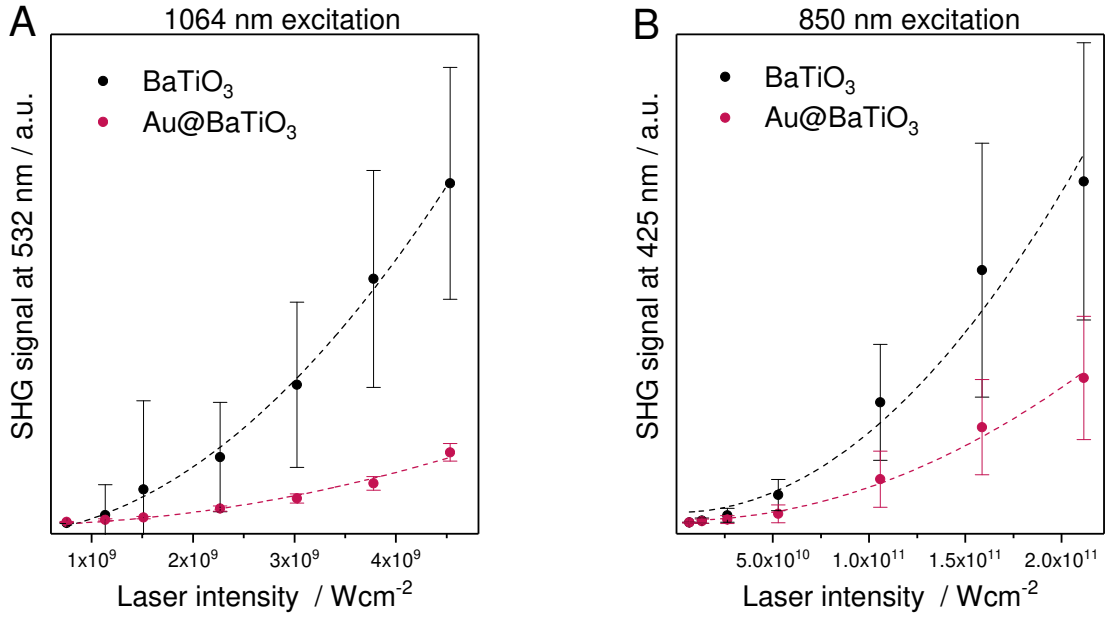

Figure 6.16: SHG signal from solutions of $BaTiO_3$ nanoparticles (black) and Au@$BaTiO_3$ nanocomposites (red) with similar concentration excited at (A) 1064 nm and (B) 850 nm as a function of the peak laser intensity. The values represent the mean of 30 measurements; the dashed lines display the fitted quadratic curves ($ax^2 + b$) to the data points. Integration time: 20 s (A) and 1 s (B). Adapted from *Adv. Funct. Mater.* 2019, 29, 1904289.

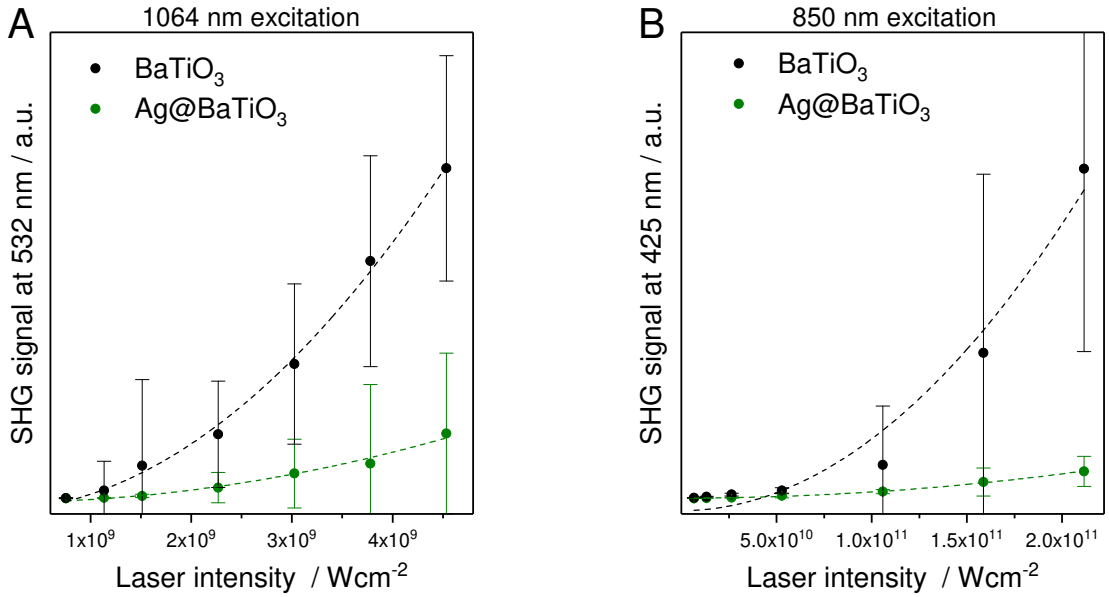

Figure 6.17: SHG signal from solutions of $BaTiO_3$ nanoparticles (black) and Ag@$BaTiO_3$ nanocomposites (green) with similar concentration excited at (A) 1064 nm and (B) 850 nm as a function of the peak laser intensity. The values represent the mean of 40 measurements; the dashed lines display the fitted quadratic curves ($ax^2 + b$) to the data points. Integration time: 20 s. Adapted from *Adv. Funct. Mater.* 2019, 29, 1904289.

6.2.2 Electrodynamic simulations

In order to gain a better understanding of why the SHG intensity from $BaTiO_3$ nanocrystals is altered when they are surrounded by plasmonic nanoparticles, the far- and near-field properties of different model systems were simulated using the finite-difference time-domain (FDTD) method. For the simulations of $BaTiO_3$ particles perfect spheres with diameters of 200 nm, 255 nm, and 300 nm as well as a 250 nm long rounded cuboid were used as model systems (Figure 6.18A). Two approaches were considered to mimic the gold shell of the composite Au@$BaTiO_3$ particles. First, the gold shell was modelled by surrounding the $BaTiO_3$ structures with many 17 nm gold nanospheres (Figure 6.18B). These model systems will be referred to as Au@$BaTiO_3$ composites. In the second approach (Figure 6.18C) the $BaTiO_3$ spheres had a homogeneous 17 nm thick shell of effective permittivity calculated according to the effective medium approximation[162,163] from the permittivities of gold and water using the same volume filling fraction of gold as in the case of the composite particle models. These models are termed here gold coated $BaTiO_3$ systems.

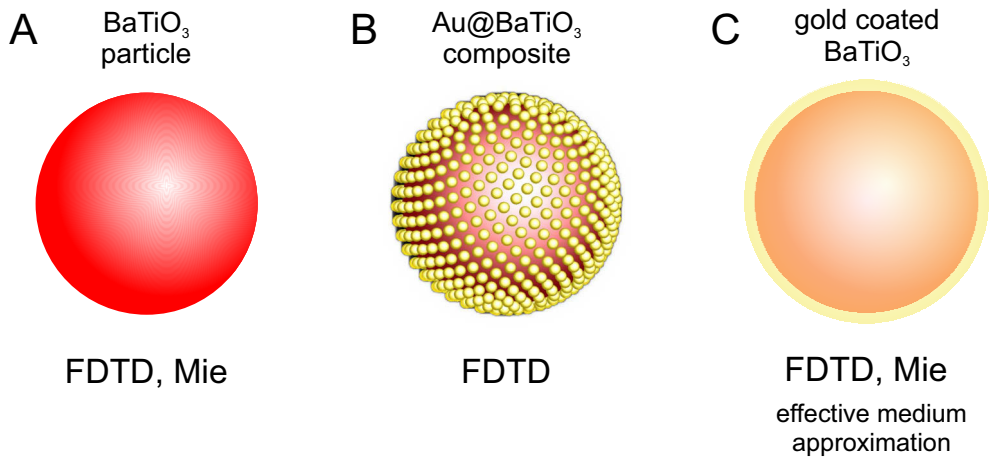

Figure 6.18: Schematic of the model systems considered in numerical simulations.

The extinction cross section of a 300 nm $BaTiO_3$ sphere in water calculated with FDTD (brown line in Figure 6.19A) or Mie theory[35] (black line in Figure 6.19A, superimposed with the brown one) has three peaks in the considered wavelength range at 447 nm, 545 nm, and 714 nm. The decomposition of the total Mie extinction cross section into separate multipole contributions (Figure 6.19A, red, green, and blue lines) shows that the peaks at 447 nm, 545 nm and 714 nm correspond to the maxima of the magnetic octopole, magnetic quadrupole and magnetic dipole modes, respectively. Similar resonances have been

found in previous studies of nanostructures with positive dielectric permittivity.[44,47,218,219] The theoretical extinction shows several narrow and well defined peaks, in contrast to the broad maxima in the experimental measurements (Figure 6.11A). This effect can be trivially assigned to an inhomogeneous broadening in the experiment due to the size and configuration dispersion within the colloids.

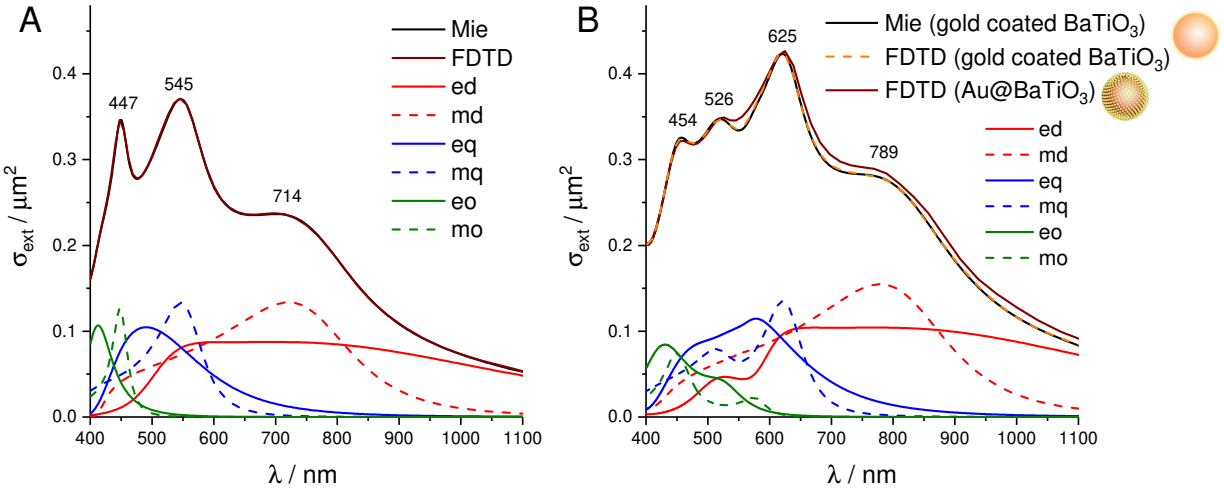

Figure 6.19: Extinction cross sections of A) 300 nm bare $BaTiO_3$ sphere, and B) 300 nm $BaTiO_3$ sphere with 17 nm thick shell of effective permittivity (mixture of gold and water with volume filling fraction of gold 0.287) in water calculated with Mie theory (continuous black line) and FDTD (dashed orange line), and of 300 nm $BaTiO_3$ sphere surrounded by 600 gold spheres (17 nm diameter) calculated with FDTD (continuous brown line). The Mie calculations were done by Alvaro Nodal. Legend for the Mie expansion: ed and md, electric and magnetic dipole; eq and mq, electric and magnetic quadrupole; eo and mo, electric and magnetic octopole. Adapted from *Adv. Funct. Mater.* 2019, 29, 1904289.

Figure 6.19B shows the extinction cross sections of a 300 nm $Au@BaTiO_3$ composite (continuous brown line), and a 300 nm gold coated $BaTiO_3$ sphere (dashed orange line) calculated with FDTD. The study of the convergence for the $Au@BaTiO_3$ composite is shown in Figure 6.20A, and for the gold coated model in Figure 6.20B. The cross section of the gold coated $BaTiO_3$ sphere was obtained also by solving the Mie problem for a core-shell system[35,164] (black line in Figure 6.19B, superimposed with the dashed orange one). Both approaches for modeling the gold shell yield very similar results, consistent with previous work,[162,216] therefore it is possible to use the contributions of each term in the Mie expansion to identify the multipole modes in the $Au@BaTiO_3$ composite particle. Figure 6.19B (red, blue, and green lines) indicates that in the gold coated $BaTiO_3$ particle, the magnetic octopole, quadrupole and dipole resonances are red-shifted to 454 nm, 625 nm and 789 nm,

respectively, compared to these modes in the bare $BaTiO_3$ sphere (Figure 6.19A, red, blue, and green lines). The fourth peak in the extinction cross section of the Au@$BaTiO_3$ composite at 526 nm has contributions from many modes, mainly the magnetic and electric quadrupoles (continuous and dashed blue lines in Figure 6.19B).

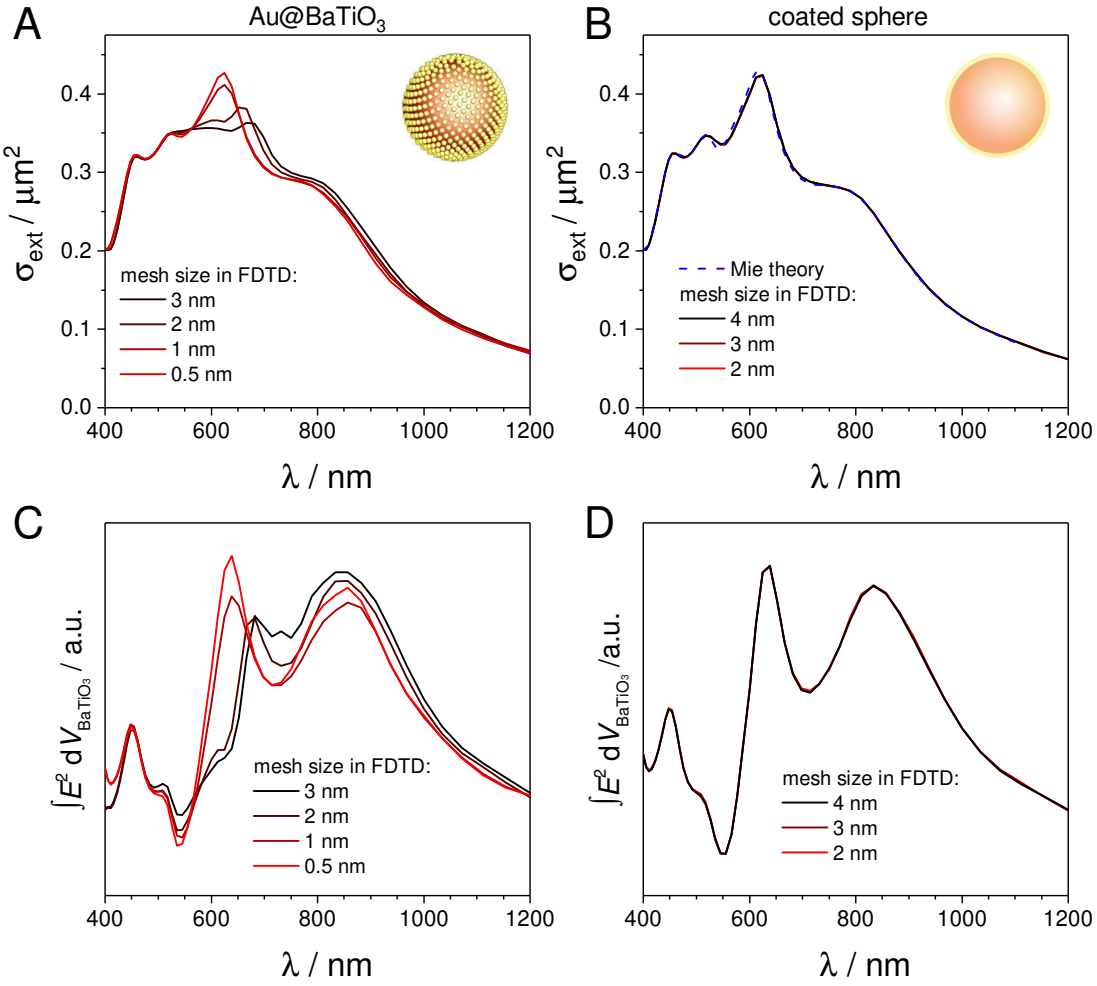

Figure 6.20: Convergence study. Extinction cross sections of A) 300 nm $BaTiO_3$ sphere with 600 17 nm gold nanospheres on its surface (Au@$BaTiO_3$ model), and B) 300 nm $BaTiO_3$ sphere with 17 nm thick shell of effective permittivity (mixture of gold and water with volume filling fraction of gold 0.287) in water calculated with FDTD using different mesh sizes. For comparison, also the extinction cross section for the system in B calculated with Mie theory (dashed blue line) is plotted. Integral over the square of the electic field amplitude inside the volume of the $BaTiO_3$ sphere for C) the composite Au@$BaTiO_3$ in A, and D) the gold coated $BaTiO_3$ sphere in B. Adapted from *Adv. Funct. Mater.* 2019, 29, 1904289.

If the size of the core particle is decreased, all resonances in both the pristine and composite barium titanate structures are blue-shifted. This is shown in Figure 6.21, where the extinction

cross sections of bare and composite 200 nm and 255 nm $BaTiO_3$ spheres as well as a 250 nm cuboid are presented. For example, while the magnetic quadrupole mode in the 300 nm $BaTiO_3$ sphere is at 545 nm (dashed blue line in Figure 6.19A), in the 255 nm particle the same mode is at 476 nm (red line in Figure 6.21A). The blue-shifting of the modes with decreasing size of the $BaTiO_3$ particle could also explain the blue-shifting of the experimental absorbance spectrum of the barium titanate nanoparticles with partially degraded surface layer (Figure 6.11A). Alike in the case of the 300 nm Au@$BaTiO_3$ composite, also in the smaller $BaTiO_3$ nanostructures the extinction cross section peaks are red-shifted when gold nanospheres are attached to their surface (compare Figure 6.21A with B).

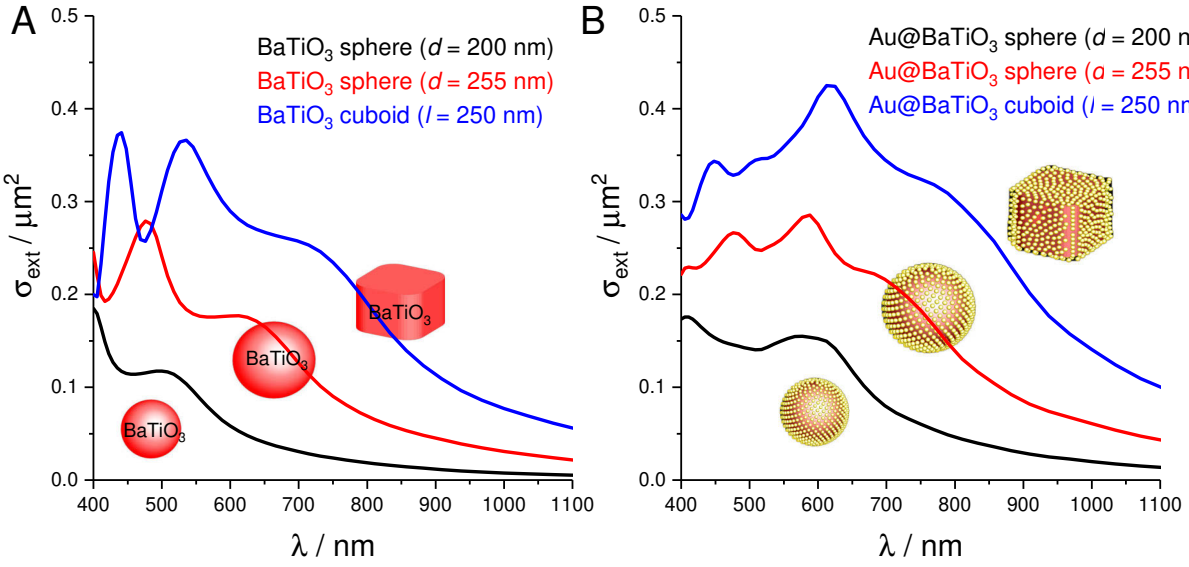

Figure 6.21: Calculated extinction cross sections with FDTD of: A) barium titanate spheres with diameters of 200 nm (black) and 255 nm (red), and a barium titanate rounded cuboid with a length of 250 nm (blue); B) the same barium titanate nanostructures from A but with many 17 nm gold spheres on their surface. The number of the gold spheres was chosen in a way that the total volume fraction of gold is 0.287 in all cases. Adapted from *Adv. Funct. Mater.* 2019, 29, 1904289.

Figure 6.22A and B show the distributions of the electric and magnetic near-field at the extinction cross section peaks of the pristine 300 nm $BaTiO_3$ sphere and 300 nm Au@$BaTiO_3$ composite calculated with FDTD. Although these peaks were assigned to a specific magnetic multipolar resonance, the near fields present mixed features due to the overlapping contribution of other off-resonant electric and magnetic multipoles.[44] For the dielectric $BaTiO_3$ sphere, the electromagnetic field is concentrated mainly inside the material, and the electric field at the surface of the particle is relatively low with values of $|E_{loc}/E_{inc}|$ of ~2 (Figure 6.22A, left panels), where E_{inc} is the amplitude of the incident electric field and E_{loc} the corre-

sponding value of the total local fields (sum of the incident and induced fields). In contrast, the densely distributed gold nanoparticles on the Au@$BaTiO_3$ composite surface provide high electric field enhancement in their proximity (Figure 6.22B, left panels). The resulting SERS enhancement, which scales approximately with $|E_{loc}/E_{inc}|^4$, reaches values up to 10^4, especially for the longer wavelengths of 625 nm and 789 nm. This indicates that, although enhancement of optical scattering processes in high refractive index dielectric nanostructures is possible,[218,219] the observed SERS and SEHRS in experiments that will be discussed in Section 6.3 mainly result from the enhanced local fields generated by the plasmonic moieties.

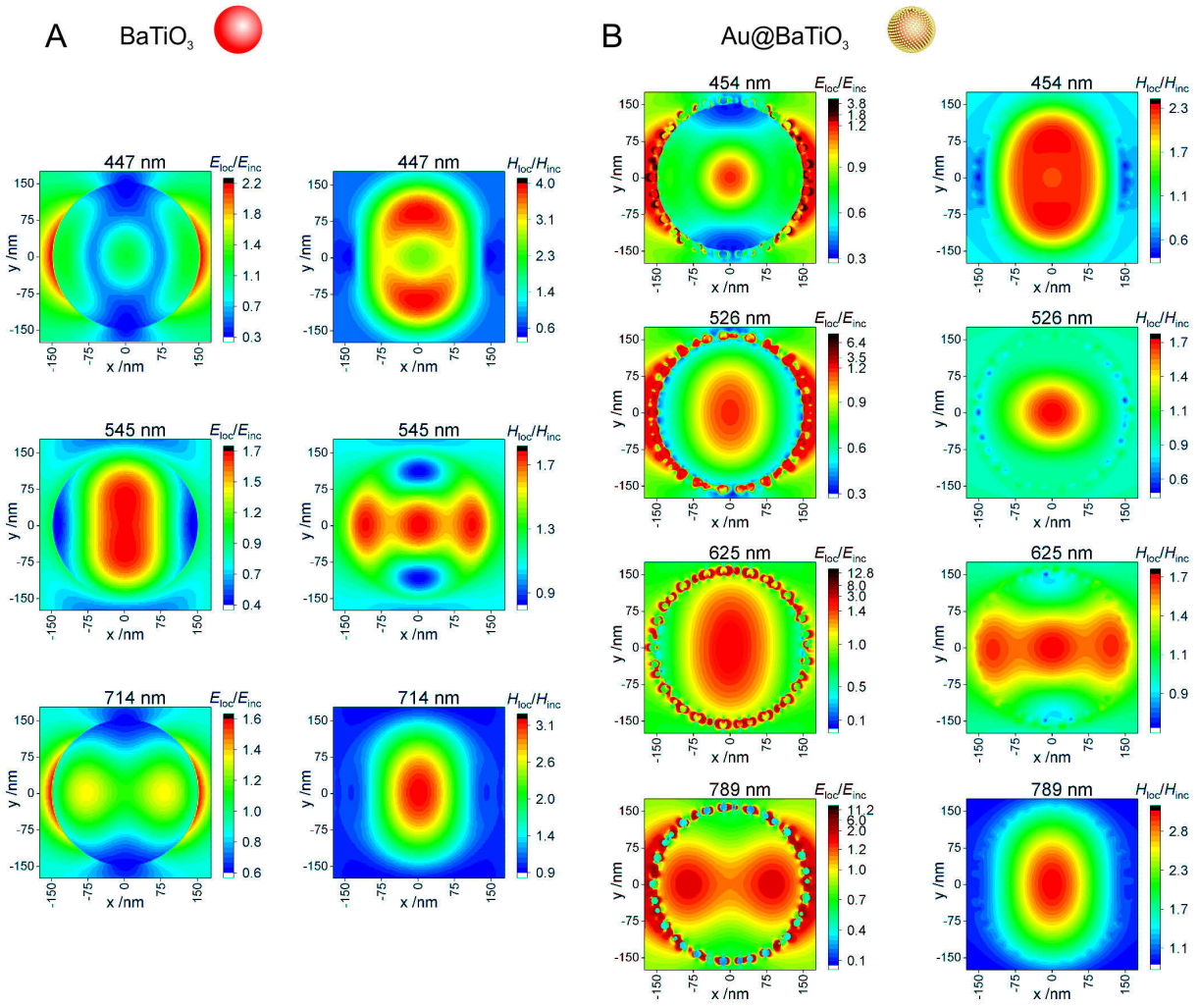

Figure 6.22: Maps for the modulus of the total local electric and magnetic field vectors normalized to the incoming fields (E_{loc}/E_{inc} and H_{loc}/H_{inc}) in the xy-plane for A) 300 nm $BaTiO_3$ sphere, and B) composite $BaTiO_3$ sphere with 600 17 nm gold spheres on its surface at the positions of the extinction cross sections peaks (see brown lines in Figure 6.19A and B for the cross sections). The fields are calculated with FDTD using a plane wave polarized in x and propagating in $-z$ direction. Adapted from *Adv. Funct. Mater.* 2019, 29, 1904289.

On the other hand, this plasmonic enhancement at the $BaTiO_3$ particle surface does not necessarily dominate the SHG. The fields inside the entire $BaTiO_3$ core must be also taken into account, and not just those in the proximity of the metallic nanoparticles. In order to understand the different ratios of the SHG from the experiments, the information of the near fields simulated in the model systems is used to estimate the SHG enhancement for excitation angular frequency ω. Here, a simplified approach that decomposes the total enhancement into two different contributions is considered, because calculating the exact SHG for polycrystalline particles is very complex. The first contribution is associated with the generation of a polarization oscillating at 2ω inside the spherical dielectric core, due to the non-linear susceptibility of $BaTiO_3$. SHG is a second-order process, leading to an enhancement that scales with the fourth power of the local electric field amplitude $E_{\mathrm{loc}}(\omega)$ (second power of the local intensity) at the excitation frequency ω. The second contribution, (which multiplies the first one), is due to the change of the emission rate of the excited 2ω polarization. Due to reciprocity,[220–222] the increase of the field emitted from each infinitesimal region of the $BaTiO_3$ sphere can be approximated as the enhancement of the local electric field amplitude $E_{\mathrm{loc}}(2\omega)$ at the same region for planewave illumination at 2ω (or, equivalently, the intensity of the emitted signal scales with the square of the local fields). The SHG intensity from the composite particle relative to the corresponding signal from the bare sphere is estimated as:

$$\frac{I_{\mathrm{SHG}}(\mathrm{Au@BaTiO_3})}{I_{\mathrm{SHG}}(\mathrm{BaTiO_3})} \propto \frac{\left(\int E^2_{\mathrm{loc}}(\omega,\mathbf{r},\mathrm{Au@BaTiO_3})\mathrm{d}V\right)^2 \int E^2_{\mathrm{loc}}(2\omega,\mathbf{r},\mathrm{Au@BaTiO_3})\mathrm{d}V}{\left(\int E^2_{\mathrm{loc}}(\omega,\mathbf{r},\mathrm{BaTiO_3})\mathrm{d}V\right)^2 \int E^2_{\mathrm{loc}}(2\omega,\mathbf{r},\mathrm{BaTiO_3})\mathrm{d}V} \tag{6.1}$$

with E_{loc} the module of the local fields $E_{\mathrm{loc}} = \sqrt{\sum_{i=x,y,z} |E_{\mathrm{loc},i}|^2}$ obtained from FDTD simulations. The integral takes into account the contributions from the entire $BaTiO_3$ sphere. The emission from the gold nanoparticles is not considered, because gold is a centrosymmetric material with no bulk SHG, and furthermore it is assumed that the surface contributions from the gold particles are negligible compared to the signal from $BaTiO_3$. Equation (6.1) integrates over the real-valued amplitudes of the fields, and thus assumes a loss of spatial coherence, which can be justified by the presence of many crystalline domains with different crystallographic orientations. A loss of SHG coherence due to polycrystallinity has already been discussed and observed in related systems.[223–225] Equation (6.1) may underestimate the role of the small regions of strong, highly-confined fields

(plasmonic-hot spots) induced inside the $BaTiO_3$ by the small gold nanoparticles, but their influence in the experiment seems to be small.

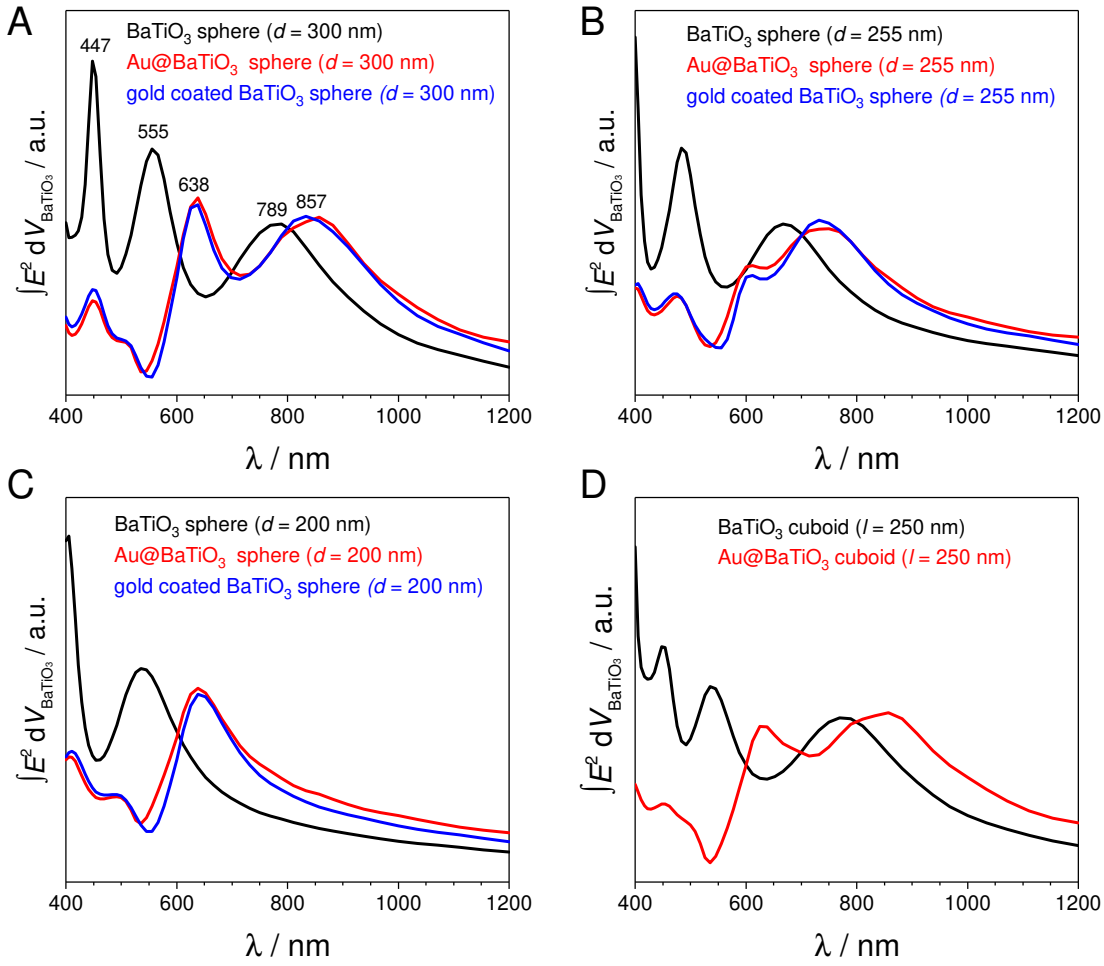

Figure 6.23: Integral over the square of the electic field amplitude inside the volume of the barium titanate structure for a bare $BaTiO_3$ particle (black lines), a composite Au@$BaTiO_3$ particle (red lines), and a gold coated $BaTiO_3$ particle (blue lines) calculated with FDTD as a function of the wavelength. The core $BaTiO_3$ particle was A) 300 nm sphere, B) 255 nm sphere, C) 200 nm sphere, and D) 250 nm long rounded cuboid, and the volume filling fraction of gold is 0.287 in all cases (red and blue lines).

Figure 6.23A shows the integral of the square of the electric field amplitude inside the core sphere in the considered wavelength range for a 300 nm bare $BaTiO_3$ particle (black line) and a 300 nm $BaTiO_3$ particle with small gold nanospheres on its surface (red line). Three clear peaks appear in both spectra due to the magnetic dipole, quadrupole and octopole (compare with the corresponding extinction cross sections in Figure 6.19A and B). The moderate spectral shift with respect to the extinction results can be attributed to the effect

of the strong losses.[226,227] While the electric field at the magnetic octopole resonance in the Au@$BaTiO_3$ composite is clearly reduced relative to that of the bare $BaTiO_3$ sphere, the field intensities at the magnetic quadrupole and dipole resonances are comparable in both structures. The latter though are red-shifted in the Au@$BaTiO_3$ composite. Because of these changes in the distribution of the local fields, according to Equation (6.1), the SHG intensity from the composite particle should be ~90 % for the excitation at 850 nm and ~60 % at 1064 nm relative to the intensity from the bare barium titanate nanocrystal.

In Table 6.1 the expected relative SHG signal strengths for core barium titanate particles of different size and shape are summarized. Both, size and shape have strong influence on the positions of the multipole resonances as discussed above (Figure 6.21), and on the electric fields inside the particle (Figure 6.23B-D). For all structures considered here, the relative SHG intensities at 850 nm are higher than at 1064 nm, which is in qualitative agreement with the experimental data (Figure 6.16). For example, while the SHG signal of a 250 nm $BaTiO_3$ cuboid surrounded by gold nanospheres is ~80 % at 850 nm and ~55 % at 1064 nm relative to the ones of a cuboid without gold particles (compare red and black lines in Figure 6.23D), the relative values for a 255 nm sphere are ~130 % and ~80 % (compare red and black lines in Figure 6.23B), respectively. Strong dependence of the SHG on the sphere size has been observed also for silicon nanoparticles, and it was attributed to resonant enhancement when the particle multipole modes match the second harmonic frequency.[228]

Table 6.1: SHG signal strength for Au@$BaTiO_3$ composite nanostructures relative to the SHG signals from the same $BaTiO_3$ structures without gold nanospheres calculated from FDTD simulations according to Equation (6.1). Adapted from *Adv. Funct. Mater.* 2019, 29, 1904289.

excitation	200 nm sphere	255 nm sphere	300 nm sphere	250 nm cuboid
850 nm	115 %	130 %	90 %	80 %
1064 nm	65 %	80 %	60 %	55 %

The near-field spectra of the investigated structures were obtained also using the effective medium approximation (Figure 6.23, blue lines), and the results are very similar to the fields obtained using the composite Au@$BaTiO_3$ particles (compare red and blue lines in Figure 6.23A-D). Therefore, it was possible to use the computationally less expensive effective medium approximation to calculate the relative SHG from particles with varying composition of the gold shell. Figure 6.24A shows the integrals of the electric field am-

plitude as a function of wavelength for a 300 nm $BaTiO_3$ particle with different gold shell thickness and constant gold filling fraction of 0.287, while in Figure 6.24B the near-field spectra for a 300 nm $BaTiO_3$ particle with 17 nm thick gold shell of varying filling fraction are presented. The relative SHG values for these structures (Figure 6.24C and D) show that, for the given core particle size, the SHG decreases with increasing amount of gold on the $BaTiO_3$ surface (except for the high filling fractions above 0.4, where the effective medium approximation might not be very accurate).

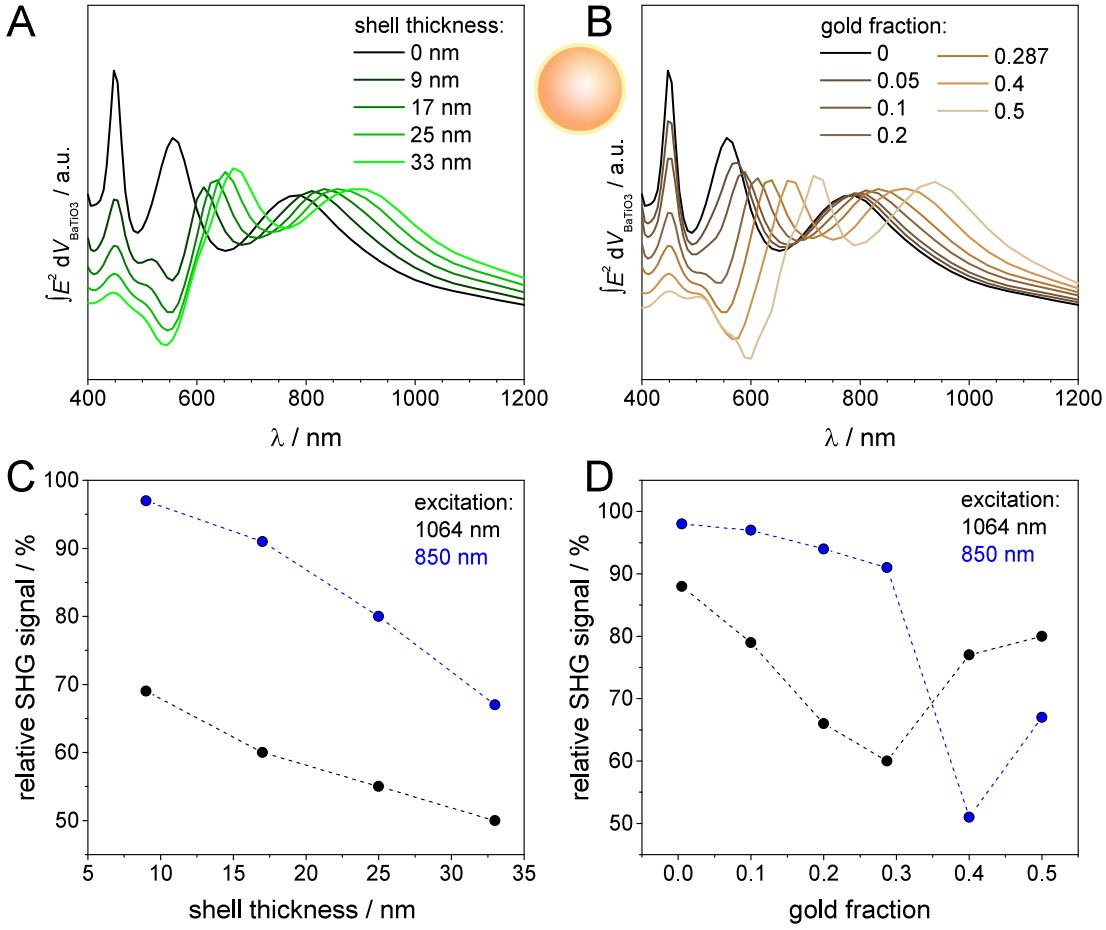

Figure 6.24: A), B) Integral over the square of the electic field amplitude inside the volume of a 300 nm barium titanate sphere with effective gold shell of varying thickness and constant filling fraction of 0.287 (A) and varying gold filling fraction and constant shell thickness of 17 nm (B) calculated with FDTD. C), D) SHG intensity from the core-shell particles in A and B relative to the bare $BaTiO_3$ sphere as a function of the effective shell thickness (C) and gold fraction (D) calculated according to Equation (6.1).

The results presented in Table 6.1 and Figure 6.24C-D demonstrate that the relative SHG efficiency depends on the plasmonic coating and even more strongly on the size and shape

of the dielectric core, which determines to a greater extent the frequencies of the composite particle resonances. The data also indicate that an enhancement of SHG due to the gold coating is possible and could be achieved by careful tuning of the nanocomposite structure or by using different excitation wavelength, e.g. further in the IR, in order to match the multipole resonances of the composite particles.

Considering the actual situation in the experiments, in particular the very broad size distribution, the non-spherical shape of the barium titanate particles (Figure 6.1), as well as the influence of surrounding nanoparticles, including, e.g., the re-absorption of the light emitted from one particle by others in the solution, the estimate of the relative SHG efficiency is in reasonable agreement with the experimental SHG data. One can conclude that the observed SHG intensity from the composite nanostructures in the experiments (Figure 6.16) is affected by shifts of the particles' electromagnetic modes, and the corresponding changes in the electric fields inside the non-linear nanocrystal when a plasmonic shell is present. On the other hand, the plasmonic nanoparticles at the outside provide enhancement of the electric fields in their proximity, which enable electromagnetic enhancement in SEHRS and SERS, as will be demonstrated in the next section.

6.3 Dual two-photon probing by SHG and SEHRS in combination with SERS

As discussed above, the plasmonic-$BaTiO_3$ nanocomposites yield strong SHG signals at low excitation intensities and short integration times of 1 s. To demonstrate that the nanocomposites can be used as nanoprobes for SHG imaging experiments of biological samples, J774 macrophage cells were used as a biological model system. In order to increase their biocompatibility and uptake by the cells, the nanoprobes were exposed to lipids following a protocol reported by Matthews et al.[151] The 785 nm excited SERS spectra generated by the plasmonic moieties of the 17 nm Au@$BaTiO_3$ (Figure 6.25, black spectrum) show characteristic bands at 761 cm^{-1}, 963 cm^{-1}, and 1449 cm^{-1} that can be assigned to the stretching vibrations of the trimethylammonium headgroup and CH_2 twisting and wagging vibrations of the CTAB capping agent.[229] After incubation with lipid vesicles, these bands disappear (Figure 6.25, red spectrum), confirming the displacement of CTAB from the nanoparticle

surface. The spectra of the lipid coated $Ag@BaTiO_3$ composites did not exhibit any characteristic bands (Figure 6.25, blue spectrum). The absence of SERS signals from CTAB as well as from other reporter molecules when 9 nm $Au@BaTiO_3$ nanocomposites were used (Figure 6.25, green spectrum), different to the 17 nm $Au@BaTiO_3$, seems to indicate that the enhancement of the Raman scattering depends on the plasmonic properties of the gold nanoparticles in such a situation, and thus it is influenced by the gold particle size and by their interaction on the surface of the $BaTiO_3$.

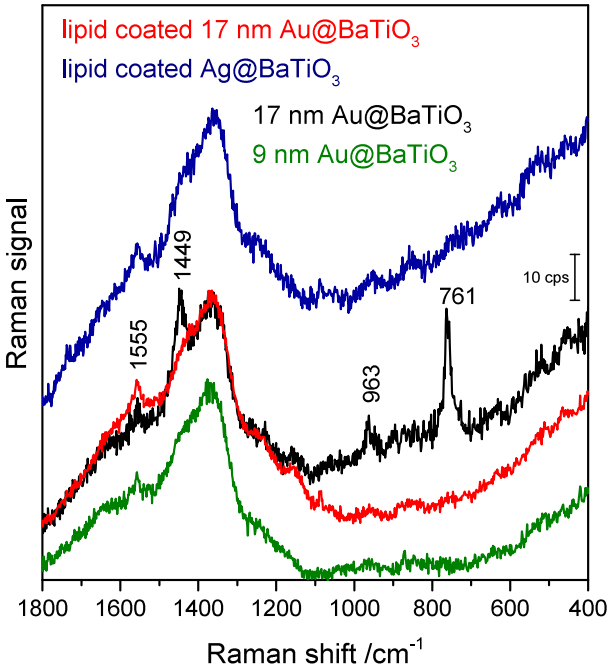

Figure 6.25: Raman spectra of 9 nm $Au@BaTiO_3$ (green line), 17 nm $Au@BaTiO_3$ (black line), lipid coated 17 nm $Au@BaTiO_3$ (red line), and lipid coated $Ag@BaTiO_3$ (blue line). Excitation: 785 nm; acquisition time: 1 s; laser intensity: 4×10^5 W cm^{-2}. Adapted from *Adv. Funct. Mater.* 2019, 29, 1904289.

Macrophage cells were incubated with culture medium containing lipid coated $Au@BaTiO_3$ and $Ag@BaTiO_3$ composite nanoprobes for 3 hours. SHG maps of the cells at 850 nm excitation are shown in Figure 6.26. According to previous discussions, the endogenous SHG from the cells is expected to be predominantly forward-propagated and much weaker than the signals from a non-linear nanocrystal.[32] Thus, one can conclude that the SHG maps show the spatial distribution of the nanoprobes inside the macrophage cells. Comparing the absolute SHG signals from the nanoprobes in the cells with those measured in solution, the former can be significantly higher at some positions in the cells, in agreement with the known formation of aggregate structures in endosomes inside the cellular ultrastructure.[230,231]

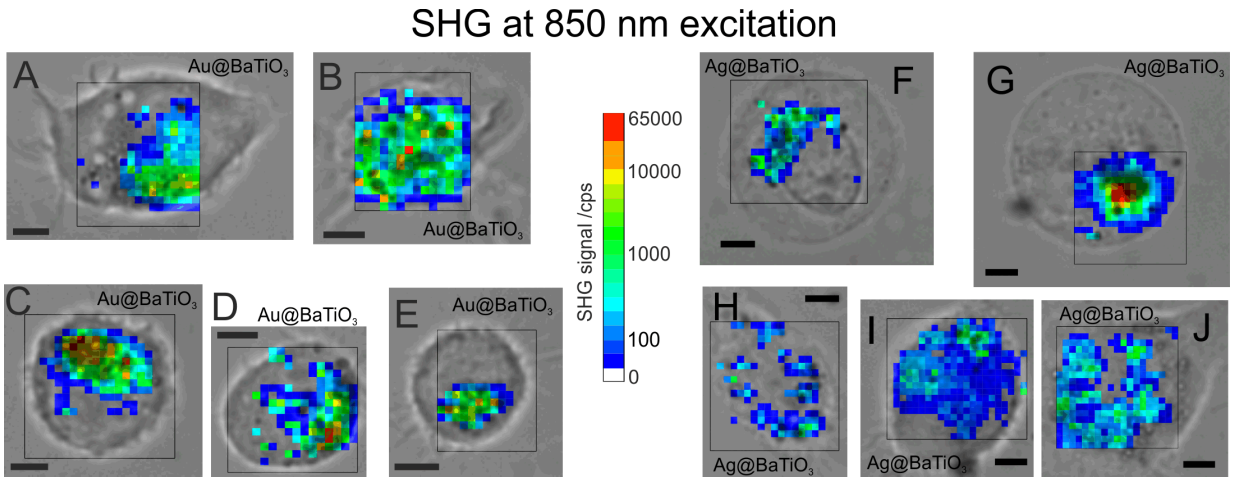

Figure 6.26: Bright-field images of J774 macrophage cells containing lipid coated 17 nm $Au@BaTiO_3$ (A-E) and $Ag@BaTiO_3$ (F-J) nanocomposites, overlaid with SHG maps. The transparent areas within the SHG maps (black frames) correspond to signals below noise level (20 cps). The color bar applies to all images. Excitation: 850 nm; acquisition time: 1 s, peak laser intensity: 1×10^{11} W cm^{-2} (5 mW average power); step size: 1 µm; scale bars: 5 µm. Adapted from *Adv. Funct. Mater.* 2019, 29, 1904289.

In addition to the possibility of obtaining such morphofunctional information from the cells by SHG imaging, the plasmonic moieties allow molecular and structural characterization of the local surface environment of the metal-barium titanate nanoprobes by means of SERS. As shown above, SERS can probe the presence of the CTAB capping agent and monitor its displacement. Moreover, SERS spectra of small molecules, such as crystal violet (CV), that were added to solutions of $Au@BaTiO_3$ and $Ag@BaTiO_3$ nanoparticles indicate that molecules interact with the surface of the nanocomposites. Figure 6.27A and B show the SERS spectra of CV obtained at 785 nm and 633 nm excitation, respectively. The CV spectra at 633 nm and 785 nm differ in relative intensities for some bands (e.g., compare the bands at 1618 cm^{-1} and 724 cm^{-1} in the red spectra in Figure 6.27A and B) because at 633 nm the Raman process benefits also from resonance enhancement (see Figure 4.6A in Chapter 4 for the absorption spectrum of CV), while the wavelength of 785 nm is not in resonance with electronic transitions in the dye molecule. The CV spectrum at 633 nm with $Ag@BaTiO_3$ (green line in Figure 6.27B) has strong fluorescence contributions. In principle, all spectra exhibit many bands characteristic for the CV molecule at these excitation wavelengths – for comparison, CV spectra obtained with citrate-stabilized gold and silver nanoparticles are displayed in Figure 6.28.

The collection of non-resonant SERS spectra is one of the main prerequisites for biological applications of the new optical probes, and for the collection of spectra from the cellular

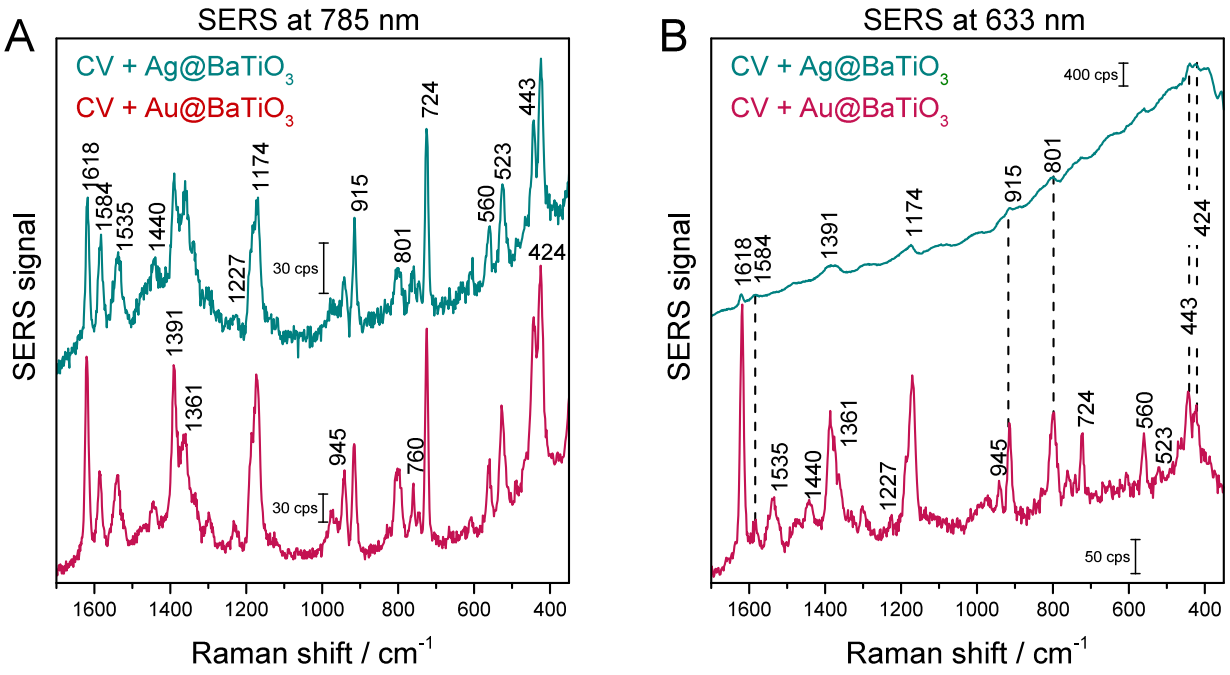

Figure 6.27: SERS spectra of CV in the local fields of 17 nm $Au@BaTiO_3$ (red) and $Ag@BaTiO_3$ (green) nanocomposites. Excitation: 785 nm (A) and 633 nm (B); acquisition time: 2 s (top spectrum in A) and 1 s (B and bottom spectrum in A); laser intensity: 4×10^5 W cm^{-2} (A) and 1×10^5 W cm^{-2} (B); crystal violet concentration: 10^{-6} M.

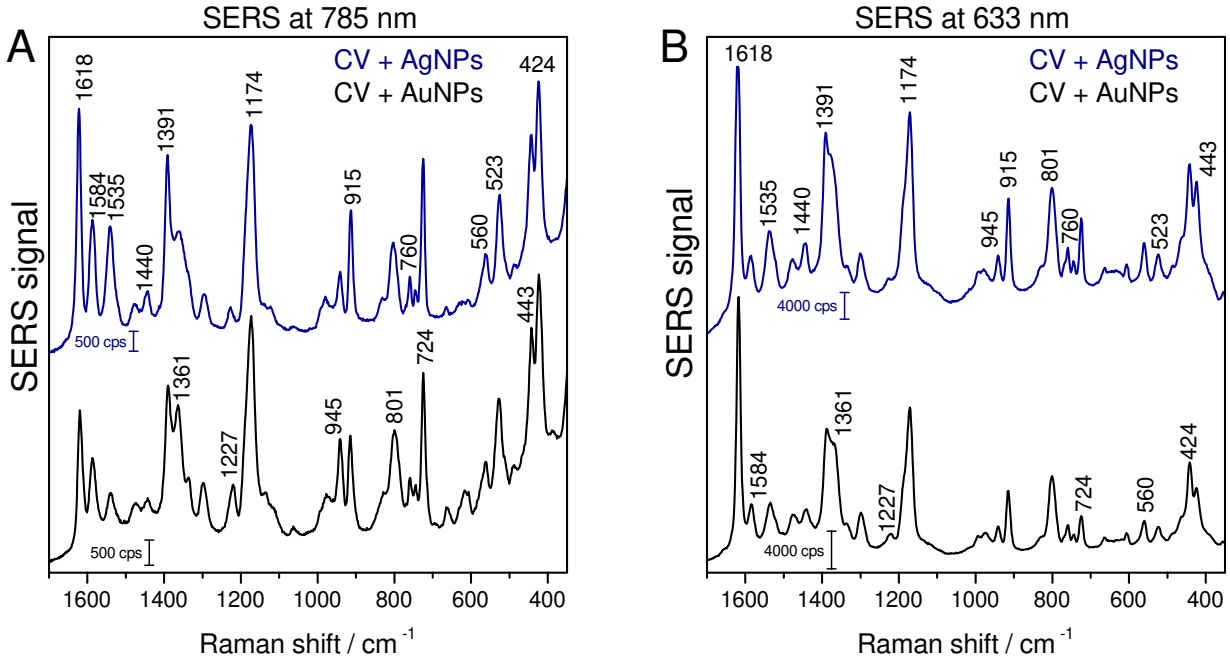

Figure 6.28: SERS spectra of CV in the local fields of citrate-stabilized gold (black) and silver (blue) nanoparticles. Excitation: 785 nm (A) and 633 nm (B); acquisition time: 1 s; laser intensity: 4×10^5 W cm^{-2} (A) and 1×10^5 W cm^{-2} (B); CV concentration: 10^{-6} M.

environment.[169] As an example of a potential application as reporters in live cells, 17 nm $Au@BaTiO_3$ and $Ag@BaTiO_3$ nanocomposites were modified with *para*-mercaptobenzoic acid (*p*MBA), and non-resonant SERS mapping of J774 macrophage cells incubated with the nanoparticles was performed. The spectra of the *p*MBA-functionalized nanoprobes outside cells are displayed in Figure 6.29, and they exhibit characteristic bands for the *p*MBA molecule.[116,232] Figure 6.30A-D show chemical maps of the cells based on the SERS intensity of the *p*MBA ring stretching vibration at 1070 cm^{-1}. The molecules remained on the surface of the nanocomposites after 3 h of cellular uptake, confirmed by the stable SERS signals of *p*MBA obtained from the cells. These results demonstrate that the metal-barium titanate composite nanostructures can be the basis of SERS tags that highlight biological structures in one-photon excited vibrational imaging experiments[169,233] in addition to the two-photon probing.

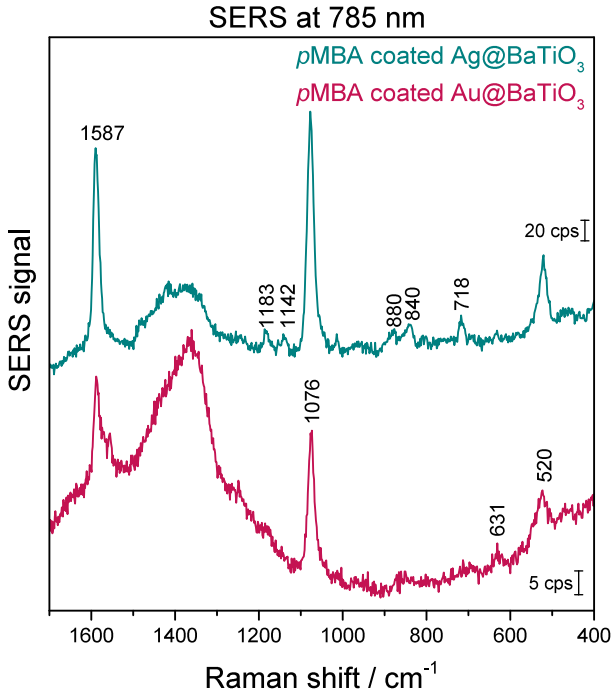

Figure 6.29: SERS spectra of *p*MBA with of 17 nm $Au@BaTiO_3$ (red) and $Ag@BaTiO_3$ (green) nanocomposites. Excitation: 785 nm; acquisition time: 5 s (top) and 10 s (bottom); laser intensity: 4×10^5 W cm^{-2}. The nanoparticles were incubated with 10^{-4} M *p*MBA for several hours and the excess *p*MBA was removed by centrifugation and washing cycles. Adapted from *Adv. Funct. Mater.* 2019, 29, 1904289.

Probing of intrinsic cellular structures without reporter molecules using lipid coated 17 nm $Au@BaTiO_3$ particles in macrophage cells is presented in Figure 6.30E. The SERS spectra show lipid bands due to the lipid coating of the nanoprobes or of cellular membranes,[234] and also bands that are characteristic of other molecules in the cells. For example, while

the band at 714 cm^{-1} present in most of the spectra is very characteristic for the C-N stretching of the choline group in lipids, the bands at 827 cm^{-1} and 853 cm^{-1} can be assigned to aromatic amino acids with high Raman cross sections that are abundant in proteins.[235] The SERS spectra of the intrinsic cellular molecules (Figure 6.30E) provide a perspective on the chemical environment of the nanoprobes, and thereby complement the morphological information obtained by SHG (Figure 6.26).

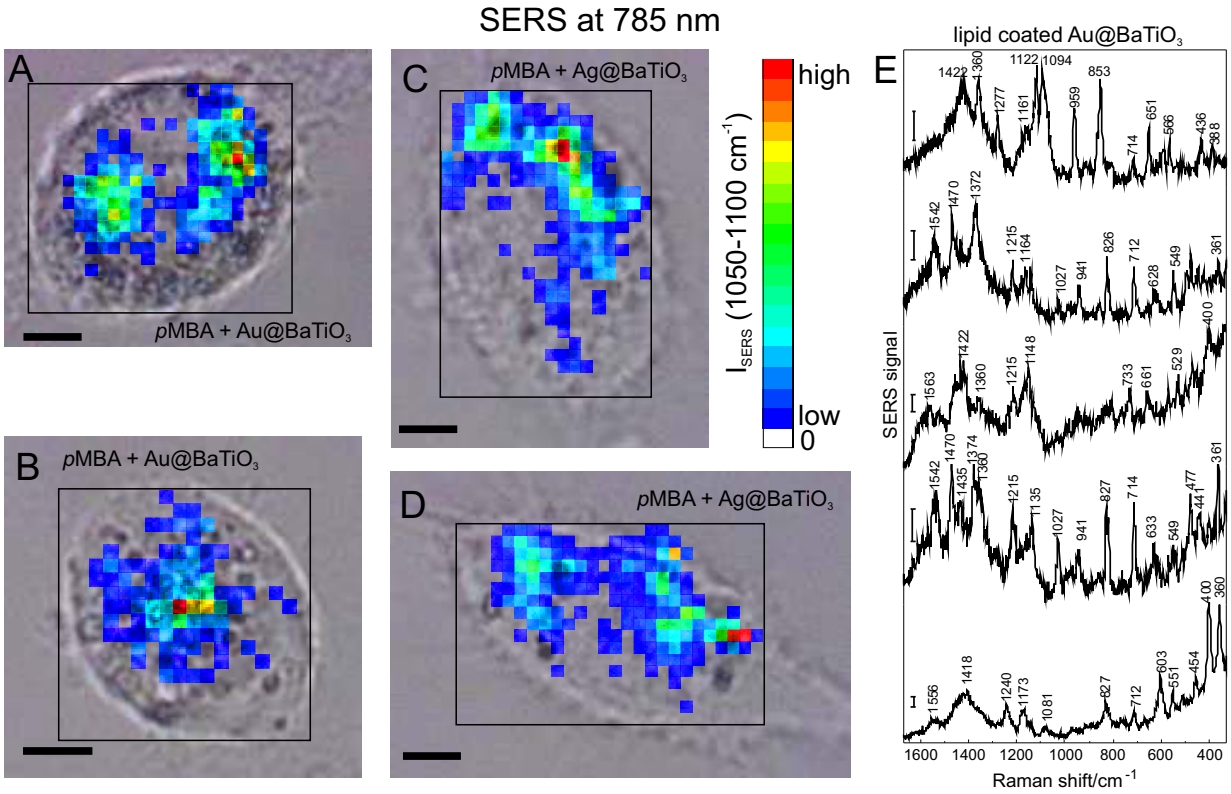

Figure 6.30: (A, B, C, D) Bright-field images of J774 macrophage cells containing *p*MBA labeled 17 nm $Au@BaTiO_3$ (A, B) and $Ag@BaTiO_3$ (C, D) nanocomposites, overlaid with Raman maps based on the integrated SERS signal of the reporter. The transparent areas within the chemical maps (black frames) correspond to spectra with no *p*MBA signals. Excitation: 785 nm; acquisition time: 1 s, laser intensity: 8×10^5 W cm^{-2} (4 mW average power); step size: 1 µm; scale bars: 5 µm. (E) SERS spectra at 785 nm from J774 cell after 3h-uptake of lipid coated 17 nm $Au@BaTiO_3$. Scale bars: 20 counts per second. Adapted from *Adv. Funct. Mater.* 2019, 29, 1904289.

As it is demonstrated in Figure 6.31, the plasmonic moiety of the $Ag@BaTiO_3$ nanoparticles permits the collection of resonant and non-resonant SEHRS spectra. Using an excitation wavelength of 1064 nm, SEHRS spectra of the dye molecule crystal violet were obtained with $Ag@BaTiO_3$ (Figure 6.31, bottom trace). They resemble the SEHRS of CV previously

reported in work using gold and silver nanoparticles.[11,113,114] The SEHRS spectrum of *p*MBA (Figure 6.31, top trace), a very sensitive indicator of pH inside and outside cells,[116,170] exhibits characteristic bands corresponding to the ring stretching and symmetric ring breathing modes of the molecule at 1578 cm^{-1} and 1072 cm^{-1}, respectively.[232] The presence of the band corresponding to the C-COO^- stretching at 1364 cm^{-1} enables pH mapping in cells with *p*MBA labeled Ag@$BaTiO_3$.[116,170] Here, SEHRS microspectra are excited at a wavelength that enables imaging of the plasmonic barium titanate nanoprobes by SHG as well, and hence two different two-photon imaging modalities can be used at the same time.

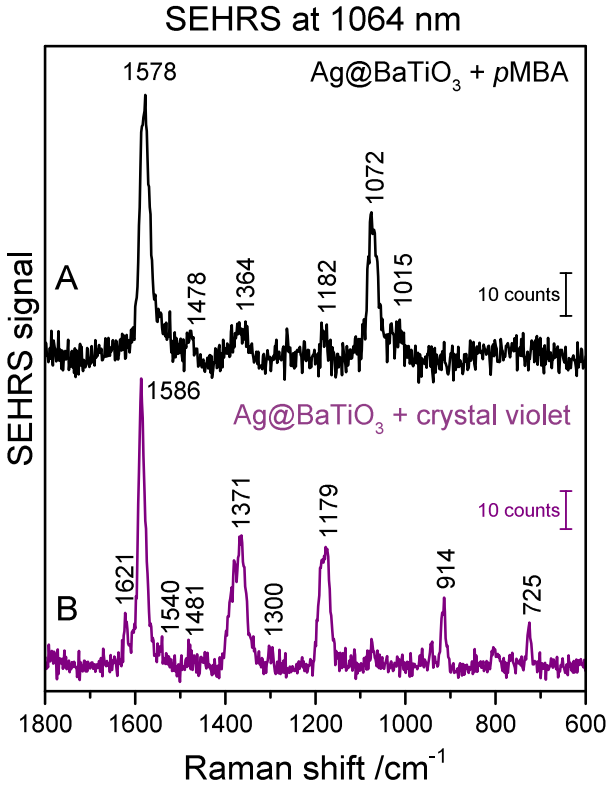

Figure 6.31: SEHRS spectra of A) *p*MBA and B) crystal violet (CV) in the local fields of Ag@$BaTiO_3$. Excitation: 1064 nm, acquisition time: 300 s (A) and 60 s (B), peak laser intensity: 2×10^{10} W cm^{-2} (A) and 6×10^{9} W cm^{-2} (B). CV concentration was 10^{-6} M; Ag@$BaTiO_3$ were incubated with 10^{-4} M *p*MBA for at least 3 h and the excess *p*MBA was removed by centrifugation and washing cycles. Adapted from *Adv. Funct. Mater.* 2019, 29, 1904289.

6.4 Conclusions

Composite nanostructures consisting of a barium titanate core, a material with high second order non-linear susceptibility, and a plasmonic moiety of gold or silver nanoparticles on the surface of the core were successfully synthetized by employing seed-mediated growth and seedless approaches adapted from methods for the preparation of similar systems such as silica-metal core-shell nanoparticles. The composite nanoparticles can act as versatile optical nanoprobes for a combination of two different two-photon excited microscopies, together with one-photon excited SERS. In the non-linear regime, the composite nanostructures function as harmonic probes for SHG, as well as plasmonic substrates that enhance resonant and non-resonant hyper Raman scattering. By delivering SEHRS spectra, the composite nanoprobes provide vibrational information that is complementary to the one-photon excited SERS spectra, also obtained here using non-resonant excitation. As demonstrated by the observation of their aggregation in live cells, the strong SHG signals at short integration times and low excitation intensities of the probes can be used to image physiological functions and nanomaterial processing in biological systems.

The optical properties of the plasmonic-$BaTiO_3$ nanocomposites were found to differ from those of the barium titanate nanocrystals. As inferred from experimental UV-vis spectroscopy data and numerical simulations, the electromagnetic modes of the composite particles are red-shifted compared to the pristine barium titanate particles. Both experimental SHG data and FDTD simulations indicate that the strength of the SHG signals from the nanocomposites is wavelength dependent. Due to changes of the optical near field properties induced by the presence of the plasmonic nanostructures, SHG can decrease moderately relative to that obtained from plain barium titanate particles. As a second aspect, the gold and silver particles on the barium titanate surface also enhance the local fields in their surroundings, which opens new opportunities for probing of the local environment by means of Raman and hyper Raman scattering. This was demonstrated by detecting molecules and their changing interaction on the surface of the composite nanostructures with SERS and SEHRS. The data show that depending on the plasmonic coating the optical properties of barium titanate nanocrystals can be tuned and optimized for a particular type of experiment. The Ag@$BaTiO_3$ composites were specifically suitable for SEHRS and SHG excited at 1064 nm, as well as SERS at 785 nm, while the Au@$BaTiO_3$ nanoparticles can be useful in experiments that combine SERS and SHG at lower wavelengths, in this case at 785 nm and 850 nm, respectively.

In conclusion, the results demonstrate that plasmonic barium titanate nanocomposites are tunable probes for multimodal multiphoton microspectroscopy and may open up new avenues for studying the morphological structure and chemical properties of biosystems.

Chapter 7

Non-resonant SEHRS of organic and bioorganic molecules

This chapter is based on the publications *J. Phys. Chem. C* 2017, 121, 2, 1235-1242 and *J. Phys. Chem. C* 2020, doi: 10.1021/acs.jpcc.0c00294.

Surface enhanced hyper Raman scattering (SEHRS) is a complementary approach to the one-photon excited surface enhanced Raman scattering (SERS), and it is therefore often used in combination with SERS for probing of organic structures and materials. In particular, SEHRS provides additional vibrational information due to the different selection rules acting in Raman and hyper Raman scattering,[236] and better insight into the structure and interaction of molecules on surfaces, as it is much more sensitive than SERS with respect to surface environmental changes.[24,25,27,83] Yet due to the extremely low HRS cross sections, plasmon enhancement of HRS in SEHRS has been typically combined with resonant enhancement for investigation of molecules with electronic transitions in the visible spectral range,[74,114,175] and so far non-resonant SEHRS spectra have been reported only for a very few molecules on silver substrates.[26,83,116] Understanding non-resonant SEHRS spectra would greatly benefit the spectroscopic characterization of complex biological materials as well as studies of molecule-metal interactions important in research areas such as catalysis and surface science.

In this chapter, SEHRS spectra of amino acids and aromatic thiols in the local fields of gold and silver nanoparticles using non-resonant excitation at 1064 nm will be presented. The SEHRS spectra will be compared with complementary one-photon excited SERS data from identical samples, and the observed variations in relative signal strengths of many molecular vibrations will be discussed in terms of the different selection rules for the one- and two-photon excited Raman process. Several examples pointing out the sensitivity of

SEHRS with respect to local environmental changes such as variation in pH and molecule concentration or interaction with different metal surfaces will be highlighted.

7.1 SEHRS of amino acids

Vibrational spectroscopy, such as Raman scattering, is one of the most important tools for the structure elucidation of amino acids as well as peptides and proteins.[237,238] For investigations in solution, Raman spectroscopy has often been combined with excitation in the UV to achieve resonance with electronic transitions in aromatic amino acids,[239–242] or surface enhanced Raman scattering (SERS) was employed to increase the Raman cross sections.[243,244]

Here, vibrational structural information of the amino acids tryptophan, histidine, phenylalanine, and tyrosine was obtained with SEHRS under non-resonant conditions using high repetition rate mode-locked picosecond excitation at 1064 nm. Figure 7.1 shows the chemical structures of the investigated molecules.

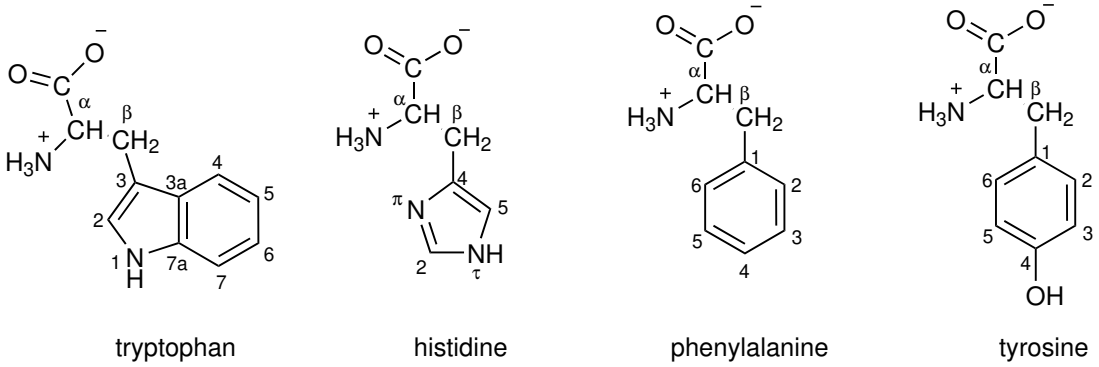

Figure 7.1: Structure and atom labelling for tryptophan (Trp), histidine (His), phenylalanine (Phe), and tyrosine (Tyr).

Taking into account that due to the non-resonant excitation, the experiment relies entirely on surface enhancement, the choice of plasmonic substrate plays a key role in the experiment. A transmission electron micrograph of the nearly spherical silver nanoparticles with an average size of 45 ± 10 nm that were used here, along with their UV-vis absorbance spectrum are displayed in Figure 7.2. As the electromagnetic enhancement in SEHRS is proportional to the absorbance at both the Stokes hyper-Raman wavelength (above 532 nm) and the wavelength of the excitation laser (1064 nm),[85] silver nanoaggregates were generated using magnesium sulfate. This increased the sample absorbance at 1064 nm significantly

(Figure 7.2, dashed line). It should be noted that SEHRS spectra could be measured only after aggregation of the nanoparticles with magnesium sulfate. One could assume that the magnesium and the sulfate ions can stabilize a high amount of nanoaggregates with optimum geometry and possibility of surface interaction of the amino acids, suitable for enhancing HRS at an excitation wavelength of 1064 nm. The background hyper Raman and Raman spectra of the silver nanoparticles and nanoaggregates are shown in Figure 7.3, and they do not exhibit any characteristic vibrational bands.

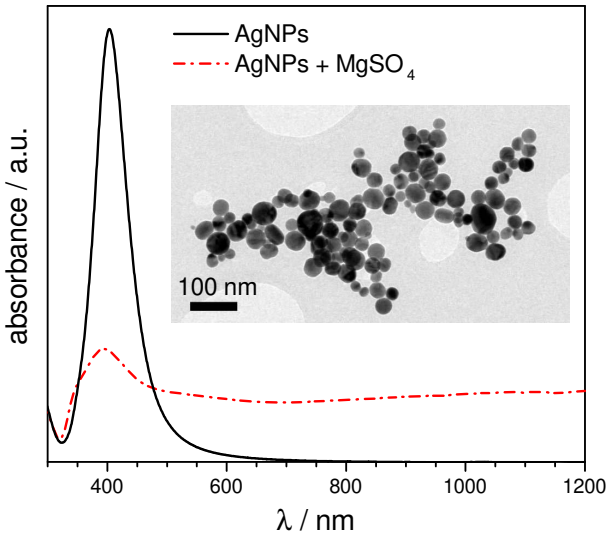

Figure 7.2: UV-vis absorbance spectra of the silver nanoparticles before (solid line) and after (dashed line) aggregation with magnesium sulfate ($MgSO_4$). The inset shows a transmission electron micrograph of the silver nanoparticles. Reprinted with permission from *J. Phys. Chem. C* 2017, 121, 2, 1235-1242. Copyright 2017 American Chemical Society.

7.1.1 Vibrational information from SEHRS spectra of phenylalanine, tryptophan, histidine and tyrosine

The SEHRS spectra of tryptophan, histidine, phenylalanine, and tyrosine obtained at 1064 nm excitation are shown in Figure 7.4A, together with the corresponding one-photon excited SERS data at 532 nm from the same samples (Figure 7.4B). All spectra discussed here were measured under basic pH in order to promote the interaction of the amino acids with the nanoparticle surface. Assignments of the SEHRS bands for each molecule based on previous SERS, UV-Raman and DFT work are proposed in Table 7.1, Table 7.2, Table 7.3, and Table 7.4. All molecules display very different SEHRS and SERS spectra (compare each spectrum from

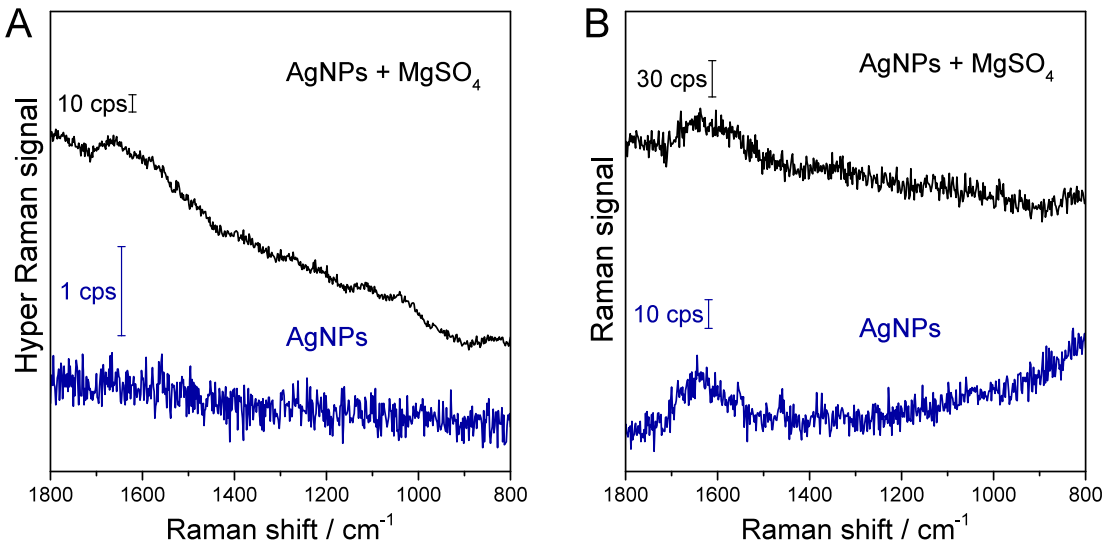

Figure 7.3: A) Hyper Raman and B) Raman spectra of the silver nanoparticles (blue) and silver nanoaggregates (black). Excitation: 1064 nm (A) and 532 nm (B); peak laser intensity: 6×10^9 W cm^{-2} (A) and 5×10^8 W cm^{-2} (B); acquisition time: 60 s (A) and 5 s (B). Reprinted with permission from *J. Phys. Chem. C* 2017, 121, 2, 1235-1242. Copyright 2017 American Chemical Society.

Figure 7.4A with the corresponding spectrum from Figure 7.4B), which can be explained by the different selection rules of the one- and two-photon excited Raman process.

In the tryptophan spectra (uppermost lines in Figure 7.4), several bands e.g. around 1620 cm^{-1}, 1580 cm^{-1} and 1552 cm^{-1} change their relative intensities (see also Table 7.1 for assignments). While the SEHRS spectrum of tryptophan is dominated by the band at 1552 cm^{-1}, its relative intensity is much smaller in the SERS spectrum (Figure 7.4, uppermost lines). In contrast, the asymmetric COO^- stretching vibration at 1620 cm^{-1} is relatively weak in the SEHRS spectrum of tryptophan, but very strong in the SERS spectrum (see the shoulder at 1619 cm^{-1}).

The most prominent differences between SEHRS and SERS are observed for the spectra of histidine and phenylalanine. The SEHRS spectrum of histidine (second line in Figure 7.4A) is dominated by three bands, those associated mainly with C=N and C−N stretching modes of the imidazole ring at 1578 cm^{-1} and 1047 cm^{-1}, respectively, and the strong band of the symmetric COO^- stretching vibration at 1394 cm^{-1} (see Table 7.2 for detailed band assignments). In contrast, the SERS data (second line in Figure 7.4B) lack this intense signal of the COO^- group, but have other strong contributions in the spectral region between 1100 cm^{-1} - 1600 cm^{-1}, represented by many overlapping bands, including those of the

C=C, C=N and C–CN stretching vibrations around 1629 cm^{-1}, 1573 cm^{-1}, and 1307 cm^{-1}, respectively (Table 7.2). Also the SEHRS spectrum of phenylalanine is clearly dominated by the symmetric COO^- stretching at 1389 cm^{-1} (third line in Figure 7.4A). In fact, pronounced contributions from the symmetric COO^- stretching mode are common for the SEHRS spectra of all four molecules: at 1355 cm^{-1} for tryptophan, at 1394 cm^{-1} for histidine, at 1389 cm^{-1} for phenylalanine, and at 1392 cm^{-1} for tyrosine. At alkaline pH, which was employed in the experiments reported here, the COO^- group probably plays an important role in the binding of the amino acids to the silver surface. This could explain the strong appearance of the COO^- group associated vibrational modes in the spectra.

The SERS spectrum of phenylalanine (third line in Figure 7.4B) exhibits very strong signals of the marker bands at 1599 cm^{-1} and 1001 cm^{-1}, assigned to the ring stretching and ring breathing modes, respectively (Table 7.3), which are less prominent in the SEHRS spectrum (third line in Figure 7.4A). In general, relatively weak signals of the ring breathing modes of the amino acids are common to all two-photon excited spectra displayed in Figure 7.4A. In contrast, in SERS, these bands are often used as Raman marker bands because of their high intensity.[245–248] Specifically in phenylalanine as mentioned above, only a very weak band in the SEHRS spectrum at 1002 cm^{-1} is observed (third line in Figure 7.4A), while the SERS signal at 1001 cm^{-1} is extremely strong (third line in Figure 7.4B). Also for tryptophan, the asymmetric ring breathing mode at 1011 cm^{-1} is missing in SEHRS, and the symmetric ring breathing mode at 760 cm^{-1} is greatly diminished (Figure 7.4, uppermost lines). In the case of tyrosine, the typical band around 850 cm^{-1}, containing the ring breathing mode,[249] shows very low contributions as a weak broad band around 860 cm^{-1} in the SERS spectrum (bottommost line in Figure 7.4B), and is not observed in the SEHRS spectrum (bottommost line in Figure 7.4A). The observations here are in agreement with those of previous SEHRS experiments with nucleic acid bases,[26] where the intensity of ring breathing modes is low as well. As was found for the ring breathing modes in the nucleic acids,[26] also the SEHRS spectra of the aromatic amino acids support their high similarity with the infrared data.[250]

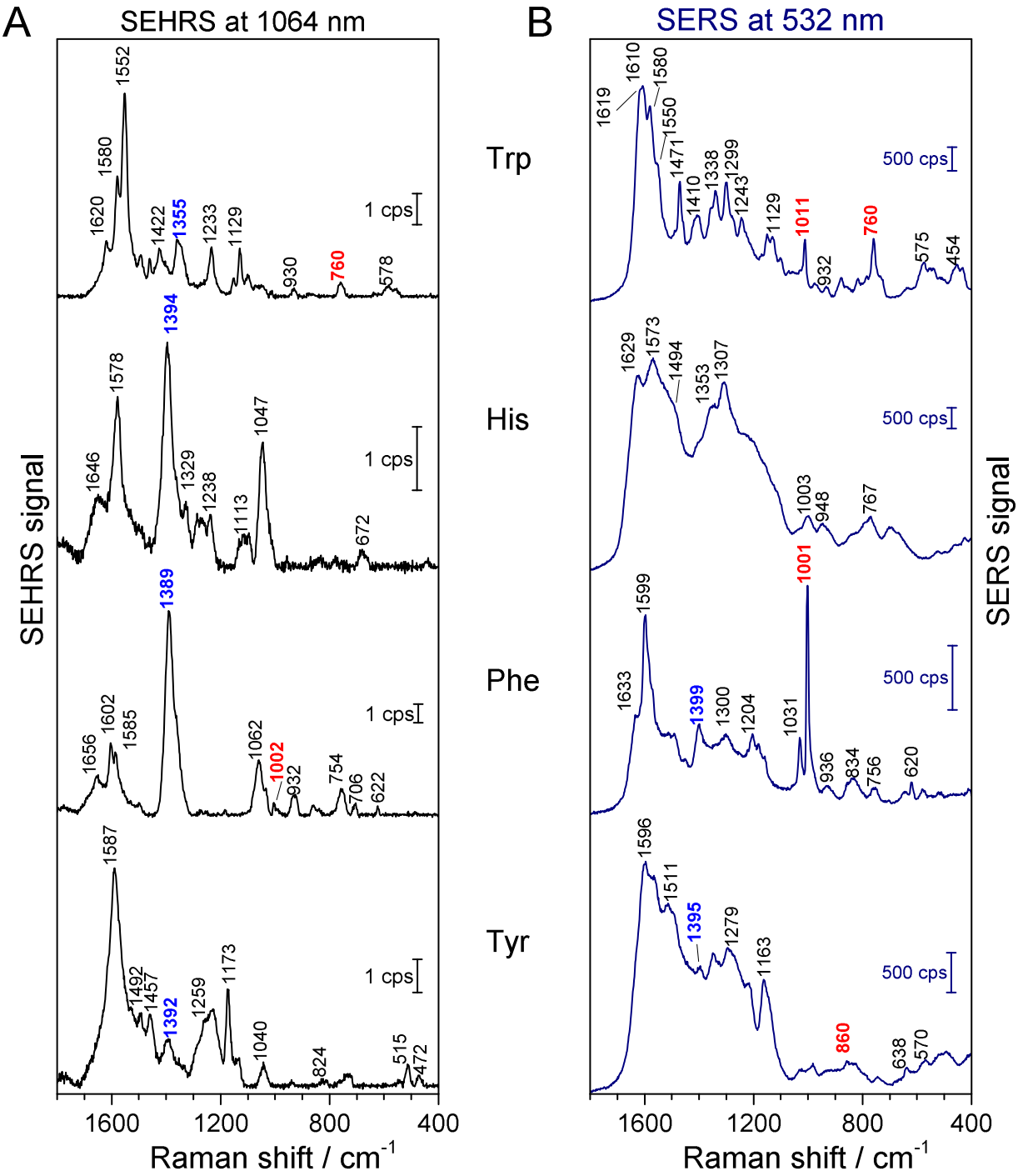

Figure 7.4: A) SEHRS spectra and B) SERS spectra of the amino acids tryptophan, histidine, phenylalanine, and tyrosine obtained with silver nanoaggregates. Bands marked in blue are assigned to vibrations of the COO^- group, and in red to the ring breathing modes (see Table 7.1, Table 7.2, Table 7.3, and Table 7.4). The SEHRS spectra are averages of 30, and are background-corrected. Excitation: 1064 nm (A) and 532 nm (B); laser intensity: 6×10^9 W cm^{-2} (pulsed, A) and 3×10^5 W cm^{-2} (CW, B); acquisition time: 60 s (A) and 5 s (B); concentration: 2×10^{-3} M; pH 10. Reprinted with permission from *J. Phys. Chem. C* 2017, 121, 2, 1235-1242. Copyright 2017 American Chemical Society.

Table 7.1: Raman shift values in the SEHRS and SERS spectra of tryptophan, and assignment to vibrations of the tryptophan molecule. Adapted with permission from *J. Phys. Chem. C* 2017, 121, 2, 1235-1242. Copyright 2017 American Chemical Society.

Raman shift / cm^{-1}		assignments[a]
SEHRS	SERS	
1620 m	-	asymm str COO^-,[251] R str[252]
-	1610 vs	R str,[251] r str[251]
1580 s	1580 s	NH_2 sciss,[251] R str,[251] r str[251,252]
1552 vs	1550 sh	R str,[251,252] r str[251,252]
1495	-	R, r str[251]
-	1471	CH_2 sciss[251]
1461	-	C^β bend[250]
1422	-	C-N-H(r) str[250]
1408 sh	1410	COO^- symm str[251]
1355	1355 sh	C-H bend,[251] r str[252,253]
-	1338	R, r str[251]
-	1299	CH_2 wag, CH bend[251]
-	1243	C^β twist[250]
1233	-	C-H(R, r) bend[251]
1153	1151	H(R) sciss,[251] R, r def,[253] N-H def[253]
1129	1129	C-H bend[251,253]
1098	1101	H(r) bend[251]
-	1011 m	R, r breathing[251–253]
-	973	H(R) twist[251]
930	932	C-COO^- str[251,254]
-	878	H(R, r) sciss,[251] N-H bend[253]
760 w	760 m	R, r breathing[251–253]
578	575	R, r def or N-H(r) bend[251]
-	549	C-COO^- asymm bend[250]
542	-	N-H(r) bend or R, r str[251]
-	454	R, r def[251]
-	433	R, r def or str[251]

[a] R, benzene ring; r, pyrrole ring; str, stretching; def, deformation; bend, bending (further categorized as sciss, scisscoring; wag, wagging; rock, rocking; twist, twisting); symm, symmetric; asymm, asymmetric; vs, very strong; s, strong; m, medium; w, weak, sh, shoulder;

Table 7.2: Raman shift values in the SEHRS and SERS spectra of histidine, and assignment to vibrations of the histidine molecule. Adapted with permission from *J. Phys. Chem. C* 2017, 121, 2, 1235-1242. Copyright 2017 American Chemical Society.

Raman shift / cm^{-1}		assignments[a]
SEHRS	SERS	
1646	-	
-	1629	R(C=C, C=N) str,[255] NH_2 def, asymm str COO^{-}[255]
1578 s	1573	R(C=C, C=N) str, N^{τ}-H bend[255]
-	1494	C^2-H bend,[255] N-H def[256]
1394 vs	-	N^{τ}-C^2=N^{π} str, COO^{-} str[255]
-	1353	CH_2 wagg,[255] R(C-N)[256]
1329	-	R(C-CN^{π}) str, R(C=N) str[256]
-	1307	R(C-CN) str, R(C-N) str,[256] R def[255]
1266	-	C-H def,[256] C-H bend[255]
1238	1238	C-H def + R(C-N) str, N^{τ}-C^2=N^{π} str + N-H def[256]
1113	-	C-N str, C-H def[256]
1047	-	C-N str[255]
-	1003	C-H def,[256] R def[255]
952	948	C-C str[255]
-	767	out-of-plane C-H bend[255]
672	-	ring def,[256] COO^{-} def[255]
-	528	COO^{-} def[255]

[a] R, imidazole ring; str, stretching; def, deformation; bend, bending; wag, wagging; symm, symmetric; asymm, asymmetric; vs, very strong; s, strong; m, medium; w, weak, sh, shoulder;

Table 7.3: Raman shift values in the SEHRS and SERS spectra of phenylalanine, and assignment to vibrations of the phenylalanine molecule. Adapted with permission from *J. Phys. Chem. C* 2017, 121, 2, 1235-1242. Copyright 2017 American Chemical Society.

Raman shift / cm^{-1}		assignments[a]
SEHRS	SERS	
1656	-	NH_2 asymm bend[250,257]
-	1633 sh	NH_2 asymm bend,[250] COO^- asymm str[250]
1602	1599	R str,[254,257–259] COO^- asymm str[259]
1585	1586 sh	R str[254,257,258]
-	1399	C^β rock,[250] COO^- symm str[250,254,259]
1389 vs	-	COO^- symm str[250,254,259]
-	1300	C-H, C-C vibrations[250,259]
-	1204	C(R)-C str,[252,253] C-C, C-C-H str,[250] NH_2 bend[259]
1062	-	C^α-N str, NH_2 bend,[250,254,258] C-CH_2 str[254]
1031 sh	1031 m	in-plane C-H(R) bend[252,259]
1002 w	1001 vs	R breathing,[253] C-C(R) str,[252,259] C-C-C bend[257]
932	936	C-COO^- str,[254,259] C-H bend[250]
860	857	C-H wag[250]
837	834	C-C str, C^α-N str[250]
754	756	COO^- def,[259] R breathing[257]
706	-	COO^- def[259]
622	620	R def,[258] R breathing[257]

[a] R, benzene ring; str, stretching; def, deformation; bend, bending; wag, wagging; symm, symmetric; asymm, asymmetric; vs, very strong; s, strong; m, medium; w, weak, sh, shoulder;

Table 7.4: Raman shift values in the SEHRS and SERS spectra of tyrosine, and assignment to vibrations of the tyrosine molecule. Adapted with permission from *J. Phys. Chem. C* 2017, 121, 2, 1235-1242. Copyright 2017 American Chemical Society.

Raman shift / cm^{-1}		assignments[a]
SEHRS	SERS	
-	1596	R str,[250,253] OH mode[254]
1587	-	
-	1566 sh	R str[250,253]
-	1511	NH_2 bend,[250] R str[253]
1492	1493 sh	C-H bend[249]
1457	-	C-C(R) str, C^4-O str,[253] C-C-H def[249]
1392	1395	COO^- symm str[254]
-	1346	C-C str, CH_2 rock[249]
-	1279	R str, C^4-O str[250,254]
1259	-	C^4-O-H,[250] C-C str[250]
-	1218	C-C str[250]
1173	-	C-C-H(R) str,[250] C-H(R) bend[253]
-	1163	NH_2 asymm rock, C-C-H(R) str[250]
1136	1140 sh	NH_2 asymm rock, C-C-H(R) str[250]
1040	-	CCC(R) str,[250] CCH(R) str[250]
-	1027	C-N str, NH_2 bend[250]
-	982	C^α-C^β , C-H wag[250]
-	859 vw	R breathing[253,254,258]
-	638	R def[249]
-	570	COO^-, C^α-C^τ, C^α-N modes[250]
515	521	
-	488	
472	-	

[a] R, benzene ring; str, stretching; def, deformation; bend, bending; wag, wagging; symm, symmetric; asymm, asymmetric; vs, very strong; s, strong; m, medium; w, weak, sh, shoulder;

7.1.2 Effects of local surface environmental changes on SEHRS spectra

As was shown for SEHRS spectra from other molecules, small differences in orientation[83] and in the interaction of organic molecules with surfaces of nanostructures, due to local surface environment changes[24,116] can lead to strong variation in the SEHRS spectra. Here, the concentration dependence of the SEHRS spectra of the amino acids was investigated in the range between 2×10^{-3} M and 1×10^{-4} M. Considering the concentration of nanoparticles and these concentrations of molecules, all non-resonant SEHRS experiments with the amino acids are carried out at relatively high surface concentration. Even at the lower concentrations of 10^{-4} M, all of the available surface of the silver nanostructures could be used up by interaction with the amino acid molecules.

For histidine and tyrosine, changes in the intensity ratios for some bands in the SEHRS and SERS spectra for relatively small differences in concentration (Figure 7.5 and Figure 7.6, respectively) were observed, while for tryptophan and phenylalanine the spectra did not show significant qualitative changes. In the case of histidine, decreasing the concentration from 2×10^{-3} M to 1×10^{-3} M induced shifts of the intensity ratios for some bands in both SEHRS (Figure 7.5A) and SERS spectra (Figure 7.5B). Lowering the histidine concentration significantly increased the intensity of the C−C stretching at 952 cm^{-1} and of the ring stretching at 1578 cm^{-1}, compared to the symmetric COO^- stretching band at 1394 cm^{-1} in the SEHRS spectrum (Figure 7.5A). In the SERS spectrum (Figure 7.5B), the intensity of the bands at 1629 cm^{-1}, associated also with ring stretching, and 1003 cm^{-1}, assigned to CH and ring deformations, was increased. These changes indicate a slightly different orientation of the probed molecules with respect to the metal surface.

Figure 7.6A presents the SEHRS spectra of tyrosine at concentrations of 2×10^{-3} M, 1×10^{-3} M, and 1×10^{-4} M. Comparing all intensities relative to the strong band at 1587 cm^{-1}, it can clearly be seen that reducing the tyrosine concentration by 50 % leads to a simultaneous increase of the band intensity at 1173 cm^{-1}, and to a decrease of the band intensities at 1457 cm^{-1} and at 1136 cm^{-1} (Figure 7.6A, top and middle lines). If the concentration is lowered further by one order of magnitude (Figure 7.6A, middle and bottom lines), the band at 1173 cm^{-1} rises further, and the bands at 1457 cm^{-1} and 1136 cm^{-1} disappear completely (Figure 7.6A, bottom line). As all these modes are associated with C−C and C−C−H vibrations of the ring (for details see Table 7.4), the changing intensities could indicate different orientation of the ring at different concentrations, which can be caused by steric

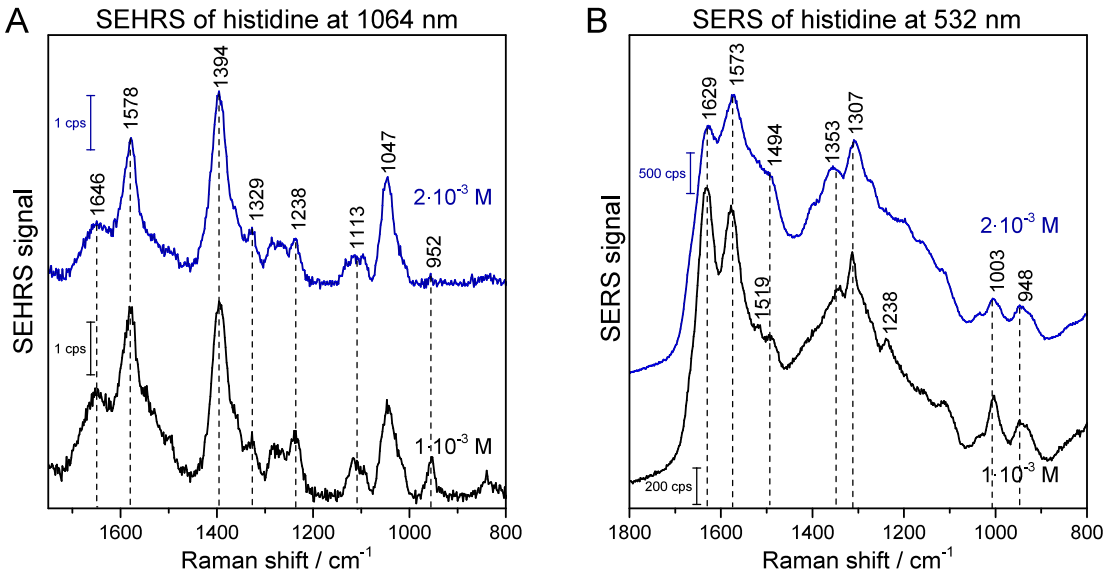

Figure 7.5: A) SEHRS spectra and B) SERS spectra of histidine at different concentrations. The SEHRS spectra are averages over 30, and are background-corrected. Excitation: 1064 nm (A) and 532 nm (B); laser intensity: 6×10^9 W cm^{-2} (pulsed, A) and 3×10^5 W cm^{-2} (CW, B); acquisition time: 60 s (A) and 5 s (B); concentration: 2×10^{-3} M (top blue lines) and 1×10^{-3} M (bottom black lines). Reprinted with permission from *J. Phys. Chem. C* 2017, 121, 2, 1235-1242. Copyright 2017 American Chemical Society.

effects. Interestingly, the SERS spectra from the identical samples (Figure 7.6B) do not show significant changes in bands associated with these vibrations for the three different concentrations though, e.g., the relative intensity at 1163 cm^{-1} ring stretching vibration remains constant (Figure 7.6B). The SERS spectra of 2×10^{-3} M and 1×10^{-3} M tyrosine (Figure 7.6B, top and middle lines) are almost identical. At a concentration of 1×10^{-4} M tyrosine (Figure 7.6B, bottom line), the shoulder of the band at 1596 cm^{-1} increases in intensity, suggesting a slight increase in contribution from a ring stretching vibration.

Considering that all experiments were performed at relatively high amino acid concentration, it is not so surprising that the SEHRS spectra and the SERS spectra of tryptophan and phenylalanine do not vary for the relatively small changes in concentration. Overall, the SEHRS spectra of histidine and tyrosine differ significantly, while their SERS spectra show only small differences. This observation is in accord with previous discussions,[24,83,116] and demonstrates that SEHRS can be much more sensitive than SERS to changes of the adsorbate geometry. The changes observed in the SEHRS spectra of histidine and tyrosine

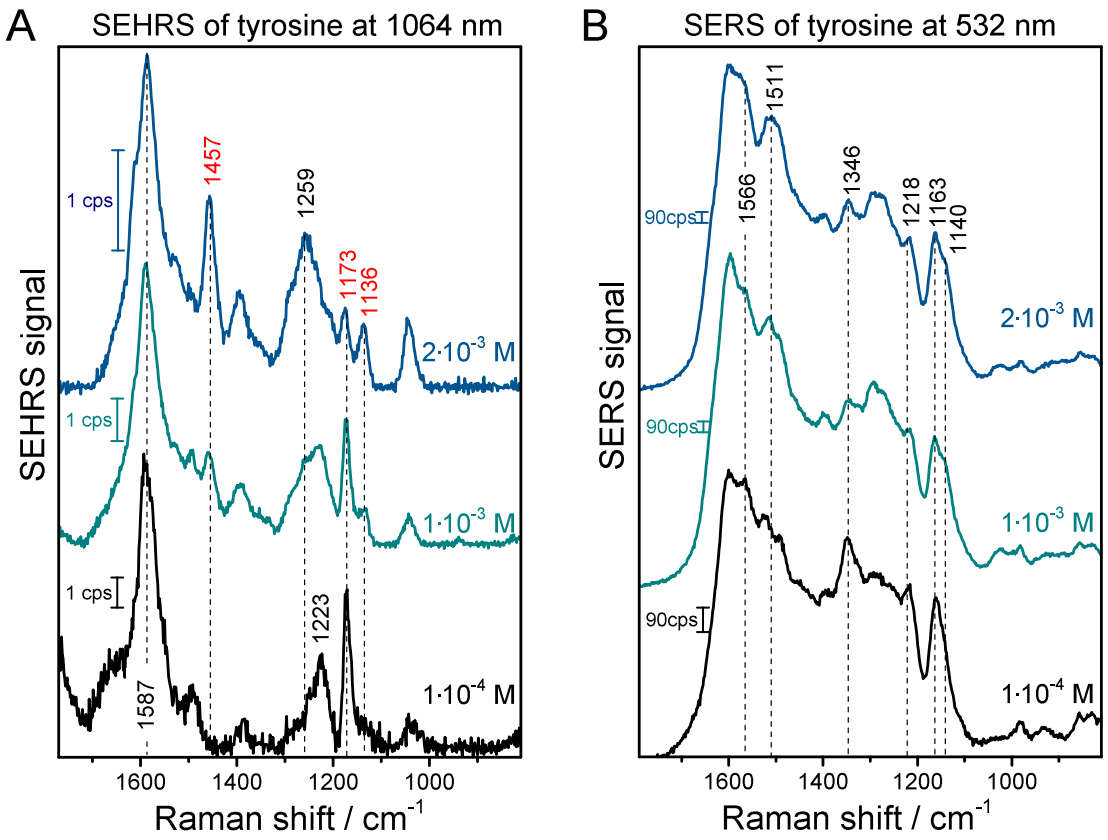

Figure 7.6: A) SEHRS spectra and B) SERS spectra of tyrosine at different concentrations. The SEHRS spectra are averages over 30, and are background-corrected. Excitation: 1064 nm (A) and 532 nm (B); laser intensity: 6×10^9 W cm^{-2} (pulsed, A) and 3×10^5 W cm^{-2} (CW, B); acquisition time: 60 s (A) and 5 s (B); concentration: 2×10^{-3} M (top blue lines), 1×10^{-3} M (middle green lines), and 1×10^{-4} M (bottom black lines). Reprinted with permission from *J. Phys. Chem. C* 2017, 121, 2, 1235-1242. Copyright 2017 American Chemical Society.

(Figure 7.5A and Figure 7.6A, respectively) indicate that the lower concentration of the molecules leads to a different interaction with the silver nanostructures.

From the aspect of probing the interaction of amino acids with the silver nanostructures, due to the different selectivity that leads to probing of different molecular species,[116] it is likely that SEHRS and SERS probe different parts of the sample. Within a silver nanoaggregate, different nanoscopic sites are responsible for high SEHRS and SERS enhancement.[25] Furthermore, in a nanostructure providing high SEHRS signals, a specific surface chemistry (e.g., surface coverage with magnesium and sulfate ions) can lead to different concentration dependence of the interaction of the tyrosine molecules than in aggregates that provide high SERS enhancement. The possibility to probe different sites of interaction between the amino acid molecules and parts of the silver nanostructures will have implications for

understanding the formation and composition of biomolecular coronae around nanoparticles in biological environments, which is mainly determined by adsorption of proteins and amino acids.[230,260] In addition to the stronger confinement of the field and the field gradients in electromagnetic enhancement of HRS,[261] also the chemical enhancement factor in SEHRS, that can greatly differ from that in SERS,[25] could contribute to the different sensitivity.

7.1.3 Background in SEHRS spectra

The raw SEHRS spectra of the amino acids exhibit strong background contributions that were found to correlate with the molecule surface concentration. This will be illustrated in the following using the example of tryptophan since its spectrum does not change qualitatively with varying concentration. Figure 7.7 shows tryptophan SEHRS spectra obtained at 1.7×10^{-4} M (black line), 3.3×10^{-4} M (brown line), and 1.0×10^{-3} M (red line) concentration using the same amount of silver nanoaggregates. As one can see from the data in Figure 7.7, the background contributions become less prominent with increasing tryptophan concentration.

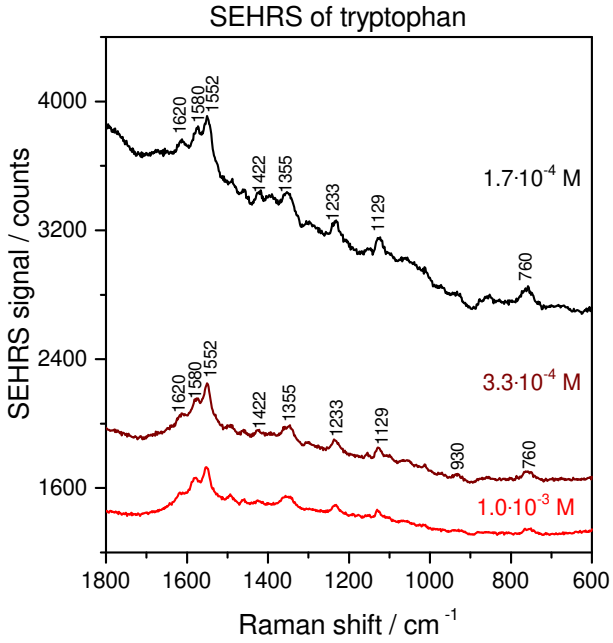

Figure 7.7: SEHRS spectra of tryptophan at different concentrations (averages of 30). Excitation: 1064 nm; peak laser intensity: 6×10^9 W cm^{-2}; acquisition time: 40 s; concentration: 1.7×10^{-4} M (black line), 3.3×10^{-4} M (brown line), and 1.0×10^{-3} M (red line).

SEHRS spectra of tryptophan were acquired using different amounts of silver nanoaggregates and the amino acid. The background in these spectra (the average signal between 1800-2000 cm^{-1} in photon counts) is plotted as a function of the theoretical surface coverage of the silver nanoparticles with tryptophan in Figure 7.8A. To estimate the surface coverage, it was assumed that the available surface in the nanoaggregates is similar as in the case of the non-aggregated silver nanoparticles, whose surface was calculated from their concentration that was determined from TEM data. The area occupied by one tryptophan molecule was set to 0.2 nm^2, considering that one crystal violet molecule occupies 0.4 nm^2.[156] The theoretical surface coverage is expected to be much higher than the real one since the equilibrium between adsorbed and free molecules in solution is not taken into consideration. The data presented in Figure 7.8A indicate that the background in SEHRS spectra depends strongly on the surface coverage, and the dependence is not linear. The background in the spectra decreases very fast with increasing surface coverage until it reaches a minimum value from which it does not change any more. This might be the point at which the real maximum coverage of the nanoaggregates' surface with tryptophan is reached. It should be noted that the hyper Raman spectra of the nanoaggregates without tryptophan exhibit even stronger background contributions, while for non-aggregated nanoparticles almost no background signal was observed (see Figure 7.3). Interestingly, the second harmonic generation (SHG) from identical samples (Figure 7.8B) shows exactly the same dependence on surface coverage as the background in SEHRS (Figure 7.8A). This implies that the properties of the silver nanoaggregates must be responsible for both the background in SEHRS and SHG, in accord with data obtained from silver nanovoid arrays discussed in Chapter 5. The influence of the nanoaggregates on the background in SEHRS has been suggested in previous discussions.[103,117] Therefore, the structural and/or plasmonic properties of nanoaggregates formed at high concentration of adsorbed tryptophan molecules must be responsible for lower background contributions and SHG signals. This could be in agreement with observations for one-photon SERS, where the background was discussed to be strongly correlated with adsorption of molecules.[262]

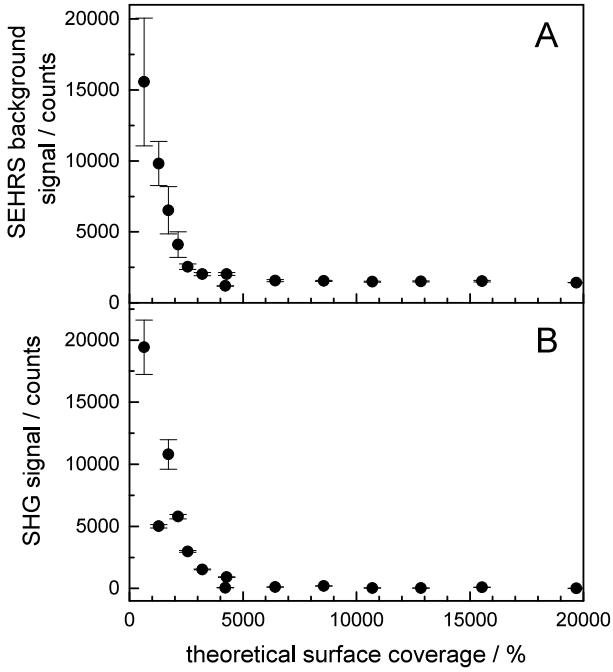

Figure 7.8: A) Background in SEHRS spectra of tryptophan as a function of the estimated surface coverage, and B) SHG signal from the identical samples. Excitation: 1064 nm; peak laser intensity: 6×10^9 W cm^{-2} (A) and 4×10^9 W cm^{-2} (B); acquisition time: 40 s (A) and 2 s (B).

7.2 SEHRS of aromatic thiols

Aromatic thiols, e.g. thiophenol or 4-aminothiophenol (4-ATP), can easily bind to the surface of gold or silver nanoparticles via the thiol group, and have served therefore often as model systems for understanding non-resonant SERS. Here, SEHRS spectra of thiophenol, benzyl mercaptan, and phenethyl mercaptan as well as 4-ATP, 3-ATP, and 2-ATP were measured at 1064 nm excitation. UV-vis spectra and TEM images of the citrate-stabilized gold and silver nanoparticles employed in the experiments are displayed in Figure 7.9. The silver particles prepared by the Lee and Meisel protocol[53] show a broad plasmon band with a maximum at 426 nm (Figure 7.9, green line), and they exhibit various shapes, including rod-like structures. This type of silver nanoparticles and their aggregates have been frequently used as SEHRS substrates. The gold nanoparticles produced by the citrate reduction method[54] exhibit a plasmon resonance at 541 nm (Figure 7.9, red line) corresponding to mostly spherical particles with an average size of ~50 nm. Utilizing aggregates formed by these gold nanostructures, which were shown to yield stronger SEHRS enhancement than aggregates of smaller gold particles (see Chapter 4), allowed the observation of non-resonant

SEHRS on gold nanosurfaces from tricyclic antidepressants,[200] and of the thiol molecules that will be discussed in the following. It should be noted that gold nanoparticles smaller in size, e.g. 30 nm, did not yield sufficient SEHRS enhancement in the non-resonant experiments.

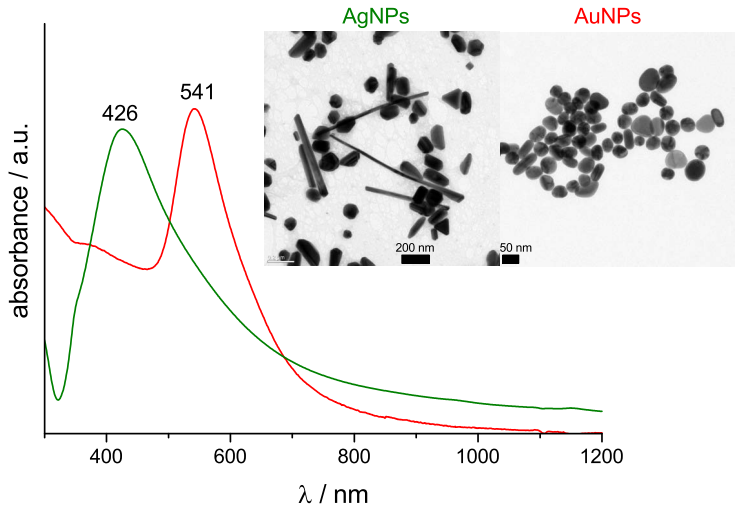

Figure 7.9: UV-vis absorbance spectra of citrate-stabilized silver (green) and gold (red) nanoparticles used in SEHRS experiments with aromatic thiols. The insets show transmission electron micrographs of the nanoparticles. The average size determined by TEM of the gold particles is 50 ± 10 nm, and of the silver particles is 115 ± 30 nm. Adapted with permission from *J. Phys. Chem. C* 2020, doi: 10.1021/acs.jpcc.0c00294. Copyright 2020 American Chemical Society.

7.2.1 SEHRS of thiophenol, benzyl mercaptan, and phenylethyl mercaptan on gold and silver nanoparticles

SEHRS spectra of thiophenol, benzyl mercaptan, and phenylethyl mercaptan were acquired using pulsed laser excitation at 1064 nm, and one-photon SERS spectra of identical samples were measured with continuous wave (CW) laser operating at 785 nm. The SEHRS spectra are shown in Figure 7.10A, Figure 7.11A, and Figure 7.12A, and the SERS spectra in Figure 7.10B, Figure 7.11B, and Figure 7.12B, blue lines correspond to data obtained with gold nanoparticles and red lines with silver nanoparticles. Lists with bands observed in the spectra of each molecule are provided in Table 7.5, Table 7.6, and Table 7.7, together with proposed band assignments based on previous Raman, SERS and DFT work,[263–266] and also on vibrational frequencies and Raman spectra of the respective molecule in the gas phase that were calculated within this work using DFT. The SEHRS spectrum of thiophenol (Figure 7.10A, red line) is in accord with the previously reported spectrum using 1550 nm

excitation.[267] The SERS spectra of thiophenol and benzyl mercaptan are consistent with the literature.[268] The SEHRS spectrum of benzyl mercaptan, and the SERS and SEHRS spectra of phenylethyl mercaptan have not been reported so far. Overall, the strongest SEHRS and SERS signals using the same excitation conditions were obtained from thiophenol, followed by benzyl mercaptan, and the weakest signals – from phenylethyl mercaptan (e.g. compare the scale bars in Figure 7.10A with those in Figure 7.11A and Figure 7.12A). The silver nanostructures yielded stronger enhancement than the gold nanostructures (compare the red and blue scale bars in each of the panels in Figure 7.10, Figure 7.11, and Figure 7.12).

First, general differences between SEHRS and SERS spectra of all three molecules will be discussed. While in the SERS spectra of all molecules (see Figure 7.10B, Figure 7.11B, and Figure 7.12B) the in plane bending modes of the phenyl ring around 1000-1100 cm^{-1} are the most prominent bands, in SEHRS (see Figure 7.10A, Figure 7.11A, and Figure 7.12A) the spectra are dominated by bands assigned to C-C stretching vibrations of the ring at 1573 cm^{-1} for thiophenol, 1600 cm^{-1} for benzyl mercaptan, and 1602 cm^{-1} for phenylethyl mercaptan. In accord with the discussion on SEHRS spectra of aromatic amino acids from Section 7.1, also here in the SEHRS spectra the ring breathing (C-C-C bending) modes at ~1000 cm^{-1} are greatly diminished compared to those in the one-photon spectra. Both SEHRS and SERS spectra of all three molecules show strong contributions from modes that include C-S stretching vibrations (bands marked in green in Figure 7.10, Figure 7.11, and Figure 7.12), especially the spectra obtained with silver nanoparticles (red lines). The SEHRS spectra of benzyl mercaptan and phenylethyl mercaptan (Figure 7.11B and Figure 7.12B) exhibit also bands that could be assigned to (Ph)C-C(alkyl chain) and CH_2 vibrations in the 1200-1230 cm^{-1} spectral range. For all three molecules, the not so strong out of plane ring deformation modes below 1000 cm^{-1} (see Table 7.5, Table 7.6, and Table 7.7) are more pronounced in the SERS spectra.

Interestingly, in the SEHRS spectrum of phenylethyl mercaptan on silver nanostructures (Figure 7.12A, red line) a strong contribution at 1015 cm^{-1} is observed, and on gold nanostructures (Figure 7.12A, blue line) this band appears as shoulder of the ring breathing at 1004 cm^{-1}. The band at 1015 cm^{-1} is assigned to C-C stretching of the ethyl group combined with C-S bending vibration because the DFT calculation indicates the existence of such mode between the strongly pronounced in plane C-H and in plane C-C-C bending (ring breathing) modes that are very characteristic for monosubstituted benzenes, and are present in the SERS spectra of phenylethyl mercaptan at 1030 cm^{-1} and 1002 cm^{-1}, respectively (Figure 7.12B). The DFT calculation shows also that this mode has low IR and Raman activity but its strong

contribution in the SEHRS spectra indicates that it might be a so-called silent mode, which can be observed neither in IR absorption nor in Raman scattering.

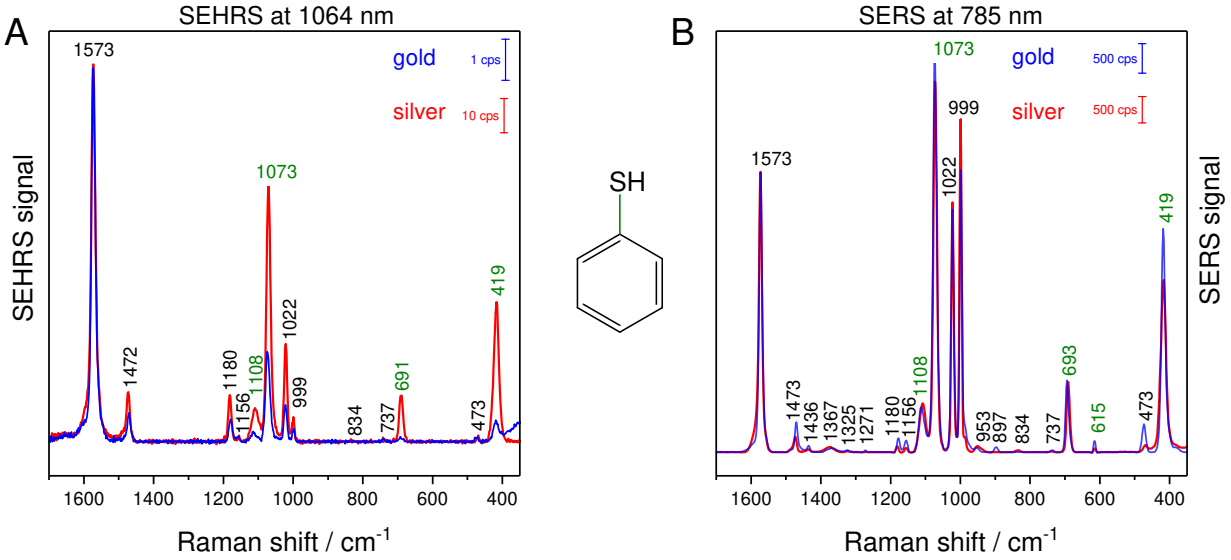

Figure 7.10: A) SEHRS spectra and B) SERS spectra of thiophenol with gold (blue lines) and silver (red lines) nanoparticles. The bands marked in green are associated with modes involving C-S vibrations. All spectra are averages of 30 single spectra, and are background-corrected. The spectra are normalized relative to the intensity of the band at 1573 cm^{-1}. Excitation: 1064 nm (A) and 785 nm (B); laser intensity in A: 4.5×10^9 W cm^{-2} (peak intensity) and in B: 4×10^5 W cm^{-2} (CW); acquisition time: 60 s (A, blue lines) and 10 s (A, red lines), and 1 s (B); concentration: 10^{-5} M. Adapted with permission from *J. Phys. Chem. C* 2020, doi: 10.1021/acs.jpcc.0c00294. Copyright 2020 American Chemical Society.

Taking a closer look at the differences of the spectra obtained with gold and silver nanostructures, both one- and two-photon excited spectra show more or less the same bands but they differ in relative intensities. To highlight the differences, the SEHRS and SERS spectra in Figure 7.10, Figure 7.11 and Figure 7.12 were normalized to the band of the symmetric C-C stretching vibration of the phenyl ring around 1600 cm^{-1} of each molecule. The most prominent changes when using the two kinds of plasmonic substrates occur in the SEHRS spectra of thiophenol (Figure 7.10). The intensity of all bands in its SEHRS spectrum with silver nanoparticles (Figure 7.10A, red line) decreases relative to the band at 1573 cm^{-1} when the spectrum is acquired with gold nanoparticles (Figure 7.10A, blue line). In particular, the bands at 1108 cm^{-1}, 1073 cm^{-1}, 691 cm^{-1} and 419 cm^{-1} that are associated with C-S vibrations and in plane C-C-C bending modes of the phenyl ring (see Table 7.5) become much less pronounced than other bands, e.g. the pure C-H bending at 1022 cm^{-1} and the ring breathing at

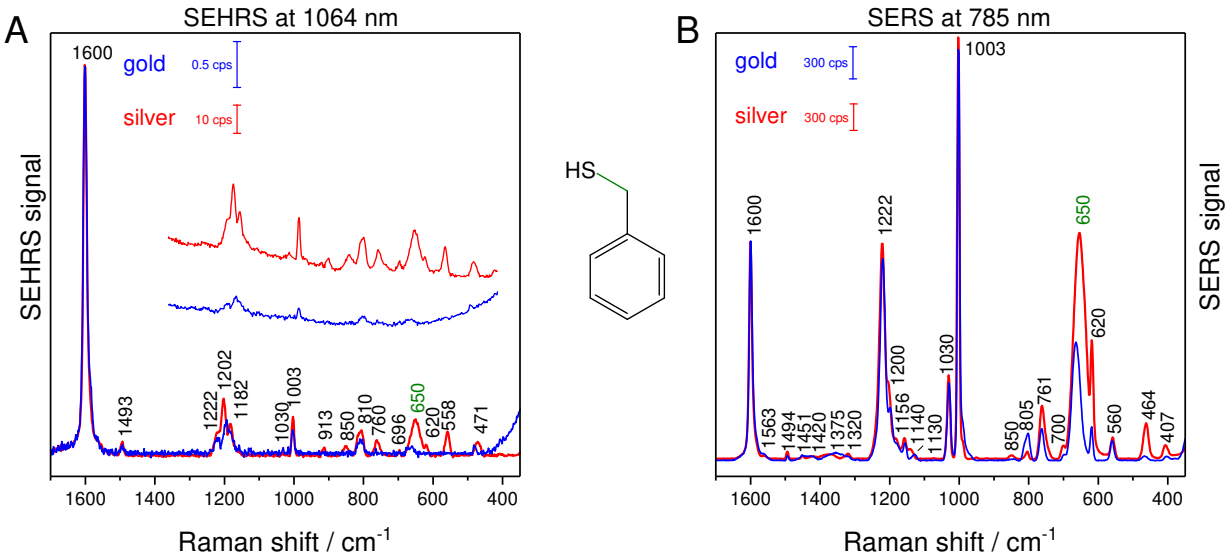

Figure 7.11: A) SEHRS spectra and B) SERS spectra of benzyl mercaptan with gold (blue lines) and silver (red lines) nanoparticles. The band marked in green is assigned to the C-S stretching. The inset in A shows the magnified not-corrected spectra in the range between 1400-400 cm^{-1}. All spectra are averages of 30 single spectra, and are background-corrected. The spectra are normalized relative to the intensity of the band at 1600 cm^{-1}. Excitation: 1064 nm (A) and 785 nm (B); laser intensity in A: 4.5×10^9 W cm^{-2} (peak intensity) and in B: 4×10^5 W cm^{-2} (CW); acquisition time: 60 s (A, blue lines) and 10 s (A, red lines), and 1 s (B); concentration: 10^{-5} M. Adapted with permission from *J. Phys. Chem. C* 2020, doi: 10.1021/acs.jpcc.0c00294. Copyright 2020 American Chemical Society.

999 cm^{-1}. Meanwhile, the SERS spectra of thiophenol with gold and silver nanoparticles are much more similar to each other than the respective SEHRS spectra (compare red and blue lines in Figure 7.10B and Figure 7.10A). Interestingly, the bands at 419 cm^{-1} and 1073 cm^{-1} involving C-S stretching modes in the SERS spectrum with gold particles are slightly more intense than with silver particles (compare red and blue line in Figure 7.10B), although in SEHRS the opposite was observed. These variations in band intensities in the spectra obtained with gold and silver nanostructures point to a different interaction of the thiophenol molecule with the nanoparticle surface, in accord with previous work based on SERS data suggesting that the azimuthal angle of rotation about the C_2 axis of the phenyl ring differs for gold and silver.[269] The spectral differences in SEHRS are more pronounced, which supports the obtained results from SEHRS of amino acids (see Section 7.1) and recent discussions[27] showing that SEHRS is more sensitive than SERS with respect to molecular orientation.

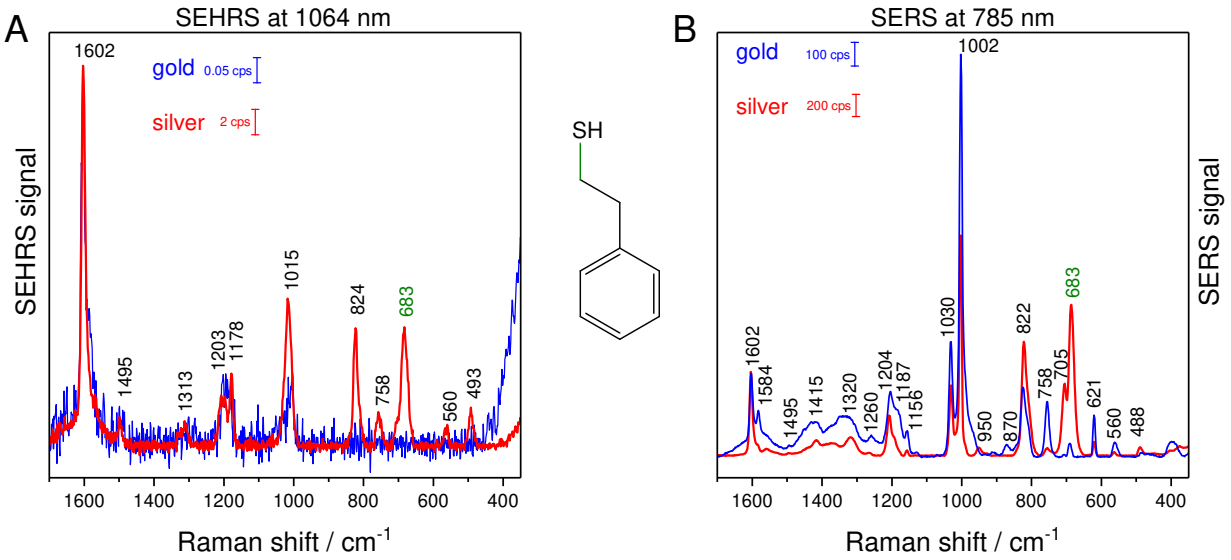

Figure 7.12: A) SEHRS spectra and B) SERS spectra of phenylethyl mercaptan with gold (blue lines) and silver (red lines) nanoparticles. The band marked in green is assigned to the C-S stretching. All spectra are averages of 30 single spectra, and are background-corrected. The spectra are normalized relative to the intensity of the band at 1602 cm^{-1}. Excitation: 1064 nm (A) and 785 nm (B); laser intensity in A: 4.5×10^9 W cm^{-2} (peak intensity) and in B: 4×10^5 W cm^{-2} (CW); acquisition time: 60 s (A, blue lines) and 10 s (A, red lines), and 1 s (B); concentration: 10^{-5} M. Adapted with permission from *J. Phys. Chem. C* 2020, doi: 10.1021/acs.jpcc.0c00294. Copyright 2020 American Chemical Society.

The SERS and SEHRS spectra of benzyl mercaptan (Figure 7.11) and phenylethyl mercaptan (Figure 7.12) on silver (red lines) also differ from the respective spectra obtained with gold nanoparticles (blue lines). In both SEHRS and SERS spectra, the bands at 650 cm^{-1} for benzyl mercaptan and at 683 cm^{-1} for phenylethyl mercaptan associated with C-S stretching vibrations are much more intense in the spectra with silver nanostructures. For phenylethyl mercaptan (Figure 7.12), the out of plane ring bending modes at 560 cm^{-1} and 758 cm^{-1} (see Table 7.7) are more pronounced in the SERS spectrum with gold nanoparticles (compare blue and red lines in Figure 7.12B) but are not observed in the respective SEHRS spectrum (Figure 7.12A, blue line). The SEHRS spectrum with silver nanoparticles (Figure 7.12A, red line) has contributions from the out of plane ring bending modes at 824 cm^{-1}, 758 cm^{-1}, 560 cm^{-1}, and 493 cm^{-1}. Additionally, the band at 1002 cm^{-1}, assigned to the ring breathing mode, is more intense in both SEHRS and SERS spectra with gold than in the spectra with silver nanoparticles. These differences between SEHRS and SERS spectra of benzyl mercaptan and phenylethyl mercaptan obtained with gold and silver nanostructures indicate

a different orientation and/or interaction of the molecules on gold and silver surfaces. The decreased intensity of bands associated with C-S vibrations in both SERS and SEHRS with gold nanoparticles, as well as different intensity ratios for some modes in the 950-800 cm^{-1} spectral region, where out of plane ring modes occur (see Figure 7.11B at 850 cm^{-1} and 805 cm^{-1}, and Figure 7.12B at 950 cm^{-1} and 870 cm^{-1} as well as Table 7.6 and Table 7.7), suggests that the orientation of the phenyl ring with respect to the metal surface should be different for gold and silver, in line with the discussion for thiophenol. Furthermore, it could point towards a direct interaction of the phenyl ring with the gold surface. This could be due to the different nature of the interaction between the thiols and gold/silver, but it might be also influenced by the amount and coverage of the different nanoparticles with the stabilizing and capping citrate molecules. The results obtained with benzyl mercaptan and phenylethyl mercaptan therefore demonstrate that the combination of SEHRS with SERS provides complementary vibration information suitable to identify the different interaction of the molecules with the two kinds of plasmonic substrates.

Table 7.5: Raman shift values in the SEHRS and SERS spectra of thiophenol, and proposed band assignment based on calculated vibrational frequencies and Raman spectra with DFT (Figure 7.16A), and refs 263,265. Adapted with permission from *J. Phys. Chem. C* 2020, doi: 10.1021/acs.jpcc.0c00294. Copyright 2020 American Chemical Society.

Raman shift / cm^{-1}				assignments[a]
SEHRS		SERS		
Ag	Au	Ag	Au	
1573	1573	1573	1573	symm i.p. C-C str
1472	1472	1474	1470	i.p. C-C str + C-H bend + C-S str
		1435	1435	i.p. C-C str + C-H bend + C-S bend
		1367	1367	i.p. C-H bend
		1325	1325	i.p. C-C str
		1271	1271	i.p. C-H bend
1181	1178	1176	1176	i.p. C-H bend
1156	1156	1156	1155	i.p. C-H bend
1108	1114	1108	1112	i.p. C-C-H bend + C-C-S bend
1073	1073	1073	1073	i.p. C-C-C bend + C-S str
1022	1022	1022	1022	i.p. C-H bend
999	999	999	998	i.p. C-C-C bend (ring breathing)
		953	953	o.o.p. C-C-H bend
		897	897	o.o.p. C-C-H bend
834		834	834	o.o.p. C-H bend
		737	737	o.o.p. C-H bend
693	693	691	695	i.p. C-C-C bend + C-S str
		615	615	i.p. C-C-C bend + C-S str
469	473	469	473	o.o.p. C-C-C bend
417	419	417	419	i.p. C-S str

[a] i.p., in plane; o.o.p., out of plane; str, stretching;
bend, bending (further categorized as wag, wagging; twist, twisting);

Table 7.6: Raman shift values in the SEHRS and SERS spectra of benzyl mercaptan, and proposed band assignment based on calculated vibrational frequencies and Raman spectra with DFT (Figure 7.16B), and refs 264,268. Adapted with permission from *J. Phys. Chem. C* 2020, doi: 10.1021/acs.jpcc.0c00294. Copyright 2020 American Chemical Society.

Raman shift / cm^{-1}				assignments[a]
SEHRS		SERS		
Ag	Au	Ag	Au	
1600	1600	1600	1600	symm i.p. C-C ring str
1563 sh	1563 sh	1563 sh	1563 sh	asymm i.p. ring C-C str + CH_2 twist
1493	1493	1494	1493	i.p. ring C-C-H bend
		1451	1451	CH_2 bend
		1420	1420	i.p. ring C-C-H bend and/or
		1375	1355	i.p. ring C-C str and/or
		1320	1320	CH_2 bend
1222 sh	1222 sh	1220	1222	CH_2 wag + C-C(Ph) str
1200	1196	1202 sh	1200 sh	C-C(Ph) str + CH_2 wag
1184 sh	1184 sh	1182 sh	1183 sh	i.p. ring C-H bend
		1156	1155	i.p. ring C-H bend
		1140	1130	i.p. ring C-H bend + CH_2 twist
1030	1032	1030	1030	i.p. ring C-H bend
1003	1003	1003	1001	i.p. ring C-C-C bend (ring breathing)
		950		o.o.p. ring C-H bend + S-C bend
913				o.o.p. ring C-H bend + S-C bend
850		850	850	o.o.p. ring C-H bend or asymm C-C-S str
810	810	805	805	o.o.p. ring C-H bend or asymm C-C-S str
760	760	761	762	o.o.p. ring C-H + ring C-C bend
696	696	700 sh	698 sh	o.o.p. ring C-H + ring C-C bend
650	667	655	664	C-S str
620		620	619	i.p. ring C-C bend
558		558	560	o.o.p. ring C-C-H bend
471	481	464	466	o.o.p. ring C-C-H bend
407		407	402	o.o.p. ring C-C-H bend

[a] i.p., in plane; o.o.p., out of plane; sh, shoulder; ring, phenyl ring; str, stretching; bend, bending (further categorized as wag, wagging; twist, twisting);

Table 7.7: Raman shift values in the SEHRS and SERS spectra of phenylethyl mercaptan, and proposed band assignment based on calculated vibrational frequencies and Raman spectra with DFT (Figure 7.16C), and ref 266. Adapted with permission from *J. Phys. Chem. C* 2020, doi: 10.1021/acs.jpcc.0c00294. Copyright 2020 American Chemical Society.

Raman shift / cm^{-1}				assignments[a]
SEHRS		SERS		
Ag	Au	Ag	Au	
1602	1602	1602	1602	symm i.p. C-C ring str
1584 sh	1584 sh	1584	1583	asymm i.p. C-C ring str + CH_2 twist
		1557		i.p. C-C-H ring bend
1497	1495	1495	1495	CH_2 bend + i.p. ring C-C-H bend
		1415	1415	CH_2 bend + i.p. ring C-C-H bend
		1373	1373	CH_2 bend + i.p. ring C-C-H bend
			1335 br	CH_2 bend + i.p. ring C-C-H bend
1313		1320		CH_2 bend + i.p. ring str
		1264	1260	(Ph)C-C(Et) bend
1203	1203	1204	1204	(Ph)C-C(Et) str
1178	1193	1190 sh	1187 sh	i.p. ring C-H bend
		1156	1156	i.p. ring C-H bend + CH_2 twist
		1030	1030	i.p. ring C-H bend
1015	1016 sh			i.p. ring C-C bend + C-C (alkyl) str + S-C bend
	1004	1002	1002	i.p. ring C-C-C bend (ring breathing)
		950		o.o.p. ring C-H bend or asymm C-C-S str
		908	908	o.o.p. ring C-H bend or asymm C-C-S str
			870	o.o.p. ring C-H bend or asymm C-C-S str
824		822	822	o.o.p. ring C-H bend
758		758	756	o.o.p. ring C-H bend
		705	707	i.p. ring C-C-H bend
683		683	685	S-C str
		621	621	o.o.p. ring C-C-H bend
560		560	558	o.o.p. ring C-C-H bend
493		488	488	o.o.p. ring bend + CH_2 bend
		403	397	o.o.p. ring bend + CH_2 bend

[a] i.p., in plane; o.o.p., out of plane; sh, shoulder; ring, phenyl ring; str, stretching; bend, bending (further categorized as wag, wagging; twist, twisting);

7.2.2 SEHRS spectra of aminothiophenols and the influence of pH

SEHRS spectra of 4-aminothiophenol (4-ATP), 2-aminothiophenol (2-ATP), and 3-aminothiophenol (3-ATP) at 1064 nm were obtained with gold nanostructures at three different pH values, and are shown in Figure 7.13A, Figure 7.14A, and Figure 7.15A, respectively. SERS spectra from identical samples at 633 nm excitation are presented in Figure 7.13B, Figure 7.14B, and Figure 7.15B. To facilitate the comparison of pH effects, all spectra were normalized to the intensity of the band at 1570-1580 cm^{-1} of each molecule. Assignments for some of the bands observed in the spectra are proposed in Table 7.8. The SERS spectra of 4-ATP (Figure 7.13B) and 2-ATP (Figure 7.14B) are in agreement with previously reported spectra from the literature.[270,271] The SEHRS spectra of 2-ATP, 3-ATP, and 4-ATP as well as the SERS spectrum of 3-ATP have not been reported so far. 4-ATP yielded stronger signals in both one- and two-photon experiments compared to 3-ATP and 2-ATP (e.g. compare the scale bars in Figure 7.13A with those in Figure 7.14A and Figure 7.15A).

The SEHRS spectra of 4-ATP under acidic conditions (Figure 7.13A, black and red lines) show strong contributions from the symmetric C-C stretching of the phenyl ring combined with the symmetric NH_2 bending at 1588 cm^{-1} (see Table 7.8) and the C-S stretching combined with C-C-C bending mode of the ring at 1076 cm^{-1}, which are also very strong in the SERS spectra (Figure 7.13B, black and red lines). Furthermore, bands associated with in plane ring bending modes that include C-S stretching vibrations at 1484 cm^{-1}, 633 cm^{-1}, and 388 cm^{-1} are observed in both one- and two-photon excited spectra. In SEHRS, the intensities of the bands at 1484 cm^{-1}, 1178 cm^{-1}, 1076 cm^{-1}, and 633 cm^{-1} decrease significantly with increasing pH (compare black, red, and blue lines in Figure 7.13A). This can be associated with changes in the degree of the protonation of 4-ATP since for pH values below 4 most of the amino groups are protonated.[272] The SERS spectrum of 4-ATP at pH 13 (Figure 7.13B, blue line) is very different compared to the spectra obtained at acidic pH (Figure 7.13B, black and red lines). Particularly, several new bands are observed in the spectral range between 1100-1500 cm^{-1}, e.g. at 1447 cm^{-1}, 1385 cm^{-1}, and 1143 cm^{-1}. The same bands were found in the SERS spectrum of 4-ATP in basic environment on gold nanoparticles using 633 nm excitation,[273] and were proven to arise from the product of the plasmon assisted catalytic dimerization of 4-ATP to 4,4'-dimercaptoazobenzene (4,4'-DMAB).[273,274] In the SEHRS spectrum at pH 13 (Figure 7.13A, blue line) none of the bands associated with 4,4'-

DMAB vibrations are present. However, the absence of 4,4′-DMAB bands in the SEHRS spectrum is not sufficient to conclude that at 1064 nm the dimerization does not take place.

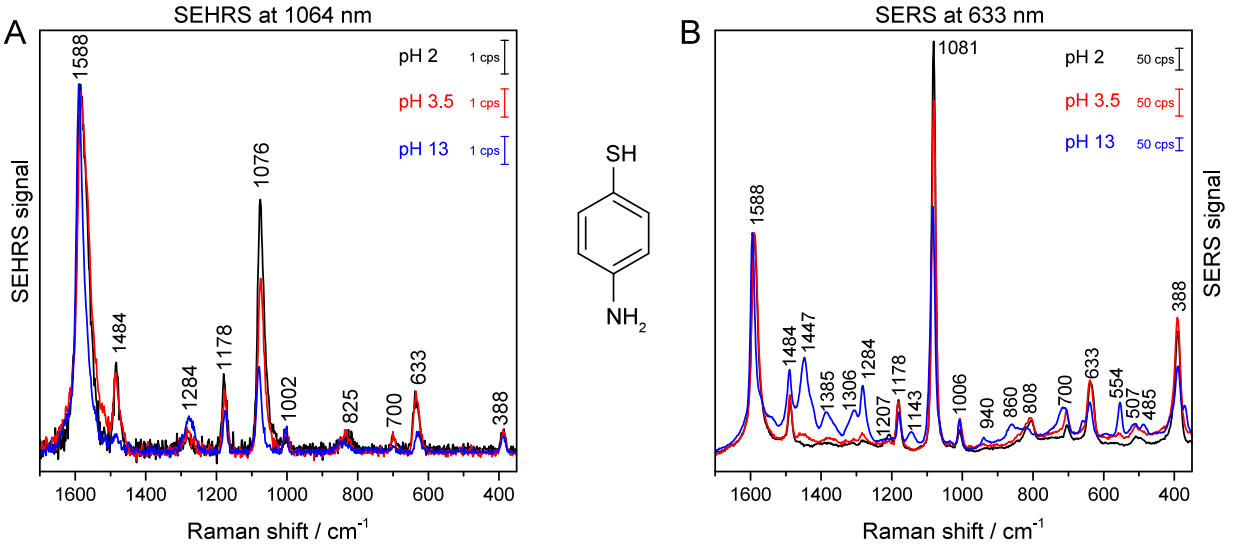

Figure 7.13: A) SEHRS spectra and B) SERS spectra of 4-aminothiophenol (4-ATP) obtained with gold nanoparticles at pH 2 (black lines), 3.5 (red lines), and 13 (blue lines). The SEHRS spectra are averaged and background-corrected. The spectra are normalized relative to the intensity of the band at 1588 cm^{-1}. Excitation: 1064 nm (A) and 633 nm (B); laser intensity in A: 6×10^9 W cm^{-2} (peak intensity) and in B: 1×10^5 W cm^{-2} (CW); acquisition time: 60 s (A) and 1 s (B); concentration: 8.3×10^{-6} M. Adapted with permission from *J. Phys. Chem. C* 2020, doi: 10.1021/acs.jpcc.0c00294. Copyright 2020 American Chemical Society.

The SEHRS spectra of 2-ATP (Figure 7.14A) and 3-ATP (Figure 7.15A) are clearly dominated by the symmetric C-C stretching and symmetric NH_2 bending mode at 1564 cm^{-1} for 2-ATP and at 1575 cm^{-1} for 3-ATP (see Table 7.8). The contributions of the second symmetric NH_2 bending combined with symmetric C-C stretching mode at 1581 cm^{-1} for 2-ATP and at 1600 cm^{-1} for 3-ATP become more prominent under acidic pH in both SEHRS and SERS spectra (compare black and blue lines in Figure 7.14A and B or Figure 7.15A and B). Bands assigned to modes including asymmetric NH_2 bending vibrations (see Table 7.8) are more pronounced in the SEHRS spectra of 2-ATP at 1092 cm^{-1} (Figure 7.14A, black line) and of 3-ATP at 1033 cm^{-1} (Figure 7.15A, black line) at pH 2 than at pH 3.5 or 13. However, more visible changes with varying pH are found in the one-photon SERS spectra of 2-ATP (Figure 7.14B) and 3-ATP (Figure 7.15B) than in the respective two-photon spectra, because of the very low signal to noise ratio. For example, the relative intensities of the bands

at 815 cm^{-1} and 838 cm^{-1} for 2-ATP and at 864 cm^{-1} and 884 cm^{-1} for 3-ATP are reversed (compare black, red, and blue lines in Figure 7.14B and Figure 7.15B).

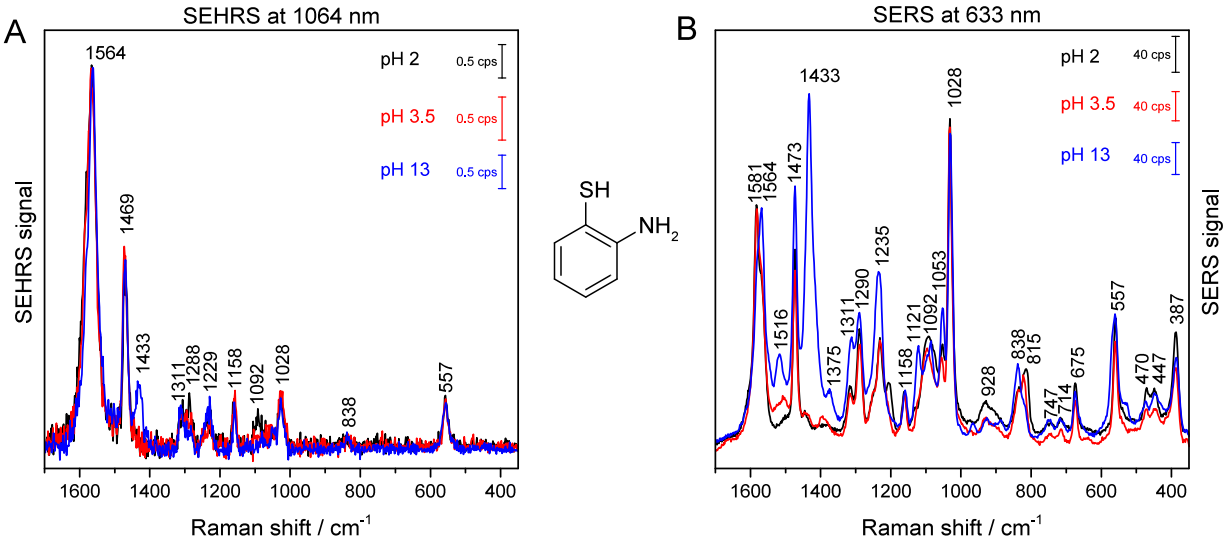

Figure 7.14: A) SEHRS spectra and B) SERS spectra of 2-aminothiophenol (2-ATP) obtained with gold nanoparticles at pH 2 (black lines), 3.5 (red lines), and 13 (blue lines). The SEHRS spectra are averaged and background-corrected. The spectra are normalized relative to the intensity of the band at 1564 cm^{-1}. Excitation: 1064 nm (A) and 633 nm (B); laser intensity in A: 6×10^9 W cm^{-2} (peak intensity) and in B: 1×10^5 W cm^{-2} (CW); acquisition time: 60 s (A) and 1 s (B); concentration: 8.3×10^{-6} M. Adapted with permission from *J. Phys. Chem. C* 2020, doi: 10.1021/acs.jpcc.0c00294. Copyright 2020 American Chemical Society.

Similar to 4-ATP, the SERS spectrum of 2-ATP at pH 13 (Figure 7.14B, blue line) shows contributions from new modes at 1433 cm^{-1}, 1375 cm^{-1}, and 1121 cm^{-1} that are absent in the spectra obtained under acidic conditions (Figure 7.14B, black and red lines). This indicates that also 2-ATP undergoes a dimerization reaction at the given excitation conditions. Moreover, the band associated with N=N stretching of the dimerization product is much more intense in the SERS spectrum of 2-ATP than in the SERS spectrum of 4-ATP (compare blue lines in Figure 7.13B and Figure 7.14B), and this band is observed in the SEHRS spectrum of 2-ATP at pH 13 as well (Figure 7.14A, blue line). The latter indicates that 2-ATP might be more reactive than 4-ATP and its dimerization could occur also when using 1064 nm laser excitation. Meanwhile, the SERS and SEHRS spectra of 3-ATP at pH 13 do not exhibit any new peaks compared to the spectra at pH 2 and 3.5 (Figure 7.15). It is expected that dimerization of 3-ATP does not occur at pH 2, thus probably all spectra from Figure 7.15 were acquired at conditions where

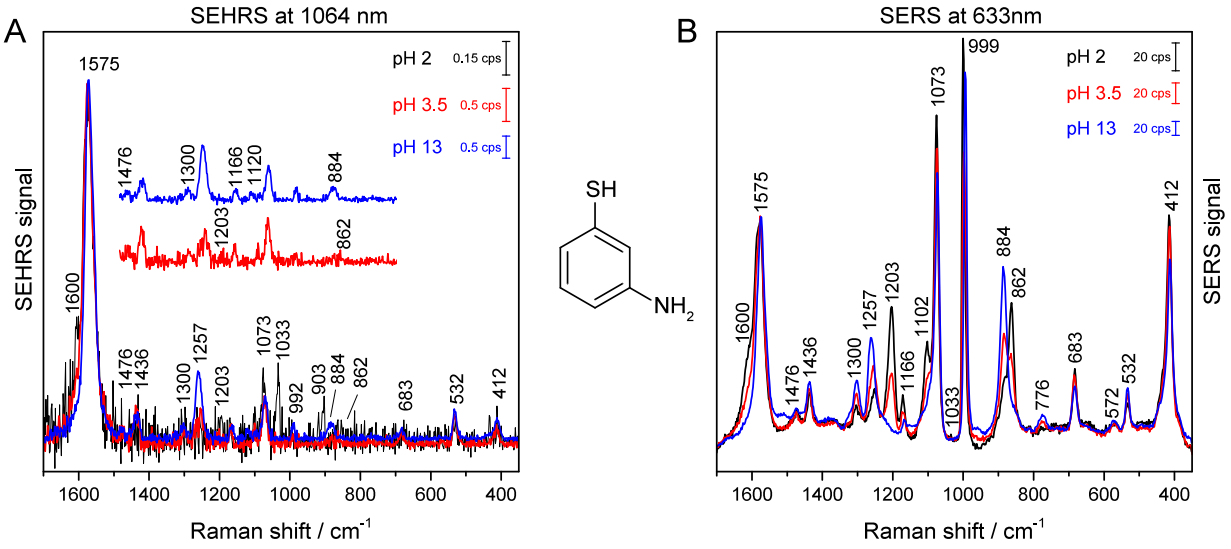

Figure 7.15: A) SEHRS spectra and B) SERS spectra of 3-aminothiophenol (3-ATP) obtained with gold nanoparticles at pH 2 (black lines), 3.5 (red lines), and 13 (blue lines). The SEHRS spectra are averaged and background-corrected. The inset in A shows the magnified spectra at pH 3.5 and 13 in the range between 1500-700 cm^{-1}. The spectra are normalized relative to the intensity of the band at 1575 cm^{-1}. Excitation: 1064 nm (A) and 633 nm (B); laser intensity in A: 6×10^9 W cm^{-2} (peak intensity) and in B: 1×10^5 W cm^{-2} (CW); acquisition time: 60 s (A) and 1 s (B); concentration: 8.3×10^{-6} M. Adapted with permission from *J. Phys. Chem. C* 2020, doi: 10.1021/acs.jpcc.0c00294. Copyright 2020 American Chemical Society.

only the monomers are present. The spectral differences, in particular the band at 1203 cm^{-1} associated with an in plane C-H bending mode that disappears at pH 13 (e.g. compare red and blue lines in Figure 7.15B and in the inset in Figure 7.15A), must be due to a different protonation state and/or different orientation with respect to the gold nanoparticle surface.

The data obtained here from aminothiophenols show that SEHRS and SERS can be used to monitor structural changes of the analyte molecules that arise due to variation of pH in the local environment. In particular, the combination of SEHRS with SERS excited at different laser wavelengths could be very beneficial for investigation of systems where plasmon-assisted reactions may occur at one of the excitation wavelengths, and thus different molecular species can be probed by SEHRS and SERS.

Table 7.8: Raman shift values in the spectra of 2-ATP, 3-ATP, and 4-ATP, and proposed band assignment based on refs 271,274–277 and calculated frequencies of the molecules in the gas phase with DFT (Figure 7.16D-F). Adapted with permission from *J. Phys. Chem. C* 2020, doi: 10.1021/acs.jpcc.0c00294. Copyright 2020 American Chemical Society.

Raman shift / cm^{-1}			assignments[a]
2-ATP	3-ATP	4-ATP	
1581	1600	1595	symm NH_2 bend + symm C-C str
1564	1575	1588	symm C-C str + symm NH_2 bend
		1484	i.p. C-C-H bend + C-S and C-N str
1469	1436		i.p. C-C str + i.p. C-H bend
1313	1300		C-N str + C-C bend
1290	1257	1284	C-N str + C-C bend
1229	1203	1179	i.p. C-H bend
1158	1166		i.p. C-H bend
1092			asymm NH_2 bend + C-S str
		1076	C-S str + i.p. C-C-C bend
	1073		C-S str + i.p. C-H bend
1053			i.p. C-H bend
	1033		i.p. C-H bend + asymm NH_2 bend
1028			i.p. C-C-C bend (ring breathing)
		1002	i.p. C-C-C bend + C-S str
	999		i.p. C-C-C bend (ring breathing)
	884		i.p. C-C-C bend + C-N str
	862		i.p. C-C-C bend + C-N str
838			
815			
		810	i.p. C-C-C bend + C-S str + C-N str (ring breathing)
	683		C-C bend + C-S str
557		633	i.p. C-C-C bend + C-S str
	532		i.p. C-C bend + o.o.p. NH_2 bend
387	415		i.p. C-S bend
		390	i.p. C-C(S)-C bend + C-S str + C-C(N)-C bend
1433		1447	N=N str of dimerization product
1375		1385	N=N str of dimerization product
1121		1143	C-N str of dimerization product

[a] i.p., in plane; o.o.p., out of plane; str, stretching; bend, bending; symm, symmetric; asymm, asymmetric;

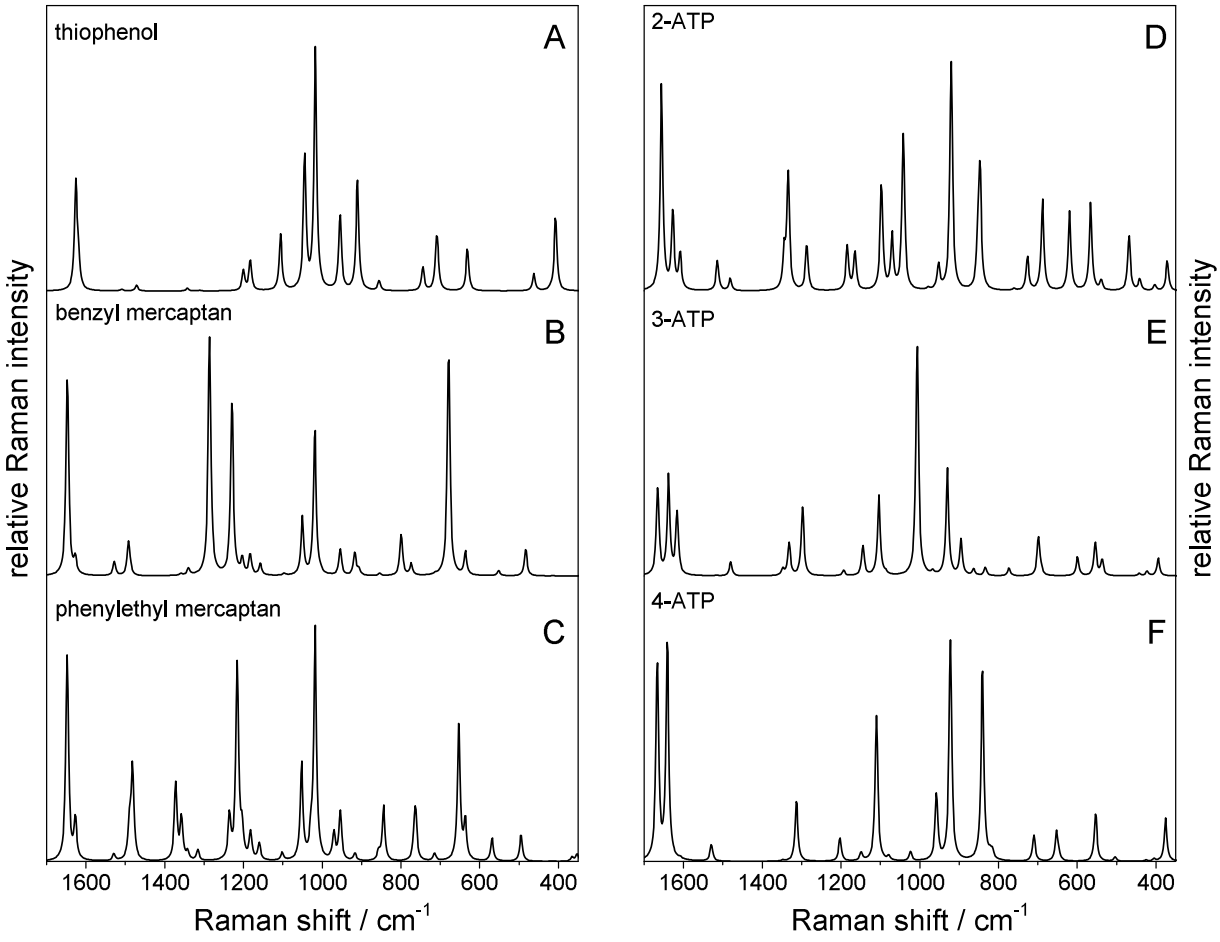

Figure 7.16: Calculated Raman spectra of A) thiophenol, B) benzyl mercaptan, C) phenylethyl mercaptan, D) 2-ATP, E) 3-ATP, and F) 4-ATP in the gas phase at 785 nm (A, B, C) and 633 nm (D, E, F) with DFT using the B3LYP functional and 6-311G** basis set. The spectra differ from the SERS spectra because the experimental data were obtained in solution, the influence of the metal surface is not considered, and the molecules bind to the surface under deprotonation. Nevertheless, the DFT calculations provide comprehensive description of all vibrational modes, and were used to improve the band assignment in cases where information from the existing literature was not sufficient. Reprinted with permission from *J. Phys. Chem. C* 2020, doi: 10.1021/acs.jpcc.0c00294. Copyright 2020 American Chemical Society.

7.3 Conclusions

The work presented in this chapter significantly expands the variety of molecular structures that were characterized by means of SEHRS so far. Non-resonant SEHRS spectra at 1064 nm excitation of the amino acids tryptophan, histidine, phenylalanine, and tyrosine as well as several aromatic thiols using aggregates of gold and silver nanoparticles are reported for the first time. Comparing the SEHRS data with SERS spectra from the identical samples, differences between the spectra provide evidence of the complementarity of both types of vibrational spectral information. As an example of the different selection rules acting in SEHRS and SERS, the ring breathing modes (in plane C-C-C bending vibrations) in the SEHRS spectra are much weaker than in the SERS spectra or even absent, which is in agreement with previous combined SEHRS/SERS studies of nucleobases.[26] Meanwhile, in plane symmetric C-C stretching vibrations of the phenyl ring show very strong contributions in SEHRS. Bands assigned to the functional groups that are expected to interact with the metal surface, such as the carboxyl group in amino acids and the thiol group in aromatic thiols, are very prominent in the SEHRS spectra as well. Moreover, SEHRS spectra can reveal silent modes that are not visible in IR or Raman spectroscopy as indicated by the example of phenylethyl mercaptan.

In particular, the results strongly suggest SEHRS as a tool to probe interactions of organic and bioorganic molecules with nanoparticles under varied environmental conditions, specifically, since different interaction sites and/or different interacting molecular species can be probed when using both SEHRS and SERS as complementary approaches. For instance, changes in the SEHRS spectra of histidine and tyrosine upon small variation of amino acid concentration were more pronounced in SEHRS than in the corresponding SERS data. These spectral changes can be understood in terms of differences in the orientation of the molecules on the nanostructure. The SEHRS spectra of thiophenol, benzyl mercaptan, and phenylethyl mercaptan obtained with silver particles show significant changes when gold nanostructures are used instead, thus pointing towards a different interaction with the two kinds of plasmonic substrates. The experiments with aminothiophenols demonstrate that the combination of SEHRS and SERS can be used to probe structural changes occurring at different pH. From a general perspective, the high sensitivity of the SEHRS spectra with respect to surface environmental changes can help to improve the understanding of molecule-nanostructure interactions, and consequent phenomena, including SERS. In conclusion, this

work reveals new biospectroscopic and analytical applications for SEHRS, which can be exploited in future investigations involving more complex systems.

Chapter 8

Summary and outlook

The main scope of this thesis was to assess the enhancement of the incoherent, two-photon exited process of hyper Raman scattering (HRS). Surface enhanced hyper Raman scattering (SEHRS) experiments probing either the plasmonic enhancement of different nanostructures or the vibrational signatures of molecules on nanosurfaces were discussed, and the data were complemented with information based on the non-linear process of second harmonic generation (SHG) and one-photon excited surface enhanced Raman scattering (SERS).

Gold nanoparticles, which have been scarcely used as SEHRS substrates so far, were shown here to provide efficient plasmonic enhancement of HRS. The results indicate that the enhancement depends on the particle size and shape with higher values for large particles as well as on their spatial arrangement in nanoaggregate structures, which is required to ensure the strong signal amplification. Both experiments and numerical simulations showed that local field enhancements at the near-IR excitation wavelength, due to plasmon resonances and/or the lightning rod effect, contribute more significantly to the total SEHRS enhancement than the near-fields at the visible HRS frequency. The possibility to obtain high local field enhancement with gold nanostructures will enable new analytical SEHRS applications since gold provides properties different from silver, e.g. biocompatibility and stability.

Aspects such as homogeneity of the SEHRS signal, reproducibility in terms of substrate fabrication, and stability were addressed in this work by employing metal films comprised of periodically arranged voids that have been previously shown to provide enhancement in SERS. As part of their consideration as substrates for analytical SEHRS applications, the plasmonic properties of gold and silver nanovoid arrays were investigated by SHG. Combined SHG/SEHRS measurements of nanovoids with different sizes and depths revealed that voids yielding the strongest SEHRS and SHG using IR excitation have nearly the

same structural parameters, thus suggesting SHG as a fast screening tool for identifying nanostructures supporting high SEHRS enhancement.

Experiments with both spherical gold nanoparticles and nanorods in solution and nanovoid arrays showed that structures giving the highest enhancement of 1064 nm excited SEHRS differ from those that provide optimum enhancement at 532 nm in one-photon SERS, pointing towards the importance of plasmon resonances at near-IR wavelengths. Furthermore, this suggests that utilizing SHG for identifying nanostructures supporting high SEHRS enhancement could provide more advantages than adapting substrates optimized for one-photon SERS in SEHRS experiments, which is a new strategy proposed here. From the perspective of future optimization of the SEHRS enhancement, these results, moreover, suggest that plasmonic substrates with resonances in the near-IR region, such as arrays of elongated nanorods or structures similar to the antennas used in surface enhanced infrared absorption (SEIRA),[19] may turn out beneficial for SEHRS. In this context, excitation profiles using molecules with electronic transitions far from the considered spectral range might provide new insights into the plasmonic properties required for the strong amplification of HRS signals. Such studies could be complemented with probing of the plasmonic modes responsible for the SEHRS enhancement by electron energy loss spectroscopy (EELS).[98] In the practical implementation, a controlled aggregation of nanoparticles in solution, as known from SERS,[108] may be useful for creating reproducible SEHRS active hot spots for applications where very strong enhancement is required.

Another subject discussed in this thesis was the design of novel nanocomposites consisting of barium titanate harmonic probes with plasmonic shell enabling enhancement of SEHRS. The nanoparticles allowed combining SHG imaging that provides morphological information of the sample with chemical information from the local environment of the nanoprobes based on SEHRS and SERS spectra. Both experiments and simulations show that depending on the plasmonic coating the optical properties of barium titanate nanocrystals can be tuned and optimized for a particular type of experiment. Specifically, as was discussed here, changes of the optical near-field properties induced by the plasmonic moieties can result in a moderate decrease of the SHG from the core-shell particles compared to the pristine barium titanate. This was found despite the presence of local field enhancement at the surface of the nanocomposites. While the work presented here was mainly focused on the preparation and optical characterization of such composite nanoprobes, future research could take advantage of the reduced two-photon interaction volumes and demonstrate optical imaging based

on SEHRS and SHG with high spatial resolution, which is one of the main advantages of multiphoton excited microspectroscopy over methods based on linear optical effects.

The information gained in the first chapters of this thesis allowed recording for the first time SEHRS spectra of important organic and bioorganic molecules exploiting the enhanced local optical fields of gold and silver nanoparticles. These spectra illustrate the capabilities of SEHRS for comprehensive vibrational probing of molecular structures in solution. The comparison of SEHRS and SERS spectra, both excited off-resonance, of identical samples provides evidence of the complementarity of both types of vibrational spectral information that arises due to the different selection rules. Spectra obtained at varied molecule concentration and pH as well as with different metal nanoparticles demonstrate the high sensitivity of the (two-photon) SEHRS over one-photon SERS with respect to orientation and local environmental changes, and reveal numerous advantages of combined SEHRS/SERS approaches for studying the interaction of molecules with metal nanostructures. This includes a better understanding of both effects themselves. The observation of reaction products by SEHRS reported here, and the known contribution of plasmon mediated processes[273] suggests to use SEHRS data together with SERS spectra excited at the same and at the double frequency to further elucidate the mechanisms of plasmon catalyzed reactions. In particular, future work could consider combining experiments with theoretical approaches, e.g. some recently developed methods for the simulation of SEHRS spectra,[278] in order to better understand how the different orientation of a molecule influences the band intensities in SEHRS spectra. From a very general and long term perspective, research areas such as surface science, bioinorganic catalysis, and nanobiophotonics may benefit from the advantages that SEHRS offers in terms of chemical and structural characterization.

Bibliography

[1] M. Fleischmann, P. J. Hendra, and A. J. McQuillan. Raman spectra of pyridine adsorbed at a silver electrode. *Chemical Physics Letters*, 26(2):163–166, 1974.

[2] M. G. Albrecht and J. A. Creighton. Anomalously intense Raman spectra of pyridine at a silver electrode. *Journal of the American Chemical Society*, 99(15):5215–5217, 1977.

[3] D. L. Jeanmaire and R. P. Van Duyne. Surface Raman spectroelectrochemistry. *Journal of Electroanalytical Chemistry and Interfacial Electrochemistry*, 84(1):1–20, 1977.

[4] K. Kneipp, Y. Wang, H. Kneipp, L. T. Perelman, I. Itzkan, R. R. Dasari, and M. S. Feld. Single molecule detection using surface-enhanced Raman scattering (SERS). *Physical Review Letters*, 78(9):1667–1670, 1997.

[5] S. Nie and S. R. Emory. Probing single molecules and single nanoparticles by surface-enhanced Raman scattering. *Science*, 275(5303):1102–6, 1997.

[6] P. K. Jain, X. Huang, I. H. El-Sayed, and M. A. El-Sayed. Review of some interesting surface plasmon resonance-enhanced properties of noble metal nanoparticles and their applications to biosystems. *Plasmonics*, 2(3):107–118, 2007.

[7] P. Stiles, J. Dieringer, N. Shah, and R. Van Duyne. Surface-enhanced Raman spectroscopy. *Annual Review of Analytical Chemistry*, 1(1):601–626, 2008.

[8] M. I. Stockman. Nanoplasmonics: past, present, and glimpse into future. *Optics Express*, 19(22):22029–22106, 2011.

[9] S. Schlücker. Surface-enhanced Raman spectroscopy: Concepts and chemical applications. *Angewandte Chemie International Edition*, 53(19):4756–4795, 2014.

[10] A. Hartstein, J. R. Kirtley, and J. C. Tsang. Enhancement of the infrared absorption from molecular monolayers with thin metal overlayers. *Physical Review Letters*, 45(3):201–204, 1980.

[11] A. V. Baranov and Ya. S. Bobovich. Super-enhanced hyper-Raman scattering from dyes adsorbed on colloidal silver particles. *JETP Letters*, 36(8):339–343, 1982.

[12] D. V. Murphy, K. U. Vonraben, R. K. Chang, and P. B. Dorain. Surface-enhanced hyper-Raman scattering from SO_3^{2-} adsorbed on Ag powder. *Chemical Physics Letters*, 85(1):43–47, 1982.

[13] E. J. Liang, A. Weippert, J. M. Funk, A. Materny, and W. Kiefer. Experimental observation of surface-enhanced coherent anti-Stokes Raman scattering. *Chemical Physics Letters*, 227(1):115–120, 1994.

[14] Y. Zhang, Y. Zhen, O. Neumann, J. K. Day, P. Nordlander, and N. J. Halas. Coherent anti-Stokes Raman scattering with single-molecule sensitivity using a plasmonic Fano resonance. *Nature Communications*, 5:4424, 2014.

[15] R. R. Frontiera, A. Henry, N. L. Gruenke, and R. P. Van Duyne. Surface-enhanced femtosecond stimulated Raman spectroscopy. *The Journal of Physical Chemistry Letters*, 2(10):1199–1203, 2011.

[16] P. D. Simmons, H. K. Turley, D. W. Silverstein, L. Jensen, and J. P. Camden. Surface-enhanced spectroscopy for higher-order light scattering: A combined experimental and theoretical study of second hyper-Raman scattering. *The Journal of Physical Chemistry Letters*, 6(24):5067–5071, 2015.

[17] K. C. Bantz, A. F. Meyer, N. J. Wittenberg, H. Im, Ö. Kurtuluş, S. H. Lee, N. C. Lindquist, S. Oh, and C. L. Haynes. Recent progress in SERS biosensing. *Physical Chemistry Chemical Physics*, 13(24):11551–11567, 2011.

[18] S. Schlücker. SERS microscopy: Nanoparticle probes and biomedical applications. *ChemPhysChem*, 10:1344–1354, 2009.

[19] F. Neubrech, C. Huck, K. Weber, A. Pucci, and H. Giessen. Surface-enhanced infrared spectroscopy using resonant nanoantennas. *Chemical Reviews*, 117(7):5110–5145, 2017.

[20] V. N. Denisov, B. N. Mavrin, and V. B. Podobedov. Hyper-Raman scattering by vibrational excitations in crystals, glasses and liquids. *Physics Reports*, 151(1):1–92, 1987.

[21] J. Kneipp, H. Kneipp, and K. Kneipp. Two-photon vibrational spectroscopy for biosciences based on surface-enhanced hyper-Raman scattering. *Proceedings of the National Academy of Sciences*, 103(46):17149–17153, 2006.

[22] J. H. Christie and D. J. Lockwood. Selection rules for three- and four-photon Raman interactions. *The Journal of Chemical Physics*, 54(3):1141–1154, 1971.

[23] W. R. Zipfel, R. M. Williams, and W. W. Webb. Nonlinear magic: multiphoton microscopy in the biosciences. *Nat Biotech*, 21(11):1369–1377, 2003.

[24] J. C. Hulteen, M. A. Young, and R. P. Van Duyne. Surface-enhanced hyper-Raman scattering (SEHRS) on Ag film over nanosphere (FON) electrodes: surface symmetry of centrosymmetric adsorbates. *Langmuir*, 22(25):10354–10364, 2006.

[25] N. Valley, L. Jensen, J. Autschbach, and G. C. Schatz. Theoretical studies of surface enhanced hyper-Raman spectroscopy: The chemical enhancement mechanism. *The Journal of Chemical Physics*, 133(5):054103, 2010.

[26] F. Madzharova, Z. Heiner, M. Gühlke, and J. Kneipp. Surface-enhanced hyper-Raman spectra of adenine, guanine, cytosine, thymine, and uracil. *The Journal of Physical Chemistry C*, 120(28):15415–15423, 2016.

[27] H. K. Turley, Z. Hu, L. Jensen, and J. P. Camden. Surface-enhanced resonance hyper-Raman scattering elucidates the molecular orientation of rhodamine 6G on silver colloids. *The Journal of Physical Chemistry Letters*, 8(8):1819–1823, 2017.

[28] S. Brasselet. Polarization-resolved nonlinear microscopy: application to structural molecular and biological imaging. *Advances in Optics and Photonics*, 3(3):205–271, 2011.

[29] P. F. Brevet. *3.11 - Second Harmonic Generation in Nanostructures*, pages 351–381. Academic Press, Amsterdam, 2011.

[30] S. Roke and G. Gonella. Nonlinear light scattering and spectroscopy of particles and droplets in liquids. *Annual Review of Physical Chemistry*, 63(1):353–378, 2012.

[31] M. I. Stockman, D. J. Bergman, C. Anceau, S. Brasselet, and J. Zyss. Enhanced second-harmonic generation by metal surfaces with nanoscale roughness: Nanoscale dephasing, depolarization, and correlations. *Physical Review Letters*, 92(5):057402, 2004.

[32] P. Pantazis, J. Maloney, D. Wu, and S. E. Fraser. Second harmonic generating (SHG) nanoprobes for in vivo imaging. *Proceedings of the National Academy of Sciences*, 107(33):14535–14540, 2010.

[33] D. Staedler, T. Magouroux, R. Hadji, C. Joulaud, J. Extermann, S. Schwung, S. Passemard, C. Kasparian, G. Clarke, M. Gerrmann, R. Le Dantec, Y. Mugnier, D. Rytz, D. Ciepielewski, C. Galez, S. Gerber-Lemaire, L. Juillerat-Jeanneret, L. Bonacina, and J. Wolf. Harmonic nanocrystals for biolabeling: A survey of optical properties and biocompatibility. *ACS Nano*, 6(3):2542–2549, 2012.

[34] J. Aizpurua and R. Hillenbrand. *Localized Surface Plasmons: Basics and Applications in Field-Enhanced Spectroscopy*, pages 151–176. Springer Berlin Heidelberg, Berlin, Heidelberg, 2012.

[35] C. F. Bohren and D. R. Huffman. *Absorption and Scattering of Light by Small Particles*. Wiley, 1998.

[36] C. B. Milojevich, B. K. Mandrell, H. K. Turley, V. Iberi, M. D. Best, and J. P. Camden. Surface-enhanced hyper-Raman scattering from single molecules. *The Journal of Physical Chemistry Letters*, 4(20):3420–3423, 2013.

[37] P. Nordlander, C. Oubre, E. Prodan, K. Li, and M. I. Stockman. Plasmon hybridization in nanoparticle dimers. *Nano Letters*, 4(5):899–903, 2004.

[38] N. J. Halas, S. Lal, W. Chang, S. Link, and P. Nordlander. Plasmons in strongly coupled metallic nanostructures. *Chemical Reviews*, 111(6):3913–3961, 2011.

[39] T. A. Kelf, Y. Sugawara, R. M. Cole, J. J. Baumberg, M. E. Abdelsalam, S. Cintra, S. Mahajan, A. E. Russell, and P. N. Bartlett. Localized and delocalized plasmons in metallic nanovoids. *Physical Review B*, 74(24):245415, 2006.

[40] R. M. Cole, J. J. Baumberg, F. J. Garcia de Abajo, S. Mahajan, M. Abdelsalam, and P. N. Bartlett. Understanding plasmons in nanoscale voids. *Nano Letters*, 7(7):2094–2100, 2007.

[41] S. Cintra, M. E. Abdelsalam, P. N. Bartlett, J. J. Baumberg, T. A. Kelf, Y. Sugawara, and A. E. Russell. Sculpted substrates for SERS. *Faraday Discussions*, 132(0):191–199, 2006.

[42] S. Mahajan, M. Abdelsalam, Y. Suguwara, S. Cintra, A. Russell, J. Baumberg, and P. Bartlett. Tuning plasmons on nano-structured substrates for NIR-SERS. *Physical Chemistry Chemical Physics*, 9(1):104–109, 2007.

[43] S. Mahajan, R. M. Cole, B. F. Soares, S. H. Pelfrey, A. E. Russell, J. J. Baumberg, and P. N. Bartlett. Relating SERS intensity to specific plasmon modes on sphere segment void surfaces. *The Journal of Physical Chemistry C*, 113(21):9284–9289, 2009.

[44] A. Garcia-Etxarri, R. Gomez-Medina, L. S. Froufe-Perez, C. Lopez, L. Chantada, F. Scheffold, J. Aizpurua, M. Nieto-Vesperinas, and J. J. Saenz. Strong magnetic response of submicron silicon particles in the infrared. *Optics Express*, 19(6):4815–4826, 2011.

[45] T. G. Habteyes, I. Staude, K. E. Chong, J. Dominguez, M. Decker, A. Miroshnichenko, Y. Kivshar, and I. Brener. Near-field mapping of optical modes on all-dielectric silicon nanodisks. *ACS Photonics*, 1(9):794–798, 2014.

[46] R. M. Bakker, D. Permyakov, Y. F. Yu, D. Markovich, R. Paniagua-Domínguez, L. Gonzaga, A. Samusev, Y. Kivshar, B. Lukyanchuk, and A. I. Kuznetsov. Magnetic and electric hotspots with silicon nanodimers. *Nano Letters*, 15(3):2137–2142, 2015.

[47] F. Timpu, A. Sergeyev, N. R. Hendricks, and R. Grange. Second-harmonic enhancement with Mie resonances in perovskite nanoparticles. *ACS Photonics*, 4(1):76–84, 2017.

[48] E. C. Le Ru and P. G. Etchegoin. *Chapter 5 - Calculations of electromagnetic enhancements*, pages 265–297. Elsevier, Amsterdam, 2009.

[49] K. Yee. Numerical solution of initial boundary value problems involving Maxwell's equations in isotropic media. *IEEE Transactions on Antennas and Propagation*, 14(3):302–307, 1966.

[50] E. C. Le Ru and P. G. Etchegoin. *Chapter 7 - Metallic colloids and other SERS substrates*, pages 367–413. Elsevier, Amsterdam, 2009.

[51] L. A. Austin, B. Kang, and M. A. El-Sayed. Probing molecular cell event dynamics at the single-cell level with targeted plasmonic gold nanoparticles: A review. *Nano Today*, 10(5):542–558, 2015.

[52] J. Turkevich, P. C. Stevenson, and J. Hillier. A study of the nucleation and growth processes in the synthesis of colloidal gold. *Discussions of the Faraday Society*, 11(0):55–75, 1951.

[53] P. C. Lee and D. Meisel. Adsorption and surface-enhanced Raman of dyes on silver and gold sols. *The Journal of Physical Chemistry*, 86(17):3391–3395, 1982.

[54] G. Frens. Controlled nucleation for the regulation of the particle size in monodisperse gold suspensions. *Nature Physical Science*, 241:20–22, 1973.

[55] N. R. Jana, L. Gearheart, and C. J. Murphy. Seed-mediated growth approach for shape-controlled synthesis of spheroidal and rod-like gold nanoparticles using a surfactant template. *Advanced Materials*, 13(18):1389–1393, 2001.

[56] L. Scarabelli, A. Sánchez-Iglesias, J. Pérez-Juste, and L. M. Liz-Marzán. A "tips and tricks" practical guide to the synthesis of gold nanorods. *The Journal of Physical Chemistry Letters*, 6(21):4270–4279, 2015.

[57] J. Li, Y. Zhang, S. Ding, R. Panneerselvam, and Z. Tian. Core–shell nanoparticle-enhanced Raman spectroscopy. *Chemical Reviews*, 117(7):5002–5069, 2017.

[58] M. B. Cortie and A. M. McDonagh. Synthesis and optical properties of hybrid and alloy plasmonic nanoparticles. *Chemical Reviews*, 111(6):3713–3735, 2011.

[59] A. V. Povolotskaya, A. V. Povolotskiy, and A. A. Manshina. Hybrid nanostructures: synthesis, morphology and functional properties. *Russian Chemical Reviews*, 84(6):579–600, 2015.

[60] Y. U. Kayran, V. Eßmann, S. Grützke, and W. Schuhmann. Selection of highly SERS-active nanostructures from a size gradient of Au nanovoids on a single bipolar electrode. *ChemElectroChem*, 3(3):399–403, 2016.

[61] R. F. Egerton. *Physical Principles of Electron Microscopy. An Introduction to TEM, SEM, and AEM*. Springer US, 2005.

[62] R. Pecora. Dynamic light scattering measurement of nanometer particles in liquids. *Journal of Nanoparticle Research*, 2(2):123–131, 2000.

[63] D. A. Long and L. Stanton. Studies of nonlinear phenomena. I. Theory of the hyper Raman effect. *Proceedings of the Royal Society of London. A. Mathematical and Physical Sciences*, 318(1535):441–457, 1970.

[64] Y. C. Chung and L. D. Ziegler. The vibronic theory of resonance hyper-Raman scattering. *The Journal of Chemical Physics*, 88(12):7287–7294, 1988.

[65] L. D. Ziegler. Hyper-Raman spectroscopy. *Journal of Raman Spectroscopy*, 21(12):769–779, 1990.

[66] J. Kneipp, H. Kneipp, and K. Kneipp. SERS - a single-molecule and nanoscale tool for bioanalytics. *Chemical Society Reviews*, 37(5):1052–1060, 2008.

[67] D. A. Long. *The Raman effect-a unified treatment of the theory of Raman scattering by molecules.* John Wiley & Sons, Ltd., 2002.

[68] L. D. Ziegler and J. L. Roebber. Resonance hyper-Raman scattering spectra of ammonia. *Chemical Physics Letters*, 136(5):377–382, 1987.

[69] A. M. Kelley. Resonance Raman and resonance hyper-Raman intensities: Structure and dynamics of molecular excited states in solution. *The Journal of Physical Chemistry A*, 112(47):11975–11991, 2008.

[70] W. Yang and G. C. Schatz. Ab initio and semiempirical molecular orbital studies of surface enhanced and bulk hyper-Raman scattering from pyridine. *The Journal of Chemical Physics*, 97(5):3831–3845, 1992.

[71] D. R. Kanis, M. A. Ratner, and T. J. Marks. Design and construction of molecular assemblies with large second-order optical nonlinearities. Quantum chemical aspects. *Chemical Reviews*, 94(1):195–242, 1994.

[72] X. Li, Q. Huang, V. I. Petrov, Y. Xie, Q. Luo, X. Yu, and Y. Yan. Surface-enhanced hyper-Raman and surface-enhanced Raman scattering from molecules adsorbed on nanoparticles-on-smooth-electrode (NOSE) substrate I. Pyridine, pyrazine and benzene. *Journal of Raman Spectroscopy*, 36(6-7):555–573, 2005.

[73] C. B. Milojevich, D. W. Silverstein, L. Jensen, and J. P. Camden. Surface-enhanced hyper-Raman scattering elucidates the two-photon absorption spectrum of rhodamine 6G. *The Journal of Physical Chemistry C*, 117(6):3046–3054, 2013.

[74] H. K. Turley, Z. Hu, D. W. Silverstein, D. A. Cooper, L. Jensen, and J. P. Camden. Probing two-photon molecular properties with surface-enhanced hyper-Raman scattering: A combined experimental and theoretical study of crystal violet. *The Journal of Physical Chemistry C*, 120(37):20936–20942, 2016.

[75] C. Cramer. *Essentials of Computational Chemistry*. John Wiley & Sons, Ltd,, 2004.

[76] F. Jensen. *Introduction to Computational Chemistry*. John Wiley & Sons, Ltd., 2007.

[77] P. Hohenberg and W. Kohn. Inhomogeneous electron gas. *Physical Review*, 136(3B):B864–B871, 1964.

[78] W. Kohn and L. J. Sham. Self-consistent equations including exchange and correlation effects. *Physical Review*, 140(4A):A1133–A1138, 1965.

[79] A. D. Becke. Density-functional thermochemistry. III. The role of exact exchange. *The Journal of Chemical Physics*, 98(7):5648–5652, 1993.

[80] L. Jensen, C. M. Aikens, and G. C. Schatz. Electronic structure methods for studying surface-enhanced Raman scattering. *Chemical Society Reviews*, 37(5):1061–1073, 2008.

[81] D. V. Chulhai, Z. Hu, J. E. Moore, X. Chen, and L. Jensen. Theory of linear and nonlinear surface-enhanced vibrational spectroscopy. *Annual Review of Physical Chemistry*, 67(1):541–564, 2016.

[82] S. M. Morton, D. W. Silverstein, and L. Jensen. Theoretical studies of plasmonics using electronic structure methods. *Chemical Reviews*, 111(6):3962–3994, 2011.

[83] J. T. Golab, J. R. Sprague, K. T. Carron, G. C. Schatz, and R. P. Van Duyne. A surface enhanced hyper-Raman scattering study of pyridine adsorbed onto silver: Experiment and theory. *The Journal of Chemical Physics*, 88(12):7942–7951, 1988.

[84] J. Mullin, N. Valley, M. G. Blaber, and G. C. Schatz. Combined quantum mechanics (TDDFT) and classical electrodynamics (Mie theory) methods for calculating surface enhanced Raman and hyper-Raman spectra. *The Journal of Physical Chemistry A*, 116(38):9574–9581, 2012.

[85] H. Kneipp, K. Kneipp, and F. Seifert. Surface-enhanced hyper-Raman scattering (SEHRS) and surface-enhanced Raman scattering (SERS) by means of mode-locked Ti:sapphire laser excitation. *Chemical Physics Letters*, 212(3):374–378, 1993.

[86] H. Yoshikawa, T. Adachi, G. Sazaki, T. Matsui, K. Nakajima, and H. Masuhara. Surface-enhanced hyper-Raman spectroscopy using optical trapping of silver nanoparticles for molecular detection in solution. *Journal of Optics A: Pure and Applied Optics*, 9(8):S164, 2007.

[87] K. Kneipp, H. Kneipp, I. Itzkan, R. R. Dasari, and M. S. Feld. Surface-enhanced nonlinear Raman scattering at the single-molecule level. *Chemical Physics*, 247(1):155–162, 1999.

[88] S. Nie, L. A. Lipscomb, and N. Yu. Surface-enhanced hyper-Raman spectroscopy. *Applied Spectroscopy Reviews*, 26(3):203–276, 1991.

[89] E. C. Le Ru and P. G. Etchegoin. *Chapter 4 - SERS enhancement factors and related topics*, pages 185–264. Elsevier, Amsterdam, 2009.

[90] D. A. Weitz, S. Garoff, and T. J. Gramila. Excitation spectra of surface-enhanced Raman scattering on silver-island films. *Optics Letters*, 7(4):168–170, 1982.

[91] H. Kneipp, K. Kneipp, and F. Seifert. Surface-enhanced hyper-Raman scattering (SEHRS) and surface-enhanced Raman scattering (SERS) by means of mode-locked Ti:sapphire laser excitation. *Chemical Physics Letters*, 212(3):374–378, 1993.

[92] W. Li, X. Li, and N. Yu. Surface-enhanced hyper-Raman spectroscopy (SEHRS) and surface-enhanced Raman spectroscopy (SERS) studies of pyrazine and pyridine adsorbed on silver electrodes. *Chemical Physics Letters*, 305(3–4):303–310, 1999.

[93] C. K. Johnson and S. A. Soper. Nonlinear surface-enhanced spectroscopy of silver colloids and pyridine: hyper-Raman and second-harmonic scattering. *The Journal of Physical Chemistry*, 93(21):7281–7285, 1989.

[94] A. V. Baranov, Y. S. Bobovich, and V. K. Petrov. Resonance inelastic three-photon scattering: physical model and experimental results. *Sov. Phys. JETP*, 61(3):435–439, 1985.

[95] S. Kadkhodazadeh, J. B. Wagner, V. Joseph, J. Kneipp, H. Kneipp, and K. Kneipp. Electron energy loss and one- and two-photon excited SERS probing of "hot" plasmonic silver nanoaggregates. *Plasmonics*, 8(2):763–767, 2013.

[96] C. G. Blatchford, J. R. Campbell, and J. A. Creighton. Plasma resonance – enhanced Raman scattering by absorbates on gold colloids: The effects of aggregation. *Surface Science*, 120(2):435–455, 1982.

[97] J. M. McMahon, S. K. Gray, and G. C. Schatz. Fundamental behavior of electric field enhancements in the gaps between closely spaced nanostructures. *Physical Review B*, 83(11), 2011.

[98] K. Kneipp, H. Kneipp, and J. Kneipp. Probing plasmonic nanostructures by photons and electrons. *Chemical Science*, 6(5):2721–2726, 2015.

[99] J. Butet and O. J. F. Martin. Surface-enhanced hyper-Raman scattering: A new road to the observation of low energy molecular vibrations. *The Journal of Physical Chemistry C*, 119(27):15547–15556, 2015.

[100] K. Kneipp, H. Kneipp, and J. Kneipp. *Plasmonics for Enhanced Vibrational Signatures*, pages 103–124. Springer Netherlands, Dordrecht, 2013.

[101] A. M. Kelley. Hyper-Raman scattering by molecular vibrations. *Annual Review of Physical Chemistry*, 61(1):41–61, 2010.

[102] T. Itoh, H. Yoshikawa, K. Yoshida, V. Biju, and M. Ishikawa. Evaluation of electromagnetic enhancement of surface enhanced hyper Raman scattering using plasmonic properties of binary active sites in single Ag nanoaggregates. *The Journal of Chemical Physics*, 130(21):214706, 2009.

[103] T. Itoh, H. Yoshikawa, K. Yoshida, V. Biju, and M. Ishikawa. Spectral variations in background light emission of surface-enhanced resonance hyper Raman scattering coupled with plasma resonance of individual silver nanoaggregates. *The Journal of Chemical Physics*, 133(12):124704, 2010.

[104] S. Zhu, C. Fan, P. Ding, E. Liang, H. Hou, and Y. Wu. Theoretical investigation of a plasmonic substrate with multi-resonance for surface enhanced hyper-Raman scattering. *Scientific Reports*, 8(1):11891, 2018.

[105] W. Leng, A. A. Yasseri, S. Sharma, Z. Li, H. Woo, D. Vak, G. C. Bazan, and A. M. Kelley. Silver nanocrystal-modified silicon nanowires as substrates for surface-enhanced Raman and hyper-Raman scattering. *Analytical Chemistry*, 78(17):6279–6282, 2006.

[106] V. Joseph, M. Gensler, S. Seifert, U. Gernert, J. P. Rabe, and J. Kneipp. Nanoscopic properties and application of mix-and-match plasmonic surfaces for microscopic SERS. *The Journal of Physical Chemistry C*, 116(12):6859–6865, 2012.

[107] M. Gühlke, Z. Heiner, and J. Kneipp. Surface-enhanced hyper-Raman and Raman hyperspectral mapping. *Physical Chemistry Chemical Physics*, 18(21):14228–14233, 2016.

[108] A. Shiohara, Y. Wang, and L. M. Liz-Marzán. Recent approaches toward creation of hot spots for SERS detection. *Journal of Photochemistry and Photobiology C: Photochemistry Reviews*, 21(Supplement C):2–25, 2014.

[109] N. Guillot and M. L. de la Chapelle. Lithographied nanostructures as nanosensors. *Journal of Nanophotonics*, 6(1):064506–1–064506–28, 2012.

[110] X. Zhang, C. R. Yonzon, and R. P. Van Duyne. Nanosphere lithography fabricated plasmonic materials and their applications. *Journal of Materials Research*, 21(5):1083–1092, 2006.

[111] K. Ikeda, M. Takase, Y. Sawai, H. Nabika, K. Murakoshi, and K. Uosaki. Hyper-Raman scattering enhanced by anisotropic dimer plasmons on artificial nanostructures. *The Journal of Chemical Physics*, 127(11):111103, 2007.

[112] S. Schneider, G. Brehm, and P. Freunscht. Comparison of surface-enhanced Raman and hyper-Raman spectra of the triphenylmethane dyes crystal violet and malachite green. *physica status solidi (b)*, 189(1):37–42, 1995.

[113] T. Itoh, Y. Ozaki, H. Yoshikawa, T. Ihama, and H. Masuhara. Hyper-Rayleigh scattering and hyper-Raman scattering of dye-adsorbed silver nanoparticles induced by a focused continuous-wave near-infrared laser. *Applied Physics Letters*, 88(8):084102, 2006.

[114] W. Leng and A. M. Kelley. Surface-enhanced hyper-Raman spectra and enhancement factors for three SERS chromophores. SEHRS spectra on Ag films at pulse energies below 2 pJ. *Journal of the American Chemical Society*, 128(11):3492–3493, 2006.

[115] C. B. Milojevich, D. W. Silverstein, L. Jensen, and J. P. Camden. Probing two-photon properties of molecules: Large non-Condon effects dominate the resonance hyper-Raman scattering of rhodamine 6G. *Journal of the American Chemical Society*, 133(37):14590–14592, 2011.

[116] M. Gühlke, Z. Heiner, and J. Kneipp. Combined near-infrared excited SEHRS and SERS spectra of pH sensors using silver nanostructures. *Physical Chemistry Chemical Physics*, 17(39):26093–26100, 2015.

[117] G. Brehm, G. Sauer, N. Fritz, S. Schneider, and S. Zaitsev. Correlation spectroscopy based on non-linear response of silver colloids (including SEHRS). *Journal of Molecular Structure*, 735–736:85–102, 2005.

[118] M. Espina Palanco, K. Bo Mogensen, M. Gühlke, Z. Heiner, J. Kneipp, and K. Kneipp. Templated green synthesis of plasmonic silver nanoparticles in onion epidermal cells suitable for surface-enhanced Raman and hyper-Raman scattering. *Beilstein Journal of Nanotechnology*, 7:834–840, 2016.

[119] L. A. Lipscomb, S. Nie, S. Feng, and N. Yu. Surface-enhanced hyper-Raman spectroscopy with a picosecond laser: gold and copper colloids. *Chemical Physics Letters*, 170(5):457–461, 1990.

[120] H. Kneipp and K. Kneipp. Surface-enhanced hyper Ramann scattering in silver colloidal solutions. *Journal of Raman Spectroscopy*, 36(6-7):551–554, 2005.

[121] S. Nie, L. A. Lipscomb, S. Feng, and N. Yu. Resonant and nonresonant surface-enhanced hyper-Raman spectroscopy with a picosecond laser. Effect of the excitation pulse width. *Chemical Physics Letters*, 167(1):35–40, 1990.

[122] A. V. Baranov and Igor R. Nabiev. Surface-enhanced resonance hyper-Raman spectra of bacteriorhodopsin adsorbed on silver colloids. volume 1403, pages 128–131.

[123] A. Palonpon, T. Ichimura, P. Verma, Y. Inouye, and S. Kawata. Halide-ion-assisted increase of surface-enhanced hyper-Raman scattering: a clear observation of the chemical effect. *Journal of Raman Spectroscopy*, 40(2):119–120, 2009.

[124] P. Duo-Hai, Z. Peng-Xiang, L. Xiang-Sheng, M. Run-Cai, and H. Yi-Xian. A study on surface-enhanced hyper-Raman scattering of basic fuchsin adsorbed on the silver colloid. *Chin. Phys. B*, 2(12):925–929, 1993.

[125] A. Palonpon, T. Ichimura, P. Verma, Y. Inouye, and S. Kawata. Direct evidence of chemical contribution to surface-enhanced hyper-Raman scattering. *Applied Physics Express*, 1(9):092401, 2008.

[126] S. E. J. Bell and N. M. S. Sirimuthu. Surface-enhanced Raman spectroscopy as a probe of competitive binding by anions to citrate-reduced silver colloids. *The Journal of Physical Chemistry A*, 109(33):7405–7410, 2005.

[127] W. Li, X. Li, and N. Yu. Surface-enhanced resonance hyper-Raman scattering and surface-enhanced resonance Raman scattering of dyes adsorbed on silver electrode and silver colloid: a comparison study. *Chemical Physics Letters*, 312(1):28–36, 1999.

[128] W. Li, X. Li, and N. Yu. Surface-enhanced hyper-Raman scattering and surface-enhanced Raman scattering studies of electroreduction of phenazine on silver electrode. *Chemical Physics Letters*, 327(3–4):153–161, 2000.

[129] W. Yang, J. Hulteen, G. C. Schatz, and R. P. Van Duyne. A surface-enhanced hyper-Raman and surface-enhanced Raman scattering study of trans-1,2-bis(4-pyridyl)ethylene adsorbed onto silver film over nanosphere electrodes. Vibrational assignments: Experiment and theory. *The Journal of Chemical Physics*, 104(11):4313–4323, 1996.

[130] J. Kneipp, H. Kneipp, B. Wittig, and K. Kneipp. One- and two-photon excited optical pH probing for cells using surface-enhanced Raman and hyper-Raman nanosensors. *Nano Letters*, 7(9):2819–2823, 2007.

[131] J. Butet, P. Brevet, and O. J. F. Martin. Optical second harmonic generation in plasmonic nanostructures: From fundamental principles to advanced applications. *ACS Nano*, 9(11):10545–10562, 2015.

[132] C. K. Chen, A. R. B. de Castro, and Y. R. Shen. Surface-enhanced second-harmonic generation. *Physical Review Letters*, 46(2):145–148, 1981.

[133] H. Aouani, M. Navarro-Cia, M. Rahmani, T. P. H. Sidiropoulos, M. Hong, R. F. Oulton, and S. A. Maier. Multiresonant broadband optical antennas as efficient tunable nanosources of second harmonic light. *Nano Letters*, 12(9):4997–5002, 2012.

[134] K. Thyagarajan, S. Rivier, A. Lovera, and O. J. F. Martin. Enhanced second-harmonic generation from double resonant plasmonic antennae. *Optics Express*, 20(12):12860–12865, 2012.

[135] A. Slablab, L. Le Xuan, M. Zielinski, Y. de Wilde, V. Jacques, D. Chauvat, and J. F. Roch. Second-harmonic generation from coupled plasmon modes in a single dimer of gold nanospheres. *Optics Express*, 20(1):220–227, 2012.

[136] S. I. Bozhevolnyi, J. Beermann, and V. Coello. Direct observation of localized second-harmonic enhancement in random metal nanostructures. *Physical Review Letters*, 90(19):197403, 2003.

[137] C. Anceau, S. Brasselet, J. Zyss, and P. Gadenne. Local second-harmonic generation enhancement on gold nanostructures probed by two-photon microscopy. *Optics Letters*, 28(9):713–715, 2003.

[138] A. Salomon, M. Zielinski, R. Kolkowski, J. Zyss, and Y. Prior. Size and shape resonances in second harmonic generation from silver nanocavities. *The Journal of Physical Chemistry C*, 117(43):22377–22382, 2013.

[139] F. Dutto, M. Heiss, A. Lovera, O. López-Sánchez, A. Fontcuberta i Morral, and A. Radenovic. Enhancement of second harmonic signal in nanofabricated cones. *Nano Letters*, 13(12):6048–6054, 2013.

[140] M. R. Shcherbakov, D. N. Neshev, B. Hopkins, A. S. Shorokhov, I. Staude, E. V. Melik-Gaykazyan, M. Decker, A. A. Ezhov, A. E. Miroshnichenko, I. Brener, A. A. Fedyanin, and Y. S. Kivshar. Enhanced third-harmonic generation in silicon nanoparticles driven by magnetic response. *Nano Letters*, 14(11):6488–6492, 2014.

[141] C. Ma, J. Yan, Y. Wei, P. Liu, and G. Yang. Enhanced second harmonic generation in individual barium titanate nanoparticles driven by Mie resonances. *Journal of Materials Chemistry C*, 5(19):4810–4819, 2017.

[142] M Horisberger and J Rosset. Colloidal gold, a useful marker for transmission and scanning electron microscopy. *Journal of Histochemistry and Cytochemistry*, 25(4):295–305, 1977.

[143] D. G. Duff, A. Baiker, and P. P. Edwards. A new hydrosol of gold clusters. 1. Formation and particle size variation. *Langmuir*, 9(9):2301–2309, 1993.

[144] N. Leopold and B. Lendl. A new method for fast preparation of highly surface-enhanced Raman scattering (SERS) active silver colloids at room temperature by reduction of silver nitrate with hydroxylamine hydrochloride. *The Journal of Physical Chemistry B*, 107(24):5723–5727, 2003.

[145] S. Chang, W. Liao, C. Ciou, J. Lee, and C. Li. An efficient approach to derive hydroxyl groups on the surface of barium titanate nanoparticles to improve its chemical modification ability. *Journal of Colloid and Interface Science*, 329(2):300–305, 2009.

[146] J. Culic-Viskota, W. P. Dempsey, S. E. Fraser, and P. Pantazis. Surface functionalization of barium titanate SHG nanoprobes for in vivo imaging in zebrafish. *Nat. Protocols*, 7(9):1618–1633, 2012.

[147] Y. Pu, R. Grange, C. Hsieh, and D. Psaltis. Nonlinear optical properties of core-shell nanocavities for enhanced second-harmonic generation. *Physical Review Letters*, 104(20):207402, 2010.

[148] E. FarrokhTakin, G. Ciofani, G. L. Puleo, G. de Vito, C. Filippeschi, B. Mazzolai, V. Piazza, and V. Mattoli. Barium titanate core – gold shell nanoparticles for hyperthermia treatments. *International Journal of Nanomedicine*, 8:2319–2331, 2013.

[149] S. J. Oldenburg, S. L. Westcott, R. D. Averitt, and N. J. Halas. Surface enhanced Raman scattering in the near infrared using metal nanoshell substrates. *The Journal of Chemical Physics*, 111(10):4729–4735, 1999.

[150] H. Kang, J. Yang, M. S. Noh, A. Jo, S. Jeong, M. Lee, S. Lee, H. Chang, H. Lee, S. Jeon, H. Kim, M. Cho, H. Lee, J. Kim, D. Jeong, and Y. Lee. One-step synthesis of silver nanoshells with bumps for highly sensitive near-IR SERS nanoprobes. *Journal of Materials Chemistry B*, 2(28):4415–4421, 2014.

[151] J. R. Matthews, C. M. Payne, and J. H. Hafner. Analysis of phospholipid bilayers on gold nanorods by plasmon resonance sensing and surface-enhanced Raman scattering. *Langmuir*, 31(36):9893–9900, 2015.

[152] D. Öhl, Y. U. Kayran, J. R. C. Junqueira, V. Eßmann, T. Bobrowski, and W. Schuhmann. Optimized Ag nanovoid structures for probing electrocatalytic carbon dioxide reduction using operando surface-enhanced Raman spectroscopy. *Langmuir*, 34(41):12293–12301, 2018.

[153] R. Meyer, K. Sliozberg, C. Khare, W. Schuhmann, and A. Ludwig. High-throughput screening of thin-film semiconductor material libraries II: characterization of Fe-W-O libraries. *ChemSusChem*, 8(7):1279–1285, 2015.

[154] K. Sliozberg, D. Schäfer, T. Erichsen, R. Meyer, C. Khare, A. Ludwig, and W. Schuhmann. High-throughput screening of thin-film semiconductor material libraries I: system development and case study for Ti-W-O. *ChemSusChem*, 8(7):1270–1278, 2015.

[155] C. A. Schneider, W. S. Rasband, and K. W. Eliceiri. NIH image to ImageJ: 25 years of image analysis. *Nat Meth*, 9(7):671–675, 2012.

[156] A. Kudelski. Raman studies of rhodamine 6G and crystal violet sub-monolayers on electrochemically roughened silver substrates: Do dye molecules adsorb preferentially on highly SERS-active sites? *Chemical Physics Letters*, 414(4–6):271–275, 2005.

[157] Z. Zhang, S. Chen, Y. Liang, Z. Liu, Q. Zhang, L. Ding, F. Ye, and H. Zhou. An intelligent background-correction algorithm for highly fluorescent samples in Raman spectroscopy. *Journal of Raman Spectroscopy*, 41(6):659–669, 2010.

[158] R Core Team. *R: A Language and Environment for Statistical Computing*. R Foundation for Statistical Computing, Vienna, Austria, 2013.

[159] P. B. Johnson and R. W. Christy. Optical constants of the noble metals. *Physical Review B*, 6(12):4370–4379, 1972.

[160] C. Wong, Y. Y. Teng, J. Ashok, and P. L. H. Varaprasad. *Barium Titanate ($BaTiO_3$) A2 - Palik, Edward D*, pages 789–803. Academic Press, Burlington, 1997.

[161] S. Berciaud, L. Cognet, P. Tamarat, and B. Lounis. Observation of intrinsic size effects in the optical response of individual gold nanoparticles. *Nano Letters*, 5(3):515–518, 2005.

[162] S. Mühlig, M. Farhat, C. Rockstuhl, and F. Lederer. Cloaking dielectric spherical objects by a shell of metallic nanoparticles. *Physical Review B*, 83(19):195116, 2011.

[163] A. Sihvola. *Electromagnetic Mixing Formulas and Applications*. Institution of Electrical Engineers, London, 1999.

[164] A. L. Aden and M. Kerker. Scattering of electromagnetic waves from two concentric spheres. *Journal of Applied Physics*, 22(10):1242–1246, 1951.

[165] M. J. Frisch et. al. Gaussian 09 Revision D.01. Gaussian Inc. Wallingford CT 2009.

[166] R. Ditchfield, W. J. Hehre, and J. A. Pople. Self-consistent molecular-orbital methods. IX. An extended gaussian type basis for molecular-orbital studies of organic molecules. *The Journal of Chemical Physics*, 54(2), 1971.

[167] E. J. Zeman and G. C. Schatz. An accurate electromagnetic theory study of surface enhancement factors for silver, gold, copper, lithium, sodium, aluminum, gallium, indium, zinc, and cadmium. *The Journal of Physical Chemistry*, 91(3):634–643, 1987.

[168] J. V. García-Ramos and S. Sánchez-Cortśs. Metal colloids employed in the SERS of biomolecules: activation when exciting in the visible and near-infrared regions. *Journal of Molecular Structure*, 405(1):13–28, 1997.

[169] J. Kneipp. Interrogating cells, tissues, and live animals with new generations of surface-enhanced Raman scattering probes and labels. *ACS Nano*, 11(2):1136–1141, 2017.

[170] Z. Heiner, Marina Gühlke, V. Zivanovic, F. Madzharova, and J. Kneipp. Surface-enhanced hyper Raman hyperspectral imaging and probing in animal cells. *Nanoscale*, 9(23):8024–8032, 2017.

[171] Y. Kitahama, H. Hayashi, T. Itoh, and Y. Ozaki. Measurement of pH-dependent surface-enhanced hyper-Raman scattering at desired positions on yeast cells via optical trapping. *Analyst*, 142(20):3967–3974, 2017.

[172] Y. Q. He, S. P. Liu, L. Kong, and Z. F. Liu. A study on the sizes and concentrations of gold nanoparticles by spectra of absorption, resonance Rayleigh scattering and resonance non-linear scattering. *Spectrochimica Acta Part A: Molecular and Biomolecular Spectroscopy*, 61(13):2861–2866, 2005.

[173] W. Haiss, N. T. K. Thanh, J. Aveyard, and D. G. Fernig. Determination of size and concentration of gold nanoparticles from UV-Vis spectra. *Analytical Chemistry*, 79(11):4215–4221, 2007.

[174] W. Leng, H. Y. Woo, D. Vak, G. C. Bazan, and A. M. Kelley. Surface-enhanced resonance Raman and hyper-Raman spectroscopy of water-soluble substituted stilbene and distyrylbenzene chromophores. *Journal of Raman Spectroscopy*, 37(1-3):132–141, 2006.

[175] M. Gühlke, Z. Heiner, and J. Kneipp. Surface-enhanced Raman and surface-enhanced hyper-Raman scattering of thiol-functionalized carotene. *The Journal of Physical Chemistry C*, 120(37):20702–20709, 2016.

[176] A. M. Kelley, W. Leng, and M. Blanchard-Desce. Resonance hyper-Raman scattering from conjugated organic donor-acceptor "push-pull" chromophores with large first hyperpolarizabilities. *Journal of the American Chemical Society*, 125(35):10520–10521, 2003.

[177] K. Kneipp, H. Kneipp, R. Manoharan, E. B. Hanlon, I. Itzkan, R. R. Dasari, and M. S. Feld. Extremely large enhancement factors in surface-enhanced Raman scattering for molecules on colloidal gold clusters. *Applied Spectroscopy*, 52(12):1493–1497, 1998.

[178] K. Kneipp, H. Kneipp, and J. Kneipp. Surface-enhanced Raman scattering in local optical fields of silver and gold nanoaggregatesfrom single-molecule Raman spectroscopy to ultrasensitive probing in live cells. *Accounts of Chemical Research*, 39(7):443–450, 2006.

[179] V. Joseph, A. Matschulat, J. Polte, S. Rolf, F. Emmerling, and J. Kneipp. SERS enhancement of gold nanospheres of defined size. *Journal of Raman Spectroscopy*, 42(9):1736–1742, 2011.

[180] M. K. Hossain, G. G. Huang, T. Kaneko, and Y. Ozaki. Surface-enhanced Raman scattering and plasmon excitations from isolated and elongated gold nanoaggregates. *Chemical Physics Letters*, 477(1):130–134, 2009.

[181] S. L. Kleinman, B. Sharma, M. G. Blaber, A. Henry, N. Valley, R. G. Freeman, M. J. Natan, G. C. Schatz, and R. P. Van Duyne. Structure enhancement factor relationships in single gold nanoantennas by surface-enhanced Raman excitation spectroscopy. *Journal of the American Chemical Society*, 135(1):301–308, 2013.

[182] R. Sasai, T. Fujita, N. Iyi, H. Itoh, and K. Takagi. Aggregated structures of rhodamine 6G intercalated in a fluor-taeniolite thin film. *Langmuir*, 18(17):6578–6583, 2002.

[183] H. Xu, J. Aizpurua, M. Käll, and P. Apell. Electromagnetic contributions to single-molecule sensitivity in surface-enhanced Raman scattering. *Physical Review E*, 62(3):4318–4324, 2000.

[184] F. Le, D. W. Brandl, Y. A. Urzhumov, H. Wang, J. Kundu, N. J. Halas, J. Aizpurua, and P. Nordlander. Metallic nanoparticle arrays: A common substrate for both surface-enhanced Raman scattering and surface-enhanced infrared absorption. *ACS Nano*, 2(4):707–718, 2008.

[185] P. F. Liao and A. Wokaun. Lightning rod effect in surface enhanced Raman scattering. *The Journal of Chemical Physics*, 76(1):751–752, 1982.

[186] B. Nikoobakht and M. A. El-Sayed. Surface-enhanced Raman scattering studies on aggregated gold nanorods. *The Journal of Physical Chemistry A*, 107(18):3372–3378, 2003.

[187] A. F. Stewart, B. P. Gagnon, and G. C. Walker. Forming end-to-end oligomers of gold nanorods using porphyrins and phthalocyanines. *Langmuir*, 31(24):6902–6908, 2015.

[188] V. P. Drachev, M. D. Thoreson, E. N. Khaliullin, V. J. Davisson, and V. M. Shalaev. Surface-enhanced Raman difference between human insulin and insulin lispro detected with adaptive nanostructures. *The Journal of Physical Chemistry B*, 108(46):18046–18052, 2004.

[189] R. F. Aroca, P. J. G. Goulet, D. S. dos Santos, R. A. Alvarez-Puebla, and O. N. Oliveira. Silver nanowire layer-by-layer films as substrates for surface-enhanced Raman scattering. *Analytical Chemistry*, 77(2):378–382, 2005.

[190] L. Chen, X. Han, J. Yang, J. Zhou, W. Song, B. Zhao, W. Xu, and Y. Ozaki. Detection of proteins on silica–silver core–shell substrates by surface-enhanced Raman spectroscopy. *Journal of Colloid and Interface Science*, 360(2):482–487, 2011.

[191] V. Joseph, C. Engelbrekt, J. Zhang, U. Gernert, J. Ulstrup, and J. Kneipp. Characterizing the kinetics of nanoparticle-catalyzed reactions by surface-enhanced Raman scattering. *Angewandte Chemie International Edition*, 51(30):7592–7596, 2012.

[192] S. Chen, L. Meng, J. Hu, and Z. Yang. Fano interference between higher localized and propagating surface plasmon modes in nanovoid arrays. *Plasmonics*, 10(1):71–76, 2015.

[193] X. Lang, T. Qiu, Y. Yin, F. Kong, L. Si, Q. Hao, and P. K. Chu. Silver nanovoid arrays for surface-enhanced Raman scattering. *Langmuir*, 28(23):8799–8803, 2012.

[194] N. G. Tognalli, A. Fainstein, E. J. Calvo, M. Abdelsalam, and P. N. Bartlett. Incident wavelength resolved resonant SERS on Au sphere segment void (SSV) arrays. *The Journal of Physical Chemistry C*, 116(5):3414–3420, 2012.

[195] M. Kahraman, P. Daggumati, O. Kurtulus, E. Seker, and S. Wachsmann-Hogiu. Fabrication and characterization of flexible and tunable plasmonic nanostructures. *Scientific Reports*, 3:3396, 2013.

[196] X. Zhu, L. Shi, M. S. Schmidt, A. Boisen, O. Hansen, J. Zi, S. Xiao, and N. A. Mortensen. Enhanced light–matter interactions in graphene-covered gold nanovoid arrays. *Nano Letters*, 13(10):4690–4696, 2013.

[197] A. Kuchmizhak, O. Vitrik, Yu Kulchin, D. Storozhenko, A. Mayor, A. Mirochnik, S. Makarov, V. Milichko, S. Kudryashov, V. Zhakhovsky, and N. Inogamov. Laser printing of resonant plasmonic nanovoids. *Nanoscale*, 8(24):12352–12361, 2016.

[198] M. Schmidt, N. G. Tognalli, M. A. Otte, M. I. Alonso, B. Sepulveda, A. Fainstein, and A. R. Goñi. Spatial distribution of optical near-fields in plasmonic gold sphere segment voids. *Plasmonics*, 8(2):921–930, 2013.

[199] F. Madzharova, Z. Heiner, J. Simke, S. Selve, and J. Kneipp. Gold nanostructures for plasmonic enhancement of hyper-Raman scattering. *The Journal of Physical Chemistry C*, 122(5):2931–2940, 2018.

[200] V. Zivanovic, F. Madzharova, Z. Heiner, C. Arenz, and J. Kneipp. Specific interaction of tricyclic antidepressants with gold and silver nanostructures as revealed by combined one- and two-photon vibrational spectroscopy. *The Journal of Physical Chemistry C*, 121(41):22958–22968, 2017.

[201] N. S. Allen, N. Hughes, and P. Mahon. Photochemical fading and photostabilization of the crystal violet lactone colour former system. *Journal of Photochemistry*, 37(2):379–390, 1987.

[202] A. C. Bhasikuttan, A. V. Sapre, K. V. S. Rama Rao, and J. P. Mittal. Photoionization of crystal violet in aqueous solution. *Photochemistry and Photobiology*, 62(2):245–250, 1995.

[203] T. Terai and T. Nagano. Small-molecule fluorophores and fluorescent probes for bioimaging. *Pflügers Archiv - European Journal of Physiology*, 465(3):347–359, 2013.

[204] M. Pawlicki, H. A. Collins, R. G. Denning, and H. L. Anderson. Two-photon absorption and the design of two-photon dyes. *Angewandte Chemie International Edition*, 48(18):3244–3266, 2009.

[205] I. L. Medintz, H. T. Uyeda, E. R. Goldman, and H. Mattoussi. Quantum dot bioconjugates for imaging, labelling and sensing. *Nature Materials*, 4:435, 2005.

[206] N. Sugiyama, A. Y. Sonay, R. Tussiwand, B. E. Cohen, and P. Pantazis. Effective labeling of primary somatic stem cells with $BaTiO_3$ nanocrystals for second harmonic generation imaging. *Small*, 14(8):1703386, 2018.

[207] G. G. Genchi, A. Marino, A. Rocca, V. Mattoli, and G. Ciofani. Barium titanate nanoparticles: promising multitasking vectors in nanomedicine. *Nanotechnology*, 27(23):232001, 2016.

[208] W. P. Dempsey, S. E. Fraser, and P. Pantazis. SHG nanoprobes: Advancing harmonic imaging in biology. *BioEssays*, 34(5):351–360, 2012.

[209] T. Pham, J. B. Jackson, N. J. Halas, and T. R. Lee. Preparation and characterization of gold nanoshells coated with self-assembled monolayers. *Langmuir*, 18(12):4915–4920, 2002.

[210] D. Yoon, B. I. Lee, P. Badheka, and X. Wang. Barium ion leaching from barium titanate powder in water. *Journal of Materials Science: Materials in Electronics*, 14(3):165–169, 2003.

[211] A. Usher, D. C. McPhail, and J. Brugger. A spectrophotometric study of aqueous Au(III) halide–hydroxide complexes at 25–80°C. *Geochimica et Cosmochimica Acta*, 73(11):3359–3380, 2009.

[212] S. L. Westcott, S. J. Oldenburg, T. R. Lee, and N. J. Halas. Formation and adsorption of clusters of gold nanoparticles onto functionalized silica nanoparticle surfaces. *Langmuir*, 14(19):5396–5401, 1998.

[213] F. Timpu, N. R. Hendricks, M. Petrov, S. Ni, C. Renaut, H. Wolf, L. Isa, Y. Kivshar, and R. Grange. Enhanced second-harmonic generation from sequential capillarity-assisted particle assembly of hybrid nanodimers. *Nano Letters*, 17(9):5381–5388, 2017.

[214] L. Jiang, Z. Wu, D. Wu, W. Yang, and R. Jin. Controllable embedding of silver nanoparticles on silica nanospheres using poly(acrylic acid) as a soft template. *Nanotechnology*, 18(18):185603, 2007.

[215] S. Mühlig, A. Cunningham, S. Scheeler, C. Pacholski, T. Bürgi, C. Rockstuhl, and F. Lederer. Self-assembled plasmonic core–shell clusters with an isotropic magnetic dipole response in the visible range. *ACS Nano*, 5(8):6586–6592, 2011.

[216] C. R. Simovski and S. A. Tretyakov. Model of isotropic resonant magnetism in the visible range based on core-shell clusters. *Physical Review B*, 79(4):045111, 2009.

[217] R. Esteban, R. W. Taylor, J. J. Baumberg, and J. Aizpurua. How chain plasmons govern the optical response in strongly interacting self-assembled metallic clusters of nanoparticles. *Langmuir*, 28(24):8881–8890, 2012.

[218] P. Albella, M. A. Poyli, M. K. Schmidt, S. A. Maier, F. Moreno, J. J. Sáenz, and J. Aizpurua. Low-loss electric and magnetic field-enhanced spectroscopy with subwavelength silicon dimers. *The Journal of Physical Chemistry C*, 117(26):13573–13584, 2013.

[219] M. Caldarola, P. Albella, E. Cortes, M. Rahmani, T. Roschuk, G. Grinblat, R. F. Oulton, A. V. Bragas, and S. A. Maier. Non-plasmonic nanoantennas for surface enhanced spectroscopies with ultra-low heat conversion. *Nat Commun*, 6, 2015.

[220] R Carminati, M. Nieto-Vesperinas, and J.-J. Greffet. Reciprocity of evanescent electromagnetic waves. *Journal of the Optical Society of America A*, 15(3):706–712, 1998.

[221] P. Bharadwaj, B. Deutsch, and L. Novotny. Optical antennas. *Advances in Optics and Photonics*, 1(3):438–483, 2009.

[222] R. Esteban, M. Laroche, and J.-J. Greffet. Influence of metallic nanoparticles on upconversion processes. *Journal of Applied Physics*, 105(3):033107, 2009.

[223] M. Baudrier-Raybaut, R. Haïdar, P. Kupecek, P. Lemasson, and E. Rosencher. Random quasi-phase-matching in bulk polycrystalline isotropic nonlinear materials. *Nature*, 432(7015):374–376, 2004.

[224] E. V. Makeev and S. E. Skipetrov. Second harmonic generation in suspensions of spherical particles. *Optics Communications*, 224(1):139–147, 2003.

[225] S. Brasselet, V. Le Floc'h, F. Treussart, J.-F. Roch, J. Zyss, E. Botzung-Appert, and A. Ibanez. In situ diagnostics of the crystalline nature of single organic nanocrystals by nonlinear microscopy. *Physical Review Letters*, 92(20):207401, 2004.

[226] J. Chen, P. Albella, Z. Pirzadeh, P. Alonso-González, F. Huth, S. Bonetti, V. Bonanni, J. Åkerman, J. Nogués, P. Vavassori, A. Dmitriev, J. Aizpurua, and R. Hillenbrand. Plasmonic nickel nanoantennas. *Small*, 7(16):2341–2347, 2011.

[227] J. Zuloaga and P. Nordlander. On the energy shift between near-field and far-field peak intensities in localized plasmon systems. *Nano Letters*, 11(3):1280–1283, 2011.

[228] S. V. Makarov, M. I. Petrov, U. Zywietz, V. Milichko, D. Zuev, N. Lopanitsyna, A. Kuksin, I. Mukhin, G. Zograf, E. Ubyivovk, D. A. Smirnova, S. Starikov, B. N. Chichkov, and Y. S. Kivshar. Efficient second-harmonic generation in nanocrystalline silicon nanoparticles. *Nano Letters*, 17(5):3047–3053, 2017.

[229] A. L. Dendramis, E. W. Schwinn, and R. P. Sperline. A surface-enhanced Raman scattering study of CTAB adsorption on copper. *Surface Science*, 134(3):675–688, 1983.

[230] D. Drescher, P. Guttmann, T. Büchner, S. Werner, G. Laube, A. Hornemann, B. Tarek, G. Schneider, and J. Kneipp. Specific biomolecule corona is associated with ring-shaped organization of silver nanoparticles in cells. *Nanoscale*, 5(19):9193–9198, 2013.

[231] D. Drescher, I. Zeise, H. Traub, P. Guttmann, S. Seifert, T. Büchner, N. Jakubowski, G. Schneider, and J. Kneipp. In situ characterization of SiO_2 nanoparticle biointeractions using BrightSilica. *Advanced Functional Materials*, 24(24):3765–3775, 2014.

[232] A. Michota and J. Bukowska. Surface-enhanced Raman scattering (SERS) of 4-mercaptobenzoic acid on silver and gold substrates. *Journal of Raman Spectroscopy*, 34(1):21–25, 2003.

[233] J. Kneipp, H. Kneipp, M. McLaughlin, D. Brown, and K. Kneipp. In vivo molecular probing of cellular compartments with gold nanoparticles and nanoaggregates. *Nano Letters*, 6(10):2225–2231, 2006.

[234] V. Zivanovic, Z. Kochovski, C. Arenz, Y. Lu, and J. Kneipp. SERS and cryo-EM directly reveal different liposome structures during interaction with gold nanoparticles. *The Journal of Physical Chemistry Letters*, pages 6767–6772, 2018.

[235] Z. Movasaghi, S. Rehman, and I. U. Rehman. Raman spectroscopy of biological tissues. *Applied Spectroscopy Reviews*, 42(5):493–541, 2007.

[236] S. J. Cyvin, J. E. Rauch, and J. C. Decius. Theory of hyper-Raman effects (nonlinear inelastic light scattering): Selection rules and depolarization ratios for the second order polarizability. *The Journal of Chemical Physics*, 43(11):4083–4095, 1965.

[237] A. Rygula, K. Majzner, K. M. Marzec, A. Kaczor, M. Pilarczyk, and M. Baranska. Raman spectroscopy of proteins: a review. *Journal of Raman Spectroscopy*, 44(8):1061–1076, 2013.

[238] R. Schweitzer-Stenner. Advances in vibrational spectroscopy as a sensitive probe of peptide and protein structure: A critical review. *Vibrational Spectroscopy*, 42(1):98–117, 2006.

[239] P. G. Hildebrandt, R. A. Copeland, T. G. Spiro, J. Otlewski, M. Laskowski, and F. G. Prendergast. Tyrosine hydrogen-bonding and environmental effects in proteins probed by ultraviolet resonance Raman spectroscopy. *Biochemistry*, 27(15):5426–5433, 1988.

[240] I. K. Lednev, V. V. Ermolenkov, W. He, and M. Xu. Deep-UV Raman spectrometer tunable between 193 and 205 nm for structural characterization of proteins. *Analytical and Bioanalytical Chemistry*, 381(2):431–437, 2005.

[241] C. Huang, G. Balakrishnan, and T. G. Spiro. Protein secondary structure from deep-UV resonance Raman spectroscopy. *Journal of Raman Spectroscopy*, 37(1-3):277–282, 2006.

[242] O. O. Oshokoya and R. D. JiJi. Parallel factor analysis of multi-excitation ultraviolet resonance Raman spectra for protein secondary structure determination. *Analytica Chimica Acta*, 892:59–68, 2015.

[243] G. Szekeres and J. Kneipp. SERS probing of proteins in gold nanoparticle agglomerates. *Frontiers in Chemistry*, 7(30), 2019.

[244] X. X. Han, G. G. Huang, B. Zhao, and Y. Ozaki. Label-free highly sensitive detection of proteins in aqueous solutions using surface-enhanced Raman scattering. *Analytical Chemistry*, 81(9):3329–3333, 2009.

[245] K. Kneipp, H. Kneipp, S. Abdali, R. W. Berg, and H. Bohr. Single molecule Raman detection of enkephalin on silver colloidal particles. *Spectroscopy*, 18(3), 2004.

[246] S. Seifert, V. Merk, and J. Kneipp. Identification of aqueous pollen extracts using surface enhanced Raman scattering (SERS) and pattern recognition methods. *Journal of Biophotonics*, 9(1-2):181–189, 2016.

[247] H. Schulz and M. Baranska. Identification and quantification of valuable plant substances by IR and Raman spectroscopy. *Vibrational Spectroscopy*, 43(1):13–25, 2007.

[248] M. Aioub and M. A. El-Sayed. A real-time surface enhanced Raman spectroscopy study of plasmonic photothermal cell death using targeted gold nanoparticles. *Journal of the American Chemical Society*, 138(4):1258–1264, 2016.

[249] B. Hernandez, Y. Coic, F. Pflüger, S. G. Kruglik, and M. Ghomi. All characteristic Raman markers of tyrosine and tyrosinate originate from phenol ring fundamental vibrations. *Journal of Raman Spectroscopy*, 47(2):210–220, 2016.

[250] B. Hernandez, F. Pflüger, A. Adenier, S. G. Kruglik, and M. Ghomi. Vibrational analysis of amino acids and short peptides in hydrated media. VIII. Amino acids with aromatic side chains: L-phenylalanine, L-tyrosine, and L-tryptophan. *The Journal of Physical Chemistry B*, 114(46):15319–15330, 2010.

[251] C. Chuang and Y. Chen. Raman scattering of L-tryptophan enhanced by surface plasmon of silver nanoparticles: vibrational assignment and structural determination. *Journal of Raman Spectroscopy*, 40(2):150–156, 2009.

[252] S. A. Asher, M. Ludwig, and C. R. Johnson. UV resonance Raman excitation profiles of the aromatic amino acids. *Journal of the American Chemical Society*, 108(12):3186–3197, 1986.

[253] R. P. Rava and T. G. Spiro. Resonance enhancement in the ultraviolet Raman spectra of aromatic amino acids. *The Journal of Physical Chemistry*, 89(10):1856–1861, 1985.

[254] S. K. Kim, M. S. Kim, and S. W. Suh. Surface-enhanced Raman scattering (SERS) of aromatic amino acids and their glycyl dipeptides in silver sol. *Journal of Raman Spectroscopy*, 18(3):171–175, 1987.

[255] S. Martusevicius, G. Niaura, Z. Talaikyte, and V. Razumas. Adsorption of L-histidine on copper surface as evidenced by surface-enhanced Raman scattering spectroscopy. *Vibrational Spectroscopy*, 10(2):271–280, 1996.

[256] J. G. Mesu, T. Visser, F. Soulimani, and B. M. Weckhuysen. Infrared and Raman spectroscopic study of pH-induced structural changes of L-histidine in aqueous environment. *Vibrational Spectroscopy*, 39(1):114–125, 2005.

[257] B. Hernandez, F. Pflüger, S. G. Kruglik, and M. Ghomi. Characteristic Raman lines of phenylalanine analyzed by a multiconformational approach. *Journal of Raman Spectroscopy*, 44(6):827–833, 2013.

[258] J. Guicheteau, L. Argue, A. Hyre, M. Jacobson, and S. D. Christesen. Raman and surface-enhanced Raman spectroscopy of amino acids and nucleotide bases for target bacterial vibrational mode identification. volume 6218, pages 62180O–62180O–11.

[259] I. R. Nabiev, V. A. Savchenko, and E. S. Efremov. Surface-enhanced Raman spectra of aromatic amino acids and proteins adsorbed by silver hydrosols. *Journal of Raman Spectroscopy*, 14(6):375–379, 1983.

[260] T. Cedervall, I. Lynch, S. Lindman, T. Berggard, E. Thulin, H. Nilsson, K. A. Dawson, and S. Linse. Understanding the nanoparticle–protein corona using methods to quantify exchange rates and affinities of proteins for nanoparticles. *Proceedings of the National Academy of Sciences*, 104(7):2050–2055, 2007.

[261] K. Kneipp and H. Kneipp. Probing the plasmonic near-field by one- and two-photon excited surface enhanced Raman scattering. *Beilstein Journal of Nanotechnology*, 4:834–842, 2013.

[262] S. Mahajan, R. M. Cole, J. D. Speed, S. H. Pelfrey, A. E. Russell, P. N. Bartlett, S. M. Barnett, and J. J. Baumberg. Understanding the surface-enhanced Raman spectroscopy "background". *The Journal of Physical Chemistry C*, 114(16):7242–7250, 2010.

[263] S. Li, D. Wu, X. Xu, and R. Gu. Theoretical and experimental studies on the adsorption behavior of thiophenol on gold nanoparticles. *Journal of Raman Spectroscopy*, 38(11):1436–1443, 2007.

[264] T. G. Lee, K. Kim, and M. S. Kim. Raman scattering of α-toluenethiol adsorbed on silver sol. *Journal of Raman Spectroscopy*, 22(6):339–344, 1991.

[265] T. H. Joo, M. S. Kim, and K. Kim. Surface-enhanced Raman scattering of benzenethiol in silver sol. *Journal of Raman Spectroscopy*, 18(1):57–60, 1987.

[266] A. I. Fishman, A. E. Klimovitskii, A. I. Skvortsov, and A. B. Remizov. The vibrational spectra and conformations of ethylbenzene. *Spectrochimica Acta Part A: Molecular and Biomolecular Spectroscopy*, 60(4):843–853, 2004.

[267] H. K. Turley and J. P. Camden. A nonlinear approach to surface-enhanced sensing in the short-wave infrared. *Chemical Communications*, 50(12):1472–1474, 2014.

[268] C. A. Szafranski, W. Tanner, P. E. Laibinis, and R. L. Garrell. Surface-enhanced Raman spectroscopy of aromatic thiols and disulfides on gold electrodes. *Langmuir*, 14(13):3570–3579, 1998.

[269] K. T. Carron and L. G. Hurley. Axial and azimuthal angle determination with surface-enhanced Raman spectroscopy: thiophenol on copper, silver, and gold metal surfaces. *The Journal of Physical Chemistry*, 95(24):9979–9984, 1991.

[270] J. Zheng, Y. Zhou, X. Li, Y. Ji, T. Lu, and R. Gu. Surface-enhanced Raman scattering of 4-aminothiophenol in assemblies of nanosized particles and the macroscopic surface of silver. *Langmuir*, 19(3):632–636, 2003.

[271] B. Nikoobakht and M. A. El-Sayed. Surface-enhanced Raman scattering studies on aggregated gold nanorods. *The Journal of Physical Chemistry A*, 107(18):3372–3378, 2003.

[272] M. A. Bryant and R. M. Crooks. Determination of surface pKa values of surface-confined molecules derivatized with pH-sensitive pendant groups. *Langmuir*, 9(2):385–387, 1993.

[273] Y. Huang, M. Zhang, L. Zhao, J. Feng, D. Wu, B. Ren, and Z. Tian. Activation of oxygen on gold and silver nanoparticles assisted by surface plasmon resonances. *Angewandte Chemie International Edition*, 53(9):2353–2357, 2014.

[274] Y. Huang, H. Zhu, G. Liu, D. Wu, B. Ren, and Z. Tian. When the signal is not from the original molecule to be detected: Chemical transformation of para-aminothiophenol on Ag during the SERS measurement. *Journal of the American Chemical Society*, 132(27):9244–9246, 2010.

[275] W. P. Griffith and T. Y. Koh. Vibrational spectra of 1,2-benzenedithiol, 2-aminothiophenol and 2-aminophenol and their SER spectra. *Spectrochimica Acta Part A: Molecular and Biomolecular Spectroscopy*, 51(2):253–267, 1995.

[276] M. Osawa, N. Matsuda, K. Yoshii, and I. Uchida. Charge transfer resonance Raman process in surface-enhanced Raman scattering from p-aminothiophenol adsorbed on silver: Herzberg-Teller contribution. *The Journal of Physical Chemistry*, 98(48):12702–12707, 1994.

[277] D. Maniu, V. Chis, M. Baia, F. Toderas, and S. Astilean. Density functional theory investigation of p-aminothiophenol molecules adsorbed on gold nanoparticles. *Journal of Optoelectronics and Advanced Materials*, 9(3):733–736, 2007.

[278] Z. Hu, D. V. Chulhai, and L. Jensen. Simulating surface-enhanced hyper-Raman scattering using atomistic electrodynamics-quantum mechanical models. *Journal of Chemical Theory and Computation*, 12(12):5968–5978, 2016.

List of abbreviations

APTES	(3-aminopropyl)triethoxysilane
ATP	aminothiophenol
CTAB	hexadecyltrimethylammonium bromide
CV	crystal violet
DFT	density functional theory
DLS	dynamic light scattering
DMAB	dimercaptoazobenzene
EF	enhancement factor
FDTD	finite-difference time-domain
HRS	hyper Raman scattering
IR	infrared
LSP	localized surface plasmon-polariton
LSPR	localized surface plasmon resonance
MPTS	(3-mercaptopropyl)trimethoxysilane
NA	numerical aperture
***p*MBA**	*para*-mercaptobenzoic acid
R6G	rhodamine 6G
RS	Raman scattering
SDC	scanning droplet cell
SEHRS	surface enhanced hyper Raman scattering
SEM	scanning electron microscopy
SERS	surface enhanced Raman scattering
SHG	second harmonic generation
TEM	transmission electron microscopy
THPC	tetrakis(hydroxymethyl)phosphonium chloride
UV	ultraviolet
vis	visible

List of figures

List of tables

List of publications

Journal articles discussed in this thesis

1. **F. Madzharova**, Z. Heiner, and J. Kneipp. Surface Enhanced Hyper Raman Spectra of Aromatic Thiols on Gold and Silver Nanoparticles. *J. Phys. Chem. C* **2020**, doi: 10.1021/acs.jpcc.0c00294.
2. **F. Madzharova**, A. Nodar, V. Živanović, M. Huang, C. Koch, R. Esteban, J. Aizpurua, and J. Kneipp. Gold and silver coated barium titanate nanocomposites as probes for two-photon multimodal microspectroscopy. *Advanced Functional Materials* **2019**, *29*, 1904289.
3. **F. Madzharova**, D. Öhl, J. Junqueira, W. Schuhmann, and J. Kneipp. Plasmon enhanced two-photon probing with gold and silver nanovoid structures. *Advanced Optical Materials* **2019**, *7*, 1900650.
4. **F. Madzharova**, Z. Heiner, J. Simke, S. Selve, and J. Kneipp. Gold Nanostructures for Plasmonic Enhancement of Hyper-Raman Scattering. *The Journal of Physical Chemistry C* **2018**, *122*, 2931-2940.
5. **F. Madzharova**, Z. Heiner, and J. Kneipp. Surface enhanced hyper Raman scattering (SEHRS) and its applications. *Chemical Society Reviews* **2017**, *46*, 3980-3999.
6. **F. Madzharova**, Z. Heiner, and J. Kneipp. Surface Enhanced Hyper-Raman Scattering of the Amino Acids Tryptophan, Histidine, Phenylalanine, and Tyrosine. *The Journal of Physical Chemistry C* **2017**, *121*, 1235-1242.

Other journal articles

1. V. Živanović, **F. Madzharova**, Z. Heiner, C. Arenz, and J. Kneipp. Specific Interaction of Tricyclic Antidepressants with Gold and Silver Nanostructures as Revealed by

Combined One- and Two-Photon Vibrational Spectroscopy. *The Journal of Physical Chemistry C* **2017**, *121*, 22958-22968.

2. Z. Heiner, M. Gühlke, V. Živanović, **F. Madzharova**, and J. Kneipp. Surface-enhanced hyper Raman hyperspectral imaging and probing in animal cells. *Nanoscale* **2017**, *9*, 8024-8032.

3. V. Andrei, K. Bethke, **F. Madzharova**, A. C. Bronneberg, J. Kneipp, and K. Rademann. In Situ Complementary Doping, Thermoelectric Improvements, and Strain-Induced Structure within Alternating PEDOT:PSS/PANI Layers. *ACS Applied Materials & Interfaces* **2017**, *9*, 33308-33316.

4. V. Andrei, K. Bethke, **F. Madzharova**, S. Beeg, A. Knop-Gericke, J. Kneipp, and K. Rademann. Size Dependence of Electrical Conductivity and Thermoelectric Enhancements in Spin-Coated PEDOT:PSS Single and Multiple Layers. *Advanced Electronic Materials* **2017**, *3*, 1600473.

5. **F. Madzharova**, Z. Heiner, M. Gühlke, and J. Kneipp. Surface-Enhanced Hyper-Raman Spectra of Adenine, Guanine, Cytosine, Thymine, and Uracil. *The Journal of Physical Chemistry C* **2016**, *120*, 15415-15423.

6. M. P. Lara-Castells, R. Fernández-Perea, **F. Madzharova**, and E. Voloshina. Post-Hartree-Fock Studies of the He/Mg(0001) Interaction: Anti-Corrugation, Screening, and Pairwise Additivity. *The Journal of Chemical Physics* **2016**, *144*, 244707.

Conference contributions

1. **F. Madzharova**, Z. Heiner, and J. Kneipp. Plasmonic enhancement of hyper Raman scattering by gold nanostructures. *Molecular Plasmonics*, Jena, Germany, May 2019 (Abstract & **Talk**).

2. **F. Madzharova**, Z. Heiner, and J. Kneipp. Gold Nanorods and Nanoparticles for Surface Enhanced Hyper Raman Scattering. *International Conference on Raman Spectroscopy*, Jeju, Republic of Korea, August 2018 (Abstract & **Talk**). Travel grant awarded by the German Research Foundation (Deutsche Forschungsgemeinschaft, DFG) and Society of German Chemists (Gesellschaft Deutscher Chemiker, GDCh)

3. **F. Madzharova**, Z. Heiner, and J. Kneipp. Surface enhanced hyper-Raman scattering of biomolecules on silver nanostructures. *Adlershofer Forschungsforum 2017*, Berlin, Germany, Novermber 2017 (Abstract & **Poster**).

4. Z. Heiner, **F. Madzharova**, V. Zivanovic, M. Gühlke, and J. Kneipp. Surface enhanced hyper Raman scattering for bioapplications. *FTIR Spectroscopy in Microbiological and Medical Diagnostics*, Berlin, Germany, October 2017 (Abstract & **Poster**, **poster prize**).

5. **F. Madzharova**, Z. Heiner, and J. Kneipp. Hyper Raman scattering enhanced by gold nanostructures. *International Conference on Enhanced Spectroscopies*, Munich, Germany, September 2017 (Abstract & **Talk**).

6. **F. Madzharova**, Z. Heiner, and J. Kneipp. Surface-enhanced hyper-Raman and Raman scattering of biomolecules on silver nanostructures. *Molecular Plasmonics*, Jena, Germany, May 2017 (Abstract & **Poster**).

7. **F. Madzharova**, Z. Heiner, and J. Kneipp. Surface enhanced hyper-Raman scattering from biomolecules. 4^{th} *Annual Conference on Optical Nanospectroscopy*, Lisbon, Portugal, March 2017 (Abstract & **Talk**).

8. **F. Madzharova**, Z. Heiner, and J. Kneipp. Surface enhanced hyper-Raman spectroscopic study of DNA and RNA nucleobases. *School of Photonics 2016: "Plasmonics and Nano-Optics"*, Cortona, Italy, July 2016 (Abstract & **Poster**).

9. **F. Madzharova**, Z. Heiner, and J. Kneipp. Investigation of nucleobases and their interactions with silver nanoparticles by surface enhanced hyper-Raman scattering. *606. WE-Heraeus-Seminar on "Nanophotonics and Complex Spatial Modes of Light"*, Bad Honnef, Germany, January 2016 (Abstract & **Poster**).

Acknowledgements

I want to thank here all the people who have directly or indirectly contributed to this work and have made my life easier and enjoyable in the last years.

My special thanks go to Prof. Janina Kneipp, who has been, after all, my mentor and part of my life since I joined her group as a student assistant six years ago. Dear Janina, thank you for all of your enthusiasm about hyper Raman scattering and for your optimistic approach when discussing results! This has ensured my psychological well-being as a graduate student and is highly appreciated. I thank you for everything that I have learned from you about research and scientific life. I certainly consider myself lucky to have you as a supervisor.

I thank Dr. Zsuzsanna Heiner for supporting the experiments in the optics lab and her energetic personality. I thank Dr. Harald Kneipp for supporting the laser setups. All the work of this thesis would not have been possible without their contribution to the measurement devices. I also thank Dr. Marina Gühlke for guiding me in the wet- and optics labs at the beginning of my work in the group.

I thank Prof. Wolfgang Schuhmann and Denis Öhl from Ruhr University Bochum for the fruitful and smooth collaboration on the nanovoids project. I want to acknowledge here also the contributions from the rest of their team by João Junqueira and Dr. Ugur Kayran.

I am very grateful to Dr. Rubén Esteban and Prof. Javier Aizpurua for hosting me during my short visit at Donostia International Physics Center (DIPC). I thank Rubén Esteban and Alvaro Nodar for their help and valuable contributions to the project. I also thank Dr. Luca Bergamini for helping me with Lumerical FDTD Solutions, and the people I met at CFM/DIPC for providing a nice atmosphere.

I thank Jan Simke, Sören Selve, and Dr. Ulrich Gernert from ZELMI, Technical University of Berlin, Dr. Dorota Bartkowiak and Prof. Nicola Pinna for TEM and SEM measurements. I thank Dr. Franziska Emmerling and Dr. Ralf Bienert for the opportunity to perform DLS experiments at BAM Federal Institute for Materials Research and Testing. I further thank Dr. Franziska Emmerling, Manuel Wilke, and Dominik Lubjuhn from BAM for XRD measurements and help with hydrothermal synthesis. I thank Zsuzsanna Heiner and Freeda

Yesudas for the measurements at SALSA Application lab. I thank Sabrina Diehn for system administration and Bernd Böttcher for help with Gaussian.

I want to acknowledge here the funding from the Chemical Industry Fund (FCI) that had a valuable impact on the quality of my life.

I am very thankful to all former and present members of the Kneipp group for ensuring relaxed working atmosphere and for participation in diverting group activities. I thank Barbara Franke and Annette Rothe for their excellent administrative and technical assistance. In particular, I want to name here Dr. Daniela Drescher, Dr. Virginia Merk, Dr. Cecilia Spedalieri, Sabrina Diehn, Gergő Szekeres, Victor Rodriguez, Tom Lindtner, Franziska Lauer, and Alexander Pankratov for sharing together lab, teaching, and office duties. Many words of thanks go to my friend Dr. Vesna Živanović for collaborating with me on so many scientific and non-scientific levels.

I want to thank here again Gergő, Cecilia, Tom, Daniela, Sabrina, Vesna, and Kaloyan for proofreading chapters of this dissertation.

I thank my friends and colleagues from the campus who have shared their lunchtime and life experience from all around the world with me. Thank you Marcel, Milan, Marcin, Jakob, Radek, Brian, Vesna, Sabrina, Arpan, Gergő, Victor, Tom, Stephen, Cecilia, Maristella, and Chris. In this context, I also thank the HU Oase Adlershof cafeteria team for providing me with food for these lunch breaks persistently during all years.

I am very grateful to my friends from Bulgaria for their time and effort to stay in touch despite the distance. I particularly thank Liz and Davide, and Ani, who have been by my side through my whole academic life in Berlin. Last and most important, I thank my parents Elena and George for their unconditional love and support that always makes me feel very welcome back home.

Erklärung

Hiermit versichere ich, dass ich die vorliegende Arbeit selbstständig verfasst und keine anderen als die angegebenen Quellen und Hilfsmittel benutzt habe, dass alle Stellen der Arbeit, die wörtlich oder sinngemäß aus anderen Quellen übernommen wurden, als solche kenntlich gemacht und dass die Arbeit in gleicher oder ähnlicher Form noch keiner Prüfungsbehörde vorgelegt wurde.

Berlin, März 2020

Fani Madzharova